buildings

Special Issue Reprint

Sustainable Concrete

Research on Waste Utilization and Performance Optimization

Edited by
Džigita Nagrockienė and Ramunė Žurauskienė

mdpi.com/journal/buildings

MDPI

Sustainable Concrete: Research on Waste Utilization and Performance Optimization

Sustainable Concrete: Research on Waste Utilization and Performance Optimization

Guest Editors

Džigita Nagrockienė
Ramunė Žurauskienė

MDPI

Basel • Beijing • Wuhan • Barcelona • Belgrade • Novi Sad • Cluj • Manchester

Guest Editors

Džigita Nagrockienė
Department of Building Materials and Fire Safety
Vilnius Gediminas Technical University
Vilnius
Lithuania

Ramunė Žurauskienė
Department of Building Materials and Fire Safety
Vilnius Gediminas Technical University
Vilnius
Lithuania

Editorial Office
MDPI AG
Grosspeteranlage 5
4052 Basel, Switzerland

This is a reprint of the Special Issue, published open access by the journal *Buildings* (ISSN 2075-5309), freely accessible at: https://www.mdpi.com/journal/buildings/special_issues/56J6NR28MI.

For citation purposes, cite each article independently as indicated on the article page online and as indicated below:

Lastname, A.A.; Lastname, B.B. Article Title. *Journal Name* **Year**, *Volume Number*, Page Range.

ISBN 978-3-7258-9645-5 (Hbk)
ISBN 978-3-7258-9646-2 (PDF)
https://doi.org/10.3390/books978-3-7258-9646-2

© 2026 by the authors. Articles in this reprint are Open Access and distributed under the Creative Commons Attribution (CC BY) license. The reprint as a whole is distributed by MDPI under the terms and conditions of the Creative Commons Attribution-NonCommercial-NoDerivs (CC BY-NC-ND) license (https://creativecommons.org/licenses/by-nc-nd/4.0/).

Contents

Preface . . . . . **vii**

Vilma Vaičekauskienė, Džigita Nagrockienė and Ina Pundienė
The Effect of Combining Waste-Derived Pozzolanic and Fibrous Materials with Functional Admixtures on Performance and Corrosion Resistance of Concrete
Reprinted from: *Buildings* **2026**, *16*, 767, https://doi.org/10.3390/buildings16040767 . . . . . **1**

Giedrius Girskas and Modestas Kligys
3D Concrete Printing Review: Equipment, Materials, Mix Design, and Properties
Reprinted from: *Buildings* **2025**, *15*, 2049, https://doi.org/10.3390/buildings15122049 . . . . . **21**

Oskars Lescinskis, Alise Sapata, Girts Bumanis, Maris Sinka, Xiangming Zhou and Diana Bajare
The Potential of Wood Ash to Be Used as a Supplementary Cementitious Material in Cement Mortars
Reprinted from: *Buildings* **2025**, *15*, 1507, https://doi.org/10.3390/buildings15091507 . . . . . **50**

Giedrius Girskas, Dalius Kriptavičius, Olga Kizinievič and Jurgita Malaiškienė
Effect of Pozzolanic Additive on Properties and Surface Finish Assessment of Concrete
Reprinted from: *Buildings* **2025**, *15*, 1617, https://doi.org/10.3390/buildings15101617 . . . . . **63**

Shengtian Zhai, Ran Hai, Zhihang Yu, Jianjun Ma, Chao Hou, Jiufu Zhang, et al.
Interfacial Shrinkage Properties and Mechanism Analysis of Light-Conductive Resin–Cement-Based Materials
Reprinted from: *Buildings* **2025**, *15*, 2754, https://doi.org/10.3390/buildings15152754 . . . . . **83**

Yiying Du, Ina Pundienė and Jolanta Pranckevičienė
Effects of Ca/Si and Si/Al Ratios on the Wood Biomass Ash-Based Alkali-Activated Materials with Pozzolanic Additives
Reprinted from: *Buildings* **2026**, *16*, 51, https://doi.org/10.3390/buildings16010051 . . . . . **102**

Murteda Ünverdi, Sultan Husein Bayqra, Yahya Kaya, Süleyman Özen, Ali Mardani and Kambiz Ramyar
Mechanical Performance, Statistical Optimization, and Environmental Impact of Roller-Compacted Concrete Reinforced with Waste and Industrial Fibers
Reprinted from: *Buildings* **2026**, *16*, 1167, https://doi.org/10.3390/buildings16061167 . . . . . **120**

Džigita Nagrockienė, Ela Jarmolajeva, Vilma Vaičekauskienė and Mečislavas Griškevičius
Effect of Pozzolanic Cement and Ground Glass Waste on Alkali–Silica Reaction of Mortar
Reprinted from: *Buildings* **2026**, *16*, 3519, https://doi.org/10.3390/buildings16173519 . . . . . **156**

Preface

Concrete and other cement-based materials remain among the most widely used construction materials worldwide, making the reduction of their environmental impact an important challenge in modern construction materials engineering. One of the most promising approaches is the partial replacement of cement and other primary raw materials with waste, industrial by-products, and other secondary raw materials. However, sustainability cannot be assessed solely in terms of the amount of primary material replaced. New materials must maintain or improve the required mechanical properties, durability, and technological performance, while their environmental impact should be considered alongside their performance characteristics.

The eight contributions collected in this Reprint represent different approaches to addressing these challenges. Studies on wood ash demonstrate its potential as a partial replacement for Portland cement while also highlighting the importance of pretreatment and optimization of the replacement level. Other research investigates wood biomass ash as a principal raw material for alkali-activated materials, with its properties modified through the incorporation of coal fly ash, metakaolin, and natural zeolite. These findings demonstrate the importance of Ca/Si and Si/Al ratios in the formation of the binding system and the development of mechanical properties.

The potential of waste utilization is also explored in conventional cement-based systems. The combined use of waste metakaolin, cellulose fibers derived from recycled paper, and a functional waterproofing admixture was investigated with the aim of improving the mechanical properties of concrete and its resistance to alkali-related deterioration. Another study demonstrated that replacing 5–10% of pozzolanic cement with ground waste glass can reduce mortar expansion under alkaline conditions while maintaining favorable mechanical properties. Research on natural zeolite showed that a 15% cement replacement level was beneficial to concrete resistance to freeze–thaw cycles and to the surface quality of exposed concrete.

The Reprint also demonstrates that the value of secondary raw materials extends beyond cement replacement. In a study on roller-compacted concrete, waste steel fibers recovered from end-of-life tires were compared with industrial steel and polypropylene fibers. The waste steel fibers provided mechanical performance comparable to that of industrial steel fibers while significantly reducing the embodied carbon associated with fiber reinforcement. This illustrates a broader principle of sustainability: the value of a material should be assessed by considering both its performance and its environmental impact.

In addition, this Reprint addresses topics that extend beyond direct waste utilization and focus on technological and functional advances in cement-based materials. A review of 3D concrete printing examines equipment, materials, mix design, and the key properties of printable concrete, highlighting the potential of this technology to reduce material consumption, construction waste, and labor requirements. Research on light-transmitting resin–cement composites investigates shrinkage at the interface between dissimilar materials and demonstrates that the combined optimization of casting technology, silane coupling agents, and surface geometry can significantly reduce interfacial deformation and the risk of cracking.

Taken together, these eight contributions demonstrate that the development of sustainable cement-based materials is not simply a matter of incorporating waste into conventional mixtures. It requires a comprehensive approach encompassing raw material characterization, optimization of material proportions, control of mixture design and microstructure, assessment of mechanical properties and durability, improvement of technological processes, and evaluation of environmental

impact. Only by integrating these aspects can construction materials and technologies be developed that are not only more sustainable but also technically reliable and suitable for practical application.

Džigita Nagrockienė and Ramunė Žurauskienė
Guest Editors

buildings

MDPI

Article

The Effect of Combining Waste-Derived Pozzolanic and Fibrous Materials with Functional Admixtures on Performance and Corrosion Resistance of Concrete

Vilma Vaičekauskienė [1,*], Džigita Nagrockienė [1,*] and Ina Pundienė [2,*]

[1] Faculty of Civil Engineering, Vilnius Gediminas Technical University, Saulėtekio Ave. 11, LT-10223 Vilnius, Lithuania
[2] Laboratory of Concrete Technologies, Vilnius Gediminas Technical University, Saulėtekio Ave. 11, LT-10223 Vilnius, Lithuania
* Correspondence: vilma.vaicekauskiene@vilniustech.lt (V.V.); dzigita.nagrockiene@vilniustech.lt (D.N.); ina.pundiene@vilniustech.lt (I.P.)

Abstract

This study investigates the combined effect of waste-based metakaolin, cellulose fibres and functional waterproofing additive on the physical, mechanical, and durability-related properties of sustainable concrete. A total of 12 concrete mixtures were produced, varying in cellulose fibre content (0–2%), metakaolin waste replacement levels (up to 10% of binder), and functional waterproofing additive content (1%). The experimental program assessed workability, density, compressive and flexural strength, ultrasonic pulse velocity (UPV) and alkali–silica reaction (ASR) resistance. The presence of metakaolin due to high pozzolanic activity (1451 mg/g) and fine particle size enhance the formation of additional C–S–H phases. The incorporation of cellulose fibres (1–2 mm in length) improved crack-bridging ability and structural integrity, while functional waterproofing additive enhanced water tightness. Results demonstrated that the synergistic use of these materials led to improved mechanical performance (flexural strength varies from 4.87 MPa to 6.81 MPa; compressive strength varies from 24.01 MPa to 32.97 MPa) and enhanced notable ASR resistance (decrease in expansion varies from 0.209% to 0.029%). The findings highlight the potential of combining waste-derived pozzolanic and fibrous materials with functional admixtures to develop environmentally friendly and performance-optimized concrete composites.

Keywords: cellulose fibber; metakaolin waste; functional waterproofing additive; ASR resistance; sustainable concrete

1. Introduction

Concrete is one of the most important building materials, but its performance is still limited by its tendency to crack, moisture penetration, and progressive degradation over time. With the construction sector constantly raising the bar for resistance and sustainability, scientists are increasingly researching how alternative raw materials and chemical additives could improve the properties of cementitious composites while reducing their environmental impact. In recent years, particular attention has been paid to different kinds of fibres, industrial by-products, and modifying admixtures which not only offer functional advantages for new materials but also reduce the carbon footprint.

Cement modified with industrial waste, such as activated coal gangue, significantly reduces carbon emissions while maintaining structural integrity through fibre-reinforced matrix synergy. This sustainable framework suggests the potential for integrating natural waste materials, such as cellulose fibres, as partial cementitious replacements to further enhance de-carbonization [1].

One promising direction is the use of cellulose fibres, especially those obtained from recycled paper. These fibres are lightweight, renewable, and capable of "bridging" microcracks in the early stages of concrete hardening. Their rough surface and favourable length-to-diameter ratio help to inhibit crack propagation and improve the behaviour of concrete after cracking—the same effects are observed when using other natural fibres, such as banana or vetiver [2–4]. Although cellulose fibres are shorter and more elastic than most plant fibres, their uniform distribution and compatibility with concrete matrices make them suitable for improving the structural integrity of sustainable concrete.

Another important component being studied in modern cementitious composites is metakaolin-based waste. Although it is an industrial by-product (in this case, formed during the production of foam glass granules), it can exhibit a high pozzolanic reaction. Previous studies have shown that metakaolin significantly contributes to the formation of secondary C–S–H phases, increases strength, and improves durability [5,6]. Thus, metakaolin obtained from waste provides a double benefit: it improves the properties of concrete and reduces cement consumption, which remains the main source of CO_2 emissions in concrete production.

The third group of materials, functional waterproofing additive, is particularly relevant for structures exposed to moisture and aggressive chemical environments. These materials react with unhydrated cement particles and moisture in the matrix to form insoluble crystals that fill capillaries and reduce water penetration. Numerous studies confirm their effectiveness in increasing water impermeability and long-term concrete durability [7,8]. Some authors also note that the formation and activation of crystals are strongly influenced by curing conditions [9,10], so their effectiveness may vary depending on the composition of the mixture and environmental factors.

Although each of these materials—cellulose fibre, metakaolin waste, and functional waterproofing additive—has been studied extensively individually, there is still a significant lack of knowledge about their interaction within the same concrete matrix. It is unclear whether cellulose fibres influence the ability of crystals to fill pores, how metakaolin waste affects the adhesion between the fibres and the matrix, how functional waterproofing additive improve densifying of concrete structure, and whether the combination of the three components can create a synergistic effect on strength, microstructure, or resistance to alkali–silica reaction (ASR) processes. Only a few studies have analyzed natural fibres in metakaolin-based systems [11,12], and even fewer studies have combined fibres and functional waterproofing additive.

Studies show that cellulose fibres in cementitious compositions lose their properties over time due to the effects of an alkaline corrosion environment. Although they effectively eliminate microcracks, the degradation of hemicellulose and lignin over time reduces their reinforcing effect [13].

Industrial waste such as metakaolin can improve the mechanical and physical properties: due to its high pozzolanic activity, it promotes the formation of additional C-S-H phases, reduces the amount of portlandite, and densifies the pore structure, improving strength and durability.

Functional waterproofing additives are another way to reduce water absorbability. They form insoluble crystals in pores and microcracks, which helps concrete maintain its impermeability even after repeated wetting and drying cycles [14]. It has also been found

https://doi.org/10.3390/buildings16040767

that advanced crystallization systems can reduce thermal stresses and improve resistance to freeze–thaw cycles [15], and their effect on moisture and heat transport depends on the composition of the mixture and the curing conditions [16]. SEM studies under alkaline conditions confirm significant changes in the microstructure [17], but there is little data on mixtures with fibres and functional waterproofing additive.

The combined effect of these materials—fibres, metakaolin waste, and functional waterproofing additive—in a single concrete matrix has not yet been thoroughly researched. It is clarified that hydration products intensively generate on the fibre's surface when functional waterproofing additive is used in compositions to improve the flexural and compressive strength of concrete. Overall, the combined effect of these materials—cellulose fibres, metakaolin waste, and functional waterproofing additive—improves ASR resistance of the concrete matrix. Scientific research shows that 1% cellulose fibre, together with 8% metakaolin waste and 1% functional waterproofing additive, is recommended for use especially in cases of increased danger of alkaline corrosion conditions.

This study aims to fill this knowledge gap by investigating the combined effect of cellulose fibre, metakaolin waste, and functional waterproofing additive on the mechanical properties, durability, and microstructural development of sustainable concrete. By combining renewable fibres, reactive industrial waste, and a functional waterproofing additive, the aim of this study is to determine whether a balanced combination of these materials can result in stronger and more environmentally friendly ASR-resistant concrete compositions.

2. Materials and Methods

2.1. Materials

The experimental program employed CEM II A-LL 42.5N Portland limestone cement (AB Akmenės cementas, Naujoji Akmenė, Lithuania), which conforms to the requirements of LST EN 197-1:2011 [18]. Supplementary materials included metakaolin waste (MW) and a functional waterproofing additive (CA). Concrete specimens were produced using Sika WT-200P (Sika AG, Baar, Switzerland), a grey, powder-form functional waterproofing additive. A high-performance superplasticizer (in liquid form), MC-PowerFlow 3100 (MC-Bauchemie Müller, Bottrop, Germany), produced using the latest MC polymer technology, was used. Water with a pH of 7.8 was used for preparing the specimens.

Fine aggregate consisted of washed sand of the 0/4 fraction, complying with the requirements of standard LST EN 12620:2003+A1:2008 [19]. The mineralogical and petrographic composition of the quarry sand used is presented in Table 1.

Table 1. Mineral and petrographic composition of sand from used quarry.

	Quartz	Carbonates	Feldspars	Mineral Aggregates	Amphiboles	Mica
Declared/limit value	62.80%	18.00%	15.60%	1.80%	1.60%	0.20%

The metakaolin waste used in this study was generated as a by-product of the foam glass pellet manufacturing process and has shown promise as a pozzolanic material. Previous studies have demonstrated that such metakaolin waste can increase the mechanical strength and reduce the drying shrinkage of cementitious composites due to its high reactivity and fine particle size [20].

The particle size distribution of the three binder components—Portland cement (PC), metakaolin waste (MW), and functional waterproofing additive (CA)—is presented in Figure 1. The measurements were conducted over a size range of 0.10 to 500 μm, and the mean particle sizes are as follows: PC—14.21 μm; MW—4.79 μm; CA—73.19 μm.

https://doi.org/10.3390/buildings16040767

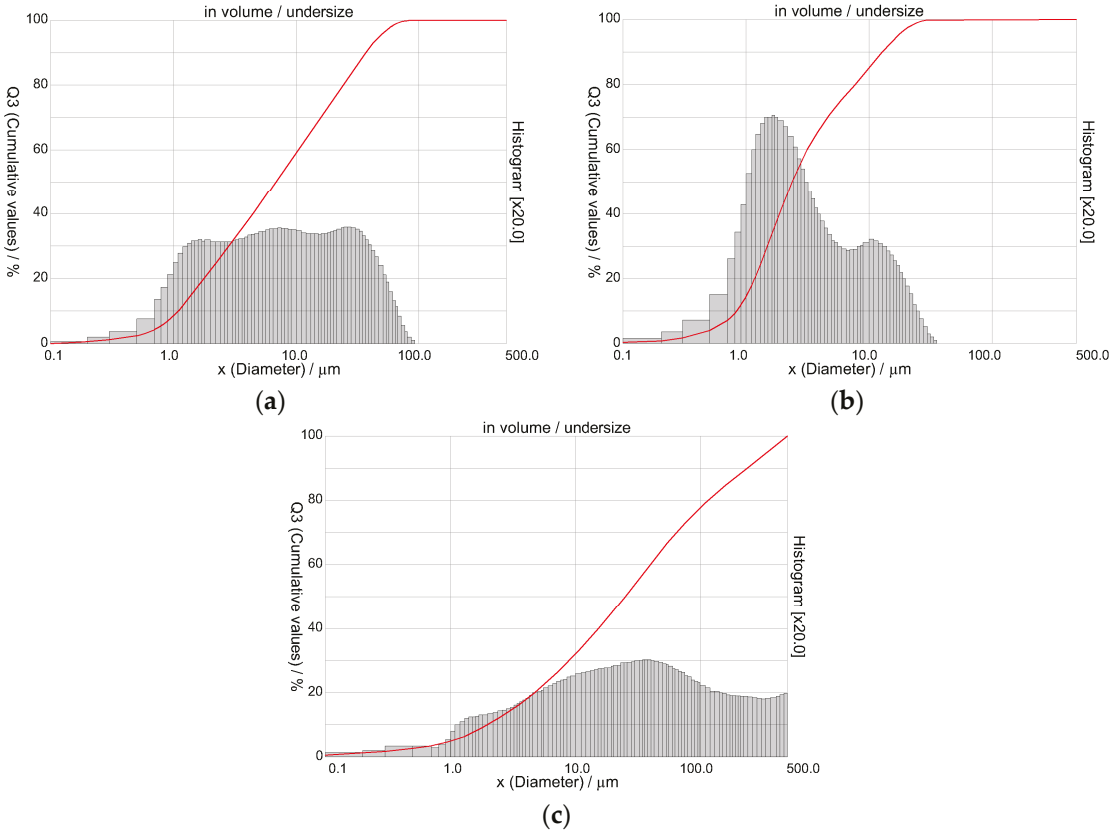

Figure 1. Particle size distribution of (**a**) Portland cement, (**b**) metakaolin waste, (**c**) functional waterproofing additive.

As seen in Table 2, the metakaolin waste exhibited the highest specific surface area (7043 cm^2/g), which is more than 80% higher than that of cement, confirming its high fineness and thus its potential for rapid reactivity [21,22]. In contrast, the functional waterproofing additive had the lowest particle density and largest average particle size, indicating a fundamentally different functional role in the composite matrix.

Table 2. Cement, metakaolin waste, and functional waterproofing additive main properties.

Properties	PC	MW	CA
Specific surface area, cm^2/g	3819	7043	3407
Particle density, kg/m^3	3130	2700	2390
Bulk density, kg/m^3	1210	3802	3406

Figure 2 presents microstructural images of cellulose fibres obtained from recycled paper, highlighting their morphological characteristics at different magnifications.

Morphological analysis of the cellulose fibres revealed that their average length ranged from 1.0 to 1.1 mm, indicating relatively short fibre geometry suitable for uniform dispersion in the cementitious matrix. The average diameter of the fibres was found to be between 0.045 and 0.05 mm, corresponding to a high aspect ratio, which may contribute positively to crack-bridging and mechanical performance enhancement in concrete [23,24].

The chemical composition of the materials is provided in Table 3. The metakaolin waste contains 50.4% SiO_2 and 20.9% Al_2O_3, indicating a strong pozzolanic potential [25,26]. Its low CaO content (5.54%) further supports its classification as a silico-aluminous pozzolanic material rather than a hydraulic one. On the other hand, the functional waterproofing additive is rich in CaO (49.59%) and contains a total alkali oxide content (K_2O + Na_2O) of 5.6%,

https://doi.org/10.3390/buildings16040767

which is consistent with materials designed to form insoluble crystalline phases that block pores and enhance the water-tightness of concrete [27,28]. However, its limited reactive silica and alumina content suggests that its pozzolanic activity is negligible or absent.

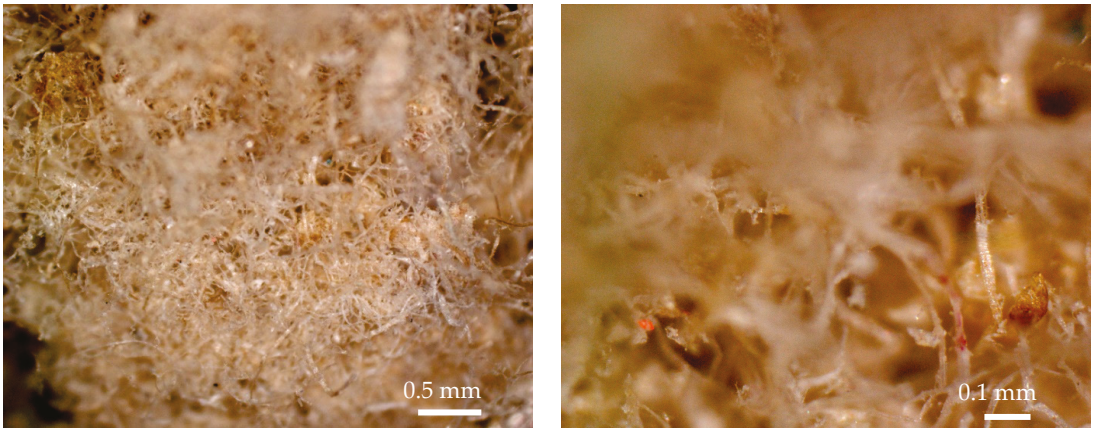

(**a**) (**b**)

Figure 2. Cellulose fibres obtained from recycled paper, shown in micro scale: (**a**) ×30 magnification, (**b**) ×112.5 magnification.

Table 3. Chemical composition of Portland cement, metakaolin waste and functional waterproofing additive.

Chemical Composition of Portland Cement, Mass %										
SiO_2	Al_2O_3	Fe_2O_3	CaO	K_2O	SO_3	Na_2O	P_2O_5	MgO	TiO_2	Cl
14.8	3.47	2.61	61.6	1.12	4.56	0.097	0.09	3.37	0.249	0.04
Chemical composition of Metakaolin waste, mass %										
50.4	20.9	0.61	5.54	0.51	0.12	11.2	0.08	2.22	0.33	0.02
Chemical composition of Functional waterproofing additive, mass %										
5.74	0.93	0.68	49.59	0.22	1.06	5.38	0.13	0.97	0.08	-

2.2. Mix Design

A total of 12 batches of concrete mixtures were prepared to investigate the influence of cellulose fibres, metakaolin waste, and a functional waterproofing additive on the properties of cementitious composites. The compositions of the mixtures are presented in Table 4. The mixing procedure was as follows: dry components—cement, sand, metakaolin waste, and, where applicable, functional waterproofing additive and cellulose fibres—were mixed for 5 min. Subsequently, water and a chemical admixture (0.4%) were added, followed by an additional 5 min mixing phase. This method of preparing the mixture ensures even distribution of dry powders and fillers before hydration begins. Scientific literature sources also refer to this technique when forming concrete specimens [29,30]. The water-to-cement ratio (W/C) was maintained at 0.3 for all batches. The batches were grouped according to the variable additive contents.

https://doi.org/10.3390/buildings16040767

Table 4. Concrete compositions, kg/m^3.

Batches	I	II	III	IV	V
Cement, kg	346.8			319.52	
Sand, kg			1793		
Cellulose fibre, kg	0	31.5	21	31.5	42
Metakaolin waste, kg	0			27.28	
Chemical admixture, kg			5.21		
W/C			0.3		

In Batches I to V, the cellulose fibre content ranged from 0% to 2% by weight of the total dry materials (cement, sand, and metakaolin, where applicable), specifically 0%, 1%, 1.5%, and 2%, respectively. The water, sand, and total binder content (cement + metakaolin) remained constant in all batches. In Batches III-V, 8% of the cement was replaced by metakaolin waste (by weight of binder). A chemical admixture was added at a constant dosage of 0.4%, and the water-to-cement (W/C) ratio was kept at 0.3 across all mixes.

Batches VI to IX in Table 5 were formulated to investigate the potential synergistic effect between cellulose fibres and metakaolin waste on the properties of cementitious composites. In these mixtures, the cellulose fibre content was varied from 0% to 2% by weight of total dry materials (cement, sand, and metakaolin where applicable), specifically 0%, 1%, 1.5%, and 2% in batches VI, VII, VIII, and IX, respectively. A constant 8% of cement (by mass of the binder) was replaced with metakaolin waste in batches VII to IX. The functional waterproofing additive was excluded from these formulations to isolate the influence of fibres and metakaolin. A chemical admixture was incorporated at a fixed dosage of 0.4%, and the water-to-cement (W/C) ratio was maintained at 0.3 across all compositions. The water and sand contents remained constant throughout.

Table 5. Concrete compositions, kg/m^3.

Batches	VI	VII	VIII	IX
Cement, kg	346.8		319.52	
Sand, kg		1793		
Cellulose fibre, kg	0	21	31.5	42
Metakaolin waste, kg	0		27.28	
Functional waterproofing additive, kg		3.39		
Chemical admixture, kg		5.21		
W/C		0.3		

Batches X to XII in Table 6, referred to as the red group, were designed to evaluate the combined effect of cellulose fibres, metakaolin waste, and a functional waterproofing additive on the properties of cementitious composites. These were the only formulations that incorporated all three types of supplementary materials simultaneously. Each mix contained a constant 10% replacement of cement with metakaolin waste (by binder mass) and 1% of a functional waterproofing additive (by weight of total dry materials). The cellulose fibre content varied across the mixes at 1%, 1.5%, and 2% by weight of total dry materials in batches X, XI, and XII, respectively. The water, sand, and total binder contents were held constant across the group. A chemical admixture was added at a uniform dosage of 0.4%, and the water-to-cement (W/C) ratio was maintained at 0.3 in all mixes.

https://doi.org/10.3390/buildings16040767

Table 6. Concrete compositions, kg/m^3.

Batches	X	XI	XII
Cement, kg		312.12	
Sand, kg		1793	
Cellulose fibre, kg	21	31.5	42
Metakaolin waste, kg		34.1	
Functional waterproofing additive, kg		3.39	
Chemical admixture, kg		5.21	
W/C		0.3	

The experimental design enables the evaluation of the impact of cellulose fibres alone, the interaction between fibres and metakaolin, and the combined effect of fibres, metakaolin, and functional waterproofing additive. All other parameters, including aggregate content, water content, and chemical admixture dosage, were kept constant to ensure comparable test conditions.

2.3. Methods

The structural and chemical characterization of the samples was carried out using X-ray fluorescence (XRF) and X-ray diffraction (XRD) techniques. The chemical composition metakaolin waste was analyzed using a Bruker S8 TIGER wavelength-dispersive X-ray fluorescence (WD-XRF) spectrometer (Bruker, Mannheim, Germany). The instrument was equipped with a Rh-target X-ray tube, operated at an anode voltage of up to 60 kV and a current of up to 130 mA. Sample preparation involved pressing the powders into pellets, which were subsequently analyzed in a helium atmosphere using the SPECTRA Plus QUANT EXPRESS method.

Structural analysis was conducted using X-ray diffraction (XRD), employing a Smart Lab diffractometer (Rigaku, Tokyo, Japan) fitted with a rotating Cu anode X-ray source rated at 9 kW. XRD scans were acquired over a 2θ range of 5° to 75°, using the Bragg–Brentano geometry. During data collection, the sample stage rotated at a speed of 0.02° per minute, while the detector scanned at 1° per minute. Phase identification was carried out using PDXL software, Version 1.8.0.3 (Rigaku), referencing the ICDD Powder Diffraction File (PDF+), 2021 edition.

Particle size distribution was determined using a Cilas 1090 LD laser diffraction particle size analyzer (Cilas, Orléans, France) capable of measuring particle sizes in the range of 0.01 μm to 500 μm, with air as the dispersing medium. All laser particle size analyzers have been designed with lasers that provide the highest resolution, accuracy, and precision across the entire range.

Microstructural imaging was performed using a Helios Nanolab 650 dual-beam scanning electron microscope (SEM) (FEI Company, Hillsboro, OR, USA) equipped with focused ion beam (FIB) technology. SEM observations were conducted in secondary electron imaging mode, at an accelerating voltage of 15 kV and an electron beam current of 0.1 nA. Compared to an optical microscope, a scanning electron microscope allows users not only to distinguish much smaller surface structure formations (magnification up to 100,000 times) but also to obtain significantly better contrast due to the large depth of field (up to 30 μm).

Six samples of the same mixture were used to determine each indicator.

Ultrasonic pulse velocity (UPV) measurements were conducted in accordance with LST EN 12504-4:2021 [31]. This non-destructive testing method enables the assessment of concrete by measuring the propagation speed of ultrasonic waves, which reflects its

https://doi.org/10.3390/buildings16040767

internal quality, homogeneity, and structural integrity. As such, UPV serves as a critical tool for both quality assurance and long-term condition monitoring of concrete structures. The ultrasonic pulse velocity (*UPV*) was calculated according to Formula (1):

$$UPV = \frac{l}{\tau'}, (\mathrm{m/s}) \quad (1)$$

where l is the length of the sample and τ' is the signal propagation time, s.

Concrete density was determined following LST EN 12390-7:2019 [32], while compressive strength and flexural strength were evaluated according to LST EN 12390-3:2019 [33] and LST EN 12390-5:2019 [34], respectively.

The alkali–silica reactivity (ASR) of concrete specimens was evaluated based on expansion testing following the RILEM AAR-2 methodology. According to this procedure, hardened mortar specimens (dimensions: 40 × 40 × 160 mm) are initially cured in water at 80 °C for 24 h and subsequently immersed in a 1 M NaOH solution at 80 °C. Expansion is measured over time to assess the potential reactivity of aggregates.

3. Results and Discussion

3.1. Parameters of Tested Materials

X-ray diffraction (XRD) analysis was conducted on four materials in Figure 3: hydrated cement, cellulose fibre, metakaolin waste, and a functional waterproofing additive.

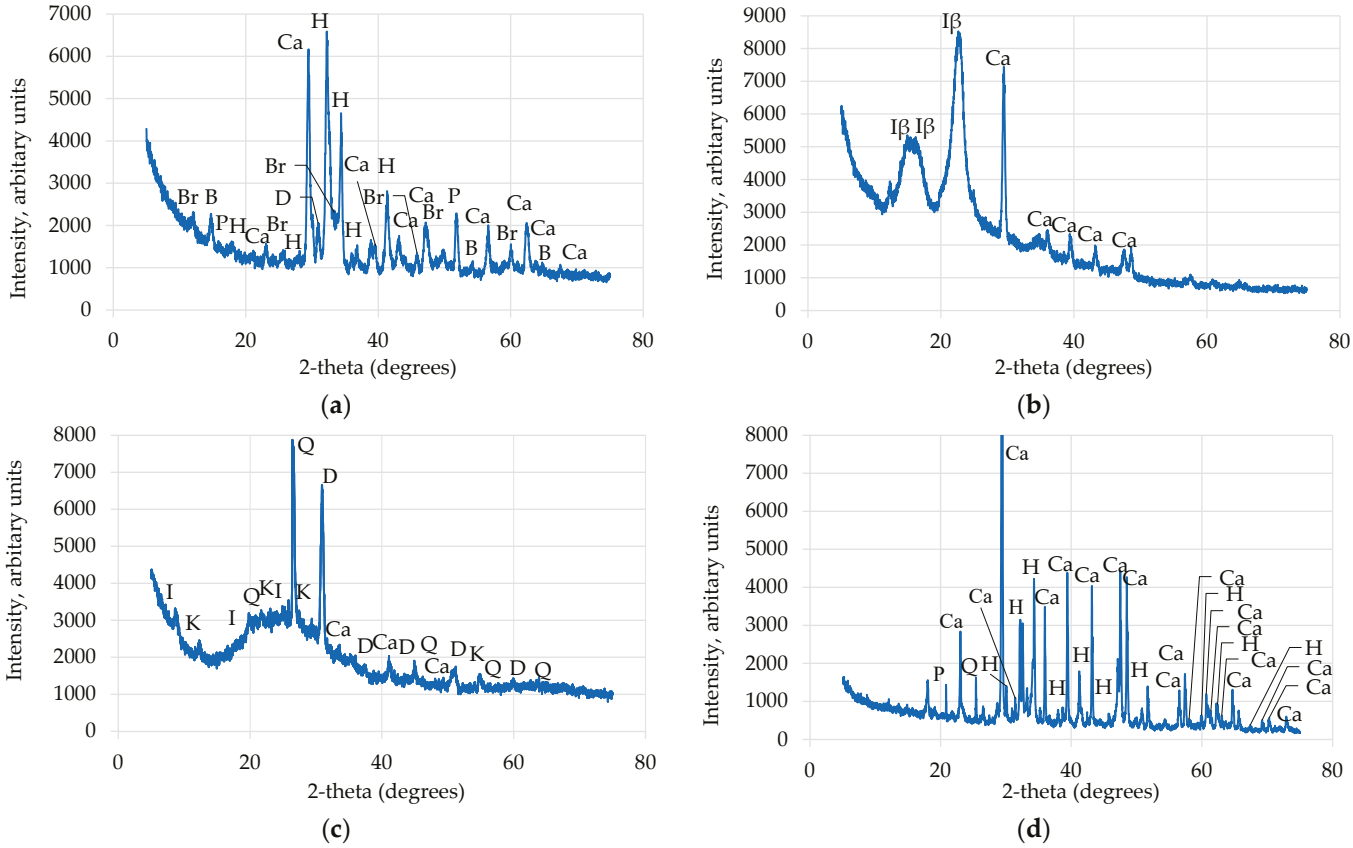

Figure 3. X-ray diagram of (**a**) cement; (**b**) cellulose fibre; (**c**) metakaolin waste; (**d**) functional waterproofing additive. Br—brownmillerite; B—bassanite; P—portlandite; H—CSH (hatrurite); D—dolomite; Ca—calcite; Iβ—cellulose; Q—quartz; K—kaolinite; I—illite.

The hydrated cement sample exhibited a complex crystalline profile dominated by calcium silicate hydrate (CSH, 60%), which is a principal hydration product, accompanied

https://doi.org/10.3390/buildings16040767

by significant amounts of brownmillerite (15.3%), calcite (13%), bassanite (6.2%), and portlandite (4.2%). A minor presence of dolomite (1%) was also observed. This mineral assemblage reflects a mature hydration process in a Portland cement system after 28 days of curing.

The cellulose sample, on the other hand, was characterized by sharp and intense peaks attributed to crystalline cellulose Iβ (96.2%), with a small fraction of calcite (3.8%), indicating high structural order and purity with only minimal inorganic impurities.

The metakaolin waste sample revealed a notably different mineral composition, consisting primarily of dolomite (34.5%), quartz (23%), and calcite (23%). Residual kaolinite (6.3%) and illite (11%) indicated that the thermal treatment did not completely dehydroxylate all clay components, suggesting partial transformation and limited pozzolanic reactivity. Metakaolin waste still contains a considerable amount of amorphous phase, which is typical for thermally activated aluminosilicates. This amorphous phase significantly contributes to the material's reactivity, providing additional sites for pozzolanic reactions.

The functional waterproofing additive displayed broad and distinct peaks associated with CSH, confirming its role as a hydration-promoting agent [35]. Minor signals of calcite and quartz were also present, likely originating from filler materials or by-products of early hydration. Overall, the XRD results highlight the distinct mineralogical fingerprints of each component and their potential contributions to composite cementitious systems in terms of hydration behaviour and structural performance.

Scanning electron microscopy (SEM) analysis was performed to evaluate the morphological characteristics of the dry components used in the cementitious mixtures, as shown in Figure 4. The SEM image of Portland cement (Figure 4a) revealed angular and irregularly shaped particles of varying sizes, which is characteristic of ground clinker and limestone constituents. These features are known to influence the packing density and initial hydration kinetics of the binder system. The cellulose fibres (Figure 4b), obtained from recycled paper, displayed elongated, ribbon-like structures with a rough surface texture, which may promote mechanical interlocking with the cement matrix and improve crack-bridging efficiency. The metakaolin waste (Figure 4c) shows a highly porous, finely textured morphology, composed of angular particles and a granular microstructure. Similar SEM image results showing an irregular and rough surface of metakaolin waste particles have also been obtained by other researchers [36]. This morphology, along with its high specific surface area, supports its classification as a reactive pozzolanic material capable of contributing to secondary hydration product formation. In contrast, the functional waterproofing additive (Figure 4d) demonstrated a coarser and more compact granular structure with distinguishable crystalline features. These characteristics suggest its role is primarily physical, contributing to pore blocking and water-tightness enhancement rather than participating in pozzolanic reactions.

The observed morphological differences confirm the distinct functional contributions of each material: Portland cement as the primary hydraulic binder, metakaolin waste as a chemically reactive additive [37], cellulose fibres as physical reinforcement [38], and the functional waterproofing additive as a densifying component improving durability-related properties [39].

Metakaolin waste demonstrated a high pozzolanic activity of 1451 mg/g, indicating its strong potential as a supplementary cementitious material [40]. Its elevated SiO_2 content enables an active reaction with $Ca(OH)_2$ in the cementitious matrix, leading to the formation of additional calcium silicate hydrate (C–S–H) and other hydration products. These compounds contribute to pore refinement, increased density, and enhanced mechanical and durability-related properties of sustainable concrete. Therefore, metakaolin waste can

https://doi.org/10.3390/buildings16040767

be effectively utilized to improve both the performance and environmental footprint of cement-based composites [41].

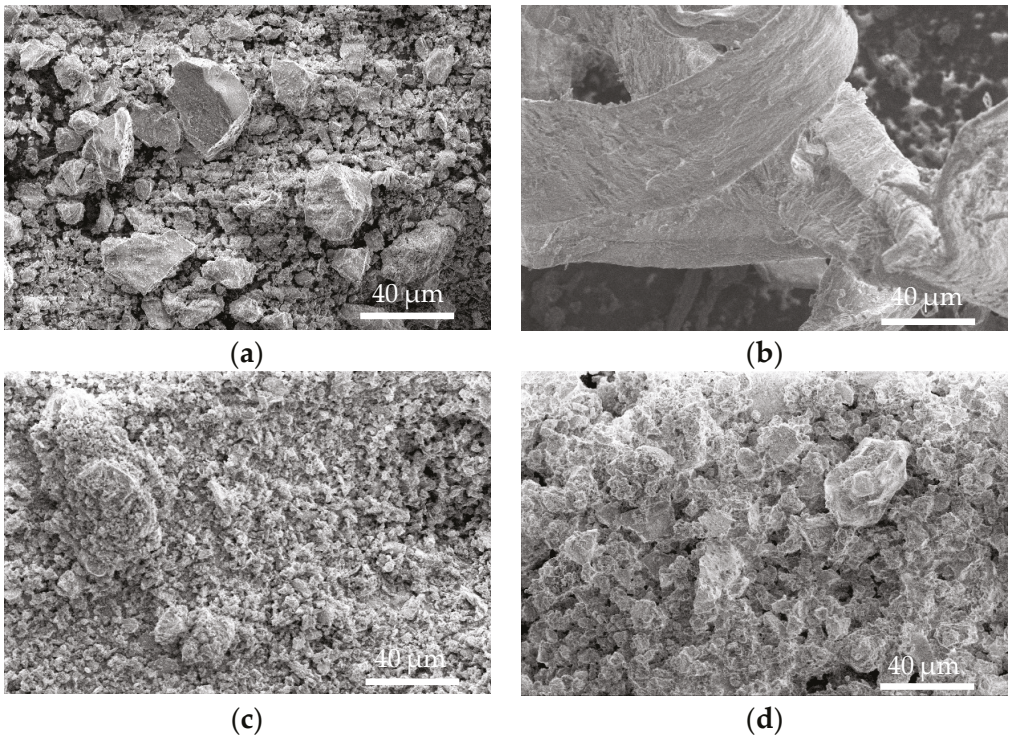

Figure 4. Microstructure 1000× magnification of (**a**) cement; (**b**) cellulose fibre, (**c**) metakaolin waste; (**d**) functional waterproofing additive.

3.2. Density and UPV

Figure 5 shows density and ultrasonic pulse velocity graphs of concrete modified with different materials before and after corrosion.

The results in Figure 5 show that both density and ultrasonic pulse velocity slightly decrease after corrosion in all mixtures, but samples with cellulose fibre, metakaolin, and functional waterproofing additive retain higher values, indicating improved durability compared to the reference concrete. The highlighted values indicate the best-performing result within the entire group of mixtures. These values were pointed out to show which mixture achieved the most suitable density and ultrasonic pulse velocity in the comparison.

The decreased density of concrete specimens after alkaline corrosion indicates internal expansion and the appearance of cracks and voids [42]. Metakaolin waste helps reduce the risk of ASR: it can react with alkalis, reducing the amount available to react with silica and helping to prevent expansion and cracking [43,44]. The functional waterproofing additive promotes the formation of insoluble crystals such as calcite that fill cracks and can appear after alkali corrosion, restore the matrix and increase density and UPV (since it is directly dependent on density) of the concrete [45].

https://doi.org/10.3390/buildings16040767

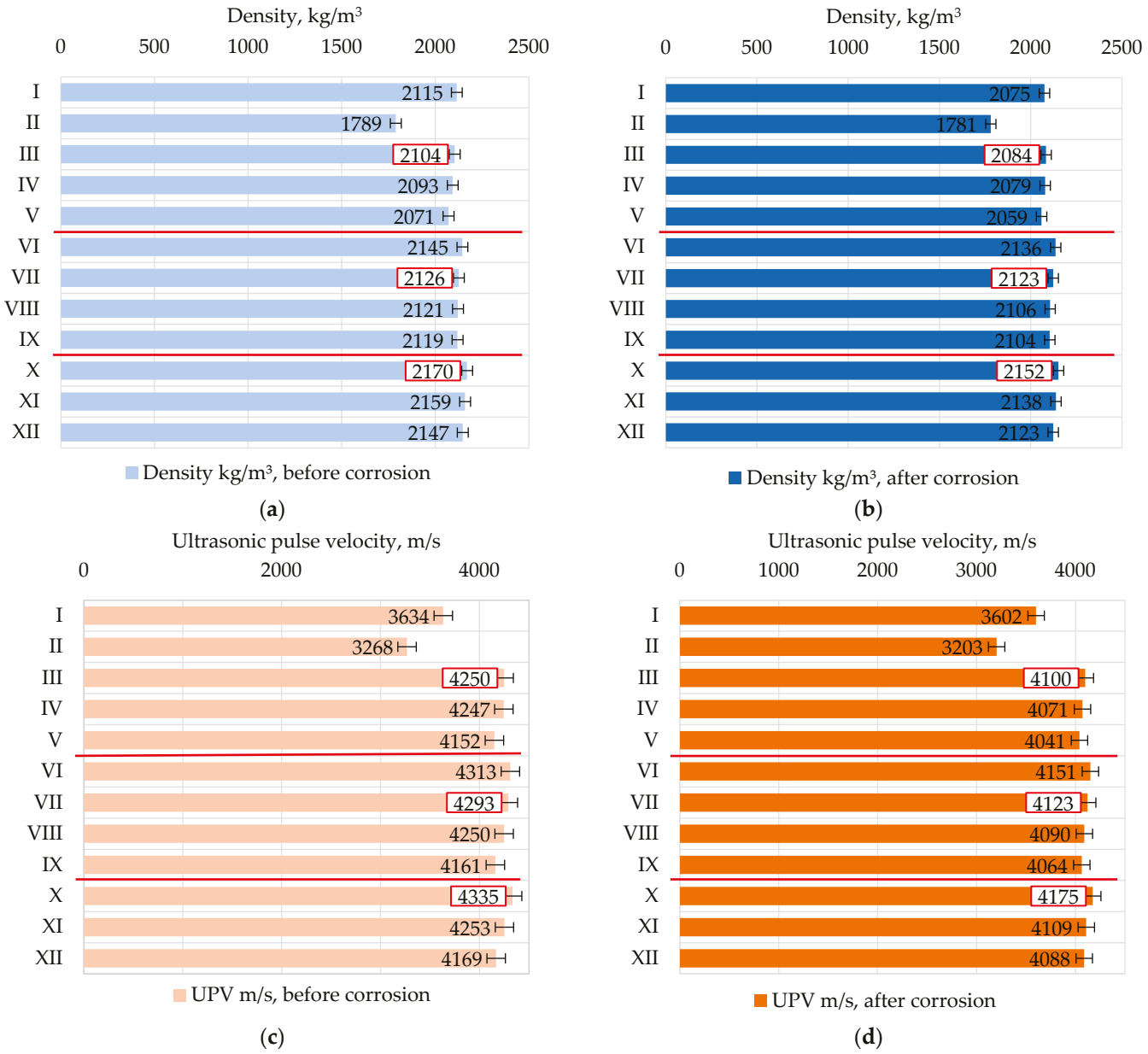

Figure 5. Density and ultrasonic pulse velocity of the hardened modified concrete before corrosion (**a**,**c**) and after corrosion (**b**,**d**). Composition sets are separated by red lines.

3.3. Flexural and Compressive Strengths

Figure 6 shows graphs with flexural and compressive strength values of concrete modified with different materials before and after corrosion. Graphs in Figure 6 show that concrete with 1% cellulose fibre, 8% metakaolin waste and 1% functional waterproofing additive has 20% increased flexural strength and 2.3% increased compressive strength compared to sample I without any additives. The highlighted values mark the mixtures that achieved the highest flexural and compressive strength within the entire group.

https://doi.org/10.3390/buildings16040767

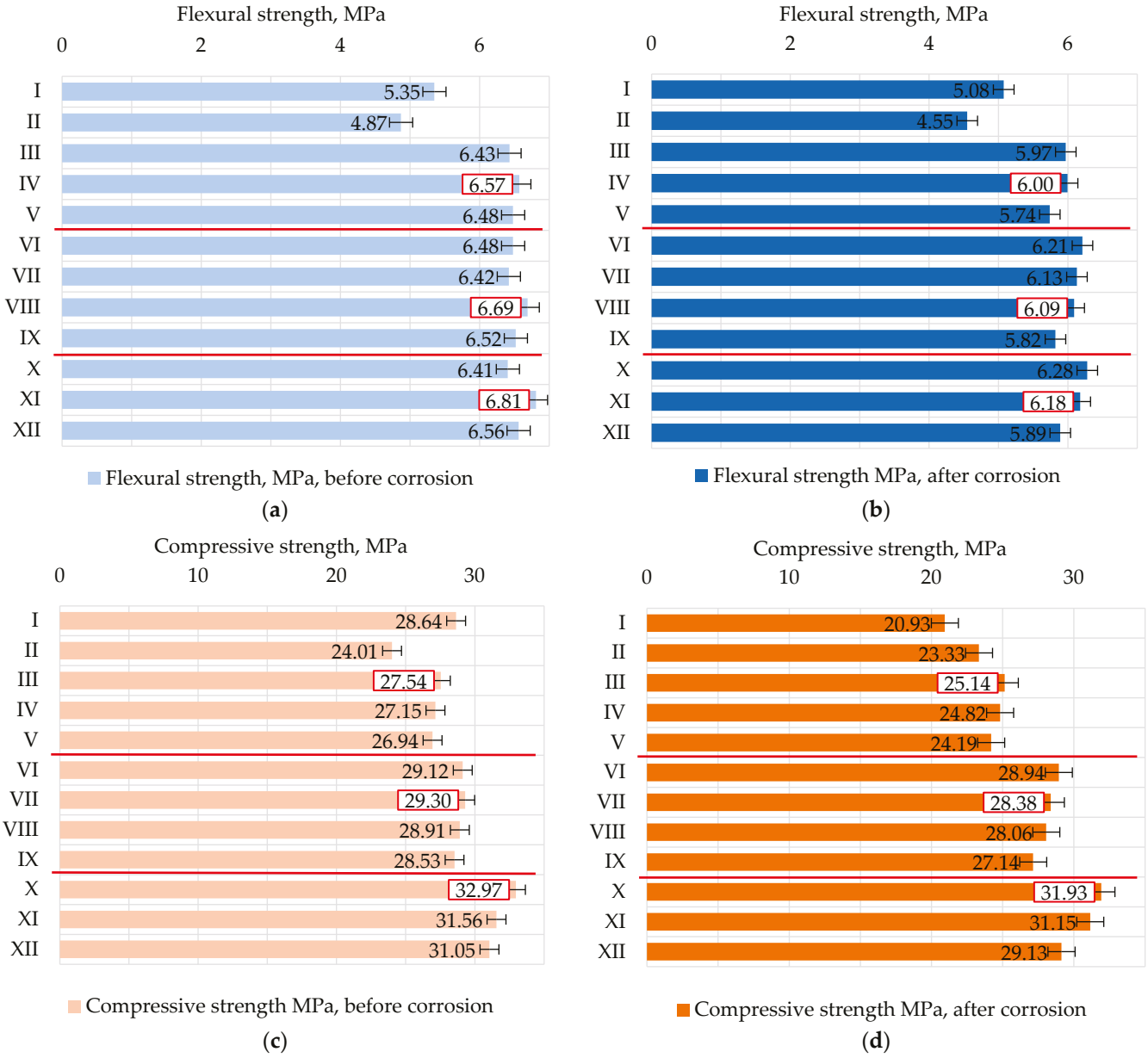

Figure 6. Flexural and compressive strength of the hardened modified concrete before corrosion (**a**,**c**) and after corrosion (**b**,**d**). Composition sets are separated by red lines.

In similar studies where concrete was modified with metakaolin waste, tests in alkaline conditions showed clear improvements: ASR was reduced because metakaolin waste lowers the alkalinity of the matrix and suppresses alkali–silica reaction, preventing expansion and cracking that would reduce strength [46]. Cellulose fibre acts as mechanical reinforcement by controlling crack propagation, but it is vulnerable to alkaline environments [47], so additives like metakaolin waste and a functional waterproofing additive are used to prevent its degradation and improve both flexural and compressive strength. However, in our case, the cellulose fibres have an additional role. The uneven surface of the cellulose fibres keeps adsorbed water and is suitable for additional hydration products precipitation. The fibre, because of its hydrophilicity, absorbs water and releases it gradually in surrounding area. This water can later participate in cement hydration reactions and create a strong bond between the fibres and cement matrix.

https://doi.org/10.3390/buildings16040767

3.4. SEM Analysis

Figure 7—SEM images of I concrete specimens without admixtures before and after corrosion. Figure 7a shows the structure of the hardened concrete surface at a magnification of ×2000, and Figure 7b shows the concrete surface at a magnification of ×5000 before corrosion. Figure 7c and d show the microstructure of concrete sample I after corrosion, with a rougher surface and ASR gel formation.

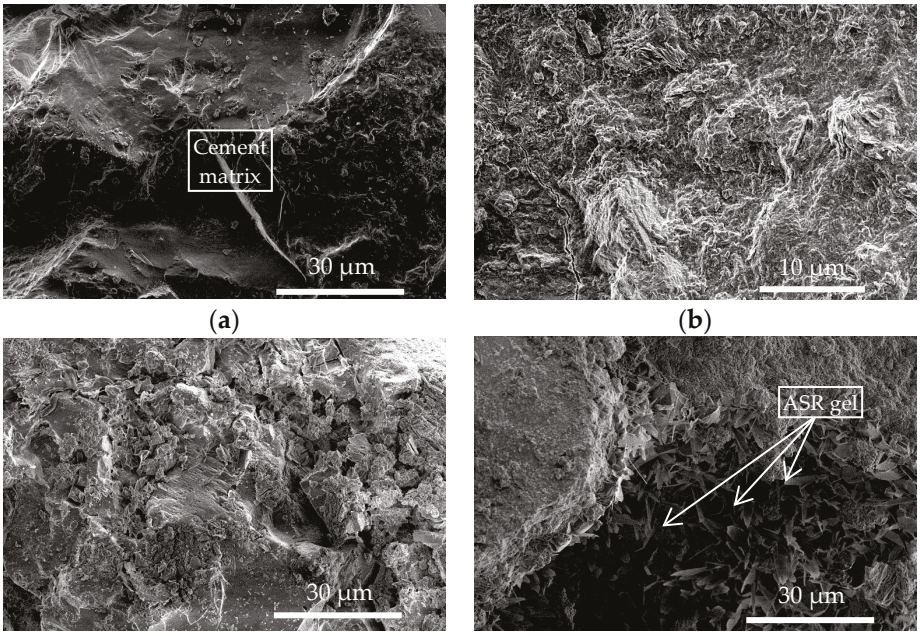

Figure 7. Sample of hardened concrete of the I composition microstructure before corrosion: (**a**) magnification ×2000; (**b**) magnification ×5000. After corrosion: (**c**) magnification ×2000; (**d**) magnification ×2000.

In the cement matrix, ASR gel forms in the damaged areas after alkali-induced degradation [48]. The ASR occurs between the alkali-affected cement paste and amorphous silica, which is found in significant amounts in the fine aggregate, such as sand.

Figure 8 shows SEM images of concrete specimens of the composition VII with admixtures before corrosion. The selected composition demonstrated the most advantageous mechanical and physical properties, combined with an optimized composition and appropriate rheological characteristics. Figure 8a–e shows cellulose fibre (CF) covered with hydration products; similar results were observed in another studies, when SEM images showed how cellulose fibres are covered with hydration products [49,50]. Figure 8f shows ettringite crystals covered with calcium silicate hydrate (C–S–H) gel.

SEM images show that concrete containing cellulose fibre, metakaolin waste, and functional waterproofing additive develops a very dense structure. This forms during the hydration process, as the dry cellulose fibre absorbs water and simultaneously catches a large amount of other hydration products, resulting in a strong bond between the fibre and matrix and a compact overall concrete structure.

https://doi.org/10.3390/buildings16040767

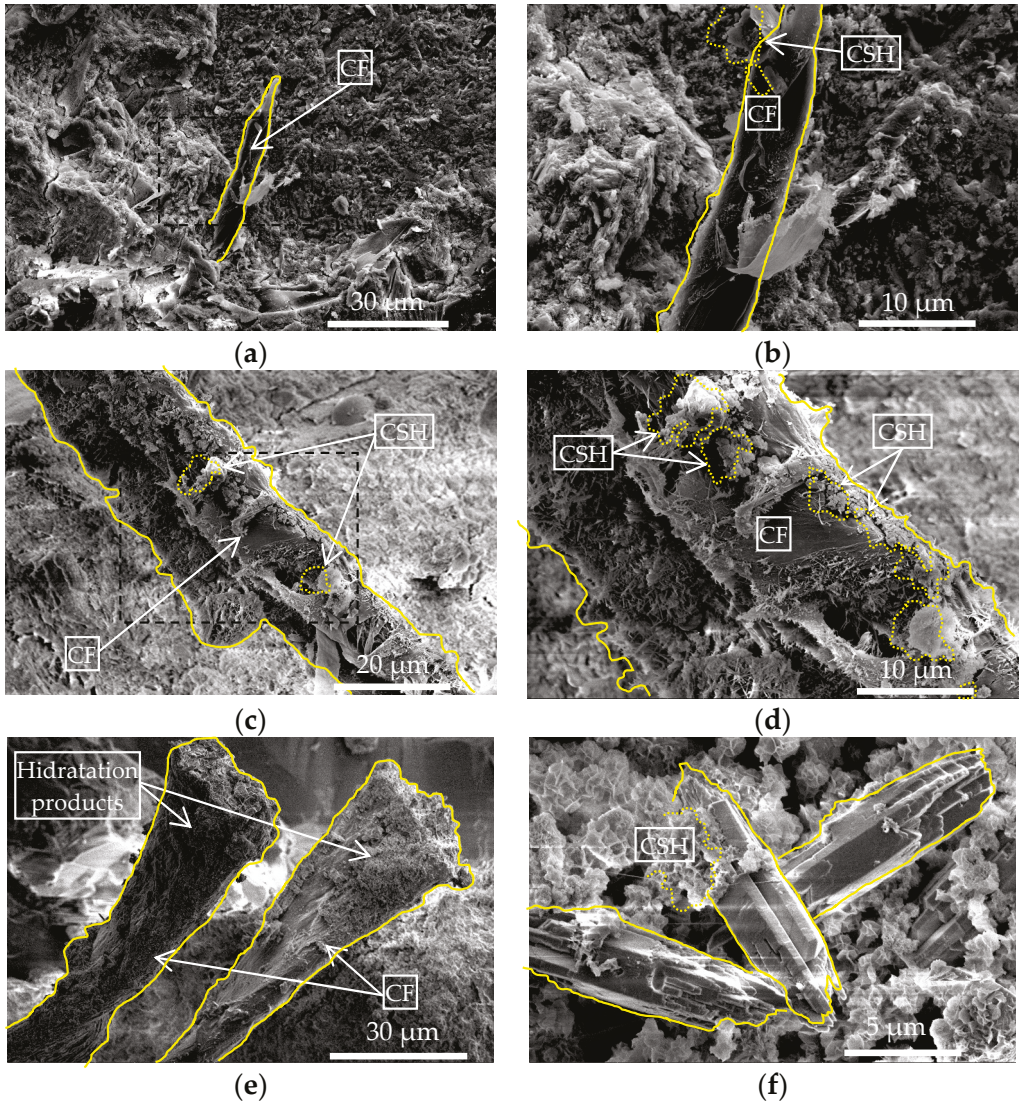

Figure 8. Hardened concrete sample with 1% cellulose fibre, 8% metakaolin waste and 1% functional waterproofing additive microstructure before corrosion: (**a**) magnification ×3500; (**b**) magnification ×10,000; (**c**) magnification ×5000; (**d**) magnification ×10,000; (**e**) magnification ×2000; (**f**) magnification ×10,000.

Figure 9 shows SEM images of concrete specimens with admixtures after corrosion. Figure 9a,b shows cellulose fibre (CF) covered with different hydration products, while Figure 9c,d shows cellulose fibre (CF) heavily covered with CSH. Cellulose fibre with well-crystallized ettringite needles (AFt) arranged in different directions after corrosion is visible in Figure 9e,f, These AFt needles were also detected using SEM analysis in a similar study investigating the impact of high-alkali biofuel fly ash on concrete [51].

SEM observations after alkali corrosion testing indicate that the cellulose fibres remain structurally unaffected and contribute to maintaining the overall dense structure of the concrete. Concrete mixtures containing cellulose fibres, metakaolin waste, and functional waterproofing additive exhibit only minor microstructural changes following alkaline exposure. The images show slight cellulose fibre shedding, yet the cellulose fibres remain present with attached hydration products.

https://doi.org/10.3390/buildings16040767

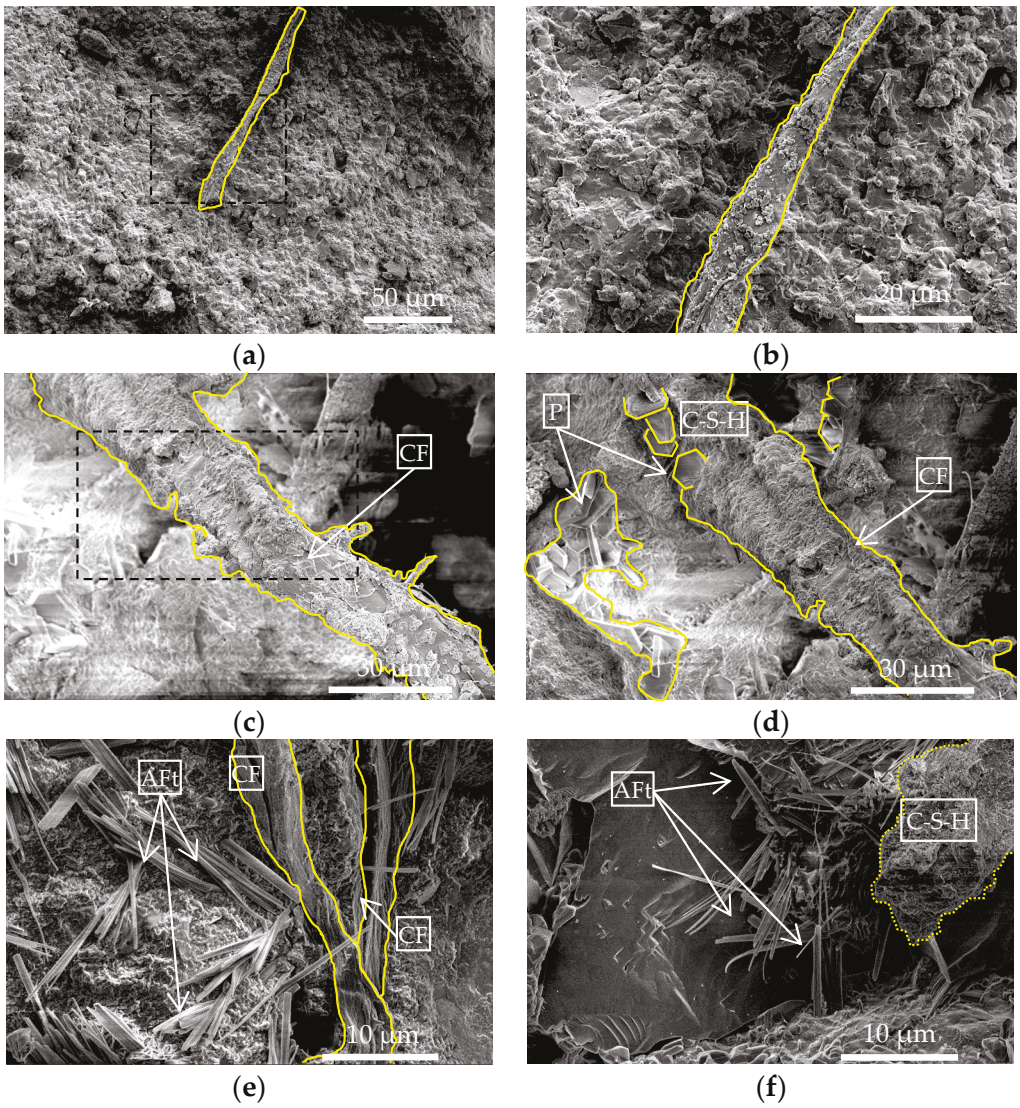

Figure 9. Hardened concrete sample with 1% cellulose fibre, 8% metakaolin waste and 1% functional waterproofing additive SEM images after corrosion: (**a**) magnification ×1500; (**b**) magnification ×5000; (**c**) magnification ×3500; (**d**) magnification ×3500; (**e**) magnification ×5000; (**f**) magnification ×5000.

3.5. XRD Analysis

The XRD analysis of two different composition samples, I and VII (1% cellulose fibre, 8% metakaolin waste and 1% functional waterproofing additive), before and after corrosion is presented in Figure 10, which shows that quartz remains the dominant crystalline phase in all specimens, and its peak intensity is largely unaffected by the corrosion exposure. More notable changes occur in phases associated with cement hydration and carbonation. In the I specimen, corrosion leads to a visible reduction in the intensity of portlandite, calcite, and ettringite peaks, indicating dissolution of calcium-rich phases and a partial loss of crystalline hydration products.

https://doi.org/10.3390/buildings16040767

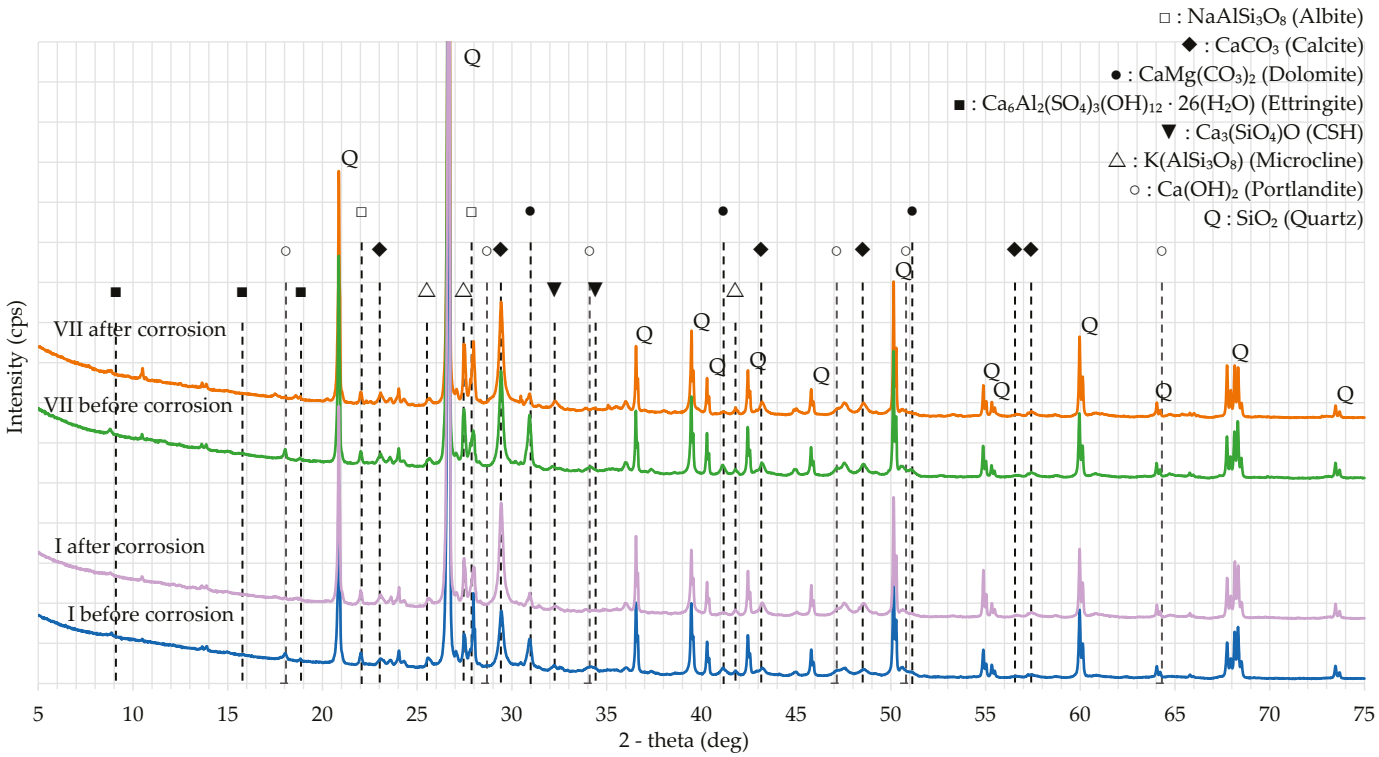

Figure 10. I and VII specimens XRD diffractogram results before and after corrosion.

In contrast, the VII mixture exhibits a more stable phase composition: the differences between its diffractograms before and after corrosion are considerably smaller than in the I sample. Most characteristic peaks remain well-defined, suggesting improved resistance to decalcification and reduced transformation of hydration products. Carbonate phases in the modified mixture also appear less affected, which points to a denser or more chemically stable microstructure.

Overall, the results indicate that the VII formulation provides better mineralogical stability under corrosive conditions compared to the unmodified I mixture.

3.6. Expansion

The alkali–silica reaction (ASR) expansion tests of concrete specimens were carried out in accordance with the RILEM AAR-2 testing methodology. The essence of the RILEM AAR-2 method is as follows: hardened specimens (40 × 40 × 160 mm) are immersed in water at 80 °C, then stored in a 1 M NaOH (sodium hydroxide) for 14 days, after which their expansion is measured. The methodology states that if the aggregates contain slowly reacting reactive rocks, the storage duration should be longer. Therefore, in this study the storage time in 1 M NaOH solution was extended to 56 days. According to the RILEM AAR-2 method, aggregates are considered reactive when the expansion of concrete specimens after 14 days in 1 M NaOH solution exceeds 0.054%. When the test is continued up to 56 days, the critical expansion threshold is 0.1%, as defined by the ASTM C441 testing method.

Figure 11 presents the ASR expansion test results of hardened modified concrete specimens. After 14 days, the expansion exceeded 0.054% in compositions I, II, III, VI, and VI. After 56 days, several mixes (I, II, and VI) exceeded the 0.1% threshold, indicating increased ASR.

https://doi.org/10.3390/buildings16040767

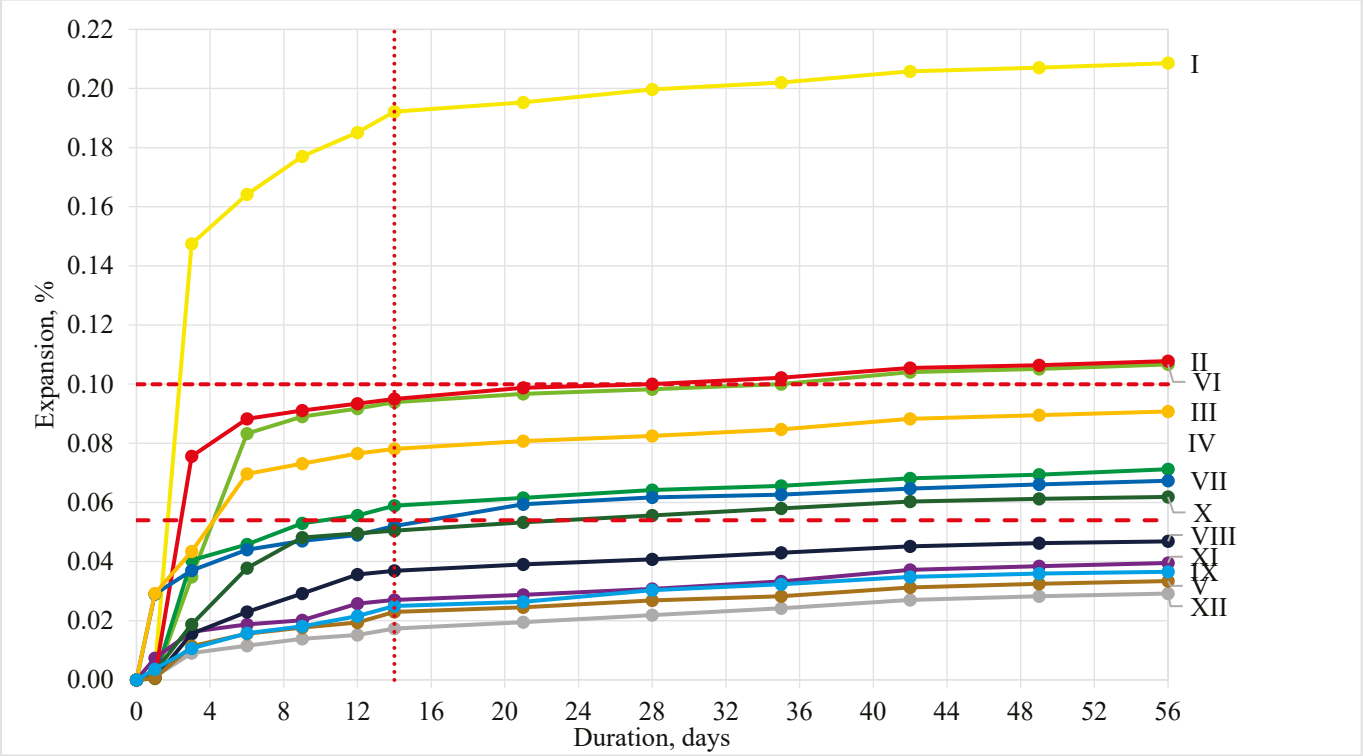

Figure 11. Expansion values of concrete specimens with different admixtures after 56 days, when kept in a 1 M NaOH solution at +80 °C. The red dotted horizontal lines indicate the reference expansion limits (0.054% at 14 days and 0.10% at 56 days). The vertical red dotted line marks the 14-day evaluation point.

Concrete expansion was tested by placing the specimens in a 1 M NaOH solution at 80 °C. Batch VII did not exceed an expansion of 0.054% after 14 days and remained below 0.1% after 56 days; this result can be considered favourable. This positive result may be associated with the combined effect of metakaolin, functional water-proofing additive, and cellulose, promoting a denser microstructure and limiting alkali–silica reaction development.

4. Conclusions

A concrete was developed, modified with 8% and 10% metakaolin waste, 1% cellulose fibre, and 1% functional waterproofing additive. This composition ensured improved structural and performance properties of the mixture, reduced the demand for primary raw materials, and enabled the utilization of secondary raw materials in concrete production.

1. Flexural strength is increased by 23% and 27% in comparison to pure cement specimens when 8% and 10% of metakaolin waste are substituted for cement and cellulose fibres in amounts varying from 1% to 2%. However, adding a 1% functional water-proofing additive also enhances specimen density by up to 2.6%, ultrasonic pulse velocity by up to 19%, and compressive strength by up to 15% due to increased crystallization of hydration products on the surface of cellulose fibre and pore filling. The functional water-proofing additive contains a large amount of CaO, and possibly actively participates in the hydration process by forming additional hydration products, such as CSH.
2. Combined utilizing of metakaolin, functional waterproofing additive and cellulose fibre positively influences concrete microstructure, displaying increased exceptional bonding with the cement matrix. An additional factor that can improve the cement hydration process is the fact that cellulose fibre is hydrophilic. The wet surface

https://doi.org/10.3390/buildings16040767

of cellulose fibre is the suitable area on which precipitation of cement hydration products occurs most visibly. As the hydration process continues, the cellulose fibre acts as a source of additional water. Cellulose fibre, because of its hydrophilicity, collects water and releases it gradually into the surrounding region, thus ensuring increased reactions between cement minerals, metakaolin and CaO- rich functional waterproofing additive on the fibre surface.

3. In a 1 M NaOH solution at 80 °C, batch VII's (with minimal 1% of cellulose fibre in composition) expansion stayed below 0.054% after 14 days and did not surpass 0.1% after 56 days, indicating that it performed excellent in the expansion tests. These findings suggest a low susceptibility to the alkali–silica interaction. This improved performance is most likely attributable to the combined use of metakaolin, a functional waterproofing additive, and an optimal amount of cellulose fibres, which led to a denser concrete structure and helped prevent ASR development.

Overall, cellulose fibre is a promising additive for improving the durability and flexural strength of concrete, especially when combined with metakaolin waste and functional waterproofing additive. Optimal fibre content depends on the mix design, with 1–1.5% providing the best balance between mechanical performance and expansion test results.

Author Contributions: Conceptualization, V.V. and D.N.; methodology, V.V., D.N. and I.P.; investigation, V.V., D.N. and I.P.; resources, V.V., D.N. and I.P.; writing—original draft preparation, V.V., D.N. and I.P.; supervision, V.V., D.N. and I.P. All authors have read and agreed to the published version of the manuscript.

Funding: This research received no external funding.

Institutional Review Board Statement: Not applicable.

Informed Consent Statement: Not applicable.

Data Availability Statement: The original contributions presented in this study are included in the article. Further inquiries can be directed to the corresponding author.

Conflicts of Interest: The authors declare no conflicts of interest.

References

1. Wang, Y.; Zhu, L.; Xue, Y. A Comprehensive Review on Dual-Pathway Utilization of Coal Gangue Concrete: Aggregate Substitution, Cementitious Activity Activation, and Performance Optimization. *Buildings* **2026**, *16*, 302. [CrossRef]
2. Kesavraman, S. Studies on Metakaolin Based Banana Fibre Reinforced Concrete. *Int. J. Civ. Eng. Technol.* **2017**, *8*, 532–543.
3. Chandra Mouli, K.; Pannirselvam, N.; Anitha, V.; Vijaya Kumar, D.; Valeswara Rao, S. Strength Studies on Banana Fibre Concrete with Metakaolin. *Int. J. Civ. Eng. Technol.* **2019**, *10*, 684–689.
4. Srivastava, S.; Roy, S.; Khan, F. Study of using Metakaolin and Vetiver Fiber as Partial Replacement of Cement in Concrete. *Int. J. Eng. Res. Technol.* **2022**, *11*, 219–221.
5. Bede Odorčić, N.; Kravanja, G. Combined Effects of Metakaolin and Hybrid Fibers on Self-Compacting Concrete. *Materials* **2022**, *15*, 5588. [CrossRef]
6. Valizadeh Kiamahalleh, M.; Gholampour, A.; Rezaei Shahmirzadi, M.; Ngo, T.D.; Ozbakkaloglu, T. Mechanical, Durability, and Microstructure Assessment of Wastepaper Fiber-Reinforced Concrete Containing Metakaolin. *Materials* **2024**, *17*, 2608. [CrossRef]
7. Pazderka, J.; Hájková, E. Crystalline admixtures and their effect on selected properties of concrete. *Acta Polytech.* **2016**, *56*, 306–311. [CrossRef]
8. Beltrán Cobos, R.; Tavares Pinto, F.; Sánchez Moreno, M. Analysis of the Influence of Crystalline Admixtures at Early Age Performance of Cement-Based Mortar by Electrical Resistance Monitoring. *Materials* **2021**, *14*, 5705. [CrossRef]
9. Sideris, K.; Chatzopoulos, A.; Tassos, C.; Manita, P. Durability of concretes prepared with crystalline admixtures. *MATEC Web Conf.* **2019**, *289*, 09003. [CrossRef]
10. Machado, B.R.; Silva, L.S.; Amario, M.; Haddad, A.N.; de Vargas, A.S.; Stolz, C.M. Effect of curing methods on the long-term properties of concrete containing crystallizing additives. *Next Mater.* **2025**, *8*, 100759. [CrossRef]

https://doi.org/10.3390/buildings16040767

11. Ayeni, O.; Mahamat, A.A.; Bih, N.L.; Stanislas, T.T.; Isah, I.; Savastano Junior, H.; Boakye, E.; Onwualu, A.P. Effect of Coir Fiber Reinforcement on Properties of Metakaolin-Based Geopolymer Composite. *Appl. Sci.* **2022**, *12*, 5478. [CrossRef]
12. Luo, R.; Liu, H.; Duan, P.; Ye, J.; Chen, W.; Zhang, Z.; Wang, A. Sulfate resistance and microstructure of metakaolin geopolymer reinforced by cellulose nanofiber and wollastonite. *J. Build. Eng.* **2023**, *64*, 105580. [CrossRef]
13. Jamshaid, H.; Ali, H.; Mishra, R.K.; Nazari, S.; Chandan, V. Durability and Accelerated Ageing of Natural Fibers in Concrete as a Sustainable Construction Material. *Materials* **2023**, *16*, 6905. [CrossRef]
14. Mircea, C.; Toader, T.-P.; Hegyi, A.; Ionescu, B.-A.; Mircea, A. Early Age Sealing Capacity of Structural Mortar with Integral Crystalline Waterproofing Admixture. *Materials* **2021**, *14*, 4951. [CrossRef]
15. Al-Rashed, R.; Al-Jabari, M. Managing Thermal Effects in Waterproofed Concrete with Multi-Crystallization Enhancer. *Cement* **2022**, *10*, 100050. [CrossRef]
16. Nagrockienė, D.; Pundienė, I.; Čepulis, A.; Pocius, E. The Effect of Crystallizing Admixture on the Properties and Shrinkage of Concrete. *Ceram. Silikáty* **2021**, *65*, 273–280. [CrossRef]
17. Tsampali, E.; Tsardaka, E.-C.; Pavlidou, E.; Stefanidou, M. The mechanism action of crystalline admixtures on hydration, microstructure, and self-healing of cementitious materials. *J. Build. Eng.* **2025**, *110*, 112987. [CrossRef]
18. *LST EN 197-1:2011*; Cement—Part 1: Composition, Specifications and Conformity Criteria for Common Cements. Lithuanian Standards Board: Vilnius, Lithuania, 2012.
19. *LST EN 12620:2002+A1:2008*; Aggregates for Concrete. Lithuanian Standards Board: Vilnius, Lithuania, 2009.
20. Malaiškienė, J.; Škamat, J.; Kizinievič, O.; Girskas, G. Synergistic Effect of Metakaolin Waste and Nano-Silica on the Properties of Ultra-High-Performance Concrete. *Processes* **2025**, *13*, 3614. [CrossRef]
21. Ahmad, J.; Majdi, A.; Arbili, M.M.; Deifalla, A.F.; Naqash, M.T. Mechanical, Durability and Microstructure Analysis Overview of Concrete Made with Metakaolin (MTK). *Buildings* **2022**, *12*, 1401. [CrossRef]
22. Majstorović, F.; Sebera, V.; Mrak, M.; Dolenec, S.; Wolf, M.; Marrot, L. Impact of metakaolin on mechanical performance of flax textile-reinforced cement-based composites. *Cem. Concr. Compos.* **2022**, *126*, 104367. [CrossRef]
23. Liu, J.; Lv, C. Research Progress on Durability of Cellulose Fiber-Reinforced Cement-Based Composites. *Int. J. Polym. Sci.* **2021**, *2021*, 1014531. [CrossRef]
24. Prashar, R. Fiber-Reinforced Cementitious Composites: A Comprehensive Review of Synthetic, Natural, and Hybrid Systems for Advanced Construction Applications. *Int. J. Multidiscip. Res.* **2025**, *7*, 5. [CrossRef]
25. Mirdamadi, A.; Layssi, H.; Eftekhar, M.H.; Shekarchi, M. Comparative Study of Metakaolin and Silica Fume to Prevent Alkali-Silica Reaction in Concrete. In Proceedings of the 13th International Conference on Alkali-Aggregate Reaction, Trondheim, Norway, 16–20 June 2008.
26. Al-Hashem, M.N.; Amin, M.N.; Ajwad, A.; Afzal, M.; Khan, K.; Faraz, M.I.; Qadir, M.G.; Khan, H. Mechanical and Durability Evaluation of Metakaolin as Cement Replacement Material in Concrete. *Materials* **2022**, *15*, 7868. [CrossRef]
27. Shumuye, E.D.; Li, W.; Fang, G.; Wang, Z.; Liu, J.; Zerfu, K. Review on the durability of eco-friendly engineering cementitious composite (ECC). *Case Stud. Constr. Mater.* **2023**, *19*, e02324. [CrossRef]
28. Zhang, G.-Z.; Liu, C.; Ma, X.; Yu, X.-K. The Effects of Crystalline Admixture on the Self-Healing Performance and Mechanical Properties of Mortar with Internally Added Superabsorbent Polymer. *Materials* **2023**, *16*, 5052. [CrossRef]
29. Rezaei Shahmirzadi, M.; Gholampour, A.; Hosseini, S.A.; Ngo, T.D.; Nematzadeh, M. Wastepaper fiber-reinforced concrete containing metakaolin: Effect on fracture behavior. *Struct. Concr.* **2024**, *25*, 2931–2946. [CrossRef]
30. Raveendran, N.; Vasugi, K. Synergistic effect of nano silica and metakaolin on mechanical and microstructural properties of concrete: An approach of response surface methodology. *Case Stud. Constr. Mater.* **2024**, *20*, e03196. [CrossRef]
31. *LST EN 12504-4:2021*; Testing Concrete—Part 4: Determination of Ultrasonic Pulse Velocity. Lithuanian Standards Board: Vilnius, Lithuania, 2021.
32. *LST EN 12390-7:2019*; Testing Hardened Concrete—Part 7: Density of Hardened Concrete. Lithuanian Standards Board: Vilnius, Lithuania, 2020.
33. *LST EN 12390-3:2019*; Testing Hardened Concrete—Part 3: Compressive Strength of Test Specimens. Lithuanian Standards Board: Vilnius, Lithuania, 2020.
34. *LST EN 12390-5:2019*; Testing Hardened Concrete—Part 5: Flexural Strength of Test Specimens. Lithuanian Standards Board: Vilnius, Lithuania, 2022.
35. Wang, R.; Ding, Z.; Zhang, Y.; Xu, Y. Self-healing of high-performance engineered cementitious materials with crystalline admixture in the seawater environment. *J. Build. Eng.* **2023**, *63*, 105472. [CrossRef]
36. Rong, Z.; Jiang, G.; Sun, W. Effects of metakaolin on mechanical and microstructural properties of ultra-high performance cement-based composites. *J. Sustain. Cem.-Based Mater.* **2018**, *7*, 296–310. [CrossRef]
37. Sofi, A.; Kumanan, T.S. Chapter 7—Metakaolin-blended cements—The past and future of sustainable concrete. In *Binding Materials for Sustainable Construction*; Singh, N.B., Goyal, R., Middendorf, B., Eds.; Woodhead Publishing: Cambridge, UK, 2025; pp. 211–232.

https://doi.org/10.3390/buildings16040767

38. Patrisia, Y.; Gunasekara, C.; Setunge, S.; Mendis, P.; Nanayakkara, O. Multi-perspective evaluation of waste-derived cellulose fiber concrete: Engineering performance, microstructure and sustainability. *Sustain. Resilient Infrastruct.* **2025**, 1–24. [CrossRef]
39. Lin, X.; Nguyen, Q.D.; Castel, A.; Deng, Z.; Li, W.; Tam, V.W.Y. Self-healing of biochar-cement composites with crystalline admixture exposed to sulphate solution and simulated seawater. *J. Build. Eng.* **2025**, *99*, 111564. [CrossRef]
40. Lo Monte, F.; Ferrara, L. Self-healing characterization of UHPFRCC with crystalline admixture: Experimental assessment via multi-test/multi-parameter approach. *Constr. Build. Mater.* **2021**, *283*, 122579. [CrossRef]
41. Kumar, R.; Singh, R.; Patel, M. Effect of metakaolin on mechanical characteristics of the mortar and concrete: A critical review. *Mater. Today Proc.* **2023**, *93*, 315–319. [CrossRef]
42. Jóźwiak-Niedźwiedzka, D.; Fantilli, A.P.; Dziedzic, K.; Lisowski, P. Effect of different fibres in mitigation of alkali-silica reaction. *Mater. Today Proc.* 2023, *in press*.
43. Jagtap, S.A.; Shirsath, M.N.; Palaskar, S.M.; Karpe, S.L. Effect of metakaolin and basalt fibre on mechanical properties of conventional concerete. *Int. J. Adv. Res. Innov. Ideas Educ.* **2022**, *3*, 1–5.
44. Velastegui, L.; Velasco, N.; Sanchez Quispe, H.R.; Barahona, F.; Onyelowe, K.C.; Hanandeh, S.; Ebid, A.M.; John, T.A. Predicting the impact of adding metakaolin on the flexural strength of concrete using ML classification techniques—A comparative study. *Front. Built Environ.* **2024**, *10*, 1434159. [CrossRef]
45. Lauch, K.S.; Desmettre, C.; Charron, J.-P. Self-healing of concrete containing different admixtures under laboratory and long-term real outdoor expositions based on water permeability test. *Constr. Build. Mater.* **2022**, *324*, 126700. [CrossRef]
46. Luo, D.; Sinha, A.; Adhikari, M.; Wei, J. Mitigating alkali-silica reaction through metakaolin-based internal conditioning: New insights into property evolution and mitigation mechanism. *Cem. Concr. Res.* **2022**, *159*, 106888. [CrossRef]
47. Jaberizadeh, M.; Danoglidis, P.; Shah, S.P.; Konsta-Gdoutos, M. Harnessing Waste Cellulose Fibers for Developing Highly Resilient and Durable Cementitious Composites. In Proceedings of the C3 Symposium 2025, Chicago, IL, USA, 2–5 October 2025; Volume 6.
48. Oyan, V.; Özvan, A.; Tapan, M. Effectiveness of Pumice and Scoria Aggregates in Controlling Alkali Silica Reaction. In Proceedings of the Ninth International Concrete Conference and Exhibition for Sustainable Construction, Manama, Bahrain, 11–13 February 2013.
49. Veliseicik, T.; Zurauskiene, R.; Kligys, M.; Dauksevic, M. Influence of Short Carbon Fibers on the Properties of Autoclaved Fiber Cement in Standard Fire Environment. *Materials* **2023**, *16*, 2513. [CrossRef]
50. Ren, G.; Guo, Y.; Shen, A.; Pan, H.; Wu, H.; Deng, S. Effects of cellulose fiber on shrinkage, anticrack performance, and mechanical properties of concrete. *Constr. Build. Mater.* **2024**, *451*, 138824. [CrossRef]
51. Nagrockienė, D.; Pundienė, I.; Kanapeckienė, L.; Jarmolajeva, E. The Impact of High-Alkali Biofuel Fly Ash on the Sustainability Parameters of Concrete. *Buildings* **2023**, *13*, 3015. [CrossRef]

Disclaimer/Publisher's Note: The statements, opinions and data contained in all publications are solely those of the individual author(s) and contributor(s) and not of MDPI and/or the editor(s). MDPI and/or the editor(s) disclaim responsibility for any injury to people or property resulting from any ideas, methods, instructions or products referred to in the content.

https://doi.org/10.3390/buildings16040767

buildings

MDPI

Review

3D Concrete Printing Review: Equipment, Materials, Mix Design, and Properties

Giedrius Girskas and Modestas Kligys *

Institute of Building Materials, Faculty of Civil Engineering, Vilnius Gediminas Technical University (VILNIUS TECH), LT-10223 Vilnius, Lithuania; giedrius.girskas@vilniustech.lt
* Correspondence: modestas.kligys@vilniustech.lt

Abstract: 3D concrete printing (3DCP) technology holds significant potential to revolutionise traditional concrete production methods, offering designers and architects greater flexibility in creating intricate and innovative structures. Beyond structural applications, 3D printed concrete products encompass decorative elements, customised design solutions, and even artistic installations. The 3DCP process is highly automated, often integrating building information modelling (BIM) systems, minimising the need for manual labour and generating minimal material waste. 3DCP is regarded as one of the most advanced and efficient methods for fabricating concrete components in the future. This paper examines 3DCP technology and equipment, focusing on the selection of binder types, aggregates, and chemical admixtures, suitable for printable concrete mixes. Particular attention is given to the consistency and workability of 3DCP mixtures. Furthermore, the study evaluates the influence of 3D printing parameters on the mechanical properties of hardened concrete. The insights presented in this review contribute to a deeper understanding of 3D concrete printing technologies, equipment, and materials, benefiting researchers, structural engineers, and designers in the pursuit of enhanced durability and performance of 3D printed concrete structures.

Keywords: 3D concrete printing (3DCP); printed concrete; concrete mix; contour crafting; D-shape technology; air-entraining agent; geopolymers

1. Introduction

3D concrete printing (3DP) is an additive manufacturing technology based on the layer-by-layer deposition of a specially designed concrete mixture, without the need for formwork or compaction of the placed material. The practical implementation of 3D printing technology in construction requires an interdisciplinary approach, drawing on the expertise of specialists in robotics, computational design, materials science, and architecture [1].

J. Pegna made the first attempt to apply additive manufacturing technology to cement-based materials in 1997 (USA) [2]. Over the past decade, the development of 3D concrete printing (3DP) has accelerated significantly, accompanied by a growing number of research groups active in this field of construction (Figure 1) [3]. Several pioneering companies have taken early steps in large-scale concrete additive manufacturing, including ICON (Texas, USA), Apis Cor (USA, Russia), XtreeE (France), WinSun (China), CyBe (Netherlands), Mighty Buildings (California, USA), and WASP (Italy) [4].

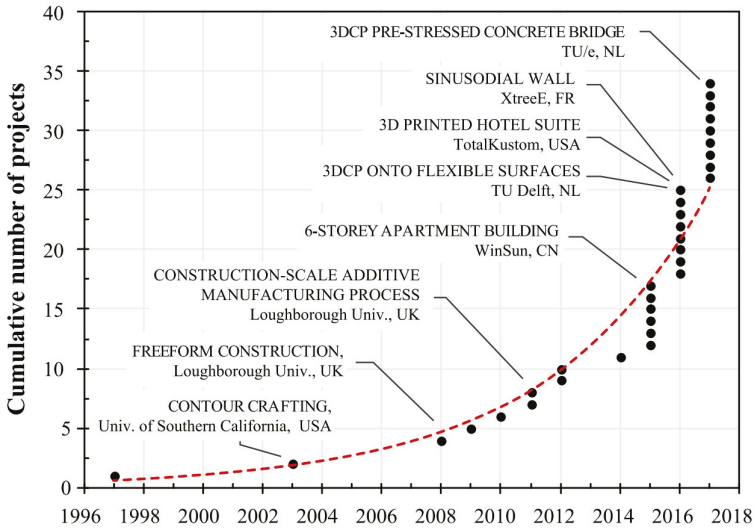

Figure 1. The rise in additive manufacturing since 1997 [3].

According to forecasts, 3DCP is a promising technology that could significantly reduce construction waste (~30–60%), labour costs (~50–80%), and production time (~50–70%) [1]. However, contrasting views also exist. G. De Schutter et al. noted that while 3DCP offers various opportunities to lower economic costs compared to traditional construction methods, some uncertainty remains, particularly regarding its environmental impact [5].

Nonetheless, it is widely believed that 3DCP will enable the rapid construction of sustainable and affordable housing, especially in low-income regions of the world, facilitate the creation of complex designs, support repair and reconstruction efforts, and even allow for building structures on the Moon or Mars [1].

Several impressive projects have already been realised worldwide. In 2014, the Chinese company WinSun presented a five-storey 3D printed apartment building and 1100 sq. meters villa. 3D printed elements were produced off-site and assembled on-site [6].

In December 2015, the company AMT SPECAVIA (Yaroslavl, Russia) printed a house of 298.5 m^2 area in one month (Figure 2) [7]. Apis Cor Company printed a house in the Moscow region (Russia) in 24 h [8]. The examples of the first 3D printed commercial buildings were presented in the Southern Hemisphere (Figure 3) [9] and United Arab Emirates [10].



(**a**) (**b**)

Figure 2. Printed house by a company AMT SPECAVIA [7]: (**a**) printing process; (**b**) final product.

In addition to the printing of houses and commercial buildings, 3D printing technology has also been applied to the production of infrastructure elements, such as bridges (Figure 4a), bus stops, and a fountain restoration (Figure 4b) [11–13].



Figure 3. The first 3D printed commercial building in Hamilton (New Zealand) [9].



(**a**) (**b**)

Figure 4. 3D printed infrastructure elements: (**a**) the first 3D printed bridge in Madrid (Spain) [11]; (**b**) restoration of the fountain in Palekh (Russia) [13].

3DCP was also used in the production of architectural forms of different functionality (Figure 5) [14]. Digital fabrication has opened for architecture unexpected new possibilities for previously unachievable materiality, detail, and complexity, but deeper findings into a holistic perspective of the 3D printing technologies as factors, which can influence architecture, are missed [15,16].



Figure 5. Concrete choreography at the Origen Festival of Culture (Switzerland). Photo by Benjamin Hofer [14].

The intensive development of 3DCP in the construction industry is continuing nowadays. The American company SQ4D offered the first 3D printed houses holding the certificates of occupancy in Riverhead, New York [17]. Texas Military Department's Joint Force Headquarters in Austin is another example [18]. An affordable 3D printed neighbourhood for poor families was built in Mexico [19]. A company "Kamp C" (Belgium) built a two-storey house of 90 sq. metres in situ (Figure 6), rather than assembling it from pre-printed elements [20]. Developers in Southern California offer 30 beautifully designed zero net energy 3D printed single-family homes in Rancho Mirage [21]. Cazza Technologies, a pioneer in exploring large-scale 3D printing, has plans to build the world's first 3D printed skyscraper using a "crane printing" technique [22].

Despite the remarkable interest in 3DCP and examples of the successful application of this technology, certain limitations still hinder its widespread adoption. Challenges relate to the properties of fresh concrete, including the open time, setting behaviour, layer cycle time, deformation control, rheological characteristics, and workability. In the hardened state, key issues involve anisotropic mechanical properties, interlayer bond strength, bulk density variations, underfilling, shrinkage, tensile reinforcement, durability, and the standardisation of testing the properties of hardened concrete. Dimensional stability also presents difficulties, such as achieving minimum printable dimensions and tolerances, ensuring the appropriate density, optimising hatching strategies, modelling and simulating the printing process, and producing overhanging structures [3,23]. Also, there are challenges of upscaling 3DCP to larger buildings and the limited number of printing methods available, each requiring specifically engineered concrete mix designs [23].



Figure 6. Two-storey 3D house in Belgium. Photo by "Kamp C" and Jasmien Smets [20].

2. 3D Concrete Printing Settings and Equipment

2.1. Main Phases of 3D Concrete Printing Process

The 3D concrete printing process can be divided into two main phases: delivery and deposition. In the delivery phase, the concrete mixture is prepared for 3D printing and delivered through the hose to the nozzle. In the deposition phase, the materials are extruded through the moving nozzle onto the surface of a supporting platform or previously printed layers. The delivery phase can be linked with off-line or in-line mixing, which determines further properties of the 3D printed concrete.

The key equipment in the delivery phase is the pump (piston pump, peristaltic squeeze pump, or screw pump), while in the deposition phase, the core equipment is an end effector which controls the movement of the nozzle. For a successful 3D printing process,

the concrete mixture must have suitable pumpability for delivery and buildability for deposition [24]. The 3D concrete printing system layout is shown in Figure 7 [25].

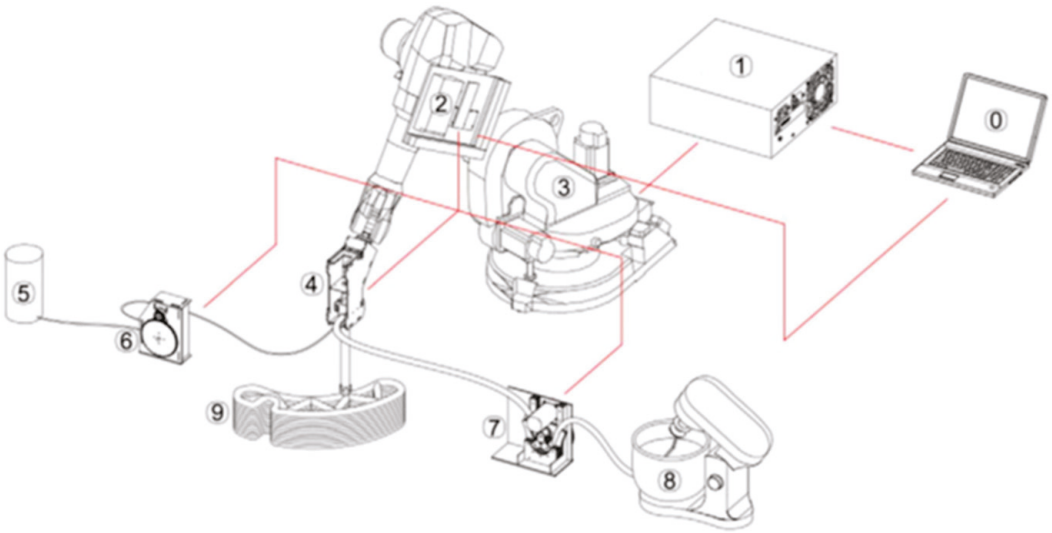

Figure 7. Schematic diagram of a 3D concrete printing system. The system includes the system command unit (0) coordinating the robot controller (1) and printing controller (2); a robotic arm (3) handling the printhead (4); separate peristaltic pumps delivering the accelerating agent (6) and premix material (7); a premix mixer (8); and the 3D printed object produced by the process (9) [25].

At present, contour crafting, concrete printing, and D-shape technologies represent the most intensively researched approaches within the domain of 3D concrete printing.

2.2. Contour Crafting (CC)

CC is a gantry-based 3D cementitious material printing system (Figure 8) for large-scale applications developed by B. Khoshnevis [24,26].

The 3D mixture is extruded through the nozzle, which forms the perimeter of the designed structure. The layers are formed when the nozzle returns to the original position and forms a closed loop. The nozzle then rises and starts printing the next layer atop the previous one. With CC technology, a permanent 3D formwork of the future 3D printed structure is created [24]. CC is an additive manufacturing technology that uses computer-controlled top and side trowels to create a superior surface finish of the final objects. The concrete mix is extruded to the area bounded by the rim walls [26].

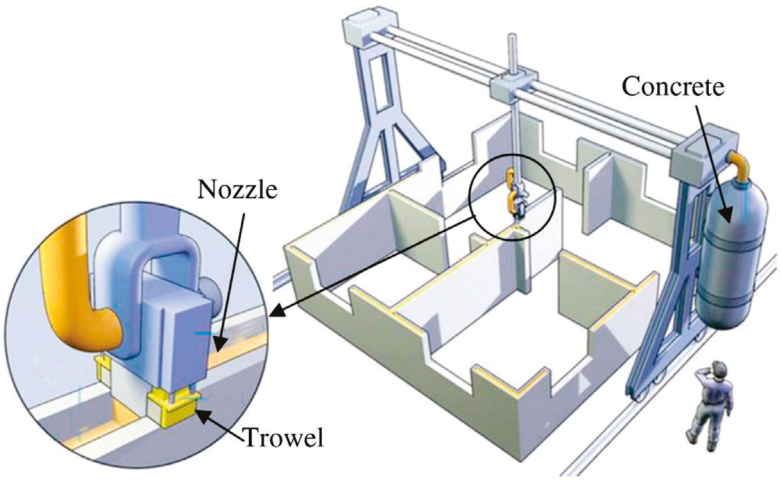

Figure 8. Contour crafting 3D printing system [27].

In the (CC) 3D printing process, construction begins with a digital building model, requiring seamless interoperability between various components of the construction system, and the selected Building Information Modelling (BIM) software platform (Figure 9) [28].

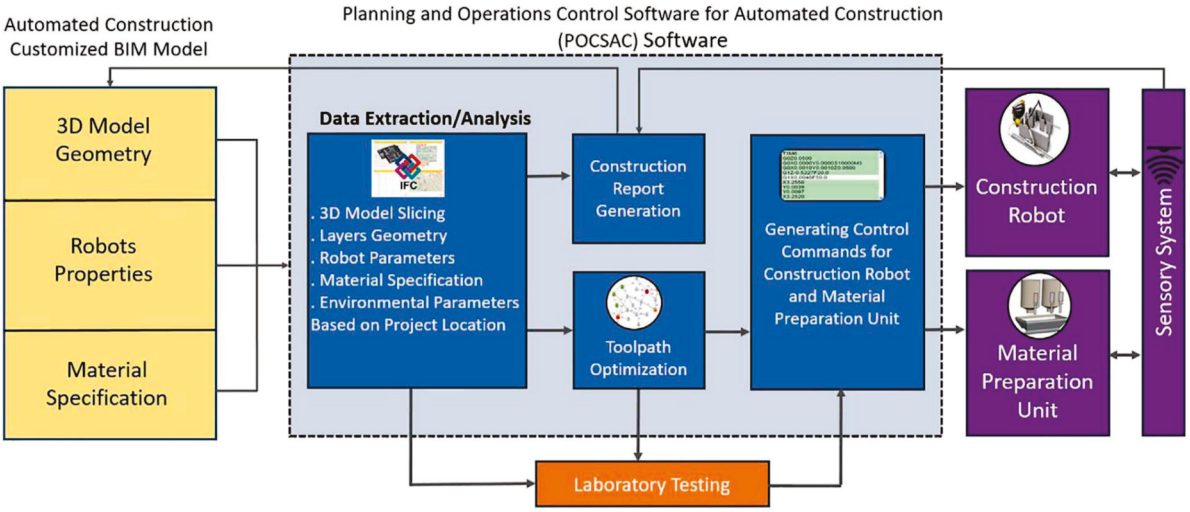

Figure 9. Methodology and framework for operations control software for automated construction [28].

The entire construction workflow in the CC system is driven by the generation of a tool path, which defines the nozzle's position, orientation, velocity, and material deposition rate throughout the building process. This tool path information is then translated into a sequence of machine-specific commands and uploaded to the CC machine. To ensure efficient fabrication of complex structures, researchers focus on the tool path optimisation by developing collision-free strategies, including path cycling, buffer zone path cycling, and auxiliary buffer zones [27].

CC printing technology contributes to better surface quality, higher speed of production, and a choice of materials [26]. However, despite these advantages, CC has several drawbacks, such as vertical extrusion limitations, the complexity of the initial formwork and trowel system, interruption of the sequential casting of concrete due to hydrostatic pressure, insufficient mechanical properties, and poor interfacial performance of the printed layers [25].

Along with the gantry-based system, the arm-based system had started its development (Figure 10). This system differs by the additional print nozzle yaw, pitch, and roll control. The tangential continuity method enables the print nozzle to create more articulate print designs [29]. The robot-based system has a wider variety of designed structures compared to CC. This technology is suitable for onsite printing due to its mounting on the movable platform [24].

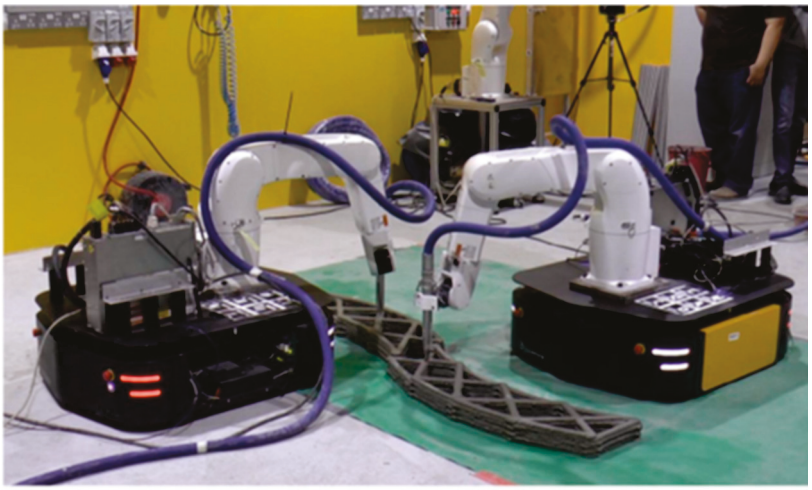

Figure 10. 3D printing by the team of mobile robots [29].

2.3. Concrete Printing (CP)

Similar to the CC system, the CP system (Figure 11) created by Lim et al. [30] is based on the extrusion process of cementitious materials. The main advantages of CP compared CC are better printing system control and higher printing resolution. The absence of surface scraping in CP makes the layered texture of the printed structure visible. Compared to CC technology, the CP printing system creates filaments of smaller dimensions [24].



(**a**) (**b**)

Figure 11. The CP system: (**a**) gantry framework; (**b**) details of printed structure [30].

In the (CP) system, the entire geometry of each layer can be printed continuously, rather than beginning with the outer perimeter [1]. The system consists of a large frame equipped with a movable beam and a mounted nozzle. The nozzle travels along the beam, while the beam itself moves in a direction orthogonal to the nozzle's path, enabling free-form 3D printing in the horizontal plane [24]. The raw material is premixed and stored in a pump located outside the printer. It is then fed through a pipe to a small hopper positioned above the nozzle [1].

2.4. D-Shape Printing

Binder jetting, powder bed printing, or D-shape printing technology (Figure 12) was first applied by architect Enrico Dini to create complex elements (with cement binder).

It is based on powder deposition and the bonding of powder with a chemical agent (binder) [1,31,32].

The system consists of a printing head containing a series of nozzles used to dispense the chemical agent and the solid powder. Initially, the powder is dispensed to form a layer of designed thickness. After that, rolling cylinders apply a homogeneous pressure to the powder and the chemical agent is sprayed onto the powder layer in predetermined locations [1]. D-shape printing technology contributes to a high degree of geometric freedom. However, the system has some disadvantages related with reinforcement, the layer height determined by the binding process, recycling of unbound cement powder, and required post-manufacture processing after printing [31,33].

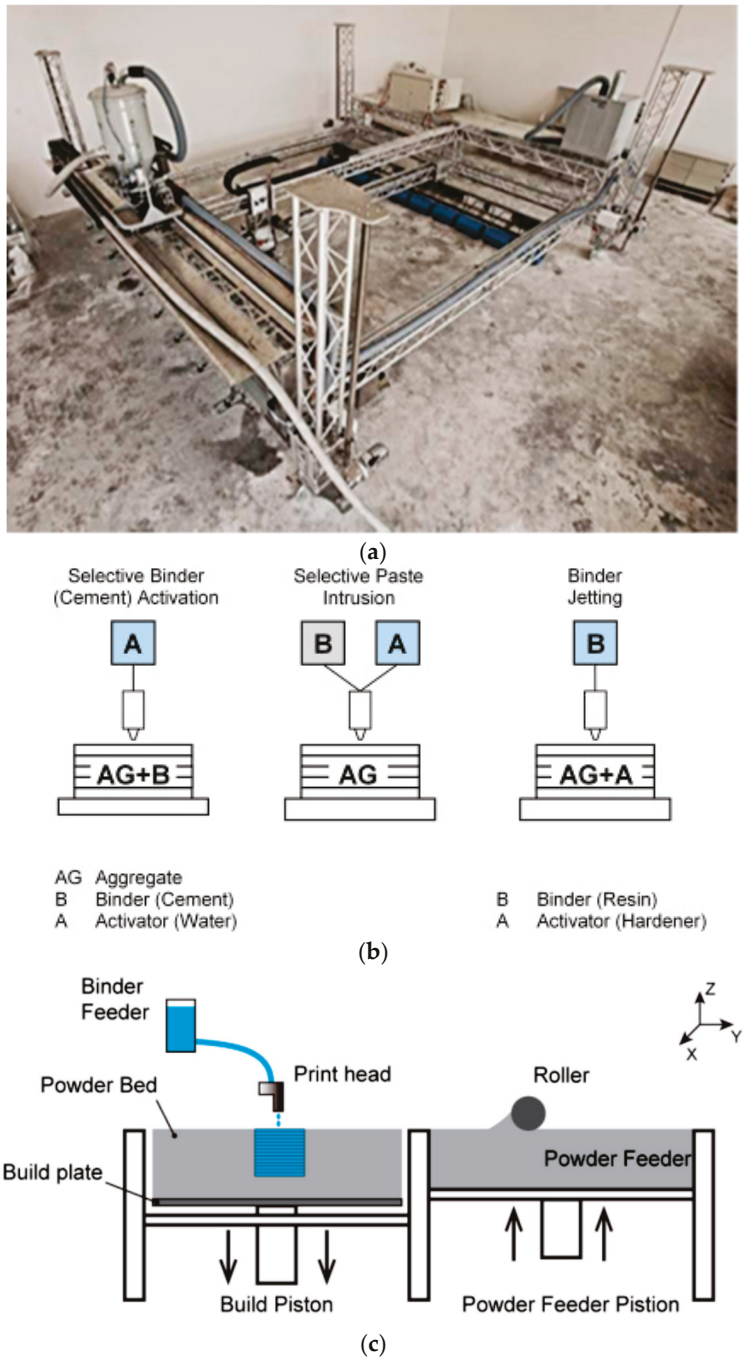

(**a**)

(**b**)

(**c**)

Figure 12. 3D technology: (**a**) D-shape printer [34], (**b**) schematic diagram of selective binding particle-bed 3D printing [35]; (**c**) schematic diagram of powder-based method [36].

2.5. Comparison of 3D Printing Systems

The geometric parameters of the printer limit the large-scale application of 3D printed concrete in construction practice [1]. CP- and D-shape systems are considered as more suitable for off-site printing, while CC is more applicable for producing construction elements in situ [32]. However, the development of 3D printing systems expands the possibilities of applying them both off-site and in situ with local construction materials used [25,34]. The main features of currently available 3D printing systems are compared in Table 1 [1].

Table 1. Comparison of 3D printing systems [1].

Methods	Contour Crafting	Concrete Printing	D-Shape
Printing process	Extruding	Extruding	Spreading
Raw materials	Mortar or cementitious materials	Mixed 3D printed concrete	Powdered materials and chemical agents
Resolution	Smooth surface	4–6 mm	~13 mm
Printing speed	Low	High	Medium
Printing dimension	Large-scale structure	Large-scale structure	Medium-size structure
Advantages	Smooth surface formed by trowels	High strength and building speed	High strength
	Conduits can be embedded into components		
	Intelligent switching of printing materials		
Disadvantages	Slower speed of construction due to trowels	High performance requirements for 3D printed concrete, such as setting and hardening times	Lower resolution
	Low bonding strength between layers caused due to longer intervals		Big quantities of powdered materials required
			Redundant powder materials have to be removed

3. Binder Type and Technical Characteristics

In the context of 3D concrete printing, printable concrete mixtures are often referred to as “inks”, reflecting their function as flowable, extrudable materials that must possess specific rheological properties, such as pumpability, extrudability, and buildability. These properties primarily depend on the type of binder used, which determines the rheological properties of the mixtures and their hydration behaviour, essential for printability and buildability.

Different types of binder materials were proposed for 3D printing. The possibility of using ordinary Portland cement (OPC) of CEM 42.5 R strength class was studied [37–40]. D. Weger and C. Gehlen used CEM 42.5 R cement to print elements using the particle-bed-based method [38]. A. Vespalec et al. analysed 3D printing possibilities using a mix of CEM I 42.5 R cement modified with metakaolin [39]. The concrete mix formulations with CEM I 52.5 R or CEM I 52.5 N cement for 3D concrete printing are presented in other studies [40–43]. Le et al. [40] chose CEM I 52.5 cement to obtain high-performance printed concrete having a compressive strength above 100 MPa and a flexural strength above 10 MPa. The cement CEM I 52.5 content in 3D printing mix formulations studied

varies from ~330 kg/m^3 [41] to ~550–620 kg/m^3 [42,43], depending on the amounts of supplementary cementitious materials used to replace cement.

The setting parameters are crucial for 3D printing mixture. To control the printability of a 3D mixture, researchers suggest to mix OPC and calcium sulfoaluminate (CSA) cement [44–48]. Khalil et al. developed a printable mix containing 7% CSA and 93% OPC, and reached a compressive strength of the printed samples equal to 79 MPa [44]. Mohan et al. compared the impact of CSA and the OPC-CEM I 52.5 N mix on 3D printable concrete. The researchers found that the mixture based on CSA had a significantly lower open time and a higher plastic viscosity than the OPC-based mixture, whereas the yield stress and the lubricating layer were similar for both types of cement [45]. B. Zareiyan and B. Khoshnevis noticed that CSA works as a catalyst in the concrete hardening process, and, therefore, contributes to higher early strength development. The researchers tested the binder for a 3D printing mixture based on 60% CSA and 40% type I OPC [46].

Y. Weng et al. proposed a formulation for a sustainable and rapid hardening 3D printing mix based on magnesium potassium phosphate cement (MPC), replaced by a combination of fly ash and silica fume at different rates [49].

Along with mineral binders, geopolymers can be applied as a binder for 3D printing mixture. S. Muthukrishnan et al. investigated a geopolymer based on ground granulated blast furnace slag and fly ash activated by the anhydrous sodium metasilicate (Na_2SiO_3) in a 3D printing mix design [50]. O. Ly et al. compared a geopolymer based on fly ash activated by sodium hydroxide (NaOH) and CEM III/B 32.5 N-S class cement. The researchers produced artificial 3D printed concrete reefs and found that cement was a better binder for this application [51]. The commonly used binders in 3D concrete printing are presented in Table 2.

Table 2. Characteristics of different binders, used in 3D concrete printing [52].

	OPC	CSA	CSA-OPC	Geopolymer	MPC
Characteristics suitable for 3D printing	High strength, high stability	High early strength, short setting time, less impact on the environment	Short setting time, high early strength	High durability, high chemical resistance, eco-friendly	Rapid setting time, high early strength, low shrinkage
Limitations	Long setting time, weak early strength	Low printing open time, high pumping pressure	Reduction in later strength and cracking due to high CSA content	High drying shrinkage, harsh curing conditions	Low printing open time

4. Aggregate Fineness and Optimisation of Particle Size Distribution

The type of aggregates used has a significant impact on the properties of 3D printed concrete. Aggregates determine early-age behaviour, mechanical properties, and shrinkage resistance of concrete [37]. In most cases, the composition of 3D printed concrete includes up to 2 mm fraction sand as a fine aggregate, whereas coarse aggregates are not used in a 3D printed concrete mix design [40,41,43–45,53]. Le et al. used up to 2 mm sand with a sand/binder ratio of 60:40 and water/cement ratio of 0.37 for a printer with a nozzle diameter of 9 mm [40]. Calcareous crushed 0/2 mm sand with 19% of particles smaller than 63 mm in the mixture with an OPC/sand ratio of about 1.2, and a W/C ratio of about 0.35 was suggested for a 3D concrete mixture in the study [44]. Concrete compositions with a binder-to-sand ratios of 1:1.5 and 1:2 and water-to-binder ratios of 0.3 and 0.37 were proposed in the studies [41] and [43], respectively, where sand with a maximum grain size

of 2 mm was used as a fine aggregate. Mohan et al. applied sand with a nominal size of 2 mm and specific gravity of 2.65 g/cm^3 and varied aggregate-to-binder ratios from 1.0 to 1.8 to reduce the binder content. The researchers observed that the increase in aggregate content leads to an increase in yield stress, viscosity, and pumping pressure of a 3D printed concrete mixture [54]. Kazemian et al. tested 3D concrete, in which artificial sand with a nominal maximum aggregate size of 2.36 mm, specific gravity of 2.6 g/cm^3, fineness modulus of 2.9, and absorption capacity of 1.3% was used as a fine aggregate [55].

Zhang et al. used three types of sand as fine aggregates: 0/4.75 mm natural sand with a 2.61 fineness modulus, 0/1.18 mm fine sand with a 2.02 fineness modulus screened from natural sand through a 1.18 mm square hole sieve, and 0/2.36 mm sand with a 2.33 fineness modulus screened from natural sand through a 2.36 mm square hole sieve. The researchers noticed a linear relationship between the flowability of cement paste and the optimum aggregate content in a printable mortar with a given buildability. The flowability and rheological properties of cement pastes containing sand with different aggregate sizes were tested in the study (Figures 13 and 14) [56].

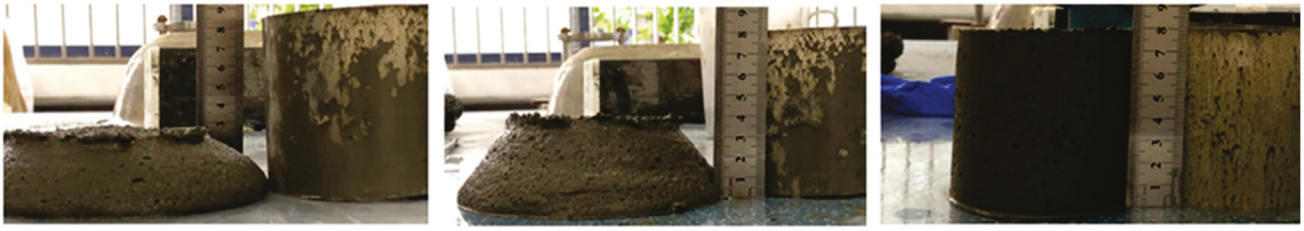

Figure 13. Buildability assessment of 3D printed concrete with sand of different fineness [56].

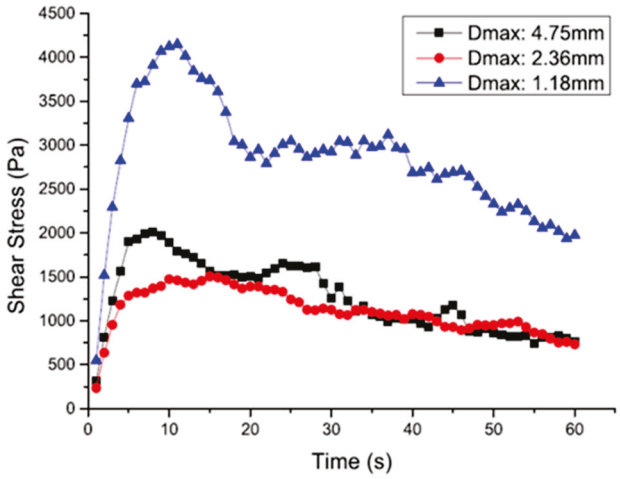

Figure 14. Results of rheological tests on mortars with different sand fineness (tests with a constant shear rate of 0.2 s^{-1}) [56].

Rigid surface aggregates with maximum sizes of 3/32″, 3/16″, 1/4″, and 1/2″ and different aggregate-to-cement ratios varying from 1.1 to 2.75 were researched [46]. The researchers identified the increase in the compressive strength of the mixtures with smaller-size aggregates and explained it by the decrease in aggregate volume relative to the total composite volume.

In other studies, a 3D printed concrete mixture was designed using sand with a maximum grain size of 4 mm [39,42]. Meurer and Classen used sand with a maximum grain size of 4 mm and the aggregate ratio of 25%, 30%, 25%, and 20% for the sieve fractions of 0.0–0.2, 0.2–1.0, 1.0–2.0, and 2.0–4.0, respectively. The researchers highlighted that only a

small portion of the aggregate with 2–4 mm grains can ensure a dense structure and a good buildability [42].

A study [39] demonstrated the applicability of fine and coarse aggregate combinations in a 3D printed concrete mix design. The mortar was extruded using a specially designed extruder at a constant speed of 10 mm/s in a horizontal direction. 0–4 mm sand was chosen as a fine aggregate, and 4–8 mm crushed stone was used as a coarse aggregate. The concrete mixture was prepared with a water-to-binder ratio of 0.57, and the binder–fine–coarse aggregate ratio was approximately 1:2.26:0.6 [39]. Rahul and Santhanam evaluated the 3D printability of concrete prepared with lightweight expanded clay aggregates with a maximum size of 10 mm. The concrete mixture was extruded from a piston pump-based 3D printer system. Concrete mixtures with quartz sand as fine aggregates were also studied. The binder-to-aggregate ratio was 60:40 for all tested samples [57].

The 3D printed concrete mix design should also meet sustainability requirements. Therefore, the origin of the aggregates for concrete should be considered, and the possibilities of using different types of waste materials as a replacement for traditional aggregates in 3D printed concrete compositions should be investigated.

Bai et al. investigated the application of desert sand (small size), river sediment sand (medium size), and recycled concrete (large size) as aggregates in the development of eco-friendly 3D concrete composition. In the course of research, it was observed that desert sand has more uniform gradation, with more than 90% of the grains smaller than 0.20 mm and a maximum sand grain diameter of 0.30 mm, whereas the river-sediment sand has spherical shape grains and more than 50% and 90% of the grains are smaller than 2.3 and 4.0 mm, respectively. Recycled concrete aggregate was of a cuboid shape and had a maximum particle size of up to 1/3 of the printing nozzle diameter to avoid blockage of the printing nozzle. The researchers highlighted that the interlayer distribution and skeleton of the graded aggregate contribute to improving the interfacial interlocking capacity and contact bonding between layers. Also, the mitigation of shrinkage of the cement matrix was observed with the addition of aggregates due to the reduction in cementitious material content in the concrete mixture [37]. Ly et al. tested compositions with recycled sand (limestone sand, glass sand, and seashell sand) mixed with geopolymer or cement for 3D printing of artificial reefs [51]. Ting et al. applied recycled glass in a 3D printed concrete mix design. The researchers compared 3D printed concrete formulations with recycled glass and with river sand. The recycled glass of medium, fine, and super fine grading with particle size ranges of 1000–1700, 500–1000, and 150–710 μm, respectively, was tested. The recycled glass-based mixture demonstrated better flow behaviour but lower mechanical properties compared to the river sand-based mixture [58].

5. Control of Bonding Parameters with Chemical Admixtures

Chemical admixtures, such as superplasticisers (SPs), viscosity-modifying agents (VMAs), setting retarders (SRs), and accelerators (SAs), are important components in a 3D printed concrete mix design. The properties of 3D concrete mixture, such as workability, adhesion, rigidity, a short setting time, and high early strength, are controlled by the chemical admixtures mentioned above [1].

It is expected that in the course of the 3D printing, the cement suspension with the addition of SP will become more fluid during pumping and recover its shape after printing quickly enough to support the next printed filament. It makes the open time shorter for printing and requires constant concrete feeding. The important aspect in the selection of SP is the length of the filament printing path and the place of printing (on-site or off-site). The rheological properties of concrete mixture usually change during the hydration process; therefore, set retarders are necessary to mitigate the changes and extend the open time

before printing. Set retarders can have a negative impact on buildability, but it is possible to overcome this disadvantage by using retarders together with accelerators. The 3D concrete printing mixture must be consistent after the printing, but it should have a minimum fluidity to be extruded through the nozzle. To achieve it, SP is added in combination with VMAs. VMAs prevent segregation, bleeding, and reduce water evaporation and drying shrinkage. The properties of a 3D printed concrete mixture are also controlled by air-entraining agents (AEAs). AEAs improve workability, reduce the exudation tendency and drying shrinkage, contribute to stability during pumping and extrusion/printing, and preserve the geometric shape of the 3D printed concrete elements [59].

Frequently, a 3D printed concrete mixture includes a complex of chemical admixtures in order to regulate the properties of the mixture in different ways.

Kazemian et al. focused on the workability of a fresh "printing mixture" in terms of print quality, shape stability, and printability window. For this purpose, the concrete mixture was prepared with the addition of a polycarboxylate-based high-range water reducing admixture at 0.05 wt% to achieve the required flowability for the mixtures and viscosity-modifying admixture at 0.11 wt% for anti-washout concrete to ensure the increase in the plastic viscosity and cohesion of printing mixtures when the water to cement ratio was of 0.43 [55].

Manu K. Mohan et al. tested gluconate and borax as retarders in the calcium sulfoaluminate (CSA) cement system. Concrete formulation also included a viscosity-modifying admixture dosed at 0.1% by weight of the binder. Both retarders were added at 0.5% by weight of cement to increase the open time; however, they had different effects on the early-age strength. The researchers stated that gluconate has a more remarkable impact on the early-age compressive strength than borax [45].

K. Manikandan et al. used a polycarbonate-based superplasticizer [60] in combination with silica fume in a 3DPC mixture and noticed SP's capacity to act as a viscosity-modifying admixture. The tested polycarbonate SP improved yield stress and maintained the required viscosity of a 3D concrete mixture for a long time.

Le et al. developed a composition for high-performance 3D printed concrete. Polycarboxylate-based SP was added into the concrete mixture to lower the water/binder ratio and, consequently, to increase the workability and strength of concrete. A constant flow during printing and sufficient open time were maintained by using a retarder based on amino-tris (methylenephosphonic acid), citric acid, and formaldehyde. SP and SR were dosed at 1% and 0.5% by weight of binder, respectively. The chosen chemical admixtures provided the optimum workability, optimum open time of up to 100 min, and the ability to print many layers with various filament groups [40].

Khalil et al. developed a manually printable mix based on 93% OPC and 7% calcium sulfoaluminate cement with a W/C ratio of 0.35, a sand-to-cement ratio of 2, and of a polyvalent non-chlorated acrylic copolymer superplasticizer added at 0.26% of the total weight of the binder [44].

Zhang et al. studied the dependence of the flowability of a 3D printed concrete mixture on the optimum aggregate content with the addition of polycarboxylate ether SP at 0.8–1.0 wt% of the binder [56]. Polycarboxylate ether SP dosed at 1.5–1.8 wt% was also used in the research on 3D printed concrete properties prepared with underutilised or waste solids [37].

Chen et al. designed a composition for 3D printed concrete, which involved a polycarboxylate ether-based SP and a hydroxypropyl methylcellulose-based viscosity-modifying admixture dosed at 2 wt% and 0.14–0.48 wt%, respectively. The researchers stated that the composition with 0.24% VMA produced a small extrusion pressure at different ages or under different extrusion rates and good shape stability after 25 min [41].

3D printed concrete implies the application of new approaches in concrete technology, and is primarily linked with a concrete mix design. It is reasonable to develop new chemical admixtures and complex admixtures to achieve concrete mixtures with new properties. For instance, Salman et al. [61] described the possibility of grafting polycarboxylate ether molecules onto the surface of nano-cellulosic fibres, which can improve extrudability and the hardened properties of 3D printed concrete.

6. Mineral Additives and Micro-Fillers

In addition to chemical admixtures, the properties of 3D printable concrete mixtures can be tuned by various mineral additives [24].

Kazemian et al. [55] investigated four different 3D printable concrete mixtures containing densified silica fume, highly purified attapulgite (nano clay) with an average particle length of 1.75 mm, and polypropylene fibers for shrinkage reinforcement. They observed that modifying the fresh mixtures with silica fume and nano clay enhanced shape stability, whereas no significant improvement was recorded when adding fibres [55].

The effectiveness of clay addition in improving 3D printable concrete mixture properties was reported in [59]. According to that study, the water adsorption capacity of clay leads to increases in viscosity, initial yield stress, plasticity, and flowability of the mixture during printing. Clay's plasticity and moldability are attributed to its sheet-like silicate structure and variable amounts of entrapped water [59].

Mineral additives are frequently used as partial cement replacements in 3D printable concrete mixtures. Limestone is one of the widely used Supplementary Materials. Mohan et al. [45] replaced calcium sulfoaluminate (CSA) cement with limestone powder and found that this substitution significantly reduced the plastic viscosity and, consequently, required a lowered pressure to pump the mixture. The limestone replacement did not alter the rheological properties of the lubricating layer and slightly extended the dormant period. Furthermore, the CSA cement–limestone blend enabled higher print heights compared to OPC-based mixtures, thereby improving the buildability of the 3D printed concrete.

Le et al. [40] investigated concrete modified with fly ash and silica fume. The researchers found the optimal mix to consist of 70% cement, 20% fly ash, and 10% silica fume. Zhang et al. [56] studied a concrete mixture containing silica fume, nanosilica, and micro-sized attapulgite clay to increase the yield stress of the mixture.

Ly et al. [51] compared the 3D printing results of cementitious concrete based on CEM III/B 32.5 N-SR and modified with fly ash and kaolin with geopolymer-modified concrete. The cementitious concrete exhibited superior mechanical properties compared to the geopolymer-modified concrete [51].

A comprehensive investigation into the effects of supplementary cementitious materials (SCMs) on the structural build-up of cement-based materials for 3D printing is presented in [62]. The authors examined mixtures containing various SCMs, including fly ash, silica powder, rice husk ash, and metakaolin. They determined that the particle density and surface potential of these SCMs govern their impact on the structural build-up behaviour of 3D printed concrete.

Yuan et al. [63] studied how mineral admixtures impact the development of the cement paste matrix. They examined additives such as blast ground slag, fly ash, silica fume, nanosilica, nano calcium carbonate, and attapulgite. The research results showed that granulated blast furnace slag and nanosilica were the most effective in accelerating the structural build-up rate.

A summary of the influence of mineral additives on the rheology and buildability of 3D mixtures is presented in Table 3.

Table 3. The influence of mineral additives on rheology and buildability of 3D concrete mixtures.

Reference	[55,56,62]	[51,62]	[45]	[63]	[62]	[56,59]
Material	Silica fume	Fly ash	Limestone	Blast furnace slag	Metakaolin	Clay
Effect on viscosity	Reduced	Reduced	Reduced	Reduced	Increased	Increased
Effect on yield stress	Increased	Reduced	Increased	Reduced	Increased	Increased
Effect on workability	Reduced	Enhanced	Reduced	Enhanced	Reduced	Reduced
Effect on buildability	Enhanced	Reduced	Increased	Reduced	Enhanced	Enhanced
Effect on green strength	Enhanced	Increased	Reduced	Reduced	Increased	Enhanced

7. Fiber-Reinforced Plastics

Steel corrosion is the main factor causing the deterioration of reinforced concrete structures [64,65]. It is recognised that the higher porosity of concrete negatively affects the durability of steel bars. A layered structure increases the porosity of 3D printed concrete and thus reduces the suitability of steel bars for use in 3D printed concrete structures [66–68]. Various reinforcement methods have been proposed and applied to 3D printed concrete. Polymers represent one of multiple 3D printed concrete reinforcement techniques. Fibre-reinforced polymer (FRP), a promising alternative to steel reinforcement, is characterised by its excellent anti-corrosion performance, low cost, ease of use, fatigue resistance, high strength-to-weight ratio, and good electromagnetic properties. FRP is a promising alternative to steel reinforcement in both conventional steel-reinforced concrete structures and 3D printed concrete structures [69–74]. Yan et al. applied FRP reinforcement in 3D printed concrete [75]. Feng et al. proposed using FRP as a reinforcement material for 3D printed concrete columns and beams [76,77]. Sun et al. applied flexible and rigid materials (stainless steel wire, carbon fibre reinforced wire, etc.) to reinforce 3D printed concrete [78]. Other authors proposed an attractive method of using FRP grids as internal reinforcement in 3D printed high-performance concrete structures [79–81]. There are standards and design guidelines governing the application of FRP reinforcement bars in cast concrete; however, little research and information are available on FRP reinforcement in 3D printed concrete structures [82–84]. Flexible FRP grids can be printed simultaneously with 3D concrete [85], but the key issue is the nature of the bond between 3D concrete and FRP reinforcement. The FRP bar bond behaviour in cast concrete, including the stress transfer mechanism and load–slip relationship, has been extensively analysed [86–88]. The unique anisotropic properties of 3D printed concrete can significantly reduce its bonding characteristics with FRP bars [89]. Although FRP reinforcement has been used in 3D concrete, a comprehensive evaluation of FRP and 3D concrete bond performance, with particular attention to anchor length and concrete strength, has not yet been adequately addressed.

8. Consistency and Technological Properties of Fresh Mixture

The properties of concrete in the fresh state are the most important for the performance of 3D printed concrete.

3D printed concrete mixture should be both pumpable and keep its shape with little or no deformation after extrusion. Researchers introduced a list of qualitative descriptors such as pumpability, extrudability, and buildability, specifically for the description of 3D printed concrete in the fresh state [3]. The study of the properties of 3D printed concrete mixture should focus on such aspects as open time (time during which it can be used in the printing process); the influence of open time on pumpability and extrusion; the setting and layer cycle time (the time required to complete one build layer); the influence of the cycle time on the vertical build rate; the deformation of material under the addition of the subsequent

layer; and the rheological parameters of concrete mixture and their applicability for quality control [3].

3D printed concrete mixture should maintain the viscosity and yield stress of the mix, which is critical for the suitable open time during the process. At the same time, the batching process before printing plays a significant role in 3D printing technology. The extrusion of a 3D printed concrete mixture is determined by several factors, such as the shape (round or rectangular) and size of the extrusion nozzle, nozzle movement, and its position in relation to the previous layer. The length of the extrusion path and the speed of the mixture placement define the production time of the printed component and the time needed to overlay the layers and provide a suitable interlayer bond strength [3].

Researchers offer different approaches to test the rheological properties of the mixture for 3D printing. Along with rotational and oscillatory rheological methods, hand-held rotational rheometer, ultrasonic pulse velocity, and penetrometer tests are used as novel techniques in 3D printed concrete mixtures. New testing methods are required to measure high yield stress and the plastic viscosity of 3D printed mixtures [3].

A. Kazemian et al. [55] noticed three main workability aspects for 3D printed concrete mixtures, such as print quality, shape stability, and printability window. The proposed testing procedures were mainly focused on the properties of the printed layer rather than the mixture pumpability or extrusion mechanism. The researchers evaluated the 3D printed concrete mixture as acceptable when it met the following requirements: absence of surface defects of the printed layers, visible and squared layer edges, proper dimension conformity, and dimension consistency. In addition, authors proposed two tests for laboratory testing—layer settlement and cylinder stability—to evaluate the shape stability of 3D printed concrete.

M.K. Mohan et al. investigated the rheological properties and buildability of a 3D printed concrete mixture based on calcium sulfoaluminate cement. The researchers identified that the modified mixture had a shorter open time and higher plastic viscosity than the OPC-based mixture. However, the mixture based on calcium sulfoaluminate cement in combination with limestone showed better buildability compared to the reference OPC-based mixture. Buildability was evaluated according to the critical failure height during the printing [45].

Zhang et al. [56] focused on identifying the relationship between the flowability of the paste, the optimum sand content, and sand fineness. The researchers evaluated the mixture properties basing on the Murata model, the build-up theory proposed by Perrot et al., the yield stress relationship between mortar and cement paste, the relationship between the flowability and yield stress of the cement paste, and stated that the buildability of 3D printed concrete depends on the yield stress of the mortar. From the test results, the authors established a linear relationship between the flowability of cement paste and the optimum aggregate content for the 3D printable mixture of given buildability.

Jacquet et al. noticed that the extrusion of 3D printable concrete is performed through two strategies. The first of them consists of the massive acceleration of material to ensure the stability of the structure, and the second one assumes the usage of firm mortar, which is able to sustain its own weight. At the same time, researchers highlighted that the extrusion-based printing process requires the analysis of the rheological behaviour not only under the stress but also under compression and tension [63]. In the course of the research [90], Jacquet et al. investigated the fresh properties of paste and mortar under shear, compression, and tension, and described the transition between the ductile fluid materials with symmetry in tension and compression and brittle (firm) materials with asymmetry in tension and compression.

N. Roussel [91] developed the requirements for printable concrete in terms of the yield stress, viscosity, elastic modulus, critical strain, and structuration rate. The rheological requirements are listed in Table 4.

Rahul et al. noticed the importance of the stability and homogeneity of the extrusion of cementitious materials. The researchers offer the parameter "desorptivity" to evaluate the water retaining capability of cement mortar at different constant pressures. In the course of the research, the index based on the desorptivity measurements was obtained for extrudable mixtures [92].

The research [93] describes the application of active rheology control using vibration to make 3D printed concrete flowable during pumping and set immediately after layer deposition. Moreover, J.G. Sanjayan et al. stated that in terms of buildability, the vibration–extrusion gives a similar failure height compared to the non-vibrated extrusion.

In work [94], Zhang et al. investigated the properties of fresh 3D printed concrete and evaluated its buildability, rheological properties (viscosity, yield stress, and thixotropy), workability, green strength, open time, and hydration heat. The researchers modified the mix with clay and silica fume and found that the buildability of this concrete containing a small quantity of nano clay or silica fume increased by 150% and 117%, respectively. At the same time, the remarkable enhancement of the thixotropy and green strength was observed. The buildability of 3D printed concrete was optimised by doubling the content of nano clay and silica fume.

Table 4. Rheological requirements for 3D printable concrete as a function of input printing parameters [91].

Printing Requirement	Individual Strength-Based Layer Stability	Collective Strength-Based Layer Stability	Individual Layer Geometry Control	Collective Geometry Control	Collective Buckling Failure	Plastic Cracking
Illustration	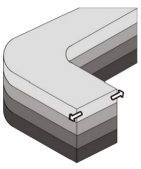	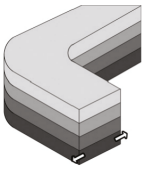	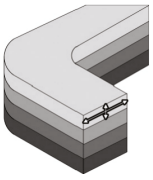	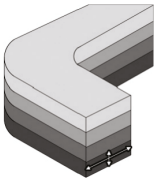	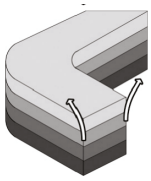	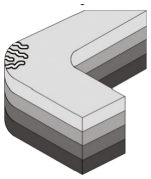
Input printing process parameters	Layer thickness h_0	Total height H	Layer thickness h_0	Total height H	Total height H layer width δ	Radius of curvature and layer width

Moeini et al. considered the effectiveness of different rheometric methods to evaluate the structuration of the mortar mixtures used for the 3D printing process [95]. The researchers noticed different rheometric methods applied for the evaluation of the build-up of the cement-based mixtures such as the static yield stress evolution, which involves the measurement of static yield stress at various time intervals after the mixing; the small amplitude oscillatory shear method, which assesses the evolution of the storage modulus and the loss modulus with time; and the hysteresis loop (re-building energy) method, which consists of the determination of the ascending and the descending flow curves. Along with rheometric methods, the authors listed the non-rheometric approaches, including the penetration resistance, undisturbed mini-slump spread loss, and the inclined plate testing method, which can be applied for the evaluation of build-up. Based on these methods, it is possible to derive the value of yield stress of the tested concrete mixture.

To sum up the results of the above-mentioned studies, the properties of 3D printable fresh concrete are determined by the open and cycle time, extrudability, pumpability,

buildability, setting parameters of the mixture, and deformations during the placement of the following layers. The rheological properties also play an important role in managing the properties of the 3D printable concrete mixture. The development of new testing methods for the 3D printable concrete mixture is required due to its differences from traditional concrete.

9. Properties of 3D Printed Concrete

The main feature of the 3D printed concrete in the hardened state is its anisotropy. The properties of 3D printed concrete in the hardened state requires to take into account such aspects as layer adhesion, bulk density, under-filling, tensile reinforcement, shrinkage, durability, and the methodology of the testing of the hardened properties [3].

T.T. Le et al. studied the hardened properties of a high-performance fibre-reinforced fine aggregate concrete extruded through a 9 mm diameter nozzle. The researchers determined the density, compressive strength, flexural strength, tensile bond strength, and drying shrinkage of 3D printed concrete. In the course of the research, it was established that well-printed concrete has a density of 2350 kg/m^3, compressive strength of 75–102 MPa, flexural strength of 6–17 MPa, depending on the testing direction, and tensile bond strength between layers varying from 2.3 to 0.7 MPa [40].

Bai et al. investigated the influence of the particle grading characteristics on the printability-related early-age behaviours, mechanical properties, and shrinkage resistance. The research showed that the interlayer distribution and skeleton of the gradated aggregate contribute to improving the interfacial interlocking effect and contact bonding between layers. Moreover, the authors stated that the addition of aggregates contributes to the mitigation of the cement matrix shrinkage due to the reduction in the cementitious material content [37].

The research [96] focused on the evaluation of the effect of interlocking on bond strength between the layers of the contour-crafted structure. In the course of the research, it was observed that bonding strength is sensitive to interlocking.

Wolfs et al. studied the relation between 3D printing process parameters and the bond strength of 3D printed concrete. The impact of the parameters, such as the interlayer interval time, nozzle height, and surface dehydration on compressive and tensile strength was evaluated. The researchers stated that with the increase in the interlayer interval time, the bond strength between layers reduced. Moreover, they highlighted the need for the standardisation of the test methods of 3D printed concrete in terms of the materials used and process parameters [97].

Ye et al. developed a novel ultra-high ductile concrete containing polyethylene fibre for 3D printing technology. The researchers conducted mechanical tests in different directions to evaluate the mechanical anisotropy of the studied concrete. The specimen printed from the fibre-modified concrete mixture demonstrated 1.5% higher mechanical performance [98].

Ding et al. evaluated the flexural properties of 3D printed concrete, which included recycled sand and fibre [99]. The test of the concrete samples in different directions (Figure 15) revealed that flexural stiffness decreased by 15–20% after the addition of 50% of recycled sand, while the negative impact of the recycled sand on the flexural strength was compensated by the presence of the fibre.

Authors also assessed the early age mechanical properties of 3D printable materials. In the course of the research, it was established that low stiffness causes elastic deformation, while a lack of green strength leads to plastic failure or brittle failure in older age specimens [99]. They applied small amounts of nano clays to improve the early age properties.

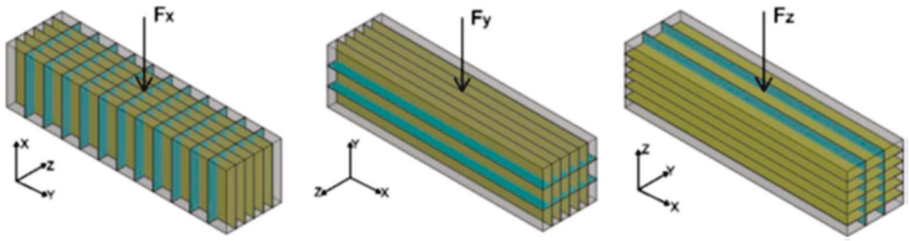

Figure 15. Layer and loading orientations of the 3D printed specimens [99].

Xiao et al. considered the impact of the nozzle dimensions, interfacial bond strength, and concrete properties on the compressive and flexural strengths. This study revealed that the horizontal shear deformation between printed filaments leads to the strength reduction in 3D printed specimens under compression. Moreover, the compressive strength is relatively lower while the flexural strength is much higher in the specimens loaded in the Y and Z directions [100].

K. Cuevas et al. developed 3D printable lightweight concrete by replacing natural aggregates with waste glass at 50% and 100%. The researchers reported an improvement in the flexural and compressive strength of the composite when 50% of the cement was replaced with waste glass. However, a 100% replacement resulted in a slight reduction in mechanical performance [101].

A summary of the influence of different raw materials on the performance in 3D printing is presented in Table 5.

Table 5. The influence of different raw materials on the performance in 3D printing.

Raw Materials	References		Pros	Cons
Binders	[3,37,97,99–101]	Ordinary Portland cement	Widely available, predictable performance, good early strength	High CO_2 footprint, moderate shrinkage
	[40]	Ordinary Portland cement (high strength)	Achieves high compressive strength, good early age strength	High content increases shrinkage, high CO_2 emissions
	[98]	UHPC	High strength and durability	Expensive
	[3]	Geopolymer	Low carbon, good buildability, reduced shrinkage	Less standardized, variable strength development
Mineral additives	[3,40,99]	Fly ash	Improves durability, workability, and pumpability, reduces heat and shrinkage, long-term strength gain, reduces CO_2	Slower strength gain, reduced early age strength
	[3,40,98]	Silica fume	Increases compressive and flexural strength, reduces permeability, porosity, and shrinkage	Expensive, increases water demand, can affect workability, requires more superplasticizer
	[3]	Slag	Improves buildability, reduces shrinkage	May reduce early strength depending on proportion

Table 5. *Cont.*

Raw Materials	References		Pros	Cons
Aggregates	[3,40,97,100]	Natural fine sand	Stable rheology, good flowability and strength, suitable for extrusion, smooth surface finish	Higher density, limited contribution to strength, neutral sustainability impact, weaker mechanical bond, potential for nozzle clogging
	[3,37]	Lightweight aggregates	Reduces density, enhances insulation	Reduces strength, increases shrinkage
	[3,37,101]	Recycled waste aggregates	Lightweight. eco-friendly, cost-effective, promotes circular economy	Variable quality, lower mechanical performance, higher shrinkage, inconsistent printability
		Expanded microspheres	Thermal insulation	Lower strength, higher shrinkage
Reinforcement	[3]	Steel fibers	Greatly improves tensile and flexural strength, controls cracking	Difficult to extrude, may clog nozzle
	[3]	Polymeric fibers	Enhance ductility, improve green strength	Can reduce flowability, may lead to anisotropy in printed layers
	[40]	Polypropylene microfibers	Reduces plastic shrinkage, enhances green strength	Slight workability reduction if not dispersed well
	[98]	Polyethylene fibers	Improved ductility, reduced cracks	Difficult to mix evenly
Chemical admixtures	[3,37,40,97–101]	Superplasticizers	Improve flowability, workability, and strength, enhanced interlayer adhesion, improved pumpability and print quality	Expensive, risk of segregation and delay in early strength development, require precise control, complicated mix design
	[3,40]	Retarders	Extend open time, allow for longer print sessions	Can delay setting and reduce early strength and buildability
	[3]	Accelerators	Improve buildability, allow faster layer stacking	May reduce open time, harder to control in varying temperatures

In summary, the evaluation of 3D printed concrete in the hardened state should consider key properties such as bulk density, interlayer bonding strength, shrinkage, durability, compressive strength, and tensile strength. Furthermore, there is a pressing need to develop standardised testing methods tailored to the specific characteristics of 3D printable concrete and the parameters of the printing process.

10. Sustainability and Future Trends of 3D Printed Concrete

The conventional construction of engineering structures involves different stages, such as planning and design, selection of suitable materials and their transportation, assembly of structural elements, etc.). These are labour-intensive activities, which typically give rise to

such issues as occupational safety risks, budget overruns, and project delays [102]. Despite its substantial contribution to the global economy, with projected expenditures reaching USD 14 trillion by 2025, the construction industry continues to lag behind other sectors in terms of technological advancement, productivity, and the adoption of automation and robotics [103]. Research [104] conducted in Central and Northern Europe shows that the biggest incentive for companies to invest in 3D printing technologies is related only to the possibility of increasing automation to address the shortage of skilled labour in the construction sector, rather than environmental benefits. The adoption of 3D printing technologies in the construction industry has the potential to facilitate the production of complex structures with exceptional precision and speed, thereby conserving natural resources, reducing pollution, and lowering labour costs [102,105]. As shown by recent studies [106], beyond its economic advantages, 3D printing technology also holds significant potential for reducing the environmental impact of construction. It contributes to lowering the global warming potential, smog formation, eutrophication, acidification, and fossil fuel consumption. Although the research on the recycling potential of 3D printed structures at the end of their service life is scarce, existing technological solutions already demonstrate considerable potential for the reuse of demolition waste. This reuse capability also supports reductions in the overall environmental footprint [107].

Moreover, 3D printing technologies have notable potential to limit emissions of greenhouse gases throughout the cement supply chain, from the production of printable mixtures to their application in newly built structures. Researchers [108] have compiled a list of production strategies focused on 3D printable mixtures and their application in structural elements, accompanied by detailed policy recommendations aimed at optimising the mitigation of climate-related impacts. These strategies and associated policy guidelines are summarised in Table 6.

Table 6. Strategy for comparing 3D printable cementitious mixtures across five policy areas [108].

Policy Area	Advanced C3DP Manufacturing Strategy	Climate-Optimized C3DP Strategy
Research and development	Continue funding studies related to material compositions and printing protocols that improve the strength, durability, and long-term performance of 3D printed structures.	Increase funding for the development of low-carbon 3D printable cementitious mixtures.
		Fund studies that improve knowledge of structural design optimisation to reduce material use and waste with C3DP.
Information dissemination and workforce development	Establish open-source data repositories for industry and academia to share data on reliable materials' manufacturing and printing protocols.	Encourage reporting and sharing of data on LCA studies, GHG inventories, and other environmental metrics within the open-source repositories.
	Commission demonstration projects with long-term performance testing plans to increase trust and the uptake of C3DP in construction projects.	Conduct environmental assessments and LCA studies in the demonstration projects to test and showcase the environmental impact of C3DP compared to conventional construction.
		Encourage construction firms to carry out GHG inventories and share data in open-source repositories.
	Establish training programs to produce skilled workers with knowledge of C3DP materials and processes.	Upskill the workforce by integrating courses on sustainability and the environmental impacts of C3DP into training programs.

Table 6. *Cont.*

Policy Area	Advanced C3DP Manufacturing Strategy	Climate-Optimized C3DP Strategy
Standards and codes	Develop manufacturing standards to ensure the strength and durability of 3D printable cementitious materials.	Include guidelines in the standards for low-carbon 3D printable cementitious mixtures containing materials like slag, fly ash, clay, and geopolymers.
		Consider designing emission product standards for the materials.
	Update building codes to include safe, replicable, and low-cost 3D printing protocols.	Integrate design optimisation into building codes to encourage an increase in material use efficiency and reduce waste.
		Include GHG inventories for printable cementitious materials and printing processes in building codes.
Public procurement and partnerships	Commission construction projects employing C3DP in publicly funded construction to increase demand.	Drive innovation by prioritising the use of low-carbon 3D printable cementitious mixtures and design optimisation in the publicly funded C3DP projects.
	Establish public–private partnerships with construction firms to increase uptake of C3DP construction.	Encourage construction firms to use low-carbon 3D printable cementitious mixtures and design optimization in their projects.
Financial and structural incentives	Offer loans and rebates to conventional cement and concrete producers manufacturing 3D printable cementitious mixtures to increase material supply and reduce costs.	Offer additional grants to producers of low-carbon printable cementitious mixtures.
	Offer financial and structural incentives to construction firms to increase the uptake of C3DP in construction projects.	Award tax credits, rebates, and building permits to C3DP construction projects with sustainability objectives such as reduced material use, formwork, and waste.

Overview of the manufacturing strategies that target the production of 3D printable cementitious mixtures. For each of the five policy areas identified, we recommend strategies for using C3DP in construction to bolster climate mitigation and to incorporate greenhouse gas emissions criteria in the technology from the outset.

Global warming potential is a commonly used metric to quantify the environmental impact of 3D printing technologies. It measures the total emissions of greenhouse gases (primarily carbon dioxide (CO_2) and methane (CH_4)) generated during the production process, expressed in terms of carbon dioxide equivalent (CO_2-e) [52]. Recent advances in 3D printing technology have led to the development of concrete mixtures with reduced cement content by incorporating low-carbon Supplementary Materials, such as recycled glass [109], fly ash [110], various types of slag [111–113], silica fume [114–116], and metakaolin [117,118].

Geopolymers are amorphous ceramic systems produced from widely available raw materials [119]. It has been estimated that the production of 1 kg of geopolymer releases nearly five times less CO_2 compared to Portland cement manufacturing [120]. Geopolymers were first applied in 3D printing in 2016. In recent years, a growing body of significant research [119–122] has focused on adapting alternative binders to replace cement in 3D printing technologies. These developments indicate that the rapid advancement of cement-free 3D printed structures may soon become a reality. However, the sustainability and industrial viability of geopolymers, both economically and environmentally, are currently

limited by the high cost of alkaline activators, such as sodium silicate (Na_2SiO_3) and sodium hydroxide (NaOH) [121]. Cost-effective and environmentally friendly alternatives to conventional alkaline activators must be explored with the aim of expanding the application of geopolymers in 3D printing technologies and securing a share of the construction industry market [122].

Several directions for the development of 3D printing technologies are envisioned. Current building regulations do not yet cover large-scale 3D printing applications in construction and the absence of a normative framework presents significant barriers to a practical implementation of 3D printing in construction. Achieving a breakthrough in 3D printing technologies will require research to focus on the critical review, harmonisation, and reformulation of design principles and standards. This effort should support the development of design guidelines, calculation methodologies, and construction techniques specifically tailored to 3D printed structures [123].

The automation of 3D printing processes and their integration with artificial intelligence could fundamentally transform conventional construction practices, enabling autonomous and adaptive building systems [102]. Further investigation is also needed into topological optimisation strategies [124], which offer opportunities to refine the internal structure of 3D printed components and enhance resource efficiency.

Substantial advances in printing hardware, raw materials, structural systems, and design methodologies are expected to lead to the next technological milestone—4D printing [123]. This emerging technology, inspired by the fascinating process of spider silk spinning, enables printed structures to change shape and function in response to external stimuli [125].

11. Conclusions

1. The concrete 3D printing process can be realised with the application of the contour crafting, concrete printing, and D-shape printing methods. Each of these methods has advantages and disadvantages which should be taken into account in relation to the type of 3D printed structural element.
2. Cement CEM I 42.5 (52.5) N (R), calcium sulfoaluminate cement can be applied as a binder material for 3D printed concrete.
3. The 3D printed concrete mixture is mainly prepared using only fine aggregates, and 0/2 mm fraction sand is most widely used as the fine aggregate. However, some research demonstrates the possibility of applying 0/4 mm faction sand, and even coarse aggregates (crushed stone) of 4/8 mm fraction for 3D printed concrete.
4. Chemical admixtures such as superplasticisers, viscosity-modifying agents, setting retarders, and accelerators are used to manage by the workability, adhesion, rigidity to print high-rise structures without failure, short setting time, and high early strength of 3D printed concrete.
5. Silica fume, ground slag, fly ash, and attapulgite can be used as mineral additives, including nano additives such as nano calcium carbonate, nanosilica, and nano clay.
6. The terms “pumpability”, “extrudability”, and “buildability” were introduced for the characterisation of 3D printable concrete in a fresh state. The fresh properties of 3D printable concrete involve the evaluation of such parameters as the open and cycle time, deformation of the material after the addition of the subsequent layer, and rheological properties of the concrete mixture.
7. 3D printable concrete is characterised by the anisotropy in the hardened state. The properties of hardened 3D printable concrete should be considered concerning the layer adhesion, bulk density, under-filling, tensile reinforcement, shrinkage, and durability.

8. The development of 3D printed concrete technology requires the creation of specific methodologies for the testing of concrete properties in fresh and hardened states due to the differences of this concrete in comparison with traditional ones.

Author Contributions: Conceptualisation, G.G. and M.K.; methodology, G.G. and M.K.; software, G.G. and M.K.; validation, G.G. and M.K.; formal analysis, G.G.; investigation, G.G. and M.K.; resources, G.G. and M.K.; data curation, G.G.; writing—original draft preparation, G.G. and M.K.; writing—review and editing, G.G. and M.K.; visualisation, G.G.; supervision, M.K.; project administration, M.K.; funding acquisition, M.K. All authors have read and agreed to the published version of the manuscript.

Funding: This research received no external funding.

Institutional Review Board Statement: Not applicable.

Informed Consent Statement: Not applicable.

Data Availability Statement: The original contributions presented in the study are included in the article. Further inquiries can be directed to the corresponding author.

Conflicts of Interest: The authors declare no conflicts of interest.

References

1. Zhang, J.; Wang, J.; Dong, S.; Yu, X.; Han, B. A review of the current progress and application of 3D printed concrete. *Compos. Part A* **2019**, *125*, 105533. [CrossRef]
2. Pegna, J. Exploratory investigation of solid freeform construction. *Autom. Constr.* **1997**, *5*, 427–437. [CrossRef]
3. Buswell, R.A.; Leal de Silva, W.R.; Jones, S.Z.; Dirrenberger, J. 3D printing using concrete extrusion: A roadmap for research. *Cem. Concr. Res.* **2018**, *112*, 37–49. [CrossRef]
4. Craftcloud. Available online: https://all3dp.com/2/2019-best-companies-building-3d-printed-houses/ (accessed on 24 March 2025).
5. Schutter, G.D.; Lesag, K.; Mechtcherine, V.; Nerella, V.N.; Habert, G.; Agusti-Juan, I. Vision of 3D printing with concrete—Technical, economic and environmental potentials. *Cem. Concr. Res.* **2018**, *112*, 25–36. [CrossRef]
6. Shanghai-Based WinSun 3D Prints 6-Story Apartment Building and an Incredible Home. Available online: https://3dprint.com/38144/3d-printed-apartment-building/ (accessed on 24 March 2025).
7. The First 3D-Printed Residential Building in Europe Was Presented in Yaroslavl. Available online: https://specavia.pro/articls/pervyj-v-evrope-zhiloj-dom-napechatannyj-na-3d-printere-predstavili-v-yaroslavle/ (accessed on 19 May 2025).
8. 3D Printed House by Apis Cor Entirely Created in One Day. Available online: https://www.arch2o.com/3d-printed-house-apis-cor/ (accessed on 24 March 2025).
9. First 3D Printed Commercial Building in Southern Hemisphere Completed. Available online: https://qorox.co.nz/news-and-media/first-3d-printed-commercial-building-in-southern-hemisphere-completed/ (accessed on 24 March 2025).
10. 3D Printed Office Building Unveiled in Dubai. Available online: https://all3dp.com/3d-printed-office-building/ (accessed on 24 March 2025).
11. 3D Printed Bridge. Available online: https://iaac.net/projects/3d-printed-bridge-development/ (accessed on 3 June 2025).
12. Winsun Uses Recycled Material to 3D Print Sustainable Bus Stop in China. Available online: https://3dprint.com/198751/winsun-3d-printed-bus-stop/ (accessed on 24 March 2025).
13. The Main Fountain of Palekh Was Printed on a 3D Printer. Available online: https://specavia.pro/articls/glavnyj-fontan-palexa-napechatali-na-3d-printere/ (accessed on 18 May 2025).
14. Anton, A.; Bedarf, P.; Yoo, A.; Dillenburger, B.; Reiter, L.; Wangler, T.; Flatt, R.J.; Burry, J.; Sabin, J.; Sheil, B.; et al. Concrete choreography: Prefabrication of 3D-printed columns. In *Fabricate 2020: Making Resilient Architecture*; UCL Press: London, UK, 2020; pp. 286–293.
15. XtreeE Prints Concrete 3D Printed Benches with Complex Patterns. Available online: https://www.3dnatives.com/en/xtreee-concrete-bench-3d-printed-benches-patterns-140920184/#! (accessed on 24 March 2025).
16. Žujović, M.; Obradović, R.; Rakonjac, I.; Milošević, J. 3D printing technologies in architectural design and construction: A systematic literature review. *Buildings* **2022**, *12*, 1319. [CrossRef]
17. A 3D Printed House Is for Sale in New York. Builders Say It Will Cut Housing Construction Costs. Available online: https://edition.cnn.com/2021/02/07/us/3d-printed-house-united-states-for-sale-trnd/index.html (accessed on 24 March 2025).

18. First 3D-Printed Structure to Receive Approval from a Historical Commission-Camp Mabry Innovation Center in Austin, TX. Available online: https://www.iconbuild.com/newsroom/first-3d-printed-structure-to-receive-approval-from-a-historical-commission-camp-mabry-innovation-center-in-austin-tx (accessed on 18 May 2025).
19. World's 1st 3D Printed Neighborhood Being Built in Mexico. Available online: https://www.wbur.org/hereandnow/2020/02/06/worlds-first-3d-printed-neighborhood-mexico (accessed on 24 March 2025).
20. A Belgian Company Says Its the First Ever to 3D-Print a 2-Story House in One Piece in a Breakthrough for Sustainable Design—See Inside. Available online: https://www.businessinsider.com/kamp-c-3d-printed-two-story-house-in-belgium-2020-8 (accessed on 24 March 2025).
21. The First 3D-Printed Housing Community in the US is Being Built in the California Desert. Available online: https://edition.cnn.com/2021/03/18/business/california-3d-printed-neighborhood-trnd/index.html (accessed on 24 March 2025).
22. Cazza to Build World's First 3D Printed Skyscraper. Available online: https://www.constructionweekonline.com/article-43436-cazza-to-build-worlds-first-3d-printed-skyscraper/ (accessed on 24 March 2025).
23. Ngo, T.D.; Kashania, A.; Imbalzano, G.; Nguyen, K.T.Q.; Hui, D. Additive manufacturing (3D printing): A review of materials, methods, applications and challenges. *Compos. Part B Eng.* **2018**, *143*, 172–196. [CrossRef]
24. Lu, B.; Weng, Y.; Li, M.; Qian, Y.; Leong, K.F.; Tan, M.J.; Qian, S. A systematical review of 3D printable cementitious materials. *Constr. Build. Mater.* **2019**, *207*, 477–490. [CrossRef]
25. Gosselin, C.; Duballet, R.; Roux, P.; Gaudillière, N.; Dirrenberger, J.; Morel, P. Large-scale 3D printing of ultra-high performance concrete—A new processing route for architects and builders. *Mater. Des.* **2016**, *100*, 102–109. [CrossRef]
26. Khoshnevis, B. Automated construction by contour crafting—Related robotics and information technologies. *Autom. Constr.* **2004**, *13*, 5–19. [CrossRef]
27. Zhang, J.; Khoshnevis, B. Optimal machine operation planning for construction by Contour Crafting. *Autom. Constr.* **2013**, *29*, 50–67. [CrossRef]
28. Davtalab, O.; Kazemian, A.; Khoshnevisa, B. Perspectives on a BIM-integrated software platform for robotic construction through Contour Crafting. *Autom. Constr.* **2018**, *89*, 13–23. [CrossRef]
29. Zhang, X.; Li, M.; Lim, J.H.; Weng, Y.; Tay, Y.W.D.; Pham, H.; Pham, Q.C. Large-scale 3D printing by a team of mobile robots. *Autom. Constr.* **2018**, *95*, 98–106. [CrossRef]
30. Lim, S.; Buswell, R.A.; Le, T.T.; Wackrow, R.; Austin, S.A.; Gibb, A.G.F.; Thorpe, T. Development of a viable Concrete Printing process. In Proceedings of the 28th International Symposium on Automation and Robotics in Construction (ISARC 2011), Seoul, Republic of Korea, 29 June–2 July 2011; pp. 665–670.
31. Wangler, T.; Lloret, E.; Reiter, L.; Hack, N.; Gramazio, F.; Kohler, M.; Bernhard, M.; Dillenburger, B.; Buchli, J.; Roussel, N.; et al. Digital concrete: Opportunities and challenges. *RILEM Tech. Lett.* **2016**, *1*, 67–75. [CrossRef]
32. Shakor, P.; Sanjayan, J.; Nazari, A.; Nejadi, S. Modified 3D printed powder to cement-based material and mechanical properties of cement scaffold used in 3D printing. *Constr. Build. Mater.* **2017**, *138*, 398–409. [CrossRef]
33. Wangler, T.; Roussel, N.; Bos, F.P.; Salet, T.A.M.; Flatt, R.J. Digital concrete: A review. *Cem. Concr. Res.* **2019**, *123*, 105780. [CrossRef]
34. Cesaretti, G.; Dini, E.; Kestelier, X.D.; Colla, V.; Pambaguian, L. Building components for an outpost on the Lunar soil by means of a novel 3D printing technology. *Acta Astronaut.* **2014**, *93*, 430–450. [CrossRef]
35. Lowke, D.; Dini, E.; Perrot, A.; Weger, D.; Gehlen, C.; Dillenburger, B. Particle-bed 3D printing in concrete construction—Possibilities and challenges. *Cem. Concr. Res.* **2018**, *112*, 50–65. [CrossRef]
36. Nematollahi, B.; Xia, M.; Sanjayan, J. Current Progress of 3D Concrete Printing Technologies. In Proceedings of the 34th International Symposium on Automation and Robotics in Construction (ISARC 2017), Taipei, Taiwan, 28 June–1 July 2017; pp. 260–267.
37. Bai, G.; Wang, L.; Ma, G.; Sanjayan, J.; Bai, M. 3D printing eco-friendly concrete containing under-utilised and waste solids as aggregates. *Cem. Concr. Compos.* **2021**, *120*, 104037. [CrossRef]
38. Weger, D.; Gehlen, C. Particle-bed binding by selective paste intrusion—Strength and durability of printed fine-grain concrete members. *Materials* **2021**, *14*, 586. [CrossRef]
39. Vespalec, A.; Novák, J.; Kohoutková, A.; Vosynek, P.; Podroužek, J.; Škaroupka, D.; Zikmund, T.; Kaiser, J.; Paloušek, D. Interface behavior and interface tensile strength of a hardened concrete mixture with a coarse aggregate for additive manufacturing. *Materials* **2020**, *13*, 5147. [CrossRef]
40. Le, T.T.; Austin, S.A.; Lim, S.; Buswell, R.A.; Law, R.; Gibb, A.G.F.; Thorpe, T. Hardened properties of high-performance printing concrete. *Cem. Concr. Res.* **2012**, *42*, 558–566. [CrossRef]
41. Chen, Y.; Figueireo, S.C.; Yalçinkaya, Ç.; Çopuroglu, O.; Veer, F.; Schlangen, E. The effect of viscosity-modifying admixture on the extrudability of limestone and calcined clay-based cementitious material for extrusion-based 3D concrete printing. *Materials* **2019**, *12*, 1374. [CrossRef] [PubMed]
42. Meurer, M.; Classen, M. Mechanical properties of hardened 3D printed concretes and mortars—Development of a consistent experimental characterization strategy. *Materials* **2021**, *14*, 752. [CrossRef]

43. Putten, J.V.D.; Deprez, M.; Cnudde, V.; Schutter, G.D.; Tittelboom, K.V. Microstructural characterization of 3D printed cementitious materials. *Materials* **2019**, *12*, 2993. [CrossRef]
44. Khalil, N.; Aouad, G.; Cheikh, K.E.; Remond, S. Use of calcium sulfoaluminate cements for setting control of 3D-printing mortars. *Constr. Build. Mater.* **2017**, *157*, 382–391. [CrossRef]
45. Mohan, M.K.; Rahul, A.V.; Schutter, G.D.; Tittelboom, K.V. Early age hydration, rheology and pumping characteristics of CSA cement-based 3D printable concrete. *Constr. Build. Mater.* **2021**, *275*, 122136. [CrossRef]
46. Zareiyan, B.; Khoshnevis, B. Interlayer adhesion and strength of structures in contour crafting—Effects of aggregate size, extrusion rate, and layer thickness. *Autom. Constr.* **2017**, *81*, 112–121. [CrossRef]
47. Soltan, D.G.; Li, V.C. A self-reinforced cementitious composite for building-scale 3D printing. *Cem. Concr. Compos.* **2018**, *90*, 1–13. [CrossRef]
48. Zhu, B.; Pan, J.; Zhou, Z.; Cai, J. Mechanical properties of engineered cementitious composites beams fabricated by extrusion-based 3D printing. *Eng. Struct.* **2021**, *238*, 112201. [CrossRef]
49. Weng, Y.; Ruan, S.; Li, M.; Mo, L.; Unluer, C.; Tan, M.J.; Qian, S. Feasibility study on sustainable magnesium potassium phosphate cement paste for 3D printing. *Constr. Build. Mater.* **2019**, *221*, 595–603. [CrossRef]
50. Muthukrishnan, S.; Ramakrishnan, S.; Sanjayan, J. Effect of alkali reactions on the rheology of one-part 3D printable geopolymer concrete. *Cem. Concr. Compos.* **2021**, *116*, 103899. [CrossRef]
51. Ly, O.; Yoris-Nobile, A.I.; Sebaibi, N.; Blanco-Fernandez, E.; Boutouil, M.; Castro-Fresno, D.; Hall, A.E.; Herbert, R.J.H.; Deboucha, W.; Reis, B.; et al. Optimisation of 3D printed concrete for artificial reefs: Biofouling and mechanical analysis. *Constr. Build. Mater.* **2021**, *272*, 121649. [CrossRef]
52. Wang, C.; Chen, B.; Vo, T.; Rezania, M. Mechanical anisotropy, rheology and carbon footprint of 3D printable concrete: A review. *J. Build. Eng.* **2023**, *76*, 107309. [CrossRef]
53. Perrot, A.; Jacquet, Y.; Rangeard, D.; Courteille, E.; Sonebi, M. Nailing of layers: A promising way to reinforce concrete 3D printing structures. *Materials* **2020**, *13*, 1518. [CrossRef] [PubMed]
54. Mohan, M.K.; Rahul, A.V.; Van Tittelboom, K.; De Schutter, G. Evaluating the influence of aggregate content on pumpability of 3D printable concrete. In *Second RILEM International Conference on Concrete and Digital Fabrication*; Bos, F., Lucas, S., Wolfs, R., Salet, T., Eds.; Springer: Cham, Switzerland, 2020; Volume 28, pp. 333–341.
55. Kazemian, A.; Yuan, X.; Cochran, E.; Khoshnevis, B. Cementitious materials for construction-scale 3D printing: Laboratory testing of fresh printing mixture. *Constr. Build. Mater.* **2017**, *145*, 639–647. [CrossRef]
56. Zhang, C.; Hou, Z.; Chen, C.; Zhang, Y.; Mechtcherine, V.; Sun, Z. Design of 3D printable concrete based on the relationship between flowability of cement paste and optimum aggregate content. *Cem. Concr. Compos.* **2019**, *104*, 103406. [CrossRef]
57. Rahul, A.V.; Santhanam, M. Evaluating the printability of concretes containing lightweight coarse aggregates. *Cem. Concr. Compos.* **2020**, *109*, 103570. [CrossRef]
58. Ting, G.H.A.; Tay, Y.W.D.; Qian, Y.; Tan, M.J. Utilization of recycled glass for 3D concrete printing: Rheological and mechanical properties. *J. Mater. Cycles Waste Manag.* **2019**, *21*, 994–1003. [CrossRef]
59. Souza, M.T.; Ferreira, I.M.; Moraes, E.G.; Senff, L.; Oliveira, A.P.N. 3D printed concrete for large-scale buildings: An overview of rheology, printing parameters, chemical admixtures, reinforcements, and economic and environmental prospects. *J. Build. Eng.* **2020**, *32*, 101833. [CrossRef]
60. Manikandan, K.; Wi, K.; Zhang, X.; Wang, K.; Qin, H. Characterizing cement mixtures for concrete 3D printing. *Manuf. Lett.* **2020**, *24*, 33–37. [CrossRef]
61. Salman, N.M.; Ma, G.; Ijaz, N.; Wang, L. Impact of physical and physicochemical properties of supplementary cementitious materials on structural build-up of cement-based pastes. *Constr. Build. Mater.* **2021**, *291*, 123281.
62. Navarrete, I.; Kurama, Y.; Escalona, N.; Lopez, M. Impact of physical and physicochemical properties of supplementary cementitious materials on structural build-up of cement-based pastes. *Cem. Concr. Res.* **2020**, *130*, 105994. [CrossRef]
63. Yuan, Q.; Zhou, D.; Li, B.; Huang, H.; Shi, C. Effect of mineral admixtures on the structural build-up of cement paste. *Constr. Build. Mater.* **2018**, *160*, 117–126. [CrossRef]
64. Zhou, W.; Feng, P.; Lin, H.; Zhou, P. Bond behavior between GFRP bars and coral aggregate concrete. *Compos. Struct.* **2023**, *306*, 116567. [CrossRef]
65. Guo, X.; Jin, Z.; Xiong, C.; Pang, B.; Hou, D.; Li, W. Degradation of mechanical properties and microstructure evolution of basalt-carbon based hybrid FRP bars in real seawater and sea-sand concrete. *Compos. Part B Eng.* **2024**, *271*, 111163. [CrossRef]
66. Liu, Q.; Cheng, S.; Sun, C.; Chen, K.; Li, W.; Tam, V.W.Y. Steel cable bonding in fresh mortar and 3D printed beam flexural behavior. *Autom. Constr.* **2024**, *158*, 105165. [CrossRef]
67. Zhang, Y.; Qiao, H.; Qian, R.; Xue, C.; Feng, Q.; Su, L.; Zhang, Y.; Liu, G.; Du, H. Relationship between water transport behaviour and interlayer voids of 3D printed concrete. *Constr. Build. Mater.* **2022**, *326*, 126731. [CrossRef]

68. Ma, L.; Zhang, Q.; Lombois-Burger, H.; Jia, Z.; Zhang, Z.; Niu, G.; Zhang, Y. Pore structure, internal relative humidity, and fiber orientation of 3D printed concrete with polypropylene fiber and their relation with shrinkage. *J. Build. Eng.* **2022**, *61*, 105250. [CrossRef]
69. Lin, G.; Zeng, J.J.; Li, J.X.; Chen, G.M. Chord axial compressive behavior of hybrid FRPconcrete-steel double-skin tubular member T-joints. *Thin-Walled Struct.* **2024**, *195*, 111535. [CrossRef]
70. Liao, J.J.; Zeng, J.J.; Zheng, Y.; Liu, Y.; Zhuge, Y.; Zhang, L.H. Constitutive models of ultra-high performance concrete (UHPC) under true tri-axial compression and an analysis-oriented model for FRP-confined UHPC. *Eng. Struct.* **2024**, *304*, 117656. [CrossRef]
71. Zhou, J.K.; Hao, Z.H.; Zeng, J.J.; Feng, S.Z.; Liang, Q.J.; Zhao, B.; Feng, R.; Zhuge, Y. Durability assessment of GFRP bars embedded in UHP-ECCs subjected to an accelerated aging environment with sustained loading. *Constr. Build. Mater.* **2024**, *419*, 135364. [CrossRef]
72. Zeng, J.J.; Zeng, W.B.; Zhuge, Y.; Zhou, J.K.; Quach, W.M.; Feng, R. Behavior and modeling of FRP grid-reinforced ultra-high-performance concrete under uniaxial tension. *Struct. Concr.* **2024**, *25*, 1185–1207. [CrossRef]
73. Zeng, J.J.; Xiang, H.Y.; Cai, W.J.; Zhou, J.K.; Zhuge, Y.; Zhu, J.Y. Behavior of large-scale FRP confined square RC columns with UHP-ECC section curvilinearization under eccentric compression. *Eng. Struct.* **2024**, *301*, 117288. [CrossRef]
74. Zeng, J.J.; Hao, Z.H.; Li, J.L.; Zhuge, Y.; Liu, F.; Li, L.J. Durability assessment of hybrid double-skin tubular columns (DSTCs) under simulated marine environments. *Eng. Struct.* **2024**, *301*, 117168. [CrossRef]
75. Yan, Z.T.; Zeng, J.J.; Zhuge, Y.; Liao, J.J.; Zhou, J.K.; Ma, G.W. Compressive behavior of FRP-confined 3D printed ultra-high performance concrete cylinders. *J. Build. Eng.* **2024**, *83*, 108304. [CrossRef]
76. Feng, P.; Meng, X.M.; Chen, J.F.; Ye, L.P. Mechanical properties of structures 3D printed with cementitious powders. *Constr. Build. Mater.* **2015**, *93*, 486–497. [CrossRef]
77. Feng, P.; Meng, X.; Zhang, H. Mechanical behavior of FRP sheets reinforced 3D elements printed with cementitious materials. *Compos. Struct.* **2015**, *134*, 331–342. [CrossRef]
78. Sun, X.Y.; Ye, B.X.; Lin, K.J.; Wang, H.L. Shear performance of 3D printed concrete reinforced with flexible or rigid materials based on direct shear test. *J. Build. Eng.* **2022**, *48*, 103860. [CrossRef]
79. Zeng, J.J.; Pan, B.Z.; Fan, T.H.; Zhuge, Y.; Liu, F.; Li, L.J. Shear behavior of FRP-UHPC tubular beams. *Compos. Struct.* **2023**, *307*, 116576. [CrossRef]
80. Zeng, J.J.; Feng, P.; Dai, J.G.; Zhuge, Y. Development and behavior of novel FRP-UHPC tubular members. *Eng. Struct.* **2022**, *266*, 114540. [CrossRef]
81. Zeng, J.J.; Chen, J.D.; Liao, J.; Chen, W.J.; Zhuge, Y.; Liu, Y. Behavior of ultra-high performance concrete under true tri-axial compression. *Constr. Build. Mater.* **2024**, *411*, 134450. [CrossRef]
82. Liao, J.J.; Yang, K.Y.; Zeng, J.J.; Quach, W.M.; Ye, Y.Y.; Zhang, L.H. Compressive behavior of FRP-confined ultra-high performance concrete (UHPC) in circular columns. *Eng. Struct.* **2021**, *249*, 113246. [CrossRef]
83. Liu, T.Q.; Liu, X.; Feng, P. A comprehensive review on mechanical properties of pultruded FRP composites subjected to long-term environmental effects. *Compos. Part B Eng.* **2020**, *191*, 107958. [CrossRef]
84. Zeng, J.J.; Ye, Y.Y.; Gao, W.Y.; Smith, S.T.; Guo, Y.C. Stress-strain behavior of polyethylene terephthalate fiber-reinforced polymer-confined normal-, high- and ultra high-strength concrete. *J. Build. Eng.* **2020**, *30*, 101243. [CrossRef]
85. Zeng, J.J.; Li, P.L.; Yan, Z.T.; Zhou, J.K.; Quach, W.M.; Zhuge, Y. Behavior of 3D-printed HPC plates with FRP grid reinforcement under bending. *Eng. Struct.* **2023**, *294*, 116578. [CrossRef]
86. Fan, T.H.; Zeng, J.J.; Hu, X.W.; Chen, J.D.; Wu, P.P.; Liu, H.T.; Zhuge, Y. Flexural fatigue behavior of FRP-reinforced UHPC tubular beams. *Eng. Struct.* **2025**, *330*, 119848. [CrossRef]
87. Zhou, L.; Zheng, Y.; Song, G.; Chen, D.; Ye, Y. Identification of the structural damage mechanism of BFRP bars reinforced concrete beams using smart transducers based on time reversal method. *Constr. Build. Mater.* **2019**, *220*, 615–627. [CrossRef]
88. Zeng, J.J.; Su, T.H.; Chen, J.D.; Hu, X.; Ng, C.T.; Zheng, Y.; Quach, W.M.; Zhuge, Y. Novel prefabricated FRP bar reinforced UHPC shells for column strengthening: Development and axial compression tests. *J. Build. Eng.* **2024**, *94*, 109935. [CrossRef]
89. Sun, X.; Gao, C.; Wang, H. Bond performance between BFRP bars and 3D printed concrete. *Constr. Build. Mater.* **2021**, *269*, 121325. [CrossRef]
90. Jacquet, Y.; Perrot, A.; Picandet, V. Assessment of asymmetrical rheological behavior of cementitious material for 3D printing application. *Cem. Concr. Res.* **2021**, *140*, 106305. [CrossRef]
91. Roussel, N. Rheological requirements for printable concretes. *Cem. Concr. Res.* **2018**, *112*, 76–85. [CrossRef]
92. Rahul, A.V.; Sharma, A.; Santhanam, M. A desorptivity-based approach for the assessment of phase separation during extrusion of cementitious materials. *Cem. Concr. Compos.* **2020**, *108*, 103546. [CrossRef]
93. Sanjayan, J.G.; Jayathilakage, R.; Rajeev, P. Vibration induced active rheology control for 3D concrete printing. *Cem. Concr. Res.* **2021**, *140*, 106293. [CrossRef]

94. Zhang, Y.; Zhang, Y.; Liu, G.; Yang, Y.; Wu, M.; Pang, B. Fresh properties of a novel 3D printing concrete ink. *Constr. Build. Mater.* **2018**, *174*, 263–271. [CrossRef]
95. Moeini, M.A.; Hosseinpoor, M.; Yahia, A. Effectiveness of the rheometric methods to evaluate the build-up of cementitious mortars used for 3D printing. *Constr. Build. Mater.* **2020**, *257*, 119551. [CrossRef]
96. Zareiyan, B.; Khoshnevis, B. Effects of interlocking on interlayer adhesion and strength of structures in 3D printing of concrete. *Autom. Constr.* **2017**, *83*, 212–221. [CrossRef]
97. Wolfs, R.J.M.; Bos, F.P.; Salet, T.A.M. Hardened properties of 3D printed concrete: The influence of process parameters on interlayer adhesion. *Cem. Concr. Res.* **2019**, *119*, 132–140. [CrossRef]
98. Ye, J.; Cui, C.; Yu, J.; Yu, K.; Dong, F. Effect of polyethylene fiber content on workability and mechanical-anisotropic properties of 3D printed ultra-high ductile concrete. *Constr. Build. Mater.* **2021**, *281*, 122586. [CrossRef]
99. Panda, B.; Lim, J.H.; Tan, M.J. Mechanical properties and deformation behaviour of early age concrete in the context of digital construction. *Compos. Part B Eng.* **2019**, *165*, 563–571. [CrossRef]
100. Xiao, J.; Liu, H.; Ding, T. Finite element analysis on the anisotropic behavior of 3D printed concrete under compression and flexure. *Addit. Manuf.* **2021**, *39*, 101712. [CrossRef]
101. Cuevas, K.; Chougan, M.; Martin, F.; Ghaffar, S.H.; Stephan, D.; Sikora, P. 3D printable lightweight cementitious composites with incorporated waste glass aggregates and expanded microspheres—Rheological, thermal and mechanical properties. *J. Build. Eng.* **2021**, *44*, 102718. [CrossRef]
102. Tabassum, T.; Ahmad Mir, A. A review of 3d printing technology-the future of sustainable construction. *Mater. Today Proc.* **2023**, *93*, 408–414. [CrossRef]
103. Hossain, M.A.; Zhumabekova, A.; Paul, S.C.; Kim, J.R. A review of 3D printing in construction and its impact on the labor market. *Sustainability* **2020**, *12*, 8492. [CrossRef]
104. Adaloudis, M.; Roca, J.B. Sustainability tradeoffs in the adoption of 3D concrete printing in the construction industry. *J. Clean. Prod.* **2021**, *307*, 127201. [CrossRef]
105. Dey, D.; Srinivas, D.; Panda, B.; Suraneni, P.; Sitharam, T.G. Use of industrial waste materials for 3D printing of sustainable concrete: A review. *J. Clean. Prod.* **2022**, *340*, 130749. [CrossRef]
106. Mohammad, M.; Masad, E.; Al-Ghamdi, S.G. 3d concrete printing sustainability: A comparative life cycle assessment of four construction method scenarios. *Buildings* **2020**, *10*, 245. [CrossRef]
107. Dixit, M.K. 3-D printing in building construction: A Literature Review of Opportunities and Challenges of Reducing Life Cycle Energy and Carbon of Buildings. In Proceedings of the IOP Conference Series: Earth and Environmental Science, Central Europe Towards Sustainable Building (CESB19), Prague, Czech Republic, 2–4 July 2019; Volume 290, p. 012012.
108. Gangotra, A.; Del Gado, E.; Lewis, J.I. 3D printing has untapped potential for climate mitigation in the cement sector. *Commun. Eng.* **2023**, *2*, 6. [CrossRef]
109. Liu, J.; Li, S.; Gunasekara, C.; Fox, K.; Tran, P. 3D-printed concrete with recycled glass: Effect of glass gradation on flexural strength and microstructure. *Constr. Build. Mater.* **2022**, *314*, 125561. [CrossRef]
110. Benam, S.S.; Sandalci, I.; Kara, B.; Bebek, O.; Bundur, Z.B. Improving the 3D printability of high-volume fly ash mixtures through addition of mineral admixtures. In Proceedings of the RILEM Spring Convention and Conference (RSCC 2024), Milan, Italy, 7–12 April 2024; Ferrara, L., Muciaccia, G., di Summa, D., Eds.; Springer: Cham, Switzerland, 2024; Volume 56, pp. 265–273.
111. Li, D.; Cui, X.; Jang, J.-s.; Wang, G. Sustainable application of blast furnace slag in the field of 3D printing: Material configuration and machine optimization. *Sustainability* **2024**, *16*, 4058. [CrossRef]
112. Beersaerts, G.; Soete, J.; Giels, M.; Eykens, L.; Lucas, S.; Pontikes, Y. 3D printing of an iron-rich slag based hybrid mortar. A durable, sustainable and cost-competitive product? *Cem. Concr. Compos.* **2023**, *144*, 105304. [CrossRef]
113. Butkute, K.; Vaitkevicius, V.; Sinka, M.; Augonis, A.; Korjakins, A. Influence of carbonated bottom slag granules in 3D concrete printing. *Materials* **2023**, *16*, 4045. [CrossRef] [PubMed]
114. Şahin, H.G.; Mardani, A.; Beytekin, H.E. Effect of silica fume utilization on structural build-up, mechanical and dimensional stability performance of fiber-reinforced 3D printable concrete. *Polymers* **2024**, *16*, 556. [CrossRef] [PubMed]
115. Salah, H.A.; Mutalib, A.A.; Kaish, A.B.M.A.; Syamsir, A.; Algaifi, H.A. Development of ultra-high-performance silica fume-based mortar incorporating graphene nanoplatelets for 3-dimensional concrete printing application. *Buildings* **2023**, *13*, 1949. [CrossRef]
116. Liu, Z.; Li, M.; Moo, J.G.S.; Kobayashi, H.; Wong, T.N.; Tan, M.J. Effect of nanostructured silica additives on the extrusion-based 3D concrete printing application. *J. Compos. Sci.* **2023**, *7*, 191. [CrossRef]
117. Duan, Z.; Li, L.; Yao, Q.; Zou, S.; Singh, A.; Yang, H. Effect of metakaolin on the fresh and hardened properties of 3D printed cementitious composite. *Constr. Build. Mater.* **2022**, *350*, 128808. [CrossRef]
118. Peng, Y.; Unluer, C. Development of 3D-printed magnesium silicate hydrate cement mixes involving metakaolin as a substitute for silica source. *Virtual Phys. Prototyp.* **2024**, *19*, e2382173. [CrossRef]
119. Zhong, H.; Zhang, M. 3D printing geopolymers: A review. *Cem. Concr. Compos.* **2022**, *128*, 104455. [CrossRef]

120. Ricciotti, L.; Apicella, A.; Perrotta, V.; Aversa, R. Geopolymer materials for extrusion-based 3D-printing: A Review. *Polymers* **2023**, *15*, 4688. [CrossRef]
121. Shilar, F.A.; Ganachari, S.V.; Patil, V.B.; Bhojaraja, B.E.; Khan, T.M.Y.; Almakayeel, N. A review of 3D printing of geopolymer composites for structural and functional applications. *Constr. Build. Mater.* **2023**, *400*, 132869. [CrossRef]
122. Barve, P.; Bahrami, A.; Shah, S. Geopolymer 3D printing: A comprehensive review on rheological and structural performance assessment, printing process parameters, and microstructure. *Front. Mater.* **2023**, *10*, 1241869. [CrossRef]
123. Tu, H.; Wei, Z.; Bahrami, A.; Kahla, N.B.; Ahmad, A.; Özkılıç, Y.O. Recent advancements and future trends in 3D concrete printing using waste materials. *Dev. Built Environ.* **2023**, *16*, 100187. [CrossRef]
124. Bi, M.; Tran, P.; Xia, L.; Ma, G.; Xie, Y.M. Topology optimization for 3D concrete printing with various manufacturing constraints. *Addit. Manuf.* **2022**, *57*, 102982. [CrossRef]
125. Zuo, Y.; Liu, H. Is the spider a weaving master or a printing expert? *Therm. Sci.* **2022**, *26*, 2471–2475. [CrossRef]

Disclaimer/Publisher's Note: The statements, opinions and data contained in all publications are solely those of the individual author(s) and contributor(s) and not of MDPI and/or the editor(s). MDPI and/or the editor(s) disclaim responsibility for any injury to people or property resulting from any ideas, methods, instructions or products referred to in the content.

buildings

MDPI

Article

The Potential of Wood Ash to Be Used as a Supplementary Cementitious Material in Cement Mortars

Oskars Lescinskis [1], Alise Sapata [2], Girts Bumanis [1], Maris Sinka [2], Xiangming Zhou [3] and Diana Bajare [1,*]

[1] Institute of Sustainable Building Materials and Engineering Systems, Faculty of Civil and Mechanical Engineering, Riga Technical University, 6A Kipsalas, LV-1048 Riga, Latvia; oskars.lescinskis_1@rtu.lv (O.L.); girts.bumanis@rtu.lv (G.B.)

[2] 3D Concrete Printing Laboratory, Institute of Sustainable Building Materials and Engineering Systems, Faculty of Civil and Mechanical Engineering, Riga Technical University, 1P. Valdena, LV-1048 Riga, Latvia; alise.sapata@rtu.lv (A.S.); maris.sinka@rtu.lv (M.S.)

[3] Department of Civil & Environmental Engineering, Brunel University London, Uxbridge, Middlesex, London UB8 3PH, UK; xiangming.zhou@brunel.ac.uk

* Correspondence: diana.bajare@rtu.lv

Abstract: This study explores the application of wood ash (WA) as a partial replacement for PC in mortar. Three pre-treatment methods were applied to WA to enhance its reactivity, and it was then incorporated into mortar at two different substitution levels of 10 and 30%. Tests on compressive and flexural strength were conducted on the hardened mortar samples. All hardened mortar samples containing WA showed a decrease in mechanical properties compared to the reference sample without WA. The highest compressive and flexural strength of the samples with WA were observed for those containing 10% of sieved and slaked WA. The compressive and flexural strength of these samples after 28 days were 56 and 9 MPa, respectively, whereas those of the reference samples were 62 and 10 MPa, respectively. Based on the results, the best-performing samples on the compressive test underwent additional testing for freeze–thaw resistance to assess their durability. The mass loss of the reference sample and that with 10% of sieved and slaked WA after 56 freeze–thaw cycles was 11,800 and 13,800 g/m^2, respectively. The findings revealed that increasing the proportion of WA typically led to a decline in the mechanical properties of mortar compared to conventional mixtures. However, with appropriate pre-treatment techniques, the quality and performance of mortar containing WA were significantly improved, demonstrating its potential as a sustainable alternative in reducing the carbon footprint of PC production.

Keywords: Portland cement; mortar; wood ash; cement replacement

1. Introduction

Portland cement (PC) is one of the most used materials in the concrete industry [1]. The production of PC is considered highly polluting and emits high amounts of greenhouse gasses. The production of PC alone emits up to 9% of the total anthropogenic CO_2 amount and depletes a huge amount of natural resources [2]. To reduce the global CO_2 emissions, blended cements have been developed, where some clinker is replaced with other materials [3]. Traditionally, coal fly ash, a by-product of coal combustion in thermal power plants, has been widely used as a supplementary cementitious material due to its pozzolanic properties and ability to enhance concrete durability, reduce permeability, and improve workability. However, with the global shift away from coal-fired power generation driven by decarbonization efforts and stricter environmental policies, the availability of coal fly ash has become increasingly constrained. For example, many developed nations, including

those in the EU and North America, have significantly reduced their reliance on coal for energy, leading to a scarcity of this once-abundant by-product.

In the last few years, the demand for wood as a renewable energy source has risen to achieve the goals of the European Green Deal and the 2030 Climate Target Plan. Biomass as a fuel source is considered carbon-neutral as the amount of carbon dioxide which is produced by biomass burning equals the total amount of CO_2 fixed during the biomass growth process that occurs through photosynthesis [4]. In total, about 95–97% of the world's bioenergy is produced by the direct combustion of biomass, which leads to approximately 476 million tons of biomass ash (BA) generated worldwide annually [5]. Using BA as a partial PC replacement minimizes the use of non-renewable resources, mitigates greenhouse gas emissions, and is a good solution for ash management [6]. In parallel, the use of biomass as a renewable energy source has grown significantly, with biomass combustion now replacing coal in many heating and power generation facilities. This transition has resulted in a corresponding increase in the production of BA, including wood ash (WA), rice husk ash, and sugarcane bagasse ash. These by-products are gaining attention as alternative supplementary materials (SCMs) due to their environmental benefits and pozzolanic potential [7].

To address the environmental effects that are related to cement manufacturing, the possibility of using SCMs to develop sustainable mortars and concrete needs to be emphasized. The use of WA as an SCM for the partial replacement of cement has economic, technical, and environmental benefits, such as the conservation of natural resources and a reduction in greenhouse gas emissions in the cement industry [8]. Partially replacing cement with WA will contribute to the global demand for carbon-efficient solutions that reduce CO_2 emissions and utilize waste, which is consistent with the goals of the Paris Agreement [9]. Research has demonstrated that certain types of BA, when processed and characterized appropriately, can react with calcium hydroxide, forming calcium silicate hydrates (C-S-H) like those in PC [10]. This reaction not only helps improve the mechanical properties of mortars but also addresses the issue of disposing of biomass combustion residues, promoting a circular economy [1,11]. Recent studies reveal that in general, mechanical properties, such as the compressive and bending strengths of concrete, in which part of cement is replaced with WA, decrease with an increase in the content of WA. However, it is possible to maintain or even improve the mechanical properties of concrete containing WA, compared to conventional concrete, when pre-treatment is applied to WA. Pre-treatment techniques such as sieving, grinding, washing, calcination, and chemical activation improve the reactivity and compatibility of WA with PC [12–14]. Several studies have shown that incorporating pre-treated BA at a replacement level of up to 20% by mass can achieve comparable or even superior concrete properties while significantly reducing the carbon footprint associated with PC production [14]. These innovations are paving the way for more sustainable and resource-efficient practices in the construction industry. In the work of N. Ristić [15], the compressive strength of concrete samples containing 10% WA was higher than that of the reference mixture by 1.4% and 3.2% at 28 and 90 days, respectively. This effect at longer curing ages was attributed to internal curing, which was provided by WA, and to the higher compactness of concrete due to the reduced amount of free water in the mixture. Meanwhile, in the work of Z. Yang [16], the compressive strength of all the concrete samples with WA was reduced compared to the reference sample. Overall, the use of WA as an SCM to partially replace PC offers the possibility of inserting this waste into the production chain and an alternative method for the disposal of WA. However, due to the chemical and physical characteristics of WA that depend on several factors such as combustion temperature, wood type, furnace type, and burning conditions, before incorporating WA in mortars, these characteristics should be

investigated. According to available research, the most optimal replacement percentage for WA is between 5 and 20%, where the best results are obtained with 10% replacement [14].

To better understand the chemical interaction between WA particles and those of cement, it is valuable to incorporate techniques such as FTIR and XRD. The FTIR spectrum results of hardened mortars can be used to characterize compressive strength fluctuations by determining the peak intensity of the bonds that are responsible for strength [17]. In other studies, the peak intensity changes in the bonds, such as Si-O and O-H, of a reference mortar and a mortar containing WA were analyzed [18,19]. To assess the degree of hydration in mortars at different curing times, XRD results can be used [19,20].

In this research, the influence of WA as a partial PC replacement on mortar properties, such as compressive strength, bending strength, and freeze–thaw resistance, were assessed. Three pre-treatment methods, including sieving, sieving/slaking, and sieving/grinding, were applied to WA and used at the same replacement levels of 10 and 30% in mortars in order to compare the influence of them on mechanical properties. The main aim of this study is to understand the changes in mortar properties when the same WA is pre-treated with different methods and used as a partial cement replacement.

2. Materials and Methods

2.1. Wood Ash Characterization

The WA used in the study was collected from the thermal plant Gren Latvia Ltd. (Jelgava, Latvia). The chemical composition was studied by X-ray fluorescence (XRF). The crystalline phases of WA were identified by X-ray diffraction (XRD) analysis. The size and shape of WA were analyzed by using variable pressure scanning electron microscopy (VP-SEM). In addition, energy-dispersive X-ray (EDX) analysis was performed in order to characterize the elemental composition of WA. The particle size distribution was determined by using the sieving method according to the LVS EN 933-1 standard [21].

2.2. Raw Materials and Mixture Designs

In this research, locally manufactured pure PC (>95% of cement) with the brand name Schwenk (Broceni, Latvia) CEM I 42.5 N, meeting the European Union and Latvian State standards governing the composition, specifications, and compliance criteria of the cement (LVS EN 197-1:2012 [22]), was used. The chemical composition of this PC is given in Table 1. Sand was obtained from the local manufacturer Sakret Ltd. (Riga, Latvia) with a grain size of 0–2 mm. This sand fraction is specifically manufactured for mortar applications and has an optimized particle size distribution. To improve workability and reduce cracking, liquid superplasticizer Vincents Polyline Floormix was used in the same amount in all mortar samples.

Table 1. Chemical composition of PC.

Compound	SiO_2	Al_2O_3	Fe_2O_3	CaO	MgO	SO_3	K_2O	Na_2O	Cl
Result (w%)	20.9	4.5	4.4	65.2	1.0	2.2	0.7	0.2	0.05

Three mortar series with different WA treatment methods were created, and the following WA treatment procedures were applied:

(1) In the first mortar series (WA1), the WA sample portion was subjected to sieving through a 2 mm sieve in order to separate unburnt carbon particles.
(2) In the second mortar series (WA2), the WA sample portion was sieved through a 2 mm sieve and slaked in order to prevent the ash from swelling [23]. To avoid this

phenomenon, WA was immersed in water for 24 h with a water–ash weight ratio of 1. A WA2 slurry was included in the mixture composition and water adjusted to the needed amount.

(3) In the third mortar series (WA3), the WA sample was sieved and ground by using a planetary ball mill Retsch PM400 (Dusseldorf, Germany) for 10 min at 300 rpm. Before the milling process, WA3 was dried to avoid the clumping of WA particles.

The mixture compositions of mortar samples and their designations are given in Table 2. In total, 7 mortar mixtures were prepared. WA was incorporated to replace 10 or 30% by mass of PC. The amount of water and plasticizer was constant in all mixtures with WA and was not affected by the applied WA treatment method. The sand–PC ratio increased for the mixtures with a higher WA replacement level from 2.0 to 2.9, while the total sand–(PC + WA) ratio remained the same (2.0).

Table 2. Mixture compositions of mortar with WA as supplementary cementitious material.

WA% in Mortars	WA Treatment/ Designation	Water–Binder	Sand–PC (Sand–PC + WA)	Plasticizer–Binder
0%	REF	0.4	2.0 (2.0)	0.2
10%	WA1-10%	0.4	2.2 (2.0)	0.2
30%	WA1-30%	0.4	2.9 (2.0)	0.2
10%	WA2-10%	0.4	2.2 (2.0)	0.2
30%	WA2-30%	0.4	2.9 (2.0)	0.2
10%	WA3-10%	0.4	2.2 (2.0)	0.2
30%	WA3-30%	0.4	2.9 (2.0)	0.2

2.3. Hardened Mortar Properties

Compressive and bending strengths for all mortar samples were determined according to the LVS EN 196-1 standard [24]. Hardened mortar specimens were produced in 40 × 40 × 160 mm steel molds. The mortar specimens were removed from the molds 24 h after production and placed in water. Strength tests were carried out after 2, 7, and 28 days. A three-point bending test was performed with a span of 100 mm and a test speed of 0.5 mm/min by using a WDW-20 20 kN testing machine (Jinan Hensgrand Instrument Co., Ltd., Jinan, China). A compressive test on 62.5 × 40 × 40 mm mortar specimens was performed with a test speed of 0.8 MPa/s by using a Controls 3000 kN compression machine. Freeze–thaw resistance was determined for the mixture WA2-10%. A freeze–thaw test was carried out according to the Latvian standard LVS CEN/TS 12390-9 requirements [25]. During the freeze–thaw test, five surfaces of a mortar cube of 10 × 10 × 10 cm were covered with a waterproofing material. The exposed face of the mortar cube was immersed in a 3% sodium chloride solution. The freeze–thaw mass loss was determined after 14, 28, and 56 cycles, with each cycle including 12 h of freezing to −20 °C and 12 h of thawing to 20 °C.

3. Results

3.1. XRF and XRD Results of WA

In this research, the standards applied to coal ash utilization in mortars were used as a basis for the characterization of WA [1]. The chemical compositions of the studied WA are presented in Table 3. The obtained results show a dominant content of SiO_2 (49.6%), followed by CaO (20.9%). Many types of biomasses, such as wood, agricultural residues, and grasses, naturally contain significant amounts of calcium in their structure. This calcium is absorbed from soil during the plant's growth and is present in the form of

calcium salts, such as calcium carbonate ($CaCO_3$) and calcium oxalate. During combustion, these compounds decompose, forming calcium oxide (CaO) in the ash [26].

Table 3. Chemical composition and LOI of WA.

Compound	SiO_2	Al_2O_3	CaO	MgO	SO_3	Na_2O	K_2O	Mn_2O_3	Cl	CuO	TiO_2	BaO	PbO	SrO	ZnO	LOI
Result (w%)	49.6	4.4	20.9	4.7	9	1.1	4.5	0.2	0.6	0.02	0.4	0.1	0.03	0.03	0.3	6

The sum of the total amount of SiO_2, Al_2O_3, and Fe_2O_3 was 55% by mass, which was lower than the minimal amount of 70% by mass specified by ASTM C 618 [27] and EN 450-1 [28] to be classified as a class F pozzolanic material. According to ASTM C 618, the WA used in this study falls under class C as the sum of the total amount of SiO_2, Al_2O_3, and Fe_2O_3 is between 50 and 70% by mass. Regarding the content of CaO, WA meets the criteria for class C as the amount of CaO is more than 20% by mass [1]. The WA used was very rich in alkalis with 1.12% of Na_2O and 4.51% of K_2O, both by mass, and contained significant amounts of magnesium oxides, sulfates, and chlorides [1,29]. According to the European standard EN 450-1, the WA meets the criteria for category B (<7%) in terms of the loss of ignition (LOI) value [1]. Most of the wood fly ash and coal fly ash blends are considered by ASTM C618-15, 2015 [30], as class C ashes [1]. The particle size of WA does not meet any standards (i.e., EN 450 [28], C618−22 [31]) as approximately less than 5% by mass of particles are retained when sieved on the 45 μm sieve [23].

The mineralogical composition of WA varies depending on factors such as the type of wood, the combustion process, and the combustion temperature. The main crystalline phases identified were quartz (ref. no. 00-046-1045), anhydrite (00-037-1496), and lime (00-037-1497) (Figure 1).

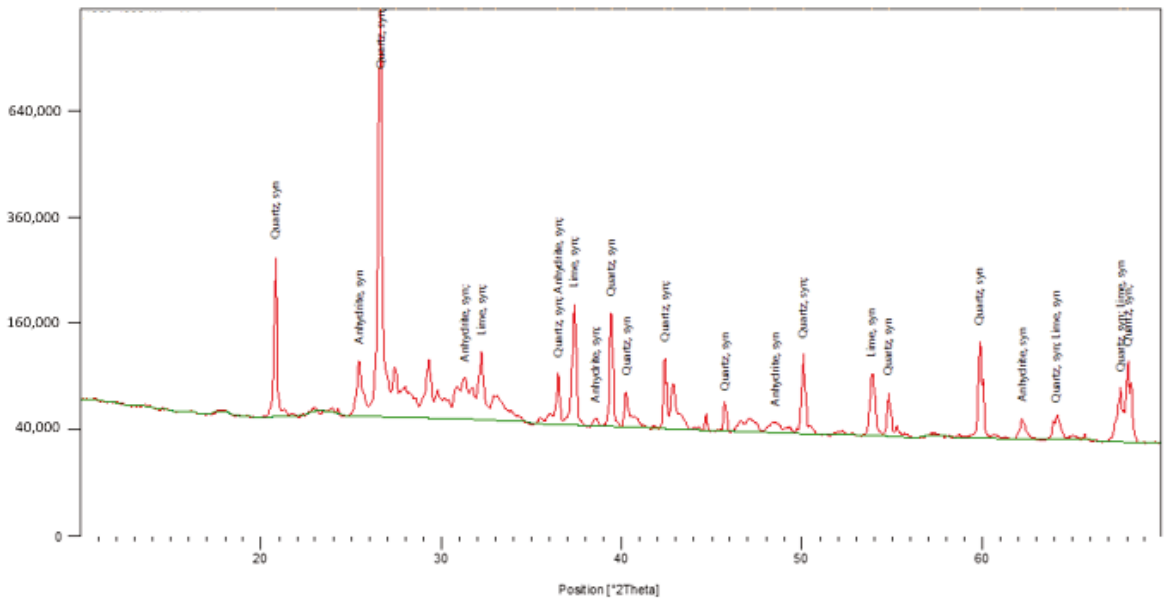

Figure 1. XRD patterns of raw WA.

3.2. SEM-EDX Results of WA

The SEM images of the sieved WA before and after ball-milling for 10 min at 300 rpm are shown in Figure 2. The particles of the sieved WA consisted of irregularly sized and shaped grains [32], and smaller particles were densely packed due to agglomeration [33]. The shapes of the sieved WA particles were irregular, rounded, and angular. The ball-milling process reduced the particle size and separated the agglomerated particles [34] and

led to homogenous shapes. Ball-milling for too long can have an adverse effect on particle size reduction. According to the work of S. Kumar [35], the biggest impact on particle size reduction occurs in the first 10 min of grinding, and then the impact decreases. However, some larger particles were present even after the ball-milling process.

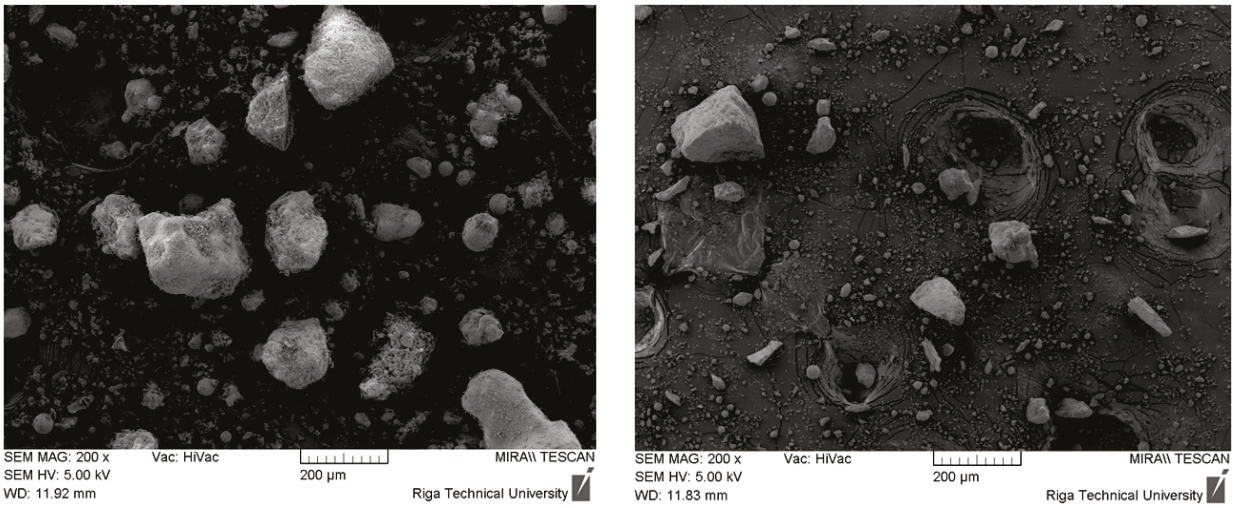

(**a**) (**b**)

Figure 2. (**a**) SEM image of sieved WA (WA1); (**b**) SEM image of sieved and ball-milled WA (WA3).

A SEM-EDX analysis of elements was performed in spot mode. In total, nine different spots of the sieved WA sample (WA1) were chosen and analyzed (Figure 3). It was concluded that when calculated according to the chemical composition of oxides, the elemental compositions were consistent with the chemical compositions found via XRF and the mineral compositions. The elemental compositions of the WA sample are shown in Table 4.

Table 4. Elemental compositions of WA.

Element	Result (w%)								
	(a)	(b)-1	(b)-2	(c)-1	(c)-2	(c)-3	(d)-1	(d)-2	(d)-3
C	9.4	78.0	13.4	9.9	8.3	8.4	8.9	9.9	17.6
O	50.9	17.0	59.5	50.2	44.0	58.3	50.6	53.2	50.6
Na	0.8	0.1	0.3	1.1	0.3	0.7	0.9	0.6	0.5
Mg	2.0	0.3	0.4	1.8	9.2	0.4	4.7	1.3	1.1
Al	1.1	0.1	0.3	2.0	0.2	0.6	2.6	1.9	0.4
Si	11.5	0.2	20.8	10.3	0.7	23.1	13.1	16.6	0.8
P	0.9	0.0	0.0	1.0	1.1	0.2	0.0	0.7	0.0
S	2.5	0.6	0.9	2.9	5.5	1.4	0.6	1.0	3.4
Cl	0.5	0.3	0.3	0.5	0.5	0.2	0.0	0.3	0.8
K	4.9	1.8	2.1	7.4	6.1	4.0	5.8	6.1	4.3
Ca	13.6	1.4	2.0	11.2	22.9	2.5	5.3	7.0	18.8
Ti	0.3	0.0	0.0	0.2	0.0	0.0	0.3	0.2	1.8
Mn	0.0	0.0	0.0	0.0	0.0	0.0	0.0	0.2	0.0
Fe	1.1	0.0	0.0	1.4	0.5	0.2	6.6	1.2	0.0
Cu	0.0	0.0	0.0	0.0	0.0	0.0	0.0	0.0	0.0
Zn	0.7	0.0	0.0	0.0	0.6	0.0	0.8	0.0	0.0

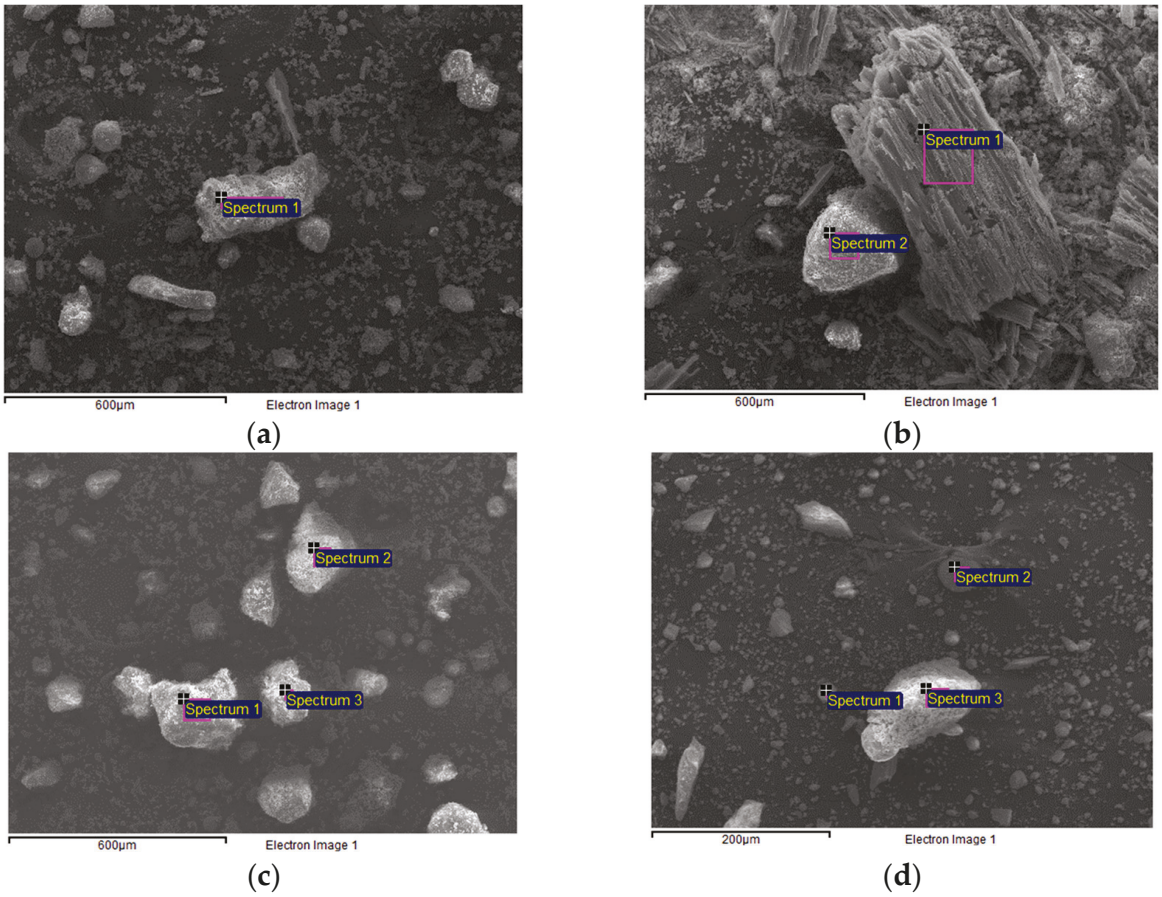

Figure 3. (**a**) spot of a particle chosen for elemental composition represented in Table 4; (**b**) spots of particles chosen for elemental composition represented in Table 4; (**c**) spots of particles chosen for elemental composition represented in Table 4; (**d**) spots of particles chosen for elemental composition represented in Table 4.

The most dominant elements of the WA particles were oxygen, silica, and calcium, according to the XRD analysis, and they were the main constituents of quartz, anhydrite, and lime. The obtained quantitative results regarding the elemental compositions had good consistency with the chemical compositions obtained via XRF. The LOI parameter indicates the percentage of unburned carbonaceous material [14]. The amount of unburned carbonaceous material in WA was rather low as the LOI value of the used WA shown in Table 3 met the European standard EN 450-1 class B (<7%) requirements. Spectrum 1 in Figure 3b represents a typical unburned carbon particle which is characterized by a rough surface, high porosity, and high specific area with carbon as its dominant element [31,36].

3.3. Particle Size Distribution of WA

The particle size distribution for sieved WA (WA1) and sieved/milled WA (WA3) was determined by the sieve analysis procedure conducted using differential sieve weighing. Before this procedure, both WA samples were dried at 110 °C to constant weight. Then, an equal amount of 200 g of both ash samples was weighed and passed through a series of sieves of different sizes organized from larger on top to smaller sizes at the bottom. After sieving the amount of retained particles, each sample was weighed, and the particle size distribution of the WA samples was determined. The obtained results are shown in Figure 4. According to Figure 4, the biggest impact of ball-milling occurred in the particle size range of 125 to 500 µm.

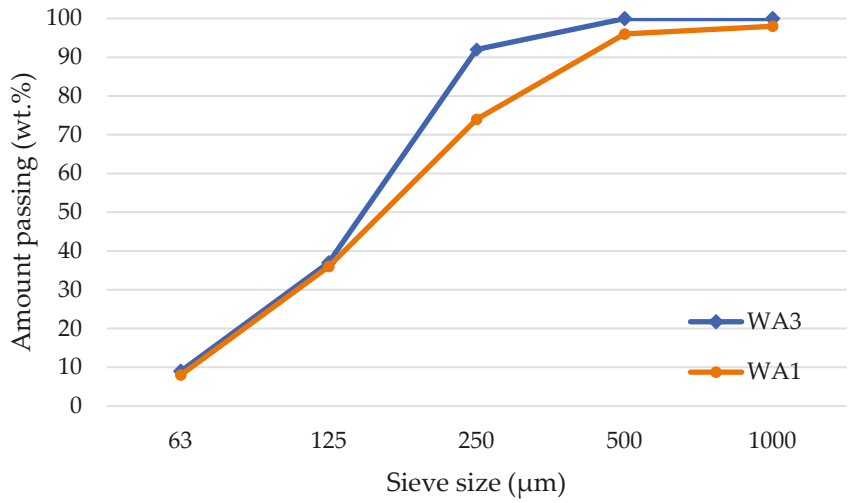

Figure 4. Particle size distribution of WA1 and WA3.

3.4. Mechanical Strength of Mortar Samples

The compressive and bending strengths of the mortar samples were determined at 3, 7, and 28 days. Figure 5 presents the compressive strength results of the mortar mixtures at various curing ages (i.e., 3, 7, 28 days). From the results of compressive strength testing, it was observed that the highest compressive strength among all mortar samples was recorded in the samples with no cement replacement by WA. With an increase in WA content, compressive strength tended to be reduced for all mixtures. Out of the three treatment methods, it was concluded that the best results were obtained for samples with WA2, although the results of the samples with WA3 were close to those with WA2.

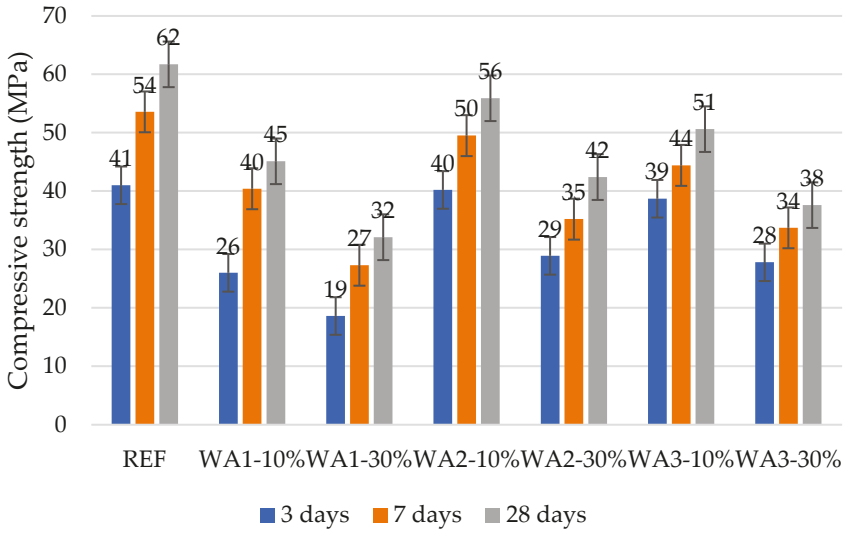

Figure 5. Comparison of compressive strength of different treatment methods with various amounts of WA.

The results of bending strength testing exhibited a similar pattern to those of compressive strength testing (Figure 6). Similar to the compressive strength results, the best tensile strength was for the samples with WA2 and WA3, and the final results between the two samples were very close.

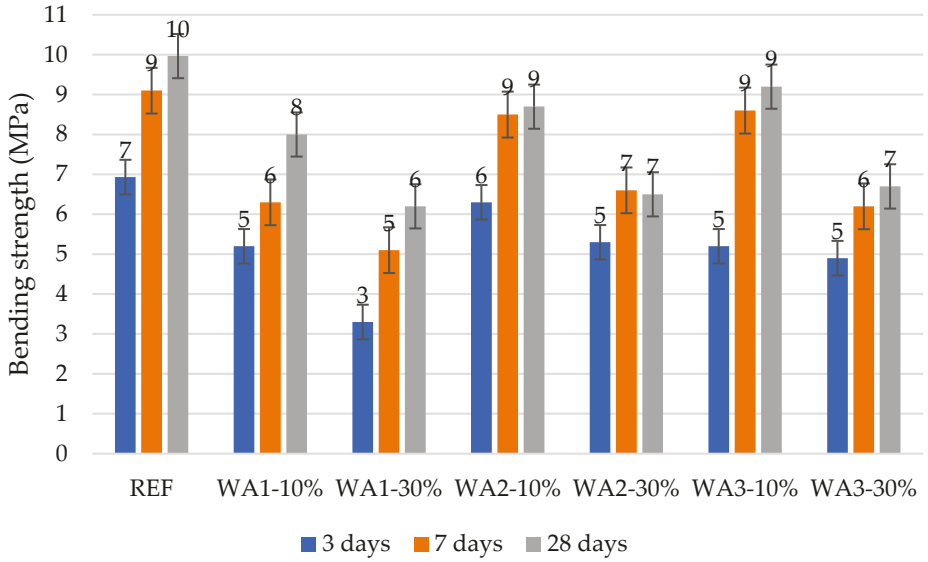

Figure 6. Comparison of bending strength of different WA treatment methods with various amounts of WA.

The reduction in both the compressive and bending strengths of the mortar samples with WA is attributed to the less dense packaging of WA, which decreases the density of the cement matrix [1] as the particles of WA are coarser than those of Portland cement, as well as the lower pozzolanic activity levels of WA [14]. This results in a higher amount of bigger closed pores that reduce the mechanical properties of the material.

The freeze–thaw test mass loss of the most promising sample WA2 and REF is shown in Figure 7. The mass loss of WA2-10% was higher than that of the reference sample (WA-0%) at all cycles. The final mass loss at 56 cycles of WA2-0% and WA2-10% was 11,800 and 13,800 g/m^2, respectively. This was attributed to higher water absorption due to larger open pores that formed due to the poor packing of WA2 particles. The freeze–thaw resistance of mortar depends on both open porosity and closed porosity [6,37].

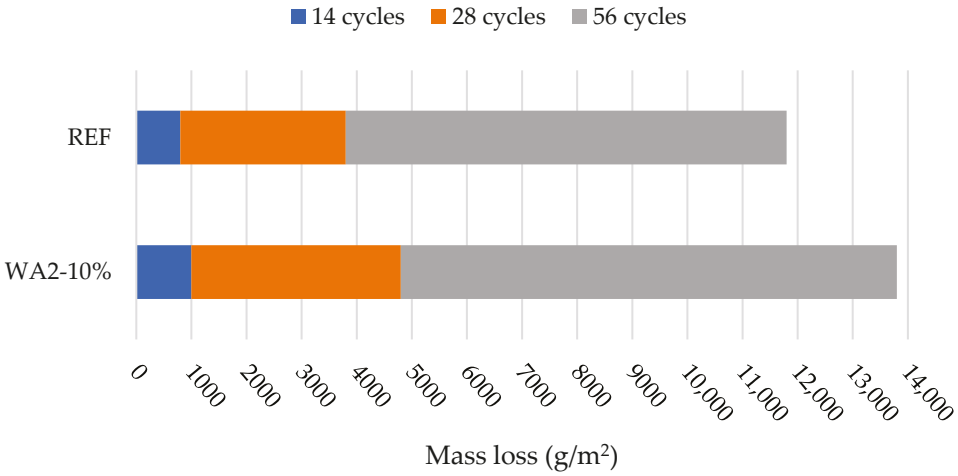

Figure 7. Mass loss of REF and WA2-10% after freeze–thaw cycles.

4. Discussion

In this study, the effects of WA on the properties of mortar were investigated. The main crystalline phases of the studied WA were quartz, anhydrite, and lime. According to ASTM C 618 and EN 450-1, which are used for coal ash classification, the WA used in this study met the criteria for the class C classification, which was consistent with other studies where

WA was used as a cement replacement [1,30,33]. From the XRF and SEM-EDX results, it was concluded that the main chemical constituents of the WA particles were oxygen, silica, and calcium. Three different WA pre-treatment methods including sieving, grinding, and slaking were applied before WA incorporation into mortar. The primary purpose of pre-treating WA was to enhance the feasibility of WA for developing cementitious materials [13]. Better results were obtained for the samples WA2 and WA3 which were pre-treated with sieving/grinding and sieving/slaking, respectively, compared to WA1 which was only sieved. Both the compressive and bending strengths of all mortar samples with WA were reduced with an increase in the WA mass content. Similar tendencies with the increase in WA content were observed in other studies as well [16]. The 28-day compressive and bending strengths for the reference sample were 62 and 10 MPa, respectively. Better mechanical results were observed for the samples where WA underwent extra treatment processes apart from sieving. The best sample containing WA was WA2-10% with 28-day compressive and bending strengths of 56 and 9 MPa, respectively. The 28-day compressive test result of WA3-10% was 51 MPa, which was close to that of WA2-10%, whereas the 28-day bending test results of WA3-10% and WA2-10% were almost the same. WA1-10%, which contained only sieved WA, performed worse in terms of mechanical properties. The compressive and bending strengths of WA1-10% were 45 and 8 MPa, respectively. Compared to WA2-10%, the compressive strength of WA1-10% was reduced by 20%. At the 30% WA replacement level, the absolute compressive and bending strength values declined compared to the 10% WA replacement level. The mechanical strength distributions at the 30% WA replacement level between the samples was similar to those at the 10% WA replacement level. The reduction in the compressive and bending strengths of the mortar samples containing WA was attributed to the less dense packaging of WA particles, which decreases the density of the cement matrix [1]. Less dense packaging results in a higher number of bigger closed pores that reduce the mechanical properties of the material. Another factor contributing to strength reduction is the presence of unburned carbon particles in WA [30]. Mortar samples with pre-treated WA showed better compressive and flexural strengths than those with untreated WA. The highest compressive strength of the mortar samples with WA was seen in the WA2-10% samples, whereas the highest flexural strength of the mortar samples with WA was seen in the WA3-10% samples.

Based on previously published data, the freeze–thaw mass loss was shown to not be significantly affected by the WA content, even up to 40% by mass [6]. This is contrary to the results obtained in this study. The freeze–thaw mass loss of WA2-10% was higher than that of the reference sample, possibly due to higher porosity. The freeze–thaw mass loss at 56 cycles for the reference sample and WA2-10% was 11,800 and 13,800 g/m^2, respectively, which accounts for an extra 14% of mass loss compared to the reference. This was attributed to higher water absorption due to larger open pores that formed due to the poor packing of WA2 particles. The freeze–thaw resistance of mortar depends on both open porosity and closed porosity [37]. Another aspect that could reduce the freeze–thaw resistance of mortar is associated with the constituents present in WA. Anhydrite and lime can cause the swelling of the cement matrix and be easily damaged by freezing and thawing. The high alkali content in WA can also contribute to a reduction in freeze–thaw resistance [6].

According to studies that focus on the life cycle analysis (LCA) of sustainable building materials and the circular economy of biomass ash, it can be concluded that incorporating biomass ash into mortars and concrete can significantly reduce the emissions of overall carbon dioxide and greenhouse gasses [38–40]. These findings suggest that although WA has promising mechanical potential when properly processed, its durability under environmental stress requires further optimization. Importantly, incorporating WA into cementitious systems can significantly reduce reliance on Portland cement, lowering carbon

emissions and promoting the circular use of biomass waste. Future work should focus on enhancing durability, scaling up mixing designs for 3D printing applications, and exploring combined SCM systems to balance mechanical performance and long-term durability in sustainable construction materials.

5. Conclusions

The importance of finding new cementitious supplementary materials in the cement industry has brought attention to wood biomass ash. The increasing availability of WA has started to pique the interest of large industries. This study highlights the feasibility of using wood ash as a supplementary cementitious material in mortar production. The application of wood ash in cement compositions remains a challenge to be investigated as the following conclusions can be drawn from this research:

1. According to the pozzolan standards used for the classification of coal ash, the WA used in this study met the criteria of the class C classification in terms of the total amount of 55% of SiO_2, Al_2O_3, and Fe_2O_3; a CaO amount of 21%; and a loss on ignition value of 6% and 5% by mass of particles retained on the 45 μm sieve.
2. The most notable impact of ball-milling wood ash occurred in the particle sizes of 125 to 500 μm. Outside this particle size range, the ball-milling impact was unnoticeable.
3. Both the compressive and bending strengths of all mortar samples containing wood ash were reduced with an increase in the wood ash mass content compared to the reference sample. The compressive and bending strengths of the reference sample after 28 days were 62 and 10 MPa, respectively. The best-performing sample with wood ash was WA2-10%, with 28-day compressive and bending strengths of 56 and 9 MPa, respectively, while the worst-performing sample was WA1-30%, with 28-day compressive and bending strengths of 32 and 6 MPa, respectively.
4. Among the three treatment methods, WA2 (sieved/slaked) and WA3 (sieved/ground) showed significant improvements in mechanical performance compared to WA1 (only sieved), with WA2-10% demonstrating the highest compressive strength and WA3-10% exhibiting the best flexural strength. The better mechanical properties of the mortar samples with WA2 were attributed to the complete water absorption of WA. The mechanical improvement in WA3 was attributed to its denser mortar matrix due to a finer particle size.
5. At 56 freeze–thaw cycles, the mass loss of the WA2-10% sample was 13,800 g/m^2, whereas that of the reference was 11,800 g/m^2, which is 14% lower compared to WA2-10%. The higher freeze–thaw mass loss of WA2-10% was attributed to bigger pores on the exposed surface of the sample.

Author Contributions: Conceptualization, O.L., G.B. and D.B.; methodology, A.S. and M.S.; validation, O.L., G.B. and D.B.; formal analysis, O.L., A.S. and G.B.; investigation, A.S. and M.S.; resources, M.S., X.Z. and D.B.; data curation, O.L., A.S. and M.S.; writing—original draft preparation, O.L. and G.B.; writing—review and editing, O.L., G.B., M.S., D.B. and X.Z.; visualization, O.L. and A.S.; supervision, G.B., M.S., X.Z. and D.B.; project administration, M.S. and D.B.; funding acquisition, G.B., M.S. and D.B. All authors have read and agreed to the published version of the manuscript.

Funding: This activity/work was supported by the EU Recovery and Resilience Facility within Project No 5.2.1.1.i.0/2/24/I/CFLA/003 "Implementation of consolidation and management changes at Riga Technical University, Liepaja University, Rezekne Academy of Technology, Latvian Maritime Academy and Liepaja Maritime College for the progress towards excellence in higher education, science and innovation" academic career doctoral grant (ID 1069).

Data Availability Statement: All results are presented in this article.

Acknowledgments: This article is based on work by COST Action (CircularB— Implementation of Circular Economy in the Built Environment, CA21103), supported by COST (European Cooperation in Science and Technology).

Conflicts of Interest: The authors declare no conflicts of interest.

References

1. Teixeira, E.R.; Camões, A.; Branco, F.G. Valorisation of Wood Fly Ash on Concrete. *Resour. Conserv. Recycl.* **2019**, *145*, 292–310. [CrossRef]
2. Eštoková, A.; Wolfová Fabiánová, M.; Ondová, M. Concrete Structures and Their Impacts on Climate Change and Water and Raw Material Resource Depletion. *Int. J. Civ. Eng.* **2022**, *20*, 735–747. [CrossRef]
3. Lothenbach, B.; Scrivener, K.; Hooton, R.D. Supplementary Cementitious Materials. *Cem. Concr. Res.* **2011**, *41*, 1244–1256. [CrossRef]
4. Lei, Z.; Pavia, S. Biomass Ash (BA) Waste as an Activator to Produce Carbon-Negative Cement. *CEMENT* **2024**, *18*, 100112. [CrossRef]
5. Vassilev, S.V.; Baxter, D.; Andersen, L.K.; Vassileva, C.G. An Overview of the Chemical Composition of Biomass. *Fuel* **2010**, *89*, 913–933. [CrossRef]
6. Fořt, J.; Šál, J.; Keppert, M.; Mildner, M.; Hotěk, P.; Ślosarczyk, A.; Klapiszewski, Ł.; Černý, R. Durability Analysis of Sustainable Mortars with Biomass Fly Ash as High-Volume Replacement of Portland Cement. *J. Build. Eng.* **2024**, *91*, 109565. [CrossRef]
7. Sigvardsen, N.M.; Geiker, M.R.; Ottosen, L.M. Reaction Mechanisms of Wood Ash for Use as a Partial Cement Replacement. *Constr. Build. Mater.* **2021**, *286*, 122889. [CrossRef]
8. Malaiškienė, J.; Vaičienė, M. The Influence of Silica Fly Ash and Wood Bottom Ash on Cement Hydration and Durability of Concrete. *Materials* **2024**, *17*, 4031. [CrossRef]
9. Hills, C.D.; Tripathi, N.; Singh, R.S.; Carey, P.J.; Lowry, F. Valorisation of Agricultural Biomass-Ash with CO_2. *Sci. Rep.* **2020**, *10*, 13801. [CrossRef]
10. Hamid, Z.; Rafiq, S. An Experimental Study on Behavior of Wood Ash in Concrete as Partial Replacement of Cement. *Mater. Today Proc.* **2020**, *46*, 3426–3429. [CrossRef]
11. Sata, V.; Tangpagasit, J.; Jaturapitakkul, C.; Chindaprasirt, P. Effect of W/B Ratios on Pozzolanic Reaction of Biomass Ashes in Portland Cement Matrix. *Cem. Concr. Compos.* **2012**, *34*, 94–100. [CrossRef]
12. Rosales, J.; Cabrera, M.; Beltrán, M.G.; López, M.; Agrela, F. Effects of Treatments on Biomass Bottom Ash Applied to the Manufacture of Cement Mortars. *J. Clean Prod.* **2017**, *154*, 424–435. [CrossRef]
13. Liang, X.; Li, Z.; Dong, H.; Ye, G. A Review on the Characteristics of Wood Biomass Fly Ash and Their Influences on the Valorization in Cementitious Materials. *J. Build. Eng.* **2024**, *97*, 110927. [CrossRef]
14. Nascimento, L.C.; Baptista Junior, G.; Xavier, G.d.C.; Monteiro, S.N.; Vieira, C.M.F.; de Azevedo, A.R.G.; Alexandre, J. Use of Wood Bottom Ash in Cementitious Materials: A Review. *J. Mater. Res. Technol.* **2023**, *23*, 4226–4243. [CrossRef]
15. Ristić, N.; Grdić, Z.; Topličić-ćurčić, G.; Grdić, D.; Dodevski, V. Properties of Self-Compacting Concrete Produced with Biomass Wood Ash. *Teh. Vjesn.* **2021**, *28*, 495–502.
16. Yang, Z.; Huddleston, J.; Brown, H. Effects of Wood Ash on Properties of Concrete and Flowable Fill. *J. Mater. Sci. Chem. Eng.* **2016**, *4*, 101–114. [CrossRef]
17. Tararushkin, E.V.; Shchelokova, T.N.; Kudryavtseva, V.D. A Study of Strength Fluctuations of Portland Cement by FTIR Spectroscopy. *IOP Conf. Ser. Mater. Sci. Eng.* **2020**, *919*, 022017. [CrossRef]
18. Wembe, J.T.; Ngueyep, L.L.M.; Elat, E.; Pliya, P.; Telefouet, A.J.P.; Ndjaka, J.M.B.; Noumowe, A. Valorization of Ashes from Different Wood Species in Cementitious Materials. *Discov. Sustain.* **2024**, *5*, 257. [CrossRef]
19. Dehkordi, B.A.; Nilforoushan, M.R.; Talebian, N.; Tayebi, M. A Comparative Study on the Self-Cleaning Behavior and Antibacterial Activity of Portland Cement by Addition of TiO2and ZnO Nanoparticles. *Mater. Res. Express.* **2021**, *8*, 035403. [CrossRef]
20. Chu, D.C.; Kleib, J.; Amar, M.; Benzerzour, M. Determination of the Degree of Hydration of Portland Cement Using Three Different Approaches: Scanning Electron Microscopy (SEM-BSE) and Thermogravimetric Analysis (TGA). *Case Stud. Constr. Mater.* **2021**, *15*, p.e00754. [CrossRef]
21. *LVS EN 933-1:2012 A*; Tests for Geometrical Properties of Aggregates—Part 1: Determination of Particle Size Distribution—Sieving Method. CEN: Brussels, Belgium, 2012.
22. *LVS EN 197-1:2012*; Cement—Part 1: Composition, Specifications and Conformity Criteria for Common Cements. CEN: Brussels, Belgium, 2012.
23. Ayobami, A.B. Performance of Wood Bottom Ash in Cement-Based Applications and Comparison with Other Selected Ashes: Overview. *Resour. Conserv. Recycl.* **2021**, *166*, 105351. [CrossRef]
24. *LVS EN 196-1:2016*; Methods of Testing Cement—Part 1: Determination of Strength. CEN: Brussels, Belgium, 2016.

25. *LVS CEN/TS 12390-9:2017*; Testing Hardened Concrete—Part 9: Freeze-Thaw Resistance with de-icing Salts—Scaling. CEN: Brussels, Belgium, 2017.
26. Nath, B.D.; Sarkar, G.; Siddiqua, S.; Rokunuzzaman, M.; Islam, M.R. Geotechnical Properties of Wood Ash-Based Composite Fine-Grained Soil. *Adv. Civ. Eng.* **2018**, *2018*, 9456019. [CrossRef]
27. Olatoyan, O.J.; Kareem, M.A.; Adebanjo, A.U.; Olawale, S.O.A.; Alao, K.T. Potential Use of Biomass Ash as a Sustainable Alternative for Fly Ash in Concrete Production: A Review. *Hybrid Adv.* **2023**, *4*, 100076. [CrossRef]
28. *EN 450-1:2012*; Fly Ash for Concrete—Part 1: Definition, Specifications and Conformity Criteria. CEN: Brussels, Belgium, 2012.
29. Berra, M.; Mangialardi, T.; Paolini, A.E. Reuse of Woody Biomass Fly Ash in Cement-Based Materials. *Constr. Build. Mater.* **2015**, *76*, 286–296. [CrossRef]
30. *ASTM C618-15*; Standard Specification for Coal Fly Ash and Raw or Calcined Natural Pozzolan for Use in Concrete. ASTM: West Conshohocken, PA, USA, 2015.
31. *C618−22*; Standard Specification for Coal Fly Ash and Raw or Calcined Natural Pozzolan for Use in Concrete. ASTM: West Conshohocken, PA, USA, 2015.
32. Tran Thi, K.D.; Liao, M.C.; Vo, D.H. The Characteristics of Alkali-Activated Slag-Fly Ash Incorporating the High Volume Wood Bottom Ash: Mechanical Properties and Microstructures. *Constr. Build. Mater.* **2023**, *394*, 132240. [CrossRef]
33. Rumman, R.; Kamal, M.R.; Bediwy, A.; Alam, M.S. Partially Burnt Wood Fly Ash Characterization and Its Application in Low-Carbon Mortar and Concrete. *Constr. Build. Mater.* **2023**, *402*, 132946. [CrossRef]
34. Yao, X.; Mao, J.; Li, L.; Sun, L.; Xu, K.; Ma, X.; Hu, Y.; Zhao, Z.; Chen, S.; Xu, K. Characterization Comparison of Bottom Ash and Fly Ash during Gasification of Agricultural Residues at an Industrial-Scale Gasification Plant—Experiments and Analysis. *Fuel* **2021**, *285*, 119122. [CrossRef]
35. Kumar, S.; Kumar, R. Mechanical Activation of Fly Ash: Effect on Reaction, Structure and Properties of Resulting Geopolymer. *Ceram Int.* **2011**, *37*, 533–541. [CrossRef]
36. Narani, S.S.; Siddiqua, S.; Perumal, P. Wood Fly Ash and Blast Furnace Slag Management by Alkali-Activation: Trace Elements Solidification and Composite Application. *J. Env. Manag.* **2024**, *354*, 120341. [CrossRef]
37. Nagrockienė, D.; Daugėla, A. Investigation into the Properties of Concrete Modified with Biomass Combustion Fly Ash. *Constr. Build. Mater.* **2018**, *174*, 369–375. [CrossRef]
38. Kumari, S.; Walia, R. Life Cycle Assessment of Sustainable Concrete by Utilizing Groundnut Husk Ash in Concrete. *Mater. Today Proc.* **2021**, *49*, 1910–1915. [CrossRef]
39. Caldas, L.R.; Da Gloria, M.Y.R.; Pittau, F.; Andreola, V.M.; Habert, G.; Toledo Filho, R.D. Environmental Impact Assessment of Wood Bio-Concretes: Evaluation of the Influence of Different Supplementary Cementitious Materials. *Constr. Build. Mater.* **2021**, *268*, 121146. [CrossRef]
40. Dufossé, K.; Marie-charlotte, M.; Augiseau, V.; Henrion, T.; Djelal, H. Quantification and Environmental Assessment of Wood Ash from Biomass Power Plants: Case Study of Brittany Region in France. *Sustainability* **2022**, *14*, 99. [CrossRef]

Disclaimer/Publisher's Note: The statements, opinions and data contained in all publications are solely those of the individual author(s) and contributor(s) and not of MDPI and/or the editor(s). MDPI and/or the editor(s) disclaim responsibility for any injury to people or property resulting from any ideas, methods, instructions or products referred to in the content.

buildings

MDPI

Article

Effect of Pozzolanic Additive on Properties and Surface Finish Assessment of Concrete

Giedrius Girskas *, Dalius Kriptavičius, Olga Kizinievič and Jurgita Malaiškienė

Faculty of Civil Engineering, Vilnius Gediminas Technical University, Sauletekio av. 11, LT-10223 Vilnius, Lithuania; dalius.kriptavicius@vilniustech.lt (D.K.); olga.kizinievic@vilniustech.lt (O.K.); jurgita.malaiskiene@vilniustech.lt (J.M.)
* Correspondence: giedrius.girskas@vilniustech.lt

Abstract: This research focuses on the impact of a pozzolanic additive (zeolite) on the durability properties of concrete and the evaluation of the surface finish of the final product (concrete). Durability is one of the key characteristics of concrete that ensures the performance of concrete structures, landscaping elements, and products over their lifetime and beyond. To reduce CO_2 emissions, replacing part of traditional cement with pozzolanic additives is necessary. We tested concrete mixes in which up to 20% of cement was replaced with a pozzolanic additive. Concrete flow and entrained air content were measured. The following properties of hardened modified concrete were determined: density, ultrasonic pulse velocity, water absorption, freeze–thaw resistance, and mechanical properties after 7 and 28 days of curing. The compressive strength values were normalised and expressed in MPa/g to obtain a deeper insight into the effect of a pozzolanic additive on the mechanical properties of concrete. The test results showed that the pozzolanic additive selected for testing reduced the flowability, density, and ultrasonic pulse velocity; increased entrained air content; and reduced the porosity of concrete. The compressive strength results at 28 days (normalised and expressed in MPa/g) showed that all specimens modified with up to 20% zeolite had a higher compressive strength than that of the reference specimen (from 0.0138 to 0.0164). Freeze–thaw resistance results showed that 15% was the optimum content of zeolite additive that could replace cement in the mix to obtain concrete with appropriate durability properties. Concrete surface finish evaluation tests showed that 15% of the pozzolanic additive is recommended to obtain a good-quality surface finish of exposed concrete.

Keywords: pozzolanic additive; durability; composites; freeze–thaw resistance; assessment of surface quality

1. Introduction

With growing concern about environmental issues, research into mitigating the deleterious effects of the concrete industry on the environment has increased. Global PC manufacturing is responsible for about 8% of the world's greenhouse gas emissions [1]. One of the ways to address this problem is to replace part of the binder with industrial waste or products of natural origin [2–6]. Research papers on the impact of supplementary cementitious materials are mainly focused on the technical characteristics of concrete, such as durability, mechanical properties, etc. In this respect, active mineral additives based on amorphous SiO_2, vitreous silicates and aluminosilicates, or their mixtures have a positive impact on the overall properties of hardened concrete [7–12].

Natural and artificial pozzolanic materials are active mineral additives containing at least 50% silica and aluminium oxides. Pozzolanic activity is the ability to react with portlandite ($Ca(OH)_2$) in the presence of free water. This reaction produces calcium silicate and calcium aluminosilicate hydrates or compounds similar to those formed in PC hydration [13–15]. The benefits of replacing part of PC with pozzolanic materials include improved PC concrete properties, lower production or maintenance costs, and reduced CO_2 emissions [16]. There are numerous advantages of modifying concrete with pozzolanic materials, such as enhanced durability of concrete [17], lower heat of hydration [18], improved sulphate resistance [19], and also lower PC industry energy costs [18].

Zeolites (ZLs), both natural and synthetic, are recognised and applied as pozzolanic materials in the cement and concrete industry. They are silicates with an open framework structure or hydrated aluminosilicate minerals. They have exceptional physical properties due to their almost ideal crystalline structure. The pozzolanic activity of ZLs is just as good as that of mineral additives having an amorphous structure [20]. Zeolites mainly consist of silicon, aluminium, and oxygen [21,22] and differ by their framework type, Si/Al ratio, sorption capacity, ion exchange potential, and types of exchangeable cations [23,24]. ZL additives reduce segregation and bleeding and thus help to maintain the homogeneity of the mixture [25,26]. However, researchers observed a higher demand for a superplasticiser in mixtures modified with 10% ZL to maintain slump properties [27]. Fragoulis et al. found that ZL increases water demand; therefore, a higher dose of superplasticiser is required to adjust the rheological properties of the mixture [28]. Uzal and Turanli argued that the absorptivity of ZL adversely affects the consistency of the mix and accelerates the initial and final setting times [29]. Valipour et al. noted that water demand increases with a higher content of ZL replacing PC in the mix [30].

Pozzolanic materials react with CH to produce an additional amount of C-S-H. This process influences the microstructure of the PC matrix [31] because most often, it causes the densification of the PC matrix [32] and reduces the total porosity and the distribution of capillary pores [33]. However, the influence of PC matrix porosity on concrete permeability does not depend merely on the pore size and volume [34]. Neithalath and Jain found that water absorption highly depends on the pore interconnectivity [35]. Sant et al. stated that the interconnectivity of capillary pores is as important an indicator as capillary porosity [36]. Yu et al. found that the interconnectivity of capillary pores was the main factor impacting the water permeability of PC pastes [37]. The authors of another study reported the ability of pozzolanic materials to change the pore structure and morphology [38] because a certain portion of the interconnected pores can be blocked as a result of pozzolanic reactions [39].

Pavlik et al. found that ZL-modified concrete specimens had a higher open porosity than reference specimens [40]. De La Cruz et al. claimed that at 28 days, specimens modified with 5% ZL had 10.4% higher compressive strength and 4.7% lower total porosity [41]. Bilim found that all test specimens in which up to 20% PC was replaced with ZL had lower porosity and water absorption compared to reference specimens [42].

Researchers reported that test specimens modified with 8% ZL showed better strength results than reference specimens, and specimens modified with 16% ZL had compressive strength equal to that of reference specimens [23]. A group of authors who analysed ZL's impact on the durability of PC concretes found that concrete modified with 20% ZL had better resistance to freezing and thawing and the effect of de-icing salts, as well as carbonation [31].

In monolithic systems, the quality of cast-in-place elements' (walls, columns, slabs, etc.) surface finish can be compromised by several factors, such as poor surface quality of the formwork, dirty formwork, inaccurate concrete mix design, failure to follow concrete placement procedures, insufficient compaction of cast concrete, and incompetence of the

workforce. These causes, or combinations of them, can affect the quality of concrete surface finish and cause the following defects to occur: surface voids (bug holes), irregular concrete surface colour, uneven concrete surface/poor compaction, etc. [43–45].

Although there are a lot of research articles on introducing pozzolanic additives to cementitious systems, little information on the evaluation of modified concrete surface finishes is available. This research work had two aims. The first was to test the effect of a pozzolanic additive on the physical and mechanical properties of concrete and find ways to extend the durability of concrete without impairing its resistance to mechanical load and stress. The second was to evaluate the porosity of the concrete surface using image processing programmes and determine the optimal amount of pozzolanic additives to obtain a high-quality surface finish on exposed concrete. Conclusions are provided based on the examination of these aspects.

2. Materials and Methods

2.1. Materials

The specimens were made using CEM I 42.5 R Portland cement (PC) according to EN 197-1:2011 [46]. A portion of the PC was replaced with an natural pozzolanic additive (NPA). NPA characteristics are provided along with ordinary PC properties in Tables 1 and 2. NPA was obtained from a Transcarpathian mine in the west of Ukraine.

Table 1. Chemical compositions of PC and NPA.

Binders	Oxide Content, %								
	CaO	**SiO_2**	**Al_2O_3**	**Fe_2O_3**	**MgO**	**SO_3**	**K_2O**	**Na_2O**	**LOI**
PC	61.4	19.5	5.0	3.1	3.9	2.5	1.1	0.1	3.4
NPA	3.3	72.5	12.5	1.7	0.6	-	3.6	0.2	5.6

Table 2. Main physical properties of PC and NPA.

Properties	PC	NPA
Specific density, kg/m^3	3150	2350
Average particle size, μm	17.6	29.0
Specific surface area, m_2/kg	440	760

Table 1 presents the chemical compositions of PC and NPA. As evident from the data, PC consists primarily of calcium and silicon oxides, which make up more than 80% of the total, while NPA is rich in silicon and aluminium oxides, accounting for 85%.

Table 2 presents the main physical properties of the binding materials. We can see that PC has higher specific density than NPA, but NPA particles are slightly larger, and their specific surface area is much larger than that of PC particles.

Figure 1 illustrates the particle size distributions of PC and NPA. The average particle size values are given in Table 2. As shown in the table, the average PC particle size is 17.6 μm, whereas NPA particles are slightly larger, with an average size of 29.0 μm.

NPA SEM images are presented in Figure 2a at ×3000 magnification and in Figure 2b at ×10,000 magnification. As shown in the images, NPA particles have a plate shape and a size of 10 μm. Agglomerations of smaller particles are also visible.

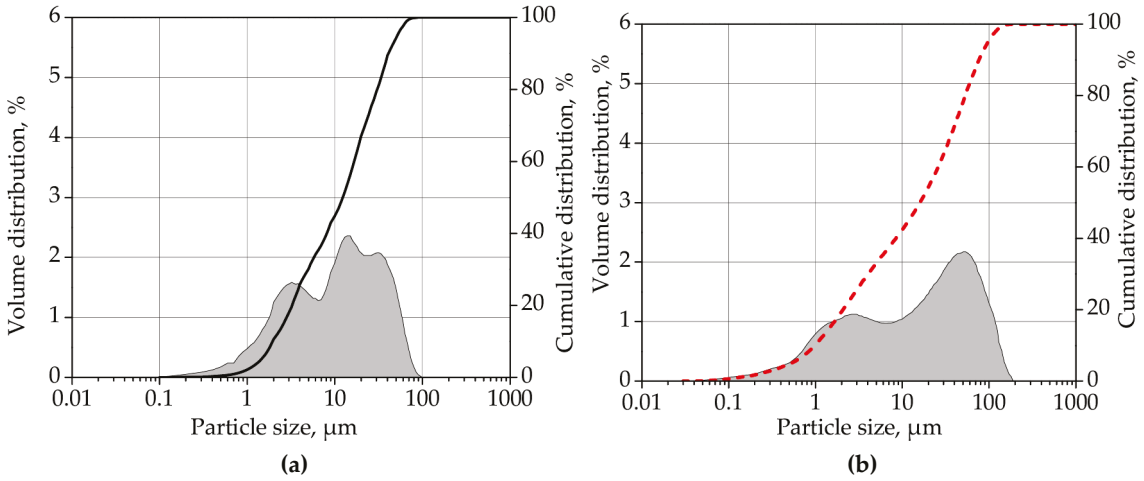

Figure 1. Particle size distribution of the reference: (**a**) PC; (**b**) NPA.

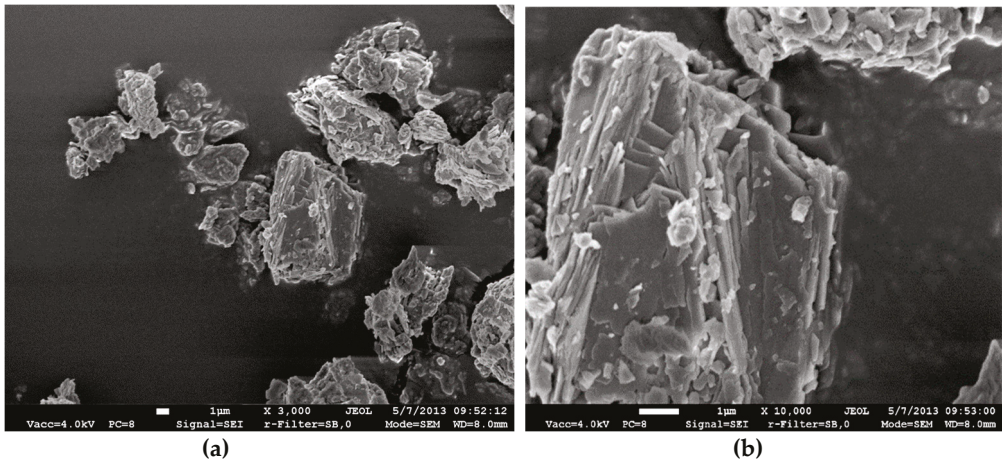

Figure 2. Images of NPA particles obtained by SEM: (**a**) magnified × 3000 (**b**) magnified × 10,000.

X-ray diffraction analysis (XRD) of the NPA (Figure 3) reveals that this material is composed of three main minerals: clinoptilolite, heulandite, and cristobalite.

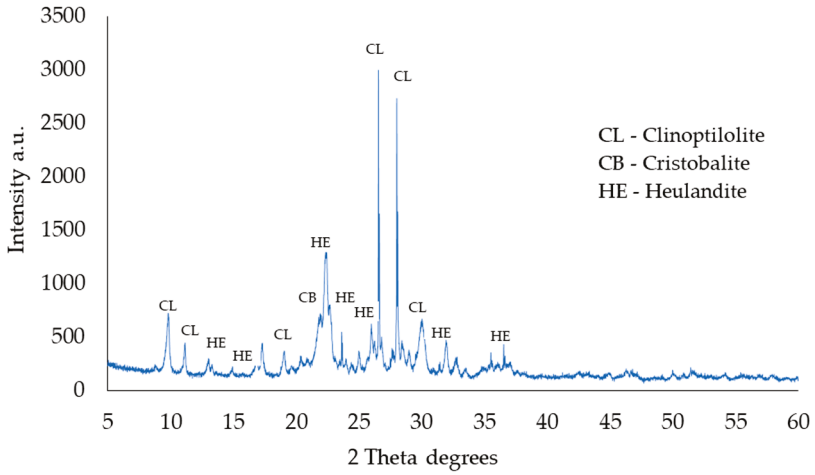

Figure 3. X-ray diffractogram of NPA.

Aggregates were used to prepare the PC mix for test specimens at a 0/4 fraction of sand and 4/16 fraction of gravel. A 0/4 fraction of sand complies with LST EN

12620:2003+A1:2008 requirements for concrete aggregates [47]. The values of essential aggregate characteristics are presented in the following tables: sand characteristics in Table 3 and gravel characteristics in Table 4.

Table 3. Sand 0/4 fr. characteristics.

Essential Characteristics	Declared/Limit Value
Grain size (fraction)	0/4
Particle density	2650 kg/m^3
Fineness modulus	4.0
Fines content	f_3
Organic impurities (humus)	none

Table 4. Gravel 4/16 fr. characteristics.

Essential Characteristics	Declared/Limit Value
Grain size (fraction)	4/16
Particle density	2600 kg/m^3
Fines content	$f_{1.5}$
Freeze–thaw resistance	F_1
Organic impurities (humus)	none

Concrete mixtures were prepared using tap water according to LST EN 1008 [48]. The water had a pH of 7.6 and temperature of 20 ± 3 °C. Polycarboxylate polymer-based superplasticiser (28% active substance) was added to the water. The superplasticiser is a brown liquid with the density of 1060 kg/m^3, pH value of 4.4, chloride content < 0.10% wt., and alkali content < 0.40% wt.

2.2. Preparation and Moulding of Concrete Specimens and Compositions

Dry raw materials were mixed in a forced action mixer according to LST EN 196-1:2016 [49]. The total mixing time did not exceed 7 min. Then, 100 × 100 × 100 mm cubes were cast in waterproof moulds made of 18 mm-thick birch plywood coated with phenolic formaldehyde (220 g/m$_2$). The concrete mix was placed into the moulds in two layers, and each layer was compacted on a vibrating table. The moulds with concrete were covered with a waterproof film and kept at an ambient temperature of 20 ± 2 °C for 24 h. After 24 h, the specimens were de-moulded and cured in water at the same temperature.

Table 5 presents the five compositions of the moulded concrete specimens. The reference composition PA0 was not modified with NPA. Compositions PA5, PA10, PA15, and PA20 were modified with NPA added by weight of PC at 5% increments. The maximum NPA content was 20%. A plasticising admixture was added at 0.8%. The control composition consistency corresponded to slump class S3.

Table 5. Compositions of concrete mixes, kg/m^3.

Compositions	PA0	PA5	PA10	PA15	PA20
PC	355.00	337.27	319.55	301.82	284.00
NPA	-	17.75	35.50	53.25	71.00
NPA, %	0	5	10	15	20
Sand	890	890	890	890	890
Gravel	1025	1025	1025	1025	1025
Plasticiser	2.84	2.84	2.84	2.84	2.84
Water	174.64	174.64	174.64	174.64	174.64
W/C	0.49	0.52	0.55	0.58	0.61

2.3. Test Methods

The specific surface area of NPA was measured using the air permeability method (Blaine method) according to LST EN 196-6:2010 [50]. Particle size distribution was determined using a Cilas 1090 LD particle size analyser (U.S. Philadelphia, Horsham). Water was used as the dispersion phase, the solid content of the suspension ranged between 12% and 14%, the ultrasonic particle dispersion lasted 100 s, and particle size was measured in the range of 0.01 to 500 μm in 15 s intervals. The qualitative analysis of mineral material phase composition was performed with an X-ray diffractometer. A graphite monochromator was employed to obtain the X-ray Cu Kα spectrum (λ = 0.154184 nm). The test parameters were set as follows: anode voltage at 30 kV, anode current at 12 mA, diffraction angle (2θ) ranging from 5° to 60°, detector step size of 0.02°, and an intensity measurement time of 0.5 s per step. PDXL software (Rigaku Corporation, Japan, Tokyo) and the PDF-4+ database of crystal structures was used for XRD analysis. Pictures of concrete specimens were processed and analysed using the image processing programmes ACDSee and ImageJ according to the methodology presented in Figure 4.

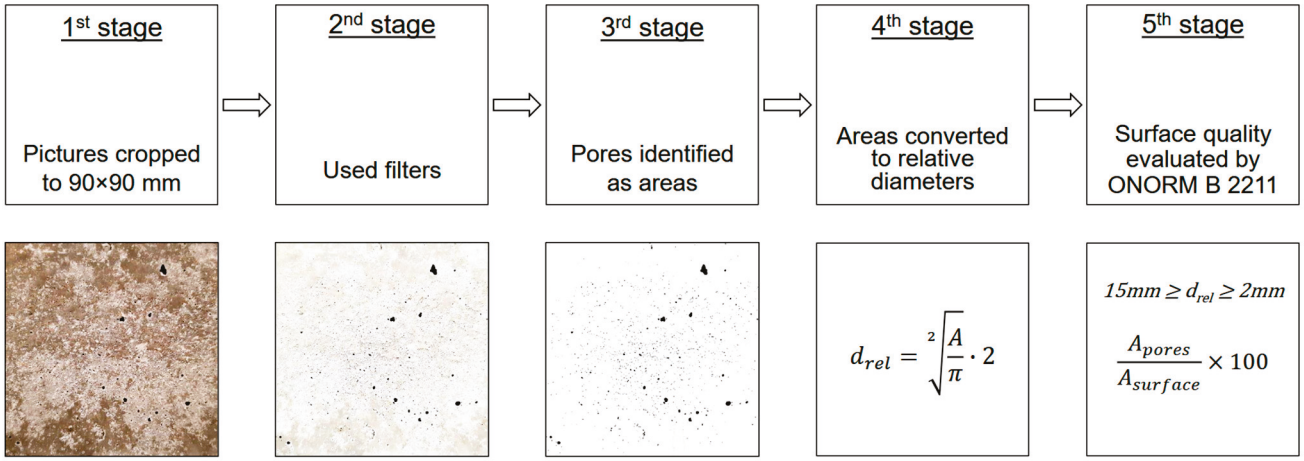

Figure 4. Image processing algorithm.

Entrained air content in concrete was determined according to LST EN 12350-2009 requirements [51]. The consistency of concrete was determined according to LST EN 12350-2009 requirements [52]. The compressive strength was tested according to LST EN 12390-3:2019—compressive strength of test specimens [53]. The specimens were loaded to failure in a compression-testing machine (hydraulic press) complying with LST EN 12390-4:2019—compressive strength technical requirement for testing machines [54]. A hydraulic press loading rate of 0.6 MPa/s was applied. The load on the specimens in the press was applied perpendicular to the casting direction. The load on the specimen was applied without shock and was increased continuously at the selected constant rate ± 10% until no greater load could be sustained. Open porosity tests were conducted according to the modified EN 1015-10:2002 method [55].

After 28 days of curing, the specimens were weighed in air and water. After recording the weight values, the specimens were dried in an oven at 100 ± 5 °C until constant mass was achieved. The water absorption rate was determined using the methodology given in EN 13369:2018 [56]. Freeze–thaw resistance was quantitatively assessed using the frost resistance coefficient. Knowing the value of frost resistance coefficient, the freeze–thaw resistance of hardened concrete can be predicted according to the function of the concrete's freeze–thaw resistance and frost resistance coefficient [57].

3. Results and Discussion

3.1. Fresh Concrete Properties

We measured entrained air content in the concrete mixture (Figure 5). Reference specimen PA0 had an entrained air content of 3.8%. Entrained air content increased with the replacement of PC with NPA. In specimens modified with 5% NPA, the entrained air content increased slightly to 4.0%. The value of entrained air increased to 4.4% in specimens modified with 10% NPA. The highest entrained air value of 4.6% was reached in the samples containing 15% NPA. With a further increase in NPA content to 20%, the entrained air content dropped to 4.1%.

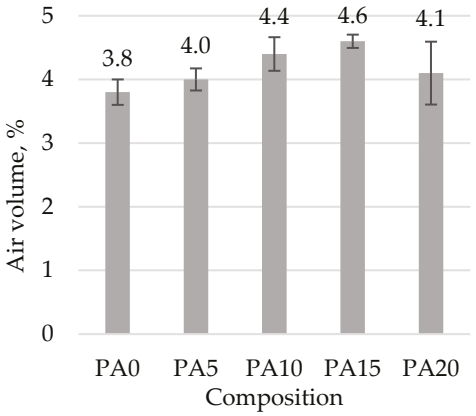

Figure 5. Air content results of fresh concrete.

The slump test of fresh concrete is the easiest and the most often used method to determine concrete consistency. The slump value is measured in mm of the vertical subsidence of concrete after the Abrams cone is lifted. Concrete mixtures are classified by slump classes (S1–S5) which indicate the subsidence of concrete.

We aimed to produce a control composition of slump class S3. The results of the tests are presented in Figure 6. The control composition met the requirements of slump class S3 with a slump of 150 mm. When NPA was added at 5%, the slump increased to 180 mm. The specimens modified with 10% NPA had a slump of 150 mm—identical to the reference composition. The slump decreased with a higher NPA content: with 15% NPA, the slump dropped to 105 mm, and with 20% NPA, the slump decreased to 30 mm.

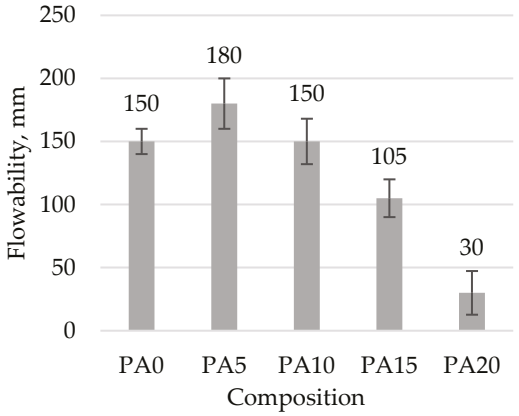

Figure 6. Results of fresh concrete flowability.

Xu et al. analysed the effect of NPA on mortar flowability. They reported that mortar flowability increased when 5% or 10% PC was replaced with NPA. The authors explained

this effect by a higher degree of cohesiveness in the mix depending on NPA particle size and amount. With the packing density of composite structure thus improved, there is more excess water in the system, and the flowability of the mixture improves [58].

3.2. Physical and Mechanical Properties of Concrete

A pozzolan typically consists of significant amounts of SiO_2 and Al_2O_3, which can react with calcium hydroxide (CH) in the presence of water to form cementitious compounds such as $3CaO{\cdot}2SiO_2{\cdot}3H_2O$ and $3CaO{\cdot}Al_2O_3{\cdot}6H_2O$. These compounds contribute to the development of a dense microstructure in the hardened PC paste and concrete [59].

Figure 7 illustrates the relationship between the cast concrete density and NPA content. The density of the reference composition shown in the figure is 2393 kg/m^3. When the binder is replaced with 5% NPA, the density drops to 2354 kg/m^3. The same downward trend is observed with an increase in NPA content.

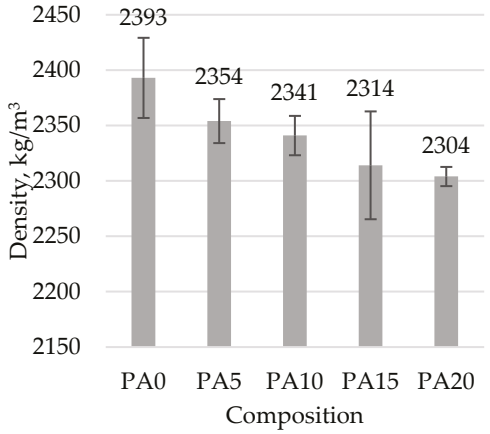

Figure 7. Density results of concrete.

The observed decrease in density values is natural considering that NPA has a lower specific density than PC. The dependence of UPV on the content of NPA added to concrete mixtures correlates with density values. Figure 8 illustrates the results of UPV tests. The UPV value in reference specimens is 4911 m/s. A higher NPA content causes UPV values to decrease to 4727 m/s in specimens modified with 20% NPA.

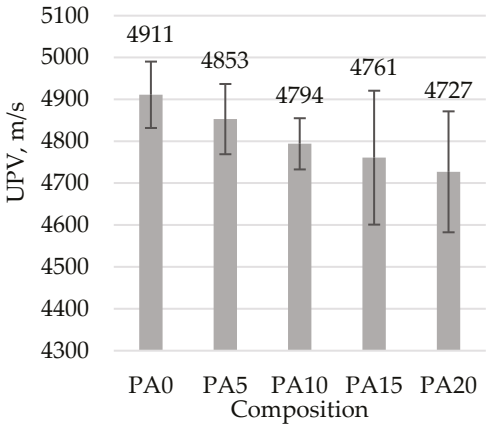

Figure 8. UPV results of concrete.

Figure 9 illustrates the dependence of compressive strength on NPA content after 7 days of curing. The reference specimen has a compressive strength of 48.4 MPa. When 5% of the binder is replaced with NPA, the compressive strength of concrete drops by 9.5%.

Bigger amounts of NPA decrease the compressive strength values even more: concrete modified with 10% NPA has a compressive strength of 41.6 MPa, 38.1 MPa with 15% NPA, and 34.3 MPa with 20% NPA.

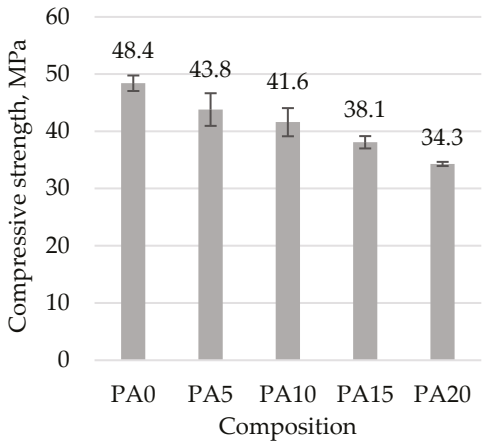

Figure 9. Compressive strength of concrete after 7 days of curing.

To better understand the effect of the NPA on the properties analysed, the test data were adjusted, i.e., recalculated to express the compressive strength achieved per unit weight of PC. This recalculation method helps to eliminate the effect of PC "dilution" and reveal the relative effectiveness of NPA on mechanical properties.

Figure 10 shows that the reference specimens had the highest compressive strength value after 7 days of curing. The specimens modified with 10% NPA had a slightly higher compressive strength, whereas other compositions had lower strength than the reference composition.

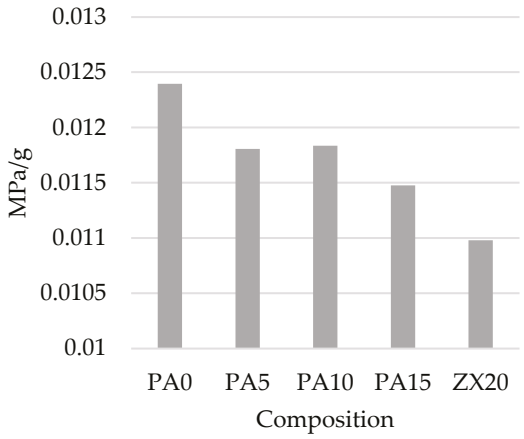

Figure 10. Normalised compressive strength after 7 days of curing.

The test results and the findings of other authors suggest that pozzolanic reactions of NPA often occur in late stages of hydration, i.e., after 14 or more days [60,61].

In a study where 0%, 5%, and 10% of the PC was replaced with NPA, it was found that after 28 days, the NPA-modified specimens exhibited compressive strength values 10.4% and 12.6% higher, respectively, than those of the reference [41]. Another study analysed the effect of varying NPA content (0%, 10%, 15%, 20%) and curing times (1, 7, and 28 days) on compressive strength. The results showed that all NPA-modified specimens outperformed the reference specimens at all curing times, with the highest compressive strength observed in the specimens modified with 20% NPA at 28 days [62].

At 28 days, the compressive strength trends were different from those at 7 days. Figure 11 shows that reference specimens have a strength of 54.2 MPa. In specimens modified with 5% NPA, the compressive strength increases 5% to 55.7 MPa. When PC is replaced with 10% NPA, the compressive strength slightly decreases to 55.5 MPa. Higher NPA content causes a decrease in compressive strength compared to that of the reference specimen: at 15%, the strength is 52.7 MPa, and at 20%, it decreases to 51.2 MPa.

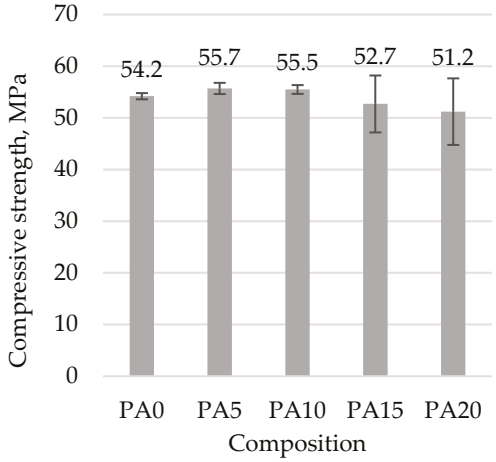

Figure 11. Compressive strength of concrete after 28 days of curing.

However, after the adjustment, i.e., the recalculation of strength results per unit weight of PC, the compressive strength of the specimens modified with up to 20% NPA was higher than the strength of reference specimens. These results are presented in Figure 12.

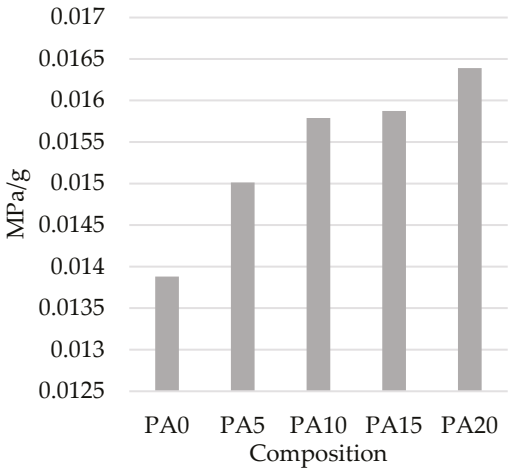

Figure 12. Normalised compressive strength after 28 days of curing.

Researchers who conducted long-term tests with NPA reported that after 28, 90, and 18 days of curing, the specimens modified with NPA showed better compressive strength results [63]. Perraki et al. performed similar tests with cements of different strength classes (CEM I 42.5 N and CEM I 52.5 N) and found that the specimens where 10% PC (CEM I 42.5 N) was replaced with NPA had slightly higher compressive strength values at 28 and 90 days. The specimens with 10% and 20% PC (CEM I 52.5 N) replaced with NPA had slightly higher compressive strength values than reference specimens at 90, 180, and 360 days [64].

The researchers explain that higher compressive strength values for pozzolanic reactions of ZL produce higher amounts of C-S-H, and therefore, higher compressive strength

values are achieved. These findings are supported by Nai-qian et al., who claim that ZL affects the mechanical properties of concrete due to reduced total porosity and improved interfacial area between the PC matrix and aggregates [65]. This information encouraged us to further analyse the effect of ZL on concrete porosity indicators.

Researchers claim that ZL used as an additive in concrete may decrease compressive strength due to the high mixing water demand because of the high surface area of ZL particles and its porous structure [66,67]. Moreover, the decline in initial compressive strength is explained by the water/binder ratio. In any case, if a suitable amount of NPA is chosen for concrete production, the benefits of applying it can outweigh the drawbacks.

3.3. Concrete Water Absorption

Given the wide use of cement-based materials in various buildings and structures, durability, which mainly refers to the resistance to temperature fluctuations (cyclic freeze–thaw) and various types of corrosion, is a very important characteristic of concrete. The durability of cement-based materials is influenced by different factors, among which water absorption of PC systems, porosity, and pore properties are the most important.

Figure 13 illustrates the relationship between NPA content and water absorption in concrete. The tests showed that water absorption increases with the NPA content in concrete. These findings corroborate density test results, which showed that density decreases with a higher NPA content. Concrete containing 5% NPA had 6.4% higher water absorption. Water absorption increases with a higher NPA content. Concrete modified with 20% NPA has a water absorption value of 5.66%, which is 24.94% higher than that of the reference composition.

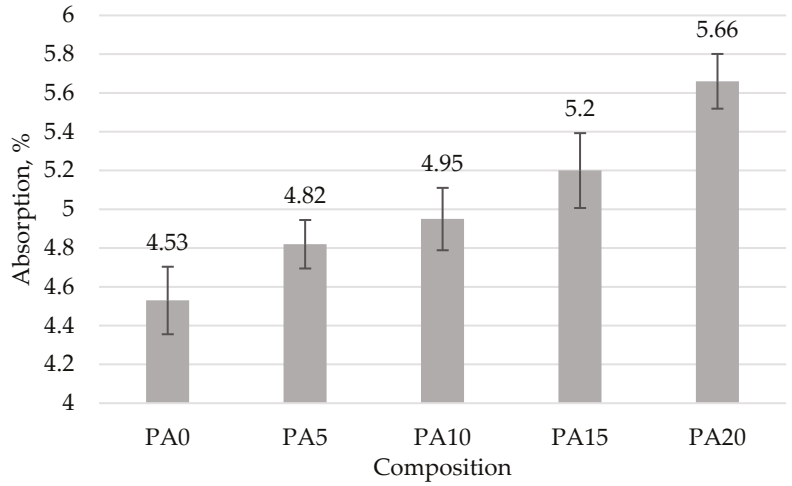

Figure 13. Water absorption results of modified concrete.

An increase in water absorption is anticipated because natural zeolite absorbs water faster than cement [68]. With the addition of natural zeolite, the depth of water penetration in concrete specimens decreased. The results after 28 days of curing showed that the depth of water penetration decreased between 13% and 40% compared to that of the reference. The performance further improved at the age of 90 days. According to water absorption tests, the specimens modified with natural zeolite absorbed more water than the reference specimen.

Concrete specimens containing natural zeolite produced fewer pores because of the zeolite's pozzolanic activity and $Ca(OH)_2$ consumption. On the other hand, the water uptake of the mixtures, particularly in the top surface of the concrete, impacted the total

water absorption. Jana and Feng et al. reported that this phenomenon can be explained by the considerable pozzolanic reactivity of the natural zeolites examined [69,70].

Zeolite particles, having a high absorption capacity, act as water reservoirs distributed throughout the concrete and facilitate internal curing. Capillary pores are formed at the start of the concrete mixing process, and water is absorbed onto these particles [71,72].

3.4. Porosity

Concrete porosity is an important characteristic for all types of concrete products. This characteristic determines not only how the product will look but also how long the cast product will last and whether it will lose its aesthetic appearance and mechanical properties.

Concrete porosity test results are presented in Figure 14. The total porosity of concretes of different compositions modified with up to 20% NPA added at 5% increments was analysed. Reference specimens had a total porosity of 11.04%, open porosity of 10.86%, and closed porosity of 0.18%. The air-entraining admixture was intentionally not used to see the direct effect of NPA on concrete porosity. With the replacement of PC with 5% NPA, the total porosity increased by 13.13% up to 12.49%. It should be noted that open porosity also increased to 11.35% and closed porosity increased significantly to 1.14%. Closed porosity is a very strong indicator of the durability properties of concrete products. Similar trends were observed in the specimens modified with 10–15% NPA, as open and closed porosity values increased along with total porosity. The closed porosity decreased in the specimens with a higher NPA content of 20%, although the total porosity increased. The porosity tests suggest that 15% is the optimum/maximum amount of NPA that can be added by weight of PC to produce durable concrete.

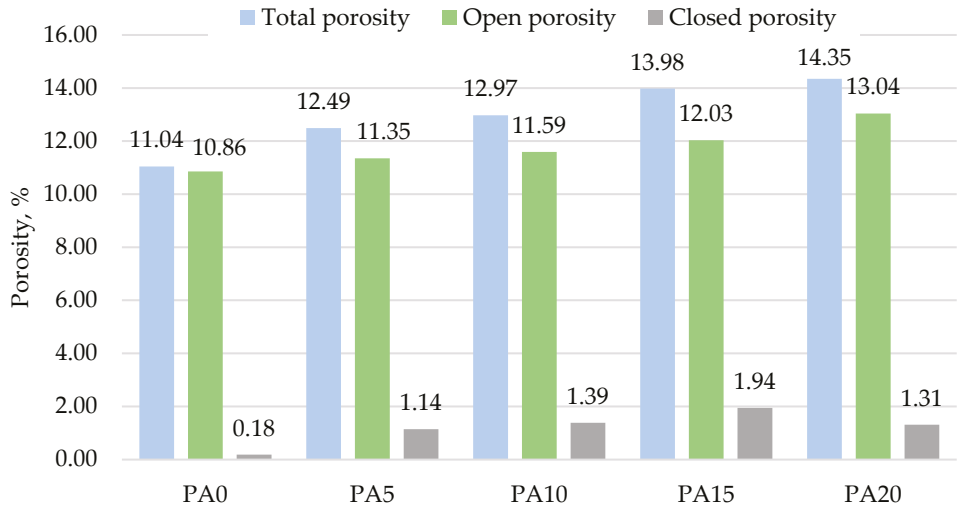

Figure 14. Results of concrete porosity (total, open, closed).

There is sufficient evidence that the durability of cementitious composites is directly related to their porosity, which determines how much water with dissolved degrading agents (chlorides, sulphates) can enter the PC matrix.

The replacement of PC with 20% ZL decreased the PC system's porosity and water absorption. Bilim explained this effect by the pozzolanic reactions of ZL, which produce more C-S-H and C-A-S-H and thus improve the concrete microstructure [42]. Uzal and Turanli support this idea based on the experimental results of hardened PC paste modified with ZL. The modified specimen had fewer pores of the size > 50 nm and thus better mechanical and permeability properties [29]. Researchers who studied water absorption and the depth of water penetration under pressure reported an inverse relationship, i.e., the specimens modified with ZL showed higher water absorption and lower penetration depth

values than reference specimens [73]. Similar results were obtained by other authors who analysed the same properties of concrete. Test results showed that at 28 and 90 days, water penetration depth decreased in the specimens where 15% and 30% PC was replaced with ZL. Researchers also found that these specimens had higher water absorption values [74].

The analysis of test results revealed that the addition of NPA can reduce the total porosity, altering pore size and distribution; therefore, the influence of this mineral on the durability properties of cementitious composites should be analysed.

3.5. Frost Resistance

Concrete's resistance to aggressive environments depends on two things: the microstructure and mineral composition of the cementitious matrix. Microstructural elements, such as the type, number, volume, shape, and distribution of pores, determine the extent to which concrete can be penetrated by degrading agents, i.e., water, which crystallises into ice at low temperatures, increases in volume, and erodes concrete from the inside, and substances dissolved in water, which, together with water, enter the concrete microstructure and form new compounds with the minerals of the PC matrix.

Figure 15 shows that reference specimens were very weak and sustained only 22 freeze–thaw cycles. Specimens of composition PA5 sustained 144 freeze–thaw cycles. These improved results are related to higher closed porosity. Specimens of composition PA10 sustained 178 freeze–thaw cycles. The highest freeze–thaw resistance value of 260 freeze–thaw cycles was obtained in the specimens modified with 15% NPA. Resistance to freeze–thaw cycles correlated directly with concrete porosity test results—concrete with more closed pores was more durable and, therefore, could withstand more freeze–thaw cycles.

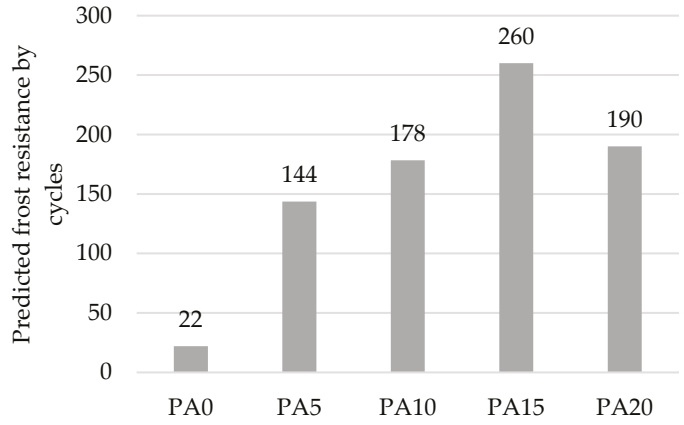

Figure 15. Results of predicted frost resistance (cycles).

High levels of reactive SiO_2 and Al_2O_3 in ZLs facilitate their reactions with $Ca(OH)_2$ generated during PC hydration to form additional C-S-H gel and hydrated aluminates, which improve the microstructure of the hardened PC paste. Improved mechanical properties, decreased permeability, reduced ASR-induced expansion, and increased resistance to sulphate attack result from replacing PC with ZL in PC and concrete composites. In addition, some research studies point out that ZL effectively improves concrete's durability [75].

Researchers who studied in detail the effect of ZL and its content on the durability of concrete focused on total porosity and pore size distribution. They reported that total porosity increased in all cases when part of PC was replaced with ZL and that the pore volume in the specimens modified with 10% and 20% ZL increased mainly due to the fine pores with diameters ranging from 0.01 to 0.1 μm. This increase might be related to a delayed reaction of ZL. They also found that concrete modified with 20% ZL had better resistance to freeze–thaw cycles in de-icing salt solution [31].

NPAs were studied regarding their potential to enhance the frost resistance of concrete. The replacement of 10% PC with ZL reduced the strength loss after 150 cycles by more than 30% in comparison to the reference value [76]. Additionally, the study indicated the enhanced freeze–thaw resistance of both ZL-modified and reference mixes with the addition of an air-entraining agent, proving the positive effect of NPA.

One study reported that only 5% PC replacement produced better values in modified specimens than in the reference [42], while another study found that 10% ZL increased freeze–thaw resistance [77]. The findings of both studies confirm that a higher ZL content will deteriorate the freeze–thaw resistance of mortars. Researchers explain these findings by the pozzolanic activity of ZL, which causes the densification of the microstructure, thus prohibiting the expansion of ice crystals and subsequent damage.

3.6. Assessment of Concrete Surface

It is not easy to obtain a perfect surface appearance of cast concrete without any changes in colour and with a faultless texture. Concrete surface repairs with various mixes are often impractical and rarely work; therefore, quality requirements must be introduced and strictly followed to assess concrete casting work [78].

In most cases, freshly placed concrete contains many entrapped air voids [79]. For the hardened concrete to reach its design requirements, the mix must be compacted. This is a process that brings the solid-phase particles closer, thereby reducing the amount of entrapped air voids in the concrete mix [80,81]. Stiffer and drier concrete mixtures require more intensive compaction and longer compaction times. Certain admixtures improve the workability of the mix and make it easier to compact without increasing the water-to-cement ratio. It is well known that properly compacted concrete with a lower water content has better physical and mechanical properties [82]. PC content can be reduced and the cost of concrete mix lowered without compromising the quality of concrete. Stiffer concrete mixes need good compaction to achieve a good-quality surface finish [83].

A technological process must be established to achieve the perfect quality of concrete surface finish: the selection of a mix composition, concrete placing and compacting method, formwork system, form-release agents, workforce, and other factors.

We aimed to assess the surface finish of NPA-modified concrete by quantifying air voids, determining the biggest effective air void diameter, and calculating the air void area and the ratio between the air void area and the surface area assessed. Uniform birch plywood moulds coated with phenolic formaldehyde were used to create identical casting conditions for all test specimens. The moulds were covered with the same type of form-release agent and polished. The concrete was placed in two layers, and each layer was compacted on a vibration table at the same frequency and for an identical duration.

There are different methods to assess concrete surface finish. We assessed the surface quality according to four indicators: the quantity of surface air voids, the effective diameter of the largest air voids, the square area of air voids on the surface assessed, and the ratio of the air void square area to the assessed surface area. The results are provided in Table 6, and Figure 16 presents natural concrete surface images and processed images to better visualise the surface defects/surface air voids.

Six specimens of each composition were formed. Out of the six surfaces of each specimen, four surfaces were analysed (only side surfaces, excluding the top and the bottom surfaces). Each surface was cut to the dimensions of 95 × 95 mm using a programme. The average composition was derived from 24 (6 × 4) surfaces, each having an area of 95 × 95 mm.

Table 6. Results of concrete surface finish assessment indicators.

Composition	Air Void Quantity	Largest Effective Air Void Diameter, mm	Air Void Sq. Area (mm^2):	Ratio of Air Void Sq. Area to Assessed Surface Area
PA0	9	4.77	69	0.19
PA5	7	4.71	58	0.16
PA10	12	4.34	74	0.21
PA15	11	4.45	74	0.21
PA20	27	6.17	212	0.60

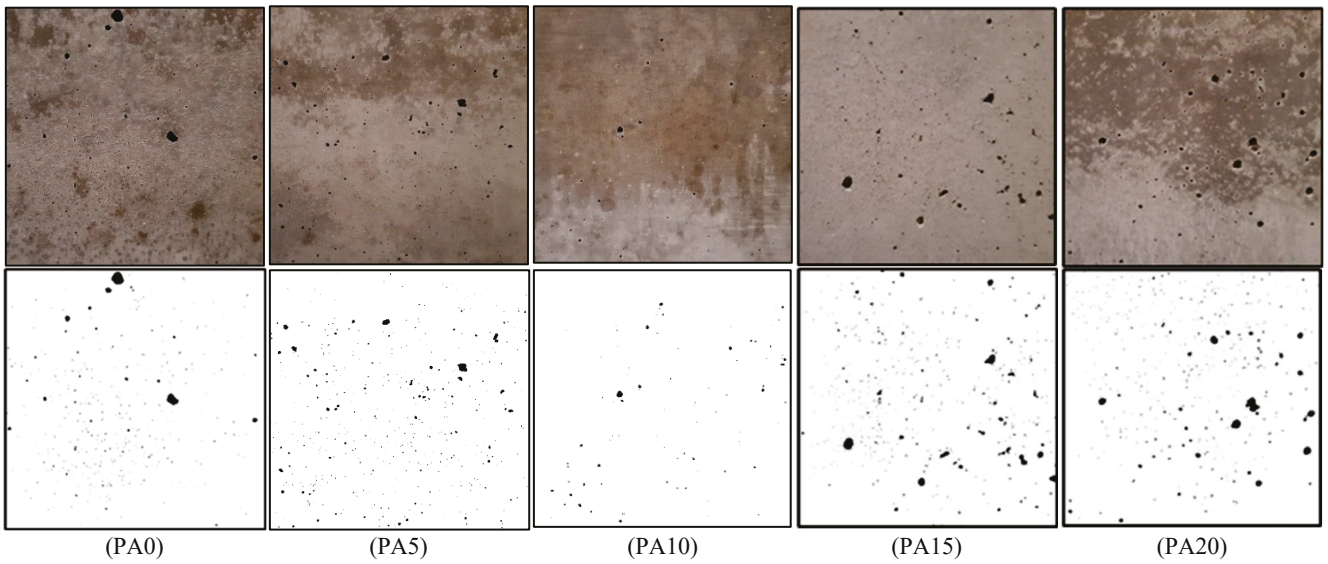

Figure 16. Photo documentation of NPA-modified concrete surfaces.

Nine air voids with the largest effective diameter of 4.77 mm and a square area of 69 mm^2 were identified in the specimen of composition PA0. When PC was replaced with 5% NPA, the number of air voids dropped to seven, the effective diameter was reduced to 4.71 mm, and the square area of assessed air voids decreased to 58 mm^2. These results show that NPA, added even in small amounts, affects the concrete's surface positively. With the increase in NPA content to 10–15%, the number of air voids assessed increased to 12 and 11, but the largest effective diameter of air voids decreased to 4.34 mm and 4.45 mm, respectively. However, the square area of the assessed air voids increased to 74 mm^2. Although the number and square area of air voids in specimens PA10 and PA15 increased, the largest effective air void diameter decreased. The specimens with the highest NPA content (20%) produced the worst results. Compared to the reference composition, specimen PA20 had three times more assessed pores, and the largest effective air void diameter was 6.17 mm or 29% larger. The square area of assessed air voids increased to 212 mm^2 or three times more than the reference specimen. A 15% NPA content could be used to achieve an excellent concrete surface finish, but the compaction time must be extended because the NPA-modified concrete mixture is less flowable. However, NPA reduces the likelihood of bleeding, the mixture is more stable and homogeneous; thus, the extended compaction time should not have any negative outcome. It should be also noted that concrete specimens containing 15% NPA had a warmer beige hue, different from the dark grey colour of reference specimens.

4. Conclusions

- The incorporation of NPA causes air entrainment in the PC mixture (3.8% in the reference composition, 4.6% in the composition with 15% NPA). A low amount of NPA added increases the slump of the mixture. The addition of NPA reduces the density of hardened concrete and increases water absorption due to the lower specific density of NPA compared to the PC density.
- The early compressive strength test results (at 7 days) showed that NPA deteriorates mechanical properties. The compressive strength gradually decreased, reaching a 29% drop in the specimens with the highest NPA content of 20%. Similar trends were observed in adjusted early compressive strength test results. Consistent with the findings of other authors, the test results suggest that pozzolanic reactions of NPA often occur in late stages of hydration, i.e., after 14 or more days.
- In the specimens modified with 5% NPA (after 28 days), the compressive strength increased by 2.7%. When PC was replaced with 10% NPA, the compressive strength decreased slightly to 55.5 MPa. After the adjustment (recalculation) of strength results per unit weight of PC, the compressive strength of all specimens modified with up to 20% NPA was higher than the strength of the reference specimen.
- The replacement of 5% PC with NPA caused a 13.13% increase in the total porosity. The open porosity also increased to 11.35%, and the closed porosity increased significantly to 1.14%. Similar trends were observed in the specimens modified with 10–15% NPA, where open and closed porosity values increased along with the total porosity. The closed porosity decreased in the specimens with a higher NPA content of 20%, although the total porosity increased. Freeze–thaw test results correlated with porosity test results—concrete with more closed pores was more durable and, thus, could sustain more freeze–thaw cycles. The porosity tests suggest that 15% is the optimum/maximum amount of NPA that can be added by weight to PC to produce durable concrete.
- The surface finish of NPA-modified concrete was evaluated by quantifying air voids, determining the largest effective air void diameter, and calculating the air void square area and the ratio between the air void square area and the surface area assessed. A proportion of 15% NPA can be added to obtain an excellent surface finish in the exposed concrete. Concrete specimens containing 15% NPA had a warmer beige hue, different from the dark grey colour of reference specimens.

This research work is beneficial for materials science and construction engineering, showing that pozzolanic materials can be used to obtain better surface finishes in exposed concrete. In the near future, the authors will focus more on the use of waste materials such as fly ash, metakaolin, and water treatment sludge in cement systems in order to develop durable concrete products. These materials will also be used to develop concrete compositions and obtain exposed concrete surfaces that can be cast as structural elements (columns, walls, etc.).

The results of this study contribute to materials science and construction engineering by demonstrating that pozzolanic additives can significantly improve the surface finish of exposed concrete. The authors will continue exploring the incorporation of industrial by-products such as fly ash, metakaolin, and water treatment sludge into cementitious systems and propose formulations for the engineering of durable concrete elements. These formulations will be evaluated for both the performance and the quality of the surface finish of exposed concrete products.

Author Contributions: Conceptualisation, G.G. and D.K.; methodology, D.K. and G.G.; validation, G.G., D.K. and O.K.; formal analysis, G.G., D.K. and J.M.; investigation, G.G and D.K.; resources, O.K.

and J.M.; data curation, J.M.; writing—original draft preparation, G.G and D.K.; writing—review and editing, G.G., D.K. and J.M.; visualisation, G.G. and D.K.; supervision, G.G. and O.K.; project administration, G.G. All authors have read and agreed to the published version of the manuscript.

Funding: This research received no external funding.

Data Availability Statement: Data are contained within the article.

Conflicts of Interest: The authors declare no conflicts of interest.

References

1. Al-Kheetan, M.J.; Al-Tarawneh, M.; Ghaffar, H.S.; Chougan, M.; Jweihan, Y.S.; Rahman, M.M. Resistance of hydrophobic concrete with different moisturecontents to advanced freeze–thaw cycles. *Struct. Concr.* **2020**, *22*, E1050–E1061.
2. Pereira, C.L.; Savastano, H.J.; Paya Bernabeu, J.J.; Santos, S.F.; Borrachero Rosado, M.V.; Monzó Balbuena, J.M.; Soriano Martinez, L. Use of highly reactive rice husk ash in the production of cement matrixreinforced with green coconut fiber. *Ind. Crops Prod.* **2013**, *49*, 88–96. [CrossRef]
3. İpek, S. Macro and micro characteristics of eco-friendly fly ash-based geopolymer composites made ofdifferent types of recycled sand. *J. Build. Eng.* **2022**, *52*, 104431. [CrossRef]
4. Öz, H.Ö.; Yücel, H.E.; Güneş, M.; Köker, T.Ş. Fly-ash-based geopolymer composites incorporating cold-bonded lightweight fly ash aggregates. *Constr. Build. Mater.* **2021**, *272*, 121963. [CrossRef]
5. Niş, A.; Eren, N.A.; Çevik, A. Effects of recycled tyre rubber and steel fibre on the impact resistance of slag-based self-compacting alkali-activated concrete. *Eur. J. Environ. Civ. Eng.* **2023**, *27*, 519–537. [CrossRef]
6. de Brito, J.; Kurda, R. The past and future of sustainable concrete: A critical review and new strategies on cement-based materials. *J. Clean. Prod.* **2021**, *281*, 123558.
7. Singh, N.; Mithulraj, M.; Arya, S. Utilization of coal bottom ash in recycled concrete aggregates based self-compacting concrete blended with metakaolin. *Resour. Conserv. Recycl.* **2019**, *144*, 240–251. [CrossRef]
8. Mangi, S.A.; Wan Ibrahim, M.H.; Jamaluddin, N.; Arshad, M.F.; Putra Jaya, R. Short-term effects of sulphate and chloride on the concrete containing coal bottom ash as supplementary cementitious material. *Eng. Sci. Technol. Int. J.* **2019**, *22*, 515–522. [CrossRef]
9. Al-Yousuf, A.; Pokharel, T.; Lee, J.; Gad, E.; Abdouka, K.; Sanjayan, J. Effect of fly ash and slag on properties of normal and high strength concrete including fracture energy by wedge splitting test: Experimental and numerical investigations. *Constr. Build. Mater.* **2021**, *271*, 121553. [CrossRef]
10. Zhang, J.; Ding, X.; Wang, Q.; Zheng, X. Effective solution for low shrinkage and low permeability of normal strength concrete using calcined zeolite particles. *Constr. Build. Mater.* **2018**, *160*, 57–65. [CrossRef]
11. Khan, M.N.N.; Saha, A.K.; Sarker, P.K. Reuse of waste glass as a supplementary binder and aggregate for sustainable cement-based construction materials: A review. *J. Build. Eng.* **2020**, *28*, 101052. [CrossRef]
12. El-Gamal, S.M.A.; Amin, M.S.; Ramadan, M. Hydration characteristics and compressive strength of hardened cement pastes containing nano-metakaolin. *HBRC J.* **2017**, *13*, 114–121. [CrossRef]
13. Cook, D.J. Natural pozzolanas. In *Cement Replacement Materials*; Swamy, R.N., Ed.; Surrey University Press: Surrey, UK, 1986; p. 259.
14. Martinez-Ramirez, S.; Blanco-Varela, M.T.; Erena, I.; Gener, M. Pozzolanic reactivity of zeolitic rocks from different Cuban deposits: Characterisation of reaction products. *Appl. Clay Sci.* **2006**, *32*, 40–52. [CrossRef]
15. Martens, G.; Snellings, R.; van Balen, K.; Bicer-Simsir, B.; Verlooy, P.; Elsen, J. Pozzolanic reactions of common natural zeolites with lime and parameters affecting their reactivity. *Cem. Concr. Res.* **2009**, *39*, 233–240. [CrossRef]
16. Chandra Paul, S.; Šavija, B.; Babafemi, A.J. A comprehensive review on mechanical and durability properties of cement-based materials containing waste recycled glass. *J. Clean. Prod.* **2018**, *198*, 891–906. [CrossRef]
17. Rojas, M.F.; Cabrera, J. The effect of temperature on the hydration rate and stability of the hydration phases of metakaolin-lime-water systems. *Cem. Concr. Res.* **2002**, *32*, 133–138. [CrossRef]
18. Shi, C. Pozzolanic reaction and microstructure of chemical activated lime-fly ash pastes. *ACI Mater. J.* **1998**, *95*, 537–545.
19. Janotka, I.; Krajci, L. Utilization of natural zeolite in Portland cement of increased sulphate resistance. *ACI Spec. Publ.* **2003**, *22*, 223–229.
20. Ahmadi, B.; Shekarchi, M. Use of natural zeolite as a supplementary cementitious material. *Cem. Concr. Compos.* **2010**, *32*, 134–141. [CrossRef]
21. Payra, P.; Dutta, P.K. Zeolites: A primer. In *Handbook of Zeolite Science and Technology*; CRC Press: Boca Raton, FL, USA, 2003; pp. 1–24.

22. Muraoka, K.; Chaikittisilp, W.; Okubo, T. Energy analysis of aluminosilicate zeolites with comprehensive ranges of framework topologies. Chemical Compositions, and Aluminum Distributions. *J. Am. Chem. Soc.* **2016**, *138*, 6184–6193. [CrossRef]
23. Rahhal, V.F.; Pavlík, Z.; Tironi, A.; Castellano, C.C.; Trezza, M.A.; Černý, R.; Irassar, E.F. Effect of cement composition on the early hydration of blended cements with natural zeolite. *J. Therm. Anal. Calorim.* **2017**, *128*, 721–733. [CrossRef]
24. Stanislao, C.; Rispoli, C.; Vola, G.; Cappelletti, P.; Morra, V.; Gennaro, M. Contribution to the knowledge of ancient Roman seawater concretes: Phlegrean pozzolan adopted in the construction of the harbour at Soli-Pompeiopolis (Mersin. Turkey). *Period Miner.* **2011**, *80*, 471–488.
25. Mumpton, F.A. Natural zeolites. In *Mineralogy and Geology of Natural Zeolites*; Mumpton, F.A., Ed.; Mineralogical Society of America: Chantilly, VA, USA, 1981; pp. 1–18.
26. Ulmanu, M. Mineralogy of natural zeolites. In *Handbook of Natural Zeolites*; Inglezakis, V.J., Zorpas, A.A., Eds.; Bentham Science Publishers: Sharjah, The United Arab Emirates, 2012; pp. 52–69.
27. Feng, N.Q.; Li, G.Z.; Zang, X.W. High-strength and flowing concrete with a zeolitic mineral admixture. *Cem. Concr. Aggreg.* **1990**, *12*, 61–69. [CrossRef]
28. Fragoulis, D.; Chaniotakis, E.; Stamatakis, M.G. Zeolitic tuffs of Kimolos Island, Aegean Sea, Greece and their industrial potential. *Cem. Concr. Res.* **1997**, *27*, 889–905. [CrossRef]
29. Uzal, B.; Turanli, L. Blended cements containing high volume of natural zeolites: Properties, hydration and paste microstructure. *Cem. Concr. Compos.* **2012**, *34*, 101–109. [CrossRef]
30. Valipour, M.; Pargar, F.; Shekarchi, M.; Khani, S. Comparing a natural pozzolan, zeolite, to metakaolin and silica fume in terms of their effect on the durability characteristics of concrete: A laboratory study. *Constr. Build. Mater.* **2013**, *41*, 879–888. [CrossRef]
31. Vejmelková, E.; Koňáková, D.; Kulovaná, T.; Keppert, M.; Žumár, J.; Rovnaníková, P.; Keršner, Z.; Sedlmajer, M.; Černý, R. Engineering properties of concrete containing natural zeolite as supplementary cementitious material: Strength, toughness, durability, and hygrothermal performance. *Cem. Concr. Compos.* **2015**, *55*, 259–267. [CrossRef]
32. Tran, Y.T.; Lee, J.; Kumar, P.; Kim, K.H.; Lee, S.S. Natural zeolite and its application in concrete composite production. *Compos. Part B Eng.* **2019**, *165*, 354–364. [CrossRef]
33. Takemoto, K.; Uchikawa, H. Hydration of pozzolanic cement. In *7th International Congress on the Chemistry of Cement*; Éditions Septima: Paris, France, 1980; Volume 1, pp. IV-2/1–IV-2/29.
34. Nguyen, Q.H.; Lorente, S.; Duhard-Barone, A. Effect of the pore size of cement based materials on ionic transport. *Constr. Build. Mater.* **2017**, *147*, 160–167. [CrossRef]
35. Neithalath, N.; Jain, J. Relating rapid chloride transport parameters of concretes to microstructural features extracted from electrical impedance. *Cem. Concr. Res.* **2010**, *40*, 1041–1051. [CrossRef]
36. Sant, G.; Bentz, D.; Weiss, J. Capillary porosity depercolation in cement-based materials: Measurement techniques and factors which influence their interpretation. *Cem. Concr. Res.* **2011**, *41*, 854–864. [CrossRef]
37. Yu, Z.; Ni, C.; Tang, M.; Shen, X. Relationship between water permeability and pore structure of Portland cement paste blended with fly ash. *Constr. Build. Mater.* **2018**, *175*, 458–466. [CrossRef]
38. Zhang, J.; Bian, F.; Zhang, Y.; Fang, Z.; Fu, C.; Guo, J. Effect of pore structures on gas permeability and chloride diffusivity of concrete. *Constr. Build. Mater.* **2018**, *163*, 402–413. [CrossRef]
39. Bernal Camacho, J.; Mahmoud Abdelkader, S.; Reyes Pozo, E.; Moragues Terrades, A. The influence of ion chloride on concretes made with sulfate-resistant cements and mineral admixtures. *Constr. Build. Mater.* **2014**, *70*, 483–493. [CrossRef]
40. Pavlík, Z.; Fořt, J.; Pavlíková, M.; Kulovaná, T.; Černý, R. Characterization of Cement Pastes Containing Natural Zeolite as a Pozzolanic Admixture. *Appl. Mech. Mater.* **2015**, *719*, 206–209. [CrossRef]
41. de La Cruz, J.C.; del Campo, J.M.; Colorado, D. Comparative study on porosity and permeability of conventional concrete and concrete with variable proportions of natural zeolite additions. *Rev. Constr.* **2015**, *14*, 72–78. [CrossRef]
42. Bilim, C. Properties of cement mortars containing clinoptilolite as a supplementary cementitious material. *Constr. Build. Mater.* **2011**, *25*, 3175–3180. [CrossRef]
43. Miller, S.A.; Horvath, A.; Ostertag, C.P. Greenhouse gas emissionsfrom concrete can be reducedbyusing mix proportions, geometricaspects, and age as designfactors. *Environ. Res. Lett.* **2015**, *10*, 114017–114028. [CrossRef]
44. Minano, I.; Benito, F.; Parra, C.; Hidalgo, P. Concrete Sustainable Light and of High Performance Sustainable. *Dev. Renov. Archit.* **2017**, 263–273. [CrossRef]
45. Liu, B.; Yang, T. Image analysis for detection of bugholeson concrete surface. *Constr. Build. Mater.* **2017**, *137*, 432–440. [CrossRef]
46. *LST EN 197-1:2011*; Cement—Part 1: Composition, Specifications and Conformity Criteria for Common Cements. Lithuanian Standards Board: Vilnius, Lithuania, 2011.
47. *LST EN 12620:2003+A1:2008*; Aggregates for Concrete. Lithuanian Standards Board: Vilnius, Lithuania, 2003.
48. *LST EN 1008:2003*; Mixing Water for Concrete—Specification for Sampling, Testing and Assessing the Suitability of Water, Including Water Recovered from Processes in the Concrete Industry, as Mixing Water for Concrete. Lithuanian Standards Board: Vilnius, Lithuania, 2003.

49. *LST EN 196-1:2016*; Methods of Testing Cement—Part 1: Determination of Strength. Lithuanian Standards Board: Vilnius, Lithuania, 2016.
50. *LST EN 196-6:2010*; Methods of Testing Cement—Part 6: Determination of Fineness. Lithuanian Standards Board: Vilnius, Lithuania, 2010.
51. *LST EN 12350-7:2009*; Testing Fresh Concrete—Part 7: Air Content—Pressure Methods. Lithuanian Standards Board: Vilnius, Lithuania, 2009.
52. *LST EN 12350-2:2009*; Testing Fresh Concrete—Part 2: Slump-Test. Lithuanian Standards Board: Vilnius, Lithuania, 2009.
53. *LST EN 12390-3:2019*; Testing Hardened Concrete—Part 3: Compressive Strength of Test Specimens. Lithuanian Standards Board: Vilnius, Lithuania, 2019.
54. *LST EN 12390-3:2019*; Testing Hardened Concrete—Part 4: Compressive Strength—Specification for Testing Machines. Lithuanian Standards Board: Vilnius, Lithuania, 2019.
55. *LST EN 1015-10:2002*; Methods of Test for Mortar for Masonry. Part 10: Determination of Dry Bulk Density of Hardened Mortar. Lithuanian Standards Board: Vilnius, Lithuania, 2002.
56. *LST EN 13369:2018*; Common Rules for Precast Concrete Products. Lithuanian Standards Board: Vilnius, Lithuania, 2018.
57. Nagrockiene, D.; Daugela, A. Investigation into the properties of concrete modified with biomass combustion fly ash. *Constr. Build. Mater.* **2018**, *174*, 369–375. [CrossRef]
58. Xu, W.; Chen, J.J.; Wei, J.; Zhang, B.; Yuan, X.; Xu, P.; Yu, Q.; Ren, J. Evaluation of inherent factors on flowability, cohesiveness and strength of cementitious mortar in presence of zeolite powder. *Constr. Build. Mater.* **2019**, *214*, 61–73. [CrossRef]
59. Mehta, P.K. *Natural Pozzolans: Supplementary Cementing Materials in Concrete*; CANMET Special Publication: Athens, Greece, 1987; pp. 1–33.
60. Tokushige, H.; Kamehima, H.; Kawakami, M.; Bier, T.A. Effect of use of natural zeolite as a mineral admixture and an aggregate on physical properties of cement mortar and porous concrete. In Proceedings of the 4th International Conference on Construction Materials: Performance, Innovations and Structural Implications, Nagoya, Japan, 24–26 August 2009; pp. 1231–1236.
61. Ramezanianpour, A.A.; Mousavi, R.; Kalhori, M.; Sobhani, J.; Najimi, M. Micro and macro level properties of natural zeolite contained concretes. *Constr. Build. Mater.* **2015**, *101*, 347–358. [CrossRef]
62. Poon, C.S.; Lam, L.; Kou, S.C.; Lin, Z.S. A study on the hydration rate of natural zeolite blended cement pastes. *Constr. Build. Mater.* **1999**, *13*, 427–432. [CrossRef]
63. Koťátková, J.; Reiterman, P. Long-term properties of special concrete with natural additive. *Sustain. Constr. Mater. Technol.* **2016**, *1*, 317–324.
64. Perraki, T.; Kontori, E.; Tsivilis, S.; Kakali, G. The effect of zeolite on the properties and hydration of blended cements. *Cem. Concr. Compos.* **2010**, *32*, 128–133. [CrossRef]
65. Feng, N.; Yang, H.; Zu, L.-H. The strength effect of mineral admixture on cement concrete. *Cem. Concr. Res.* **1988**, *18*, 464–472.
66. Shekarchi, M.; Libre, N.A.; Ahmadi, B.; Sabet, F.S. An Investigation on the effect of natural zeolite on rheology and stability of self-consolidating mortar. In Proceedings of the 6th International RILEM Symposium Self-Compacting Concrete, Montreal, QC, Canada, 26–29 September 2010; pp. 503–513.
67. Samimi, K.; Kamali-Bernard, S.; Maghsoudi, A.A.; Lgcgm, S.K.B.; Civil, E. Resistance to chloride penetration of high strength self-compacting concretes: Pumice and zeolite effect. *Int. J. Civ. Environ. Eng.* **2018**, *3*, 250–259.
68. Chan, S.Y.; Ji, X. Comparative study of the initial surface absorption and chloride diffusion of high performance zeolite, silica fume and PFA concretes. *Cem. Concr. Compos.* **1999**, *21*, 293–300. [CrossRef]
69. Jana, D. A new look to an old pozzolan, clinoptilolite–a promising pozzolan in concrete. In Proceedings of the Twenty-ninth Conference on Cement Microscopy, Quebec City, PQ, Canada, 20–24 May 2007; pp. 168–206.
70. Feng, N.; Feng, X.; Hao, T.; Xing, F. Effect of ultrafine mineral powder on the charge passed of the concrete. *Cem. Concr. Res.* **2002**, *32*, 623–627. [CrossRef]
71. Bentz, D.P.; Jensen, O.M. Mitigation strategies for autogenous shrinkage cracking. *Cem. Concr. Compos.* **2004**, *26*, 677–685. [CrossRef]
72. Lura, P.; Jensen, O.M.; Igarashi, S.I. Experimental observation of internal water curing of concrete. *Mater. Struct.* **2007**, *40*, 211–220. [CrossRef]
73. Lee, H.; Hanif, A.; Usman, M.; Sim, J.; Oh, H. Performance evaluation of concrete incorporating glass powder and glass sludge wastes as supplementary cementing material. *J. Clean. Prod.* **2018**, *170*, 683–693. [CrossRef]
74. Najimi, M.; Sobhani, J.; Ahmadi, B.; Shekarchi, M. An experimental study on durability properties of concrete containing zeolite as a highly reactive natural pozzolan. *Constr. Build. Mater.* **2012**, *35*, 1023–1033. [CrossRef]
75. Ackley, M. Application of natural zeolites in the purification and separation of gases. *Microporous Mesoporous Mater.* **2003**, *61*, 25–42. [CrossRef]
76. Markiv, T.; Sobol, K.; Franus, M.; Franus, W. Mechanical and durability properties of concretes incorporating natural zeolite. *Arch. Civ. Mech. Eng.* **2016**, *16*, 554–562. [CrossRef]

77. Milovic, T.; Šupic, S.; Malešev, M.; Radonjanin, V. The Effects of Natural Zeolite as Fly Ash Alternative on Frost Resistance and Shrinkage of Blended Cement Mortars. *Sustainability* **2022**, *14*, 2736. [CrossRef]
78. Kwasny, J.; Sonebi, M.; Amziane, S.; Plasse, J. Effect of mix composition on rheology and surface finish of cementbased mortars. *Constr. Build. Mater.* **2015**, *89*, 102–109. [CrossRef]
79. Hilal, A.A.; Thom, N.H.; Dawson, A.R. On entrained pore size distribution of foamed concrete. *Constr. Build. Mater.* **2015**, *75*, 227–233. [CrossRef]
80. Harding, M.A. Vibrating Concrete in Wall Forms. *Concr. Constr.* **1995**, *40*, 180–184.
81. Samuelsson, P. Voids in Concrete Surfaces. *ACI J.* **1970**, *67*, 868–874.
82. Han, L.H.; Yao, G.H. Influence of concrete compaction on the strength of concrete-filled steel RHS columns. *J. Constr. Steel Res.* **2003**, *59*, 751–767. [CrossRef]
83. Tastani, S.P.; Balafas, I.; Dervisis, A.; Pantazopoulou, S.J. Effect of core compaction on deformation capacity of FRP-jacketed concrete columns. *Constr. Build. Mater.* **2013**, *47*, 1078–1092. [CrossRef]

Disclaimer/Publisher's Note: The statements, opinions and data contained in all publications are solely those of the individual author(s) and contributor(s) and not of MDPI and/or the editor(s). MDPI and/or the editor(s) disclaim responsibility for any injury to people or property resulting from any ideas, methods, instructions or products referred to in the content.

buildings

MDPI

Article

Interfacial Shrinkage Properties and Mechanism Analysis of Light-Conductive Resin–Cement-Based Materials

Shengtian Zhai [1], Ran Hai [2,*], Zhihang Yu [1], Jianjun Ma [1], Chao Hou [1], Jiufu Zhang [3], Shaohua Du [1] and Xingang Wang [4]

[1] School of Civil Engineering and Architecture, Henan University of Science and Technology, Luoyang 471003, China; zstlab@163.com (S.Z.); 230320241354@haust.edu.cn (Z.Y.); majianjun@haust.edu.cn (J.M.); 9906454@haust.edu.cn (C.H.); 9906496@haust.edu.cn (S.D.)
[2] School of Materials Science and Engineering, Henan University of Science and Technology, Luoyang 471000, China
[3] School of Civil Engineering, Lanzhou University of Technology, Lanzhou 730050, China; 9096243@lut.edu.cn
[4] School of Engineering and Construction, Nanchang University, Nanchang 330031, China; wangxingang@ncu.edu.cn
* Correspondence: 9906622@haust.edu.cn

Abstract: To address the issue of interfacial shrinkage deformation in optical resin–cement-based composites, this study examined the effects of casting methods and coupling agent treatments on the interfacial deformation behavior and underlying mechanisms at the resin–cement interface. A self-developed interfacial shrinkage testing apparatus, combined with ABAQUS numerical simulations, was employed to facilitate this analysis. The results revealed that the interfacial shrinkage strain followed a characteristic distribution—higher at both ends and lower in the middle region—as the temperature increased. The experimental data showed a strong agreement with the simulation outcomes. A comparative analysis indicated that the pre-cast cement method reduced the interfacial shrinkage strain by 16% compared to the pre-cast resin method. Furthermore, treatment with a coupling agent resulted in a 31% reduction in the strain, while combining a serrated surface modification with a coupling agent treatment achieved a maximum reduction of 43.5%. Microscopic characterization confirmed that the synergy between the coupling agent and surface roughening significantly enhanced interfacial bonding by filling microcracks, improving adhesion, and increasing mechanical interlocking. This synergistic effect effectively suppressed the relative slippage caused by asynchronous shrinkage between dissimilar materials, thereby mitigating the interfacial cracking issue in optical resin–cement-based composites. These findings provide theoretical insights for optimizing the interface design in organic–inorganic composite systems.

Keywords: cement matrix; transparent resin; interfacial shrinkage; simulation analysis; matching control

1. Introduction

Driven by societal progress, global research on cement and cement-based materials has increasingly focused on the development and application of ecological and advanced cementitious systems. By emphasizing energy conservation, emission reduction, and environmental sustainability, the industry is transitioning into a sustainable development trajectory [1]. Translucent cement-based materials have emerged as advanced composites distinguished by their exceptional light-transmitting capabilities. By fully utilizing sunlight and other light sources, they significantly reduce building energy consumption

while enhancing indoor light distribution [2–4]. In 2003, Áron Löszonczi from Hungary pioneered translucent concrete by incorporating optical fibers into concrete mixtures [5]. This innovative material enables light transmission through the concrete matrix, thereby reducing the reliance on artificial lighting and lowering the energy demand [6–8]. However, the complexity of achieving uniform optical fiber distribution within the concrete matrix has posed significant technical challenges and increased production costs, limiting its broader application. In 2008, a breakthrough occurred when the Italian Cement Group introduced an alternative approach by using resin as the light-transmitting medium to prepare translucent concrete [9–11]. The shift toward resin-based translucent systems offers a promising pathway for enhancing the practical applicability of translucent concrete while retaining its energy-saving and eco-friendly benefits.

Wang [12–14] developed a resin-based translucent concrete with an enhanced light-transmitting performance and conducted comprehensive research on its mechanical properties, optical transmission characteristics, bonding behavior, and micro-mechanistic insights. This finding provided valuable contributions to understanding the fundamental properties of this material system. Guo [15] explored the use of TiO/epoxy resin composite materials in preparing cement mortar, demonstrating that increasing the TiO_2 content significantly improved the tensile strength. The SEM results showed that, after the addition of epoxy resin to the cement mortar, both the interfacial transition zone (ITZ) and the bond interface zone (BIZ) were denser, and the flexural toughness and bond strength both improved. This study highlights the potential of incorporating nanomaterials into cement-based systems for enhancing the mechanical performance. Shen [16] investigated the integration of methacrylic resin into concrete (RTCM) and evaluated its light transmittance and thermal conductivity using advanced measurement techniques, including the light-power method and flat-plate testing. These results confirmed that RTCM exhibits superior optical and thermal properties, making it a promising material for energy-efficient applications. Li [17] introduced a novel salt-resistant and super-absorbent resin (SRSAP) and evaluated its impact on concrete performance. They found that an appropriate addition of SRSAP could effectively mitigate late-stage shrinkage and cracking while improving the workability and durability. However, excessive incorporation might negatively influence strength development, suggesting the need for optimized dosage control. Zhou [18] applied polyurethane-acrylic resin through ultraviolet polymerization to the surface of slag concrete as an on-site coating. The compressive strength of the test blocks increased by 1.67 times, and the tensile strength increased by 1.8 times. The coating effectively inhibited the evaporation of moisture in the samples and provided a moist internal curing environment, thereby effectively alleviating the concrete shrinkage. Gong [19] reduced the drying shrinkage rate of the epoxy resin and enhanced its permeability by blending it with foam concrete. SEM images revealed that a micro-grid structure was formed within the foam concrete, with an increase in the number of internal pores, a more uniform distribution, and a reduction in the average pore diameter. Currently, research on translucent concrete primarily focuses on its preparation process [20], optical properties [21], mechanical behavior, and long-term durability [22–24]. Despite these advancements, challenges remain during the curing of resin-based and translucent-cement-based materials. Interface shrinkage deformation is likely to occur, leading to a reduction in the interfacial bonding strength and an increased susceptibility to stress-induced deformation, cracking, and failure at the interface between the cement matrix and the resin [25–27]. Addressing these issues is critical for advancing the practical application of translucent concrete systems.

To address the issue of a weak bonding force between the cement matrix and the resin, Xu [28] developed translucent concrete using basic magnesium sulfate cement. This approach significantly reduced the porosity at the interface between the cement matrix

and the resin. The interfacial pull-out strength at 28 days increased by 59.2%. The SEM results showed that there were almost no cracks between the substrate and the resin, and their widths were generally quite narrow compared to that of translucent concrete prepared with ordinary cement, demonstrating a substantial improvement in the interfacial performance. Coupling agents, composed of inorganic-philic and organic-philic groups, are widely recognized for their ability to enhance the bonding strength between organic and inorganic materials [29–31]. Scholars [32–34] have explored the modification of epoxy resins with silane coupling agents to improve the interfacial bonding strength in composite systems. Peng [35] and Xiao [36] focused on the modification of asphalt concrete aggregates and the interaction forces at the interface. Through Fourier transform infrared (FTIR) and scanning electron microscopy (SEM), the interfacial interactions between the coupling agent and the aggregates were investigated, confirming the role of the coupling agent in enhancing the interface bonding strength. Guo [37] investigated the influence of fire-resistant temperatures of different epoxy resin adhesives on the bonding performance at the resin–concrete interface. The results showed that, at 200 °C, the cracking load, bonding strength, and fracture properties of the interface were all superior to those observed at room temperature. Zhang [38] synthesized an organic-modified bentonite-based polymer composite material by combining water-based epoxy resin with a silane coupling agent. A microscopic analysis showed that the pores of the epoxy resin in the polymer matrix were filled, forming a dense structure. Hydrogen bonds formed between each material and water. Mo [39] synthesized a composite material using a silane coupling agent and water-based epoxy resin for a magnesium–aluminum–silicate-based geopolymer. The chemical shrinkage, self-shrinkage, and drying shrinkage of this material were reduced by 46.4%, 131.2%, and 25.2%, respectively. The addition of organic modifiers made the microstructure more dense and enabled it to resist shrinkage during the hardening and continuous reaction process of the geopolymer. The aforementioned research primarily focused on strategies to enhance the interfacial bonding strength in resin-based and translucent-cement-based materials. However, due to variations in material properties and environmental factors such as temperature and pressure, the interfacial bonding zone remains a critical weak link prone to shrinkage deformation and cracking [40,41]. Currently, there is limited research on test methods for the interfacial shrinkage strain of the cement matrix–transparent resin system. Systematic studies on the laws of interfacial shrinkage deformation at different temperatures are particularly scarce in the existing literature.

In this study, a custom-developed monitoring system was utilized to investigate the interfacial shrinkage deformation of organic–inorganic composite systems. This system enables the real-time detection of micro-scale strain fluctuations through integrated strain gauges. To complement the experimental observations, finite element simulations were conducted to model the shrinkage behavior of the composites. A detailed comparison between the experimental and simulated results provided valuable insights into the mechanisms governing interfacial shrinkage in resin-based light-transmitting cementitious materials. Moreover, environmental scanning electron microscopy (ESEM) was employed to perform a microstructural analysis, thereby elucidating the effects of casting strategies and coupling agent modifications on the shrinkage behavior at the interface between the cementitious matrix and transparent resin. Based on these findings, a systematic strategy for interfacial compatibility enhancement was proposed, offering practical guidance for improving the overall performance of composite materials.

2. Materials and Research Methods

2.1. Materials

Cement: The "Yangfang" brand P●O 42.5 ordinary silicate cement used is produced by Yadean Cement Co., Ltd. in Jiangxi Province, China. Aggregate: Ganjiang River sand with a fineness modulus of 2.5, a particle size ranging from 0.30 mm to 1.18 mm, and a reasonable gradation was selected. The water reducer used was the high-performance polycarboxylate-based water reducer produced by Nanchang Anrui Building Materials (the water reduction rate was ≥25%, and the solid content was 20%).

The cement matrix was prepared by mixing cement, aggregate, high-performance water reducer, and water. The mass ratio was as follows: 500.0 g of cement, 500.0 g of sand, 2.0 g of high-performance water reducer, and 175.0 g of water.

Transparent resin: The resin used is a type of polyesters with unsaturated groups produced by Jiangsu Nantong Mingkang Composite Materials Co., Ltd. (a colorless transparent liquid). The glass transition temperature (T g) typically ranges from 70 °C to 90 °C. The technical parameters are shown in Table 1.

Table 1. Technical parameters of ortho-phenylenic unsaturated polyester resin.

Viscosity	**0.3~0.5 Pa.s**	**Setting Time**	**8~16 min**
Solid content	59~67%	Bending strength	112 MPa
Tensile strength	65 MPa	Elongation at break	3.7%

Coupling agent: The coupling agent used is silane coupling agent A-151, which is vinyl triethoxy silane produced by Huai'an Huarun Chemical Co., Ltd., China. Its chemical structural formula is CH_2=CHSi($OC_2H5)_3$, with a molecular weight of 191, a content of ≥98%, a relative density of 0.904–0.918 g/cm^3, a refractive index of 1.396–1.400, and a boiling point of 160 °C. It functions as both a coupling agent and a cross-linking agent.

2.2. Sample Preparation

The experimental procedures for preparing the organic–inorganic composite specimens involved three distinct methods: casting the matrix first, casting the resin first, and performing the coupling agent treatment. The fabrication process was conducted using a steel mold with dimensions of 40 mm × 40 mm × 160 mm.

The experimental preparation of the organic–inorganic composite specimens involved three distinct approaches: pre-casting the cementitious matrix, pre-casting the resin phase, and applying the coupling agent surface modification. Specimen fabrication was performed using a steel mold with standardized dimensions of 40 mm × 40 mm × 160 mm.

2.2.1. Pre-Casting of the Cementitious Matrix

First, the cement mortar was poured into the mold and allowed to cure at room temperature for 24 h. After demolding, the surface of the cement mortar was mechanically roughened and polished to enhance interfacial bonding. The surface preparation involved a three-step sanding process: initial pre-treatment using 300-mesh sandpaper, followed by intermediate polishing with 600-mesh sandpaper, and finally, finishing with 1200-mesh sandpaper. The specimen was then repositioned in the mold, and the transparent resin was cast onto the prepared surface. After an additional 24 h curing period at room temperature, the mold was removed again. Finally, the interfacial region underwent post-curing polishing to improve the bonding strength, followed by shrinkage testing.

2.2.2. Pre-Casting of the Resin

The resin was first cast into a mold of the same dimensions (40 mm × 40 mm × 160 mm). After curing at room temperature for 24 h, the mold was removed. The surface of the resin was roughened to enhance interfacial adhesion, and the specimen was then placed back into the mold for cement mortar casting. Following another 24 h room-temperature curing period, the mold was removed again. Finally, after interfacial surface roughening, the test was conducted.

2.2.3. Coupling Agent Treatment

Using the matrix-first casting method, a 40 mm × 40 mm × 160 mm steel mold was employed. The cement mortar was cast initially, and after curing at room temperature for 24 h, the mold was removed. The surface of the cement mortar was mechanically roughened to enhance its interfacial properties. Subsequently, the matrix was immersed in a silane coupling agent solution for 10 s, then air-dried at room temperature for 24 h and repositioned in the mold. Resin was poured over the treated matrix, and after curing for 12 h, the mold was removed. The specimen was then subjected to an additional 12 h curing period prior to testing.

Preparation of the A-151 silane coupling agent solution: A total of 1 g of the coupling agent was added to 20 g of a mixed solution of anhydrous ethanol and deionized water at a mass ratio of 9:1. Acetic acid was then added to adjust the pH to 4.5 (pH meter model by Lifen Technology, measurement range: 0.1–14 pH, resolution: 0.1 pH, accuracy: ±0.1 pH, working temperature: 0–50 °C). The mixture was stirred thoroughly for 10–15 min, and then an additional 100 g of the same ethanol–water mixture was added and the solution was mixed evenly to obtain a 1 wt% silane coupling agent solution.

2.2.4. Coupling Agent–Sawtooth Interface Collaborative Treatment

The serrated interface was fabricated by initially casting a silicone rubber/curing agent mixture (100:5 ratio) into a customized steel mold to form a serrated imprint template, which was cured at room temperature for 24 h. The cured template was then positioned at the base of a detachable steel mold (40 mm × 40 mm × 160 mm). Cement mortar was poured into the mold and cured for an additional 24 h to form the substrate. Subsequently, 45° uniformly spaced grooves were scribed on the serrated interface using a carving tool, followed by spray-coating with a silane coupling agent A-151 solution. Finally, transparent resin was cast into the mold and demolded after 8 h for testing.

2.2.5. Strain Monitoring

To continuously monitor the interface contraction strain, a DH3815 type static strain gauge produced by Jiangsu Donghua Testing Technology Co., Ltd. of China was adopted. In this study, high-temperature foil-type resistance strain gauges produced by China Star Oriental Co., Ltd. (model BA120-3AA and BA120-5AA) were adopted. These strain gauges feature inherent temperature compensation and a fully sealed structure with a glass-fiber-reinforced substrate. Within the operating temperature range of −30 °C to +200 °C, they exhibit a thermal drift of less than 0.15 με/°C. At 60 °C, the zero-drift error remains below 5 με—approximately one-twentieth of that observed in conventional strain gauges. Strain variations were tracked over a period of 10 consecutive days to capture the evolution of interfacial deformation behavior during the curing and hardening processes.

2.3. Test Equipment and Methods

In this paper, an online monitoring device and method were employed to measure the interfacial shrinkage of organic–inorganic composite materials. The strain measurement apparatus is shown in Figure 1.

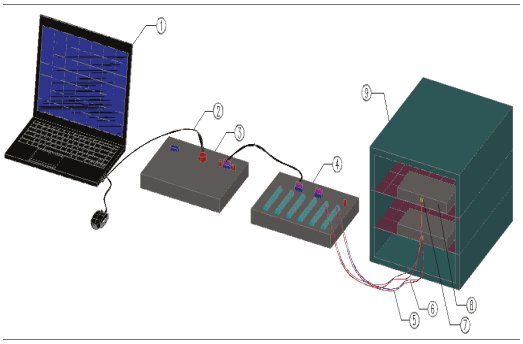

(**a**) Diagram of the strain-testing device.

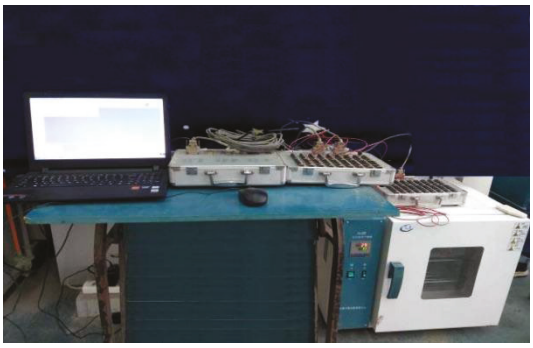

(**b**) Actual photo of the strain-testing device.

Figure 1. Online monitoring device for interface shrinkage of organic–inorganic composite materials. Note: 1—computer, 2—connecting cable, 3—controller, 4—acquisition box, 5 and 6—acquisition cables, 7—strain gauge, 8—test specimen, 9—drying oven.

The device is composed of five main components: the test specimen, the drying oven, the acquisition box, the controller, and the computer. The deformation strain of the specimen is transmitted to the acquisition box through a strain gauge, then passed to the controller, and finally input into the computer via a connecting cable between the controller and the computer. The strain data are ultimately output by the testing software on the computer, and the required values are obtained after correction. This apparatus incorporates a full-bridge temperature compensation technique. Within the Wheatstone bridge configuration, active strain gauges and temperature-compensating dummy gauges are strategically positioned. When measuring mortar specimens, the dummy gauges are bonded to separate compensation blocks fabricated from identical material with matching thermal properties. Strain gauges are symmetrically attached to the test specimen. A schematic diagram of the symmetric layout is shown in Figure 2.

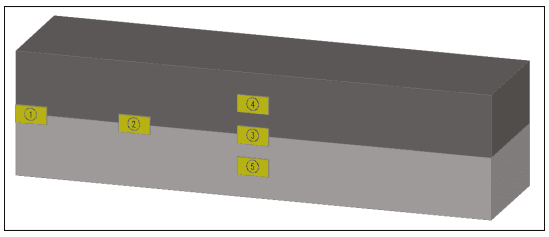

(**a**) Schematic diagram of the strain gauge layout.

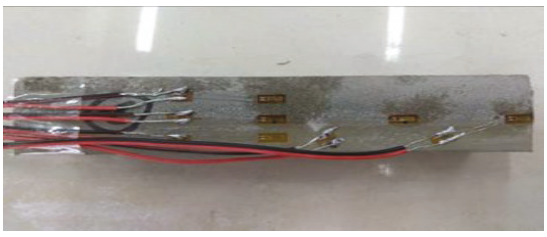

(**b**) Actual photo of the specimen.

Figure 2. Test specimens and test point distribution. Note: ①, ②, ③, ④, and ⑤ represent measuring points 1, 2, 3, 4, and 5, respectively (measuring points 1, 2, 3, 4, and 5 are located at the interface endpoints of the specimen, at the 1/4 position, at the midpoint, in the cement matrix, and in the transparent resin, respectively).

In this experiment, all the specimens used the same strain gauge attachment method, and the actual photo is provided for illustrative purposes only. During testing, a representative specimen was selected from three samples for each experimental method. The testing cycle lasted for 10 days. Since the shrinkage process of cement mortar is relatively slow, to accelerate the experiment, the specimens were placed in a drying oven at 30 °C for 7 days after demolding and strain gauge installation. Strain data were recorded every hour.

On the eighth day, the temperature was raised to 40 °C, on the ninth day to 50 °C, and on the tenth day to 60 °C. In total, 14 days were required from the beginning of casting to the completion of testing.

3. Results and Discussion

3.1. Comparison of Matrix-First and Resin-First Casting Methods

Figure 3a,b show schematic diagrams of the force analysis for the matrix-first and resin-first casting methods, respectively. When analyzing diagram (a), $f_1(t)$ represents the force acting on the cement mortar, while $f_2(t)$ denotes the force acting on the transparent resin. The cement mortar underwent shrinkage during curing at room temperature. Once the transparent resin was poured, it began to shrink significantly. At this point, the force $f_1(t)$ on the cement mortar in the interfacial bonding zone was tensile, while the force $f_2(t)$ on the transparent resin in the bonding zone was compressive.

$$F_1(t) = -f_2(t) = -f(t), \tag{1}$$



(**a**) Matrix-first casting method. (**b**) Resin-first casting method.

Figure 3. Force analysis of matrix-first and resin-first casting methods.

When analyzing diagram (b), the transparent resin was poured first and cured for 24 h, followed by the casting of cement mortar. By this time, the transparent resin had already solidified, and most of its shrinkage had been completed. Upon pouring the cement mortar, the force $f_3(t)$ on the cement mortar in the interfacial bonding zone was tensile, while the force $f_4(t)$ on the transparent resin in the bonding zone was compressive.

$$F_3(t) = -f_4(t) = -f'(t), \tag{2}$$

Figure 4a,b present the strain evolution curves at the interface-monitoring points for the matrix-first and resin-first casting methods, respectively. By comparing the two methods, it is evident that the strain evolution patterns at measuring points 1, 2, 3, 4 (cement matrix region), and 5 (transparent resin region) exhibited notable similarities and a strong correlation with temperature variations [42]. In the early stage of the experiment, the strain curves of the cement matrix points (1–4) displayed a sharp initial decline, followed by gradual stabilization. When the temperature increased abruptly, the strains at all the monitoring points rose significantly before dropping again. The behavior at measuring point 5 was markedly different from that in the matrix region: the strain remained near zero in the initial stage, then increased rapidly (positive strain) as the temperature rose, and although it slightly decreased afterward, it still exhibited a sharp increase with subsequent temperature elevations. Judging from the final shrinkage strain values, the matrix-first casting method showed a better shrinkage suppression effect. The final shrinkage strain values of measuring points 1, 2, and 3 under the two methods were -927 $\mu\varepsilon$ and -1080 $\mu\varepsilon$, -781 $\mu\varepsilon$ and -890 $\mu\varepsilon$, and -590 $\mu\varepsilon$ and -707 $\mu\varepsilon$, respectively. The corresponding shrinkage strain values were reduced by 14%, 12%, and 16%, respectively. Measuring point 4 (in the matrix area) had the fastest shrinkage rate and the largest final strain value, while the values of measuring points 1, 2, and 3 decreased successively. The shrinkage rate and the final strain in the middle area of the interface were the lowest.

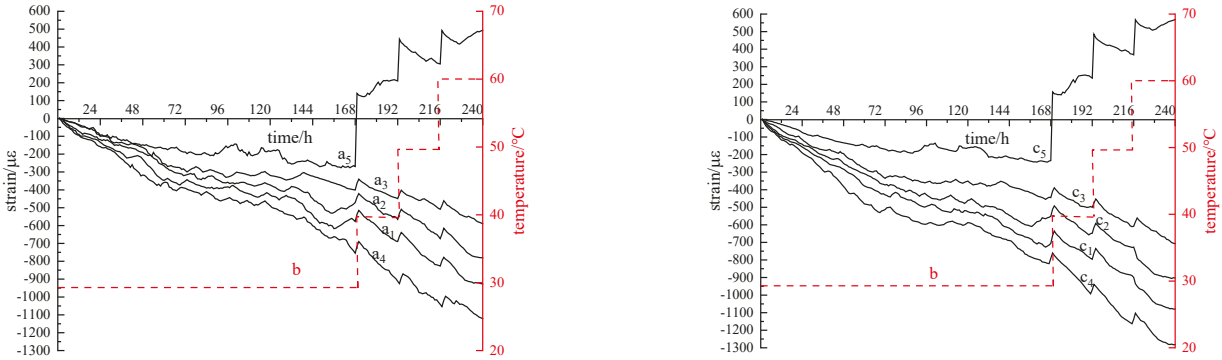

(**a**) Matrix-first casting method. (**b**) Resin-first casting method.

Figure 4. Strain curves at each measurement point for the matrix-first and resin-first casting method.

From this analysis, it can be inferred that, possibly due to the large performance differences between the organic resin and inorganic cement matrix, the deformation of the transparent resin during curing intensified the shrinkage strain at point 1. In contrast, in the middle region of the interface, mutual constraint between the materials effectively delayed shrinkage [43,44]. The superior shrinkage suppression observed in the matrix-first method may be attributed to its facilitation of a denser resin–matrix interfacial structure, thereby enhancing the cooperative deformation behavior of the materials [45].

3.2. Results of Coupling Agent Treatment

Figure 5a,b illustrate schematic diagrams of the interfacial force analysis for the group without the coupling agent treatment and the group with the coupling agent treatment, respectively. Based on the force analysis, the experimental results, and the analysis of the interface bonding situation in the previous section, the specimens prepared using the matrix-first method without the coupling agent treatment were designated as the control group. The interface bonding zone in the group treated with the coupling agent appeared darker in color, indicating that the interface became denser after treatment. At this stage, the force $f_5(t)$ acting on the cement mortar and transparent resin in the interfacial bonding zone was tensile, while the force $f_6(t)$ was compressive.

$$F_5(t) = -f_6(t) = -f'(t), \tag{3}$$



(**a**) Control group. (**b**) Coupling agent treatment group.

Figure 5. Schematic diagram of the interfacial force analysis for the control group and the coupling agent treatment group.

Figure 6a,b show the strain evolution curves at the interface-monitoring points for the control group and the coupling agent treatment group, respectively. As shown in Figure 6, the development of the strain curves at measuring points 1–4 (cement matrix region) in both groups followed a similar pattern: a sharp decline in the strain rate during the initial stage, followed by a gradual stabilization phase. When the temperature changed abruptly, an instantaneous strain spike occurred, characterized by a rapid increase followed by a quick decline. Measuring point 5 (transparent resin part) shrunk slowly at the beginning of the experiment and showed an expansion trend as the temperature rose. The final shrinkage strain values of measuring points 1, 2, and 3 in the control group and the coupling agent

treatment group were −741 $\mu\varepsilon$ and −596 $\mu\varepsilon$, −631 $\mu\varepsilon$ and −480 $\mu\varepsilon$, and −522 $\mu\varepsilon$ and −359 $\mu\varepsilon$, respectively. Compared to the control group, the final shrinkage strain values at measuring points 1, 2, and 3 in the coupling agent treatment group were reduced by 19%, 23%, and 31%, respectively. When the temperature remained constant, measuring point 4 (cement matrix part) had the fastest development rate of shrinkage strain and the largest shrinkage strain value. Measuring points 1, 2, and 3 decreased successively with a change in the interface position. The shrinkage behavior at the interface was closely related to both the temperature and the spatial position.

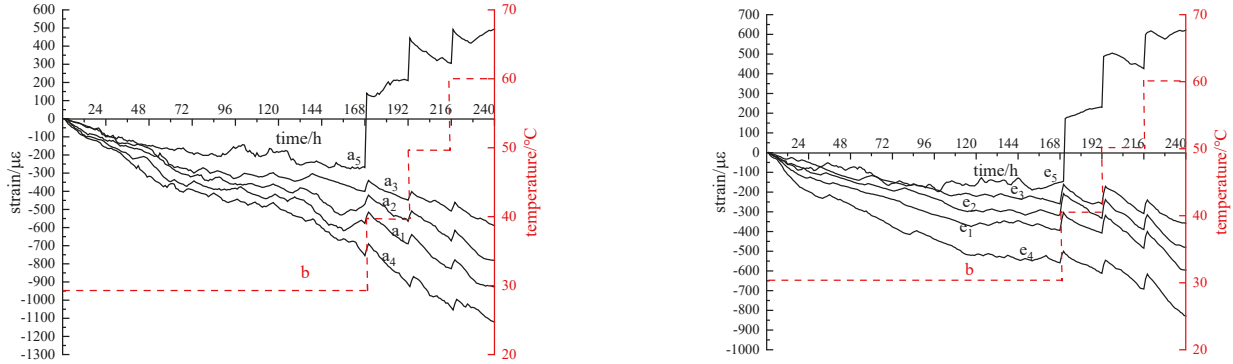

(**a**) Control group. (**b**) Coupling agent treatment group.

Figure 6. Strain evolution curves at interface-monitoring points for the control group and the coupling agent treatment group.

From the above analysis, it can be observed that, for the resin–cement matrix interface treated with a coupling agent, due to the pronounced material property differences between the resin and the cement matrix, the shrinkage rate and strain in the central region of the interface remained higher than those at the edges. Nevertheless, the shrinkage rate for the treated interface was slower than that of the control group, and the final shrinkage strain was also smaller. This may be attributed to the coupling agent enhancing the thickness and bonding strength of the interfacial zone, thereby improving the interfacial adhesion [46–49].

3.3. Results of Coupling Agent–Sawtooth Interface Collaborative Treatment

Figure 7a, b schematically illustrate the mechanical analysis of the untreated control group and the coupling-agent-treated serrated interface, respectively. This experimental group aimed to enhance interfacial bonding through the synergistic effects of a serrated surface morphology and coupling agent modification, while investigating interfacial shrinkage behavior, with the untreated control group serving as a reference for comparison. During the initial resin-pouring stage, $f_{11}(t)$ acted as a tensile force and $f_{12}(t)$ as a compressive force. These force directions reversed when the temperature increased following resin shrinkage.

$$F_{11}(t) = -f_{12}(t) = -f(t), \quad (4)$$



(**a**) Control group. (**b**) Coupling agent–sawtooth interface collaborative treatment.

Figure 7. Schematic diagram of the interfacial force analysis for the control group and the coupling agent–sawtooth interface collaborative treatment group.

Figure 8a illustrates that all the curves displayed an initial declining trend, though with varying contraction rates among the measurement points. Notably, point 4 showed

the fastest contraction rate, followed sequentially by points 1, 2, and 5, indicating spatially heterogeneous shrinkage during the early phase. From casting to 96 h (7-day age), rapid contraction occurred, while between 96 and 168 h (7–10 days), the strain trends stabilized across all points, with the contraction magnitudes ordered as point 4 > 1 > 2 > 3 > 5. At 168 h, a temperature increase of 40 °C triggered the first strain peak, followed by recurring peaks during subsequent thermal cycles.

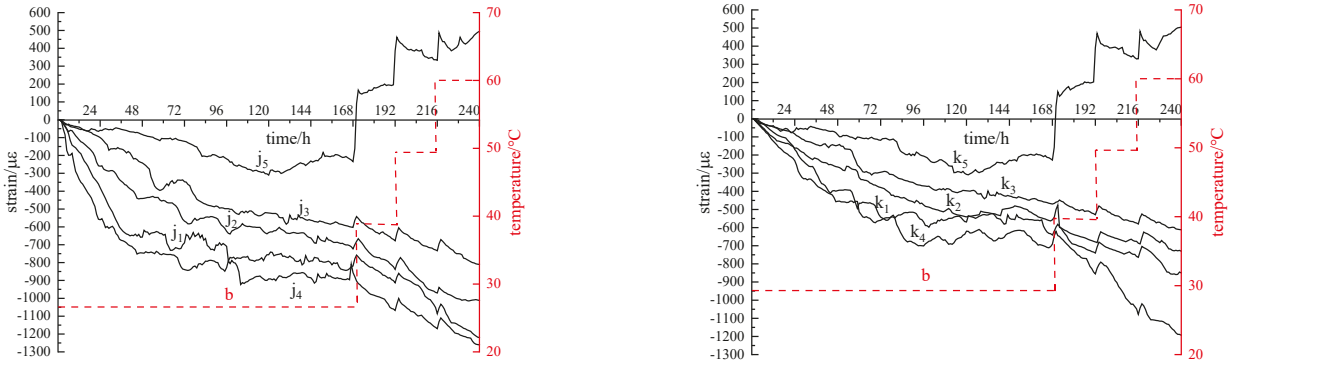

(**a**) Control group. (**b**) Coupling agent-sawtooth interface collaborative treatment.

Figure 8. Strain evolution curves at interface-monitoring points for the control group and the coupling agent-sawtooth interface collaborative treatment group.

Figure 8b presents the comparative strain curves between the control group (j) and the coupling agent-treated group (k) across five measurement points. For interfacial measurement points 1–3, all the curves exhibited a shared trend: an initial rapid decline (0–96 h) followed by temperature-dependent fluctuations. During the initial stage, the control groups exhibited significantly faster contraction rates than the treated groups (e.g., maximum contraction strains at point 1: $j_1 = -850$ $\mu\varepsilon$ and $k_1 = -680$ $\mu\varepsilon$), indicating that the coupling agent effectively mitigated early-stage contraction through interface modification. The 96–168 h phase under stable 30 °C conditions showed curve stabilization or a slight rebound, reflecting thermally induced micro-expansion. Subsequent temperature increments (40 °C, 50 °C, and 60 °C) each triggered distinct strain peaks, yet the treated groups demonstrated markedly lower strain amplification than the controls (e.g., post-third heating at point 1: $j_1 = -1220$ $\mu\varepsilon$ and $k_1 = -850$ $\mu\varepsilon$, a 30% reduction).

Meanwhile, at point 2, the control group's abrupt linear decline (j_2) likely stemmed from proximal cement matrix positioning, while the treated group's gradual contraction (k2) highlighted enhanced interfacial cohesion. Point 3 displayed spatially heterogeneous contraction, but maintained a 25% strain advantage for the treated group. The cement mortar (point 4) showed near-identical trends between the groups (final strains: $j_4 = -1223$ $\mu\varepsilon$, $k_4 = -1193$ $\mu\varepsilon$), confirming minimal coupling agent impact on bulk matrices. Resin (point 5) displayed post-curing shrinkage (initial strain: -300 $\mu\varepsilon$) followed by temperature-driven anomalous expansion (final strains: $j_5 = 495$ $\mu\varepsilon$, $k_5 = 505$ $\mu\varepsilon$). Collectively, these results demonstrate that the coupling agent treatment significantly optimized the interfacial performance, while thermal fluctuations, localized heating disparities, and measurement location variability were critical factors governing strain curve oscillations.

The analysis showed that all the measurement points initially experienced contraction strain, reflected by descending curves with varying rates. Interfacial points 1–3 followed a descending contraction sequence (point 1 > point 2 > point 3), while the cement mortar exhibited the greatest shrinkage and the transparent resin exhibited the least. Subsequent temperature variations induced strain peaks at all locations. Ultimately, the interfacial points showed reduced final shrinkage strains in the following order: point 1 > point 2 >

point 3. The transparent resin transitioned to an expanded state, producing positive strain values due to thermally induced anomalous expansion.

3.4. Establishment of the Interface Bonding Region Model

Based on the mechanical characteristics of the optical resin–cementitious interface, the following assumptions were adopted in the ABAQUS simulation: (1) Both the cement mortar and the transparent resin were modeled as homogeneous and isotropic materials. (2) Shrinkage along the height direction (perpendicular to the interface) was assumed to be uniform throughout the specimen, regardless of vertical position. (3) The transparent resin initially underwent gradual contraction, followed by thermal expansion upon temperature elevation. (4) After roughening the cementitious matrix interface prior to resin casting, perfect bonding between the materials was assumed under zero external load, and interfacial bond-slip behavior was neglected. These simplifications prioritize interfacial interaction mechanisms over secondary effects in this multi-physics coupling system.

An interface model was established using the equivalent temperature difference method, which is essentially based on the initial strain method and linear thermal expansion coefficients. Shrinkage was converted into an "equivalent temperature difference" [50], which was then applied as a field load to the resin–matrix interface to simulate interfacial shrinkage [51–53]. The elastic modulus of the cement matrix varied with curing age, and its values—determined through empirical formulas and experimental data—are presented in Table 2.

Table 2. Compressive stress, strength, and elastic modulus of cement-based materials at different ages.

Age	F (kN)	P (MPa)	E_c (GPa)
1d	197.96	39.60	20.91
2d	199.53	39.92	21.10
3d	212.34	42.48	22.18
4d	209.83	41.98	21.96
5d	222.73	44.56	23.09
6d	237.21	47.46	24.35
7d	240.76	51.41	26.04

In this section, two distinct components representing the cementitious matrix (designated as M1) and the transparent resin (designated as S1) were created, both discretized using eight-node linear brick elements with reduced integration (C3D8R). A three-dimensional finite element model was established via the direct solution method, incorporating material property definitions and mesh generation. The final model contained 70,700 elements, and Figure 9 illustrates the mesh configuration of the optical resin–cementitious material fabricated using the precast matrix method. This discretization strategy ensures computational efficiency while preserving the geometric accuracy at the resin–cement interface. Table 3 summarizes the material property parameters of both components:

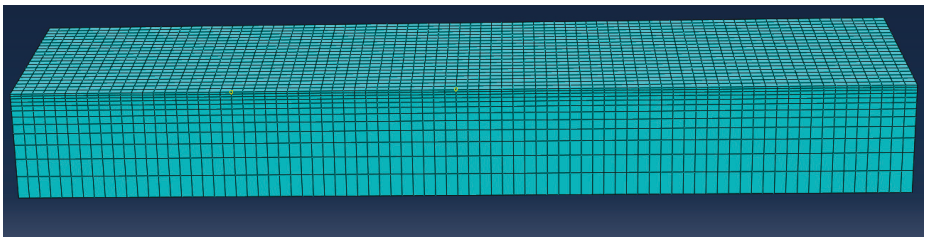

Figure 9. Common interface meshing.

Table 3. Material property parameters of unsaturated polyester resin and cement mortar.

	UPR	Cement Mortar
α_c	(130~150) $\times 10^{-6}/°C$	$12 \times 10^{-6}/°C$
γ	0.35	0.167
ρ	1.11–1.20 g/cm^3	2.07 g/cm^3
E_C	25–35 GPa	As shown in Table 1

For the interfacial system incorporating serrated geometry and coupling agent interactions, two discrete parts were modeled using C3D8R elements: M5 for the cement mortar and S5 for the transparent resin, with tie constraints applied at the interface. A three-dimensional finite element model was constructed using the direct solution method, integrating material property definitions and mesh-generation procedures. The final discretization produced 72,100 elements, as shown in Figure 10, which illustrates the mesh configuration of the optical resin–cementitious material featuring the serrated–coupling agent interfacial treatment. This modeling framework effectively captures interfacial coupling effects while ensuring numerical stability through targeted mesh refinement in critical regions.

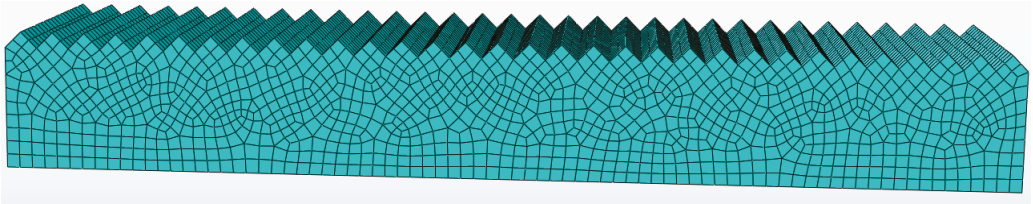

Figure 10. Interface meshing of coupling agent–sawtooth interface collaborative treatment.

3.5. Simulation Results of the Interface Bonding Zone Using the Matrix-First Pouring Method

The mechanical analysis and experimental results indicated that, compared with the resin-first pouring method, the matrix-first pouring method offers significant advantages in shrinkage control, reducing the final strain by 16%. Given that the strain evolution trends of transparent resin–cement-based composites are highly consistent under both processes, this study focused on the strain behavior at the interface midpoint in the matrix-first method for further analysis. Figure 11a,b respectively present the strain cloud diagram and the strain curve at the interface midpoint for the matrix-first pouring method.

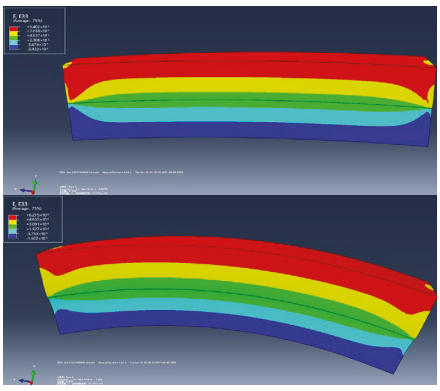

(**a**) Interface strain cloud diagram.

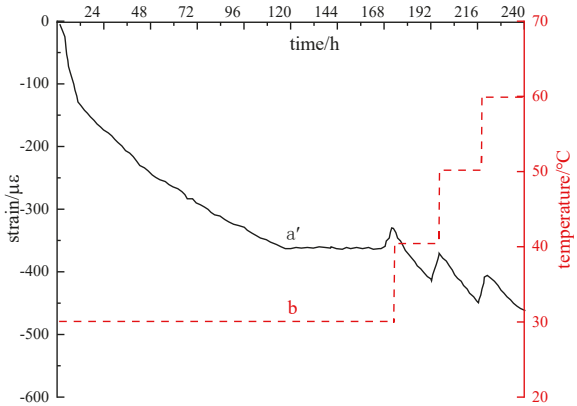

(**b**) Strain curve diagram of the midpoint of the interface.

Figure 11. Simulation result diagram of the interface using the matrix-first pouring method.

From the evolution of the cloud diagram in Figure 11a, it can be observed that, with the progression of the simulation time and dynamic temperature variation, the chromaticity distribution in different material regions evolved systematically. As shown in the upper-left corner of the diagram, the strain in the interfacial region and the cement matrix accumulated continuously, while the transparent resin transitioned from shrinkage (negative strain) to expansion (positive strain). Figure 11b reveals that the strain at the interface midpoint dropped sharply during the initial phase and then entered a stable development stage. When the temperature increased abruptly, a steep strain spike occurred. The overall simulation process was smooth, and the final strain value was -461 $\mu\varepsilon$.

3.6. Simulation Results of the Interface Bonding Zone Treated with the Coupling Agent

Figure 12a,b respectively present the interface strain cloud diagram and the strain curve diagram for the interface treated with the coupling agent. As shown in Figure 12a, with the extension of the simulation time and an increasing temperature, the chromatic regions in the cloud diagram changed significantly across different material zones. The shrinkage strain in the interface and cement matrix regions gradually increased, while the strain in the transparent resin region shifted from negative to positive. Figure 12b indicates that the strain curves at measurement points 1, 2, and 3 exhibited a rapid initial decline followed by a stabilization phase during the simulation.

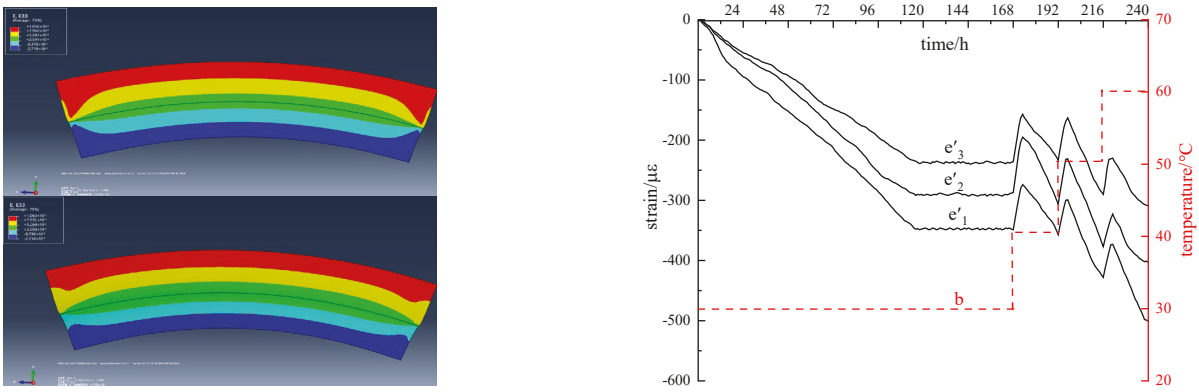

(**a**) Interface strain cloud diagram. (**b**) Interface strain curve diagram.

Figure 12. Simulation result diagram of the interface of the coupling agent treatment group.

At this time, the experimental results fluctuated greatly while the simulation results developed more stably, which may have been caused by the uneven heating of the blower in the box and instrument errors. With the sudden increase in temperature, the curve first rose sharply and then decreased. The simulation results were relatively smooth, which may have been affected by the pasting of the strain gauge or the fact that the experiment was located on the surface. The speed of the shrinkage strain at the middle position of the interface was the slowest, and the final shrinkage strain value was the smallest. The speed of the shrinkage strain at the end points was the fastest, and the final shrinkage strain value was the largest. The final shrinkage strain values of measuring points 1, 2, and 3 were -309 $\mu\varepsilon$, -403 $\mu\varepsilon$, and -501 $\mu\varepsilon$, respectively.

In conclusion, the general trends of shrinkage strain at various interface locations were consistent between the experimental and simulation results. However, due to uncontrollable factors in the experimental part, the experimental results fluctuated more, while the simulation results developed more stably. The experimental shrinkage strain values were slightly larger than the simulation results, and there was a certain deviation between the two. A comprehensive comparison of the experimental and simulation outcomes revealed that the coupling agent treatment effectively reduced both the shrinkage strain rates and

the final strain values at all the measured points. This demonstrates that the coupling agent enhanced the interfacial fusion between the cement matrix and the transparent resin, thereby improving the overall bonding strength.

3.7. Simulation Results of the Interface Bonding Zone Treated with the Coupling Agent–Sawtooth Interface Collaborative Treatment

Figure 13a displays the strain contour plots of the optical resin–cementitious material under the combined effects of a serrated interface geometry and the coupling agent treatment. Figure 13b presents the strain evolution curve extracted from the interfacial mid-region in the simulation.

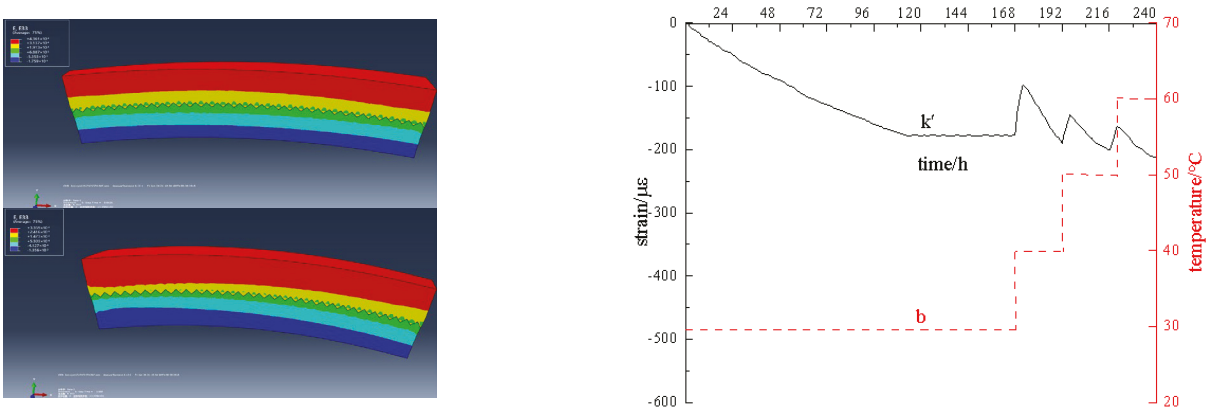

(**a**) Interface strain cloud diagram. (**b**) Interface strain curve diagram.

Figure 13. Simulation result diagram of the interface in the coupling agent–sawtooth interface collaborative treatment.

An analysis of Figure 13b revealed a progressive redistribution of strain, indicated by distinct color transitions in the contour plots and increasing legend values across the analysis steps, in correlation with advancing thermal loading. The strain curve in Figure 13b exhibits three distinct phases: an initial rapid contraction phase with steep strain reduction (0–96 h), followed by a stabilized development period (96–168 h) and subsequent strain surges coinciding with temperature increments at 40 °C, 50 °C, and 60 °C. Notably, three characteristic strain peaks occurred during these thermal transitions, and the coupling-enhanced interface ultimately reached a final strain value of -213 $\mu\varepsilon$. This evolution pattern quantitatively confirms the dual modulation mechanism—provided by the serrated geometry and the coupling agent treatment—in alleviating the interfacial strain concentrations under thermomechanical coupling conditions.

3.8. Mechanism Analysis and Matching Control

The optical resin–cement-based material, a composite system integrating organic resin and an inorganic cementitious matrix, exhibited inherent interfacial vulnerability due to mismatched thermomechanical properties between the constituent phases. This structural heterogeneity, when subjected to external mechanical stress and thermal fluctuations, tended to localize strain concentrations within the interfacial region, thereby promoting crack initiation and delamination [15]. As illustrated in Figure 14a,b, (a) and (b) respectively depict interfacial cracking behaviors induced by differential deformation under mechanical loading and thermal cycling. The observed fracture patterns were directly correlated with disparities in the mechanical and thermal properties of the constituent materials.



(**a**) (**b**)

Figure 14. Interfacial shrinkage deformation failure in light-conductive resin–cement-based materials. (**a**) Cracking of weak interfacial bond under compressive loading. (**b**) Shrinkage cracking induced by temperature variation.

Figure 15a,b display ESEM images (magnification: 10,000×) of the interface between the transparent resin and the cement matrix, with and without coupling agent treatment, respectively. A microscopic analysis of Figure 15a revealed the presence of fine cracks between the cement matrix and the transparent resin, likely resulting from defects introduced during sample preparation. This suggests that the interfacial bonding strength between the cement matrix and the transparent resin is insufficient, and cracking failure is likely to occur under external forces. The boundary between the cement matrix and the transparent resin was extremely distinct, and the two materials could be clearly distinguished. Moreover, the two substances were merely in simple contact without any signs of mutual fusion, and defects were likely to form at the interface between the cement matrix and the transparent resin.

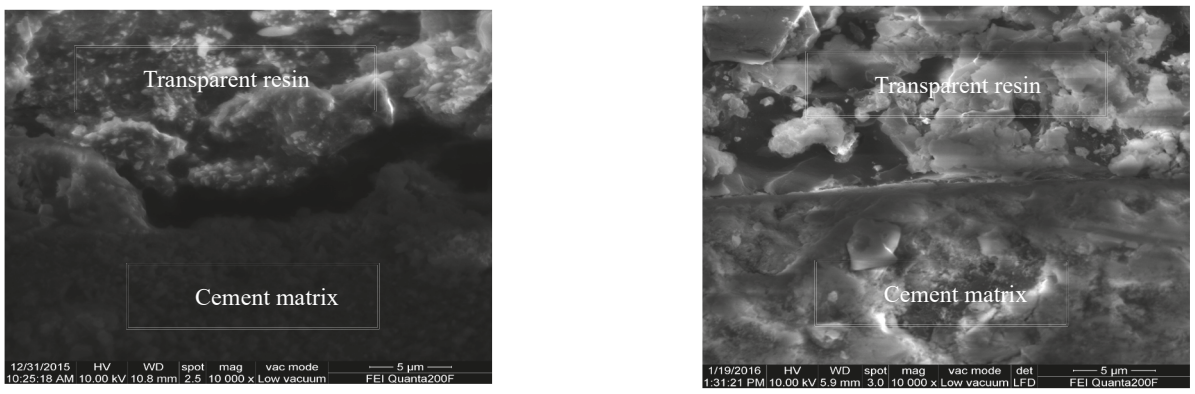

(**a**) (**b**)

Figure 15. Simulation result diagram of the interface in the coupling agent–sawtooth interface collaborative treatment. (**a**) Interfacial region between transparent resin and cement matrix. (**b**) Interfacial region between transparent resin and cement matrix subjected to collaborative treatment.

As shown in Figure 15b, although a boundary between the cement matrix and the transparent resin remained after the coupling agent treatment, the cracks between the two materials nearly vanished [54]. The inorganic-philic groups of the coupling agent chemically reacted with the cement matrix, while the organic-philic groups underwent cross-linking and entanglement with the transparent resin. As a result, a denser interfacial fusion was achieved, van der Waals forces were enhanced, and the overall interfacial bonding strength was significantly improved [55].

The reaction products contributed to filling microcracks and increasing interfacial contact, thereby enhancing the mechanical interlocking between the two phases. This led to a more stable interfacial connection [56,57]. In summary, the coupling agent exerted

a pronounced effect on the interfacial characteristics between the cement matrix and the transparent resin. It markedly improved interfacial bonding, facilitated improved phase integration, and resulted in a smoother and more continuous interfacial transition.

In summary, a comparison of shrinkage strain results across different interface treatments indicates that the matrix-first pouring method outperforms the resin-first method. The use of a coupling agent demonstrates a more pronounced interface modification effect relative to the control group, with both the shrinkage strain rate and the final shrinkage strain value significantly reduced. The synergistic treatment combining a coupling agent application with sawtooth surface chiseling produced the most significant effect, achieving the lowest shrinkage strain and the most effective suppression of interfacial sliding and cracking (Figure 16). The coupling agent effectively enhanced the bonding performance between the cement matrix and the transparent resin, allowing for a tighter interfacial connection and a more seamless transition. These simulation results are broadly consistent with the experimental findings described above. Accordingly, the coupling agent can be considered an effective strategy for improving the interfacial performance of transparent resin–cement-based composite materials.

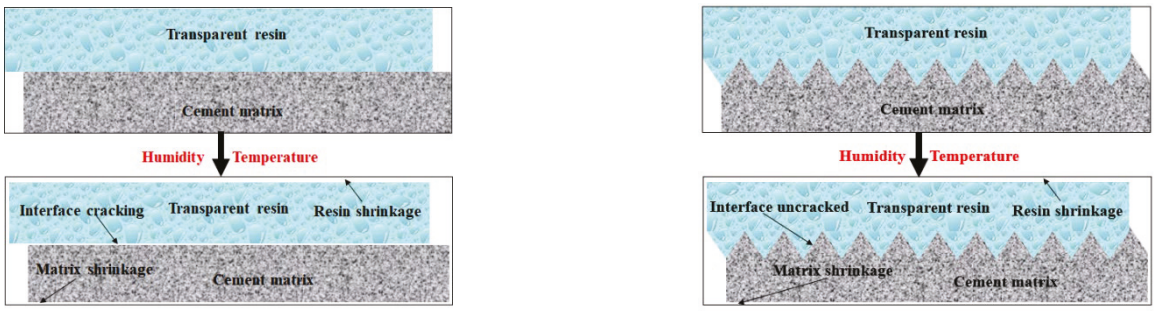

Figure 16. Dynamic contraction deformation diagram of light-conductive resin–cement-based materials.

4. Conclusions and Recommendations

1. This study developed a custom-designed monitoring system for organic–inorganic composite interfaces, integrating real-time deformation tracking capabilities. Its key innovations include synchronized strain measurements across heterogeneous interfaces and automated data visualization for time-dependent deformation analyses.
2. By comparing the interface test results under different treatments, it was observed that the matrix-first pouring method reduced the final shrinkage strain values by up to 16% compared to the resin-first method. Treatment with a coupling agent and the combined coupling agent–sawtooth interface treatment further reduced the shrinkage by up to 31% and 43.5%, respectively, relative to the control group.
3. The experimental and ABAQUS simulation results showed a strong agreement for the overall strain evolution trends. Temperature had a significant influence on strain behavior, with measuring points 1–4 exhibiting sharp strain increases followed by declines, while point 5 displayed continuous expansion as the temperature increased.
4. The coupling agent enhanced resin–cement bonding by enabling inorganic groups to chemically react with the cement matrix and organic groups to cross-link with the resin. The resulting reaction products filled interfacial microcracks and blurred phase boundaries.
5. This dual treatment strategy—chemical grafting via silane coupling agents to enhance the interfacial compatibility, and sawtooth interface structuring to induce mechanical interlocking—effectively increased the cross-linking density and interfacial strength. Together, these modifications provide a promising solution for improving the long-term service stability of photoactive resin–cement-based composites.

Author Contributions: Conceptualization, R.H.; methodology, S.Z.; validation, S.Z.; formal analysis, S.Z. and R.H.; data curation, Z.Y.; writing—original draft, S.Z. and Z.Y.; writing—review and editing, S.Z. and Z.Y.; supervision, J.M.; project administration, X.W.; funding acquisition, S.Z., R.H., C.H., J.Z. and S.D. All authors have read and agreed to the published version of the manuscript.

Funding: This research was supported by the National Natural Science Foundation of China (Nos. 52308246, 52408265, and 42202318), the Henan Province Key Research and Development Project (Nos. 241111322000 and 251111230100), and the Henan Provincial Science and Technology Research Project (Nos. 252102320018, 252300420840, and 252300421199).

Data Availability Statement: The data that support the findings of this study are available from the corresponding author upon reasonable request.

Conflicts of Interest: The authors declare no conflicts of interest.

References

1. Scrivener, K.L.; John, V.M.; Gartner, E.M. Eco-efficient cements: Potential economically viable solutions for a low-CO_2 cement-based materials industry. *Cem. Concr. Res.* **2018**, *114*, 2–26. [CrossRef]
2. Chiew, S.M.; Ibrahim, I.S.; Mohd Ariffin, M.A.; Lee, H.-S.; Singh, J.K. Development and properties of light-transmitting concrete (LTC)–A review. *J. Clean. Prod.* **2021**, *284*, 124780. [CrossRef]
3. Chiadighikaobi, P.C.; Adegoke, M.A.; Kharun, M.; Paul, V.J.; Abu Mahadi, M.I.; Finbarrs-Ezema, B. A Review of the Structural Properties of Translucent Concrete as Sustainable Material. *Open Constr. Build. Technol. J.* **2023**, *17*. [CrossRef]
4. Su, X.; Zhang, L.; Liu, Z. Daylighting and energy performance of the combination of optical fiber based translucent concrete walls and windows. *J. Build. Eng.* **2023**, *67*, 105959. [CrossRef]
5. Losonczi, A. Building Block Comprising Light Transmitting Fibres and a Method for Producing the Same. U.S. Patent No. 8,091,315, 16 May 2003.
6. Han, Y.; Zhao, W. Research development of the SACM modified cementitious materials. *Appl. Chem. Ind.* **2021**, *50*, 3463–3467+3471. [CrossRef]
7. Li, Y.; Li, J.; Wan, Y.; Xu, Z. Experimental study of light transmitting cement-based material (LTCM). *Constr. Build. Mater.* **2015**, *96*, 319–325. [CrossRef]
8. Lyu, Q.; Dai, P.; Chen, A. Mechanical strengths and optical properties of translucent concrete manufactured by mortar-extrusion 3D printing with polymethyl methacrylate (PMMA) fibers. *Compos. Part. B: Eng.* **2024**, *268*, 111079. [CrossRef]
9. Mainini, A.G.; Poli, T.; Zinzi, M.; Cangiano, S. Spectral Light Transmission Measure and Radiance Model Validation of an innovative Transparent Concrete Panel for Façades. *Energy Procedia* **2012**, *30*, 1184–1194. [CrossRef]
10. Jiang, Z.; Yu, F.; Zhang, J.; Yao, M.; Xia, C.; Yang, J. Preparation method and research progress of resin light conductive concrete. *New Chem. Mater.* **2018**, *46*, 235–238.
11. Navabi, D.; Amini, Z.; Rahmati, A. Developing light transmitting concrete for energy saving in buildings. *Case Stud. Constr. Mater.* **2023**, *18*, e01969. [CrossRef]
12. Wang, X.; Ye, X.; Song, G.; Wang, R.; Xiong, J.; Hu, M.; Luo, W.; Huang, M.; Rao, C.; Huang, J.; et al. Resin light-guiding concrete and preparation method thereof. C.N. Patent ZL 201310037937.1, 2018.
13. Wang, X.; Zhai, S.; Wang, K.; Xie, T. Modification of bonding properties and microstructure of resin-cement interface by coupling agents. *Compos. Interfaces* **2018**, *25*, 27–37. [CrossRef]
14. Wang, X.; Zhai, S.; Xie, T. Mechanism behind the improvement of coupling agent in interface bonding performance between organic transparent resin and inorganic cement matrix. *Constr. Build. Mater.* **2017**, *143*, 138–146. [CrossRef]
15. Guo, S.-Y.; Zhang, X.; Ren, J.; Chen, J.-Z.; Zhao, T.-J.; Li, T.-W.; Zhang, L. Preparation of TiO2/epoxy resin composite and its effect on mechanical and bonding properties of OPC mortars. *Constr. Build. Mater.* **2021**, *272*, 121960. [CrossRef]
16. Shen, J.; Zhou, Z. Performance and Energy Savings of Resin Translucent Concrete Products. *J. Energy Eng.* **2020**, *146*, 04020007. [CrossRef]
17. Li, N.; Shen, K.; Zhao, Y.; Zhang, G.; Lu, T.; Lu, Y.; Zhang, X. Fundamental properties of concrete with a new type of salt-resistant super absorbent polymer. *J. Railw. Sci. Eng.* **2024**, *21*, 4543–4554. [CrossRef]
18. Zhou, F.; Huang, J.; Jian, S.; Tan, H.; Lv, Y.; Hu, H.; Wang, W.; Yang, R.; Manuka, M.; Yin, Y.; et al. Photocurable resin as rapid in-situ protective coating for slag concrete against dry shrinkage. *Constr. Build. Mater.* **2023**, *396* (Suppl. C), 132171. [CrossRef]
19. Gong, J.; Li, K. Minimizing Drying Shrinkage and Enhancing Impermeability of Foam Concrete Modified with Epoxy Resin. *Adv. Civ. Eng.* **2020**, *2020*, 8897687. [CrossRef]
20. Li, Y.; Li, J.; Guo, H. Preparation and study of light transmitting properties of sulfoaluminate cement-based materials. *Mater. Des.* **2015**, *83*, 185–192. [CrossRef]

21. Luhar, I.; Luhar, S.; Savva, P.; Theodosiou, A.; Petrou, M.F.; Nicolaides, D. Light transmitting concrete: A review. *Buildings* **2021**, *11*, 480. [CrossRef]
22. Tahwia, A.M.; Abdelaziz, N.; Samy, M.; Amin, M. Mechanical and light transmittance properties of high-performance translucent concrete. *Case Stud. Constr. Mater.* **2022**, *17*, e01260. [CrossRef]
23. Tahwia, A.M.; Abdel-Raheem, A.; Abdel-Aziz, N.; Amin, M. Light transmittance performance of sustainable translucent self-compacting concrete. *J. Build. Eng.* **2021**, *38*, 102178. [CrossRef]
24. Emanet, S.; Arda Buyuktaskin, H.A. Mechanical Properties of Light-Transmitting Concrete and Its Durability Performance under the Effects of Accelerated Aging. *J. Test. Eval.* **2023**, *51*, 3273–3293. [CrossRef]
25. Wang, D.; Shi, C.; Wu, Z.; Xiao, J.; Huang, Z.; Fang, Z. A review on ultra high performance concrete: Part II. Hydration, microstructure and properties. *Constr. Build. Mater.* **2015**, *96*, 368–377. [CrossRef]
26. Pilipenko, A.; Bazhenova, S.; Kryukova, A. Decorative light transmitting concrete based on crushed concrete fines. In *IOP Conference Series: Materials Science and Engineering*; IOP Publishing: Bristol, UK, 2018.
27. Jalali, H.; Yeganeh Khaksar, R.; Mohammadzadeh, S.D. Prediction of vertical displacement for a buried pipeline subjected to normal fault using a hybrid FEM-ANN approach. *Front. Struct. Civ. Eng.* **2024**, *18*, 428–443. [CrossRef]
28. Xu, X.; Sun, Y.; Li, Y.; Wang, Z.; You, P. Interface Bonding Mechanism of Basic Magnesium Sulfate Cement-Based Resin Light-Transmitting Concrete. *Jianzhu Cailiao Xuebao/J. Build. Mater.* **2024**, *27*, 1039–1046. [CrossRef]
29. Kato, T.; Kimura, H.; Saigo, K.; Yamada, B.; Yamauchi, J.; Anraku, T. Effects of a silane coupling agent on the tensile adhesive strength between resin and titanium. *J. Appl. Polym. Sci.* **2013**, *129*, 2922–2930. [CrossRef]
30. Sharma, M.; Bishnoi, S. Influence of properties of interfacial transition zone on elastic modulus of concrete: Evidence from micromechanical modelling. *Constr. Build. Mater.* **2020**, *246*, 118381. [CrossRef]
31. Yoshida, K.; Kamada, K.; Atsuta, M. Effects of two silane coupling agents, a bonding agent, and thermal cycling on the bond strength of a CAD/CAM composite material cemented with two resin luting agents. *J. Prosthet. Dent.* **2001**, *85*, 184–189. [CrossRef]
32. Feng, Y.; Qiu, T.; Zhang, J.; Shen, C. Effects of silane coupling agent on microstructure and mechanical properties of EPDM/carbonyl iron microwave absorbing patch. *J. Wuhan. Univ. Technol. Mater. Sci. Ed.* **2006**, *21*, 78–82. [CrossRef]
33. Sharif, A.; Mohmmadi, N.; Moghbeli, M.R.; Zanjirian, E. Heterogeneity in the strength of interfacial bonds and the resultant synergism in promoting polyurethane/SBR adhesion strength. *J. Adhes. Sci. Technol.* **2003**, *17*, 1727–1739. [CrossRef]
34. Song, Y.; Wang, J.; Huang, Y.; Wang, J.; Weng, Y.; Ma, R.; Pang, K.S.H.; Ruan, S. Effects of varying grades/pretreatments of recycled aggregates on the development of pore structures and ITZs within reactive magnesia cement (RMC) concrete. *Cem. Concr. Res.* **2025**, *190*, 107782. [CrossRef]
35. Peng, C.; Chen, P.; You, Z.; Lv, S.; Zhang, R.; Xu, F.; Zhang, H.; Chen, H. Effect of silane coupling agent on improving the adhesive properties between asphalt binder and aggregates. *Constr. Build. Mater.* **2018**, *169*, 591–600. [CrossRef]
36. Xiao, Q.; Qian, C.; Xie, J. Experimental research on modification of asphalt concrete performance and asphalt-aggregate interface by coupling agent. *J. Southeast. Univ. Nat. Sci. Ed.* **2004**, *34*, 485–489. [CrossRef]
37. Guo, X.; Xie, K.; Liu, Z.; Elchalakani, M.; Zhou, Y. A study on the bond strength of interface between post-fire concrete and different epoxy resin adhesives. *Constr. Build. Mater.* **2023**, *407*, 133429. [CrossRef]
38. Zhang, M.; Xu, H.; Phalé Zeze, A.L.; Liu, X.; Tao, M. Coating performance, durability and anti-corrosion mechanism of organic modified geopolymer composite for marine concrete protection. *Cem. Concr. Compos.* **2022**, *129* (Suppl. C), 104495. [CrossRef]
39. Zhang, M.; Zang, Y.; Shan, L. Enhancing Volumetric Stability of Metakaolin-Based Geopolymer Composites with Organic Modifiers WER and SCA. *Buildings* **2024**, *14*, 586. [CrossRef]
40. Chen, H.; Sun, W.; Stroeven, P. Interfacial Transition Zone Between Aggregate and Paste in Cementitious Composites (II): Mechanism of Formation and Degradation of Interfacial Transition Zone Microstructure, and its Influence Factors. *J. Chin. Ceram. Soc.* **2004**, *32*, 70–79. [CrossRef]
41. Wu, N.; Wei, Q.-F.; Li, Q.; Xu, W.-Z. Preparation and characterization of organic/inorganic hybrid nanofibers. *J. Donghua Univ. (Engl. Ed.)* **2006**, *23*, 20–23.
42. Zhou, Z.; Gao, X.; Shen, J.; Jiao, S.; Yang, M.; Yang, H. Thermal properties and thermal insulation effect evaluation of the resin translucent concrete products. *Concrete* **2017**, 105–109. [CrossRef]
43. Chen, W.; Wang, Q.; Huang, Z.; Du, H. Hydration mechanism and mechanical properties of a developed low-carbon and lightweight strain-hardening cementitious composites. *J. Sustain. Cem. Based Mater.* **2024**, *13*, 661–677. [CrossRef]
44. Xu, S.; Nie, B.; Li, A. Bond properties for plain bars in frost-damaged concrete. *Mag. Concr. Res.* **2019**, *71*, 975–988. [CrossRef]
45. Zhao, W.; Jiang, Y.; Yu, Y.; Liu, W. Use of digital image correlation to confirm the enhancement of concrete–epoxy resin mortar adhesion through surface precoating treatment. *Constr. Build. Mater.* **2021**, *295*, 123512. [CrossRef]
46. Feng, Y.; Feng, J.; Li, L.; Li, Z.; Chen, W.; Li, Y.; Chen, W. Multi-scale analysis and structural application of the synergistic enhancement effect of silane coupling agent on the interface between PVA/rubber and cement. *J. Thermoplast. Compos. Mater.* **2025**, *38*, 209–238. [CrossRef]

47. Feng, Y.; Qin, D.; Zhao, C. The synergistic strengthening effect of silane coupling agent on the interface between PVA/EPS and cement: Experiment and molecular simulation. *Compos. Interfaces* **2023**, *30*, 21–41. [CrossRef]
48. Li, C.; Liao, H.; Gao, H.; Cheng, F. Enhancing interface compatibility in high-filled coal gangue/polyethylene composites through silane coupling agent-mediated interface modification. *Compos. Sci. Technol.* **2024**, *251*, 110546. [CrossRef]
49. Zhang, Z.; Sun, W.; Huang, W.; Zhu, Y.; Li, J.; Liang, C.; Gao, S. Interfacial and mechanical properties of silane coupling agent interface-modified basalt fiber reinforced thermoplastic polypropylene resin composites. *Polym. Compos.* **2024**, *46*, 6582–6593. [CrossRef]
50. Yi, G.-S.; Lee, H.-E. Progressive Failure Analysis of Concrete Structures Using Plasticity and Endochronic Based Models. *Ksce J. Civ. Eng.* **1998**, *2*, 1–11. [CrossRef]
51. Turcry, P.; Loukili, A.; Haidar, K.; Pijaudier-Cabot, G.; Belarbi, A. Cracking Tendency of Self-Compacting Concrete Subjected to Restrained Shrinkage: Experimental Study and Modeling. *J. Mater. Civ.* **2006**, *18*, 46–54. [CrossRef]
52. Thamburaja, P.; Chau, F.; Pan, H. The evolution of microstructure during twinning: Constitutive equations, finite-element simulations and experimental verification. *Int. J. Plast.* **2009**, *25*, 2141–2168. [CrossRef]
53. Al-Fasih, M.Y.; Mohamad, M.E.; Ibrahim, I.S. Experimental and numerical evaluations of composite concrete-to-concrete interfacial shear strength under horizontal and normal stresses. *PLoS ONE* **2021**, *16*, e0252050. [CrossRef]
54. Dai, W.; Hu, P. Molecular dynamics simulation on structure and characteristics of cement hydration products. *J. Softw.* **2011**, *6*, 2184–2188. [CrossRef]
55. Zhao, D.; Wang, H.; Zhao, Q.; Zhang, J.; Yuan, L. Strengthening the fiber-cement matrix interface by introducing functional groups on fiber surface. *J. Build. Eng.* **2024**, *91*, 109567. [CrossRef]
56. Wang, R.; Wang, X.; Xie, T. Multiscale characterization of resin-cement interface modification. *Bull. Chin. Ceram. Soc.* **2018**, *37*, 67–72. [CrossRef]
57. Yoshihara, K.; Nagaoka, N.; Sonoda, A.; Maruo, Y.; Makita, Y.; Okihara, T.; Irie, M.; Yoshida, Y.; Van Meerbeek, B. Effectiveness and stability of silane coupling agent incorporated in 'universal' adhesives. *Dent. Mater.* **2016**, *32*, 1218–1225. [CrossRef]

Disclaimer/Publisher's Note: The statements, opinions and data contained in all publications are solely those of the individual author(s) and contributor(s) and not of MDPI and/or the editor(s). MDPI and/or the editor(s) disclaim responsibility for any injury to people or property resulting from any ideas, methods, instructions or products referred to in the content.

buildings

MDPI

Article

Effects of Ca/Si and Si/Al Ratios on the Wood Biomass Ash-Based Alkali-Activated Materials with Pozzolanic Additives

Yiying Du, Ina Pundienė * and Jolanta Pranckevičienė

Laboratory of Concrete Technology, Institute of Building Materials, Vilnius Gediminas Technical University, Linkmenų Str. 28, LT-08217 Vilnius, Lithuania; yiying.du@vilniustech.lt (Y.D.); jolanta.pranckeviciene@vilniustech.lt (J.P.)
* Correspondence: ina.pundiene@vilniustech.lt

Abstract

Wood biomass ash (WBA) is a by-product from biofuel energy plants. The disposal of this waste is connected with numerous environmental concerns. A more sustainable choice is to recycle it as a raw material for building and construction materials. However, due to its unstable characteristics, its application in alkali-activated materials (AAM) poses a challenge. One issue is the development of the mechanical properties. To improve them, pozzolanic additives, including coal fly ash (CFA), metakaolin (MK), and natural zeolite (NZ), were added at replacement ratios of 10–40%. Calcium hydroxide, sodium hydroxide, and sodium silicate were used together as ternary activators. The samples were cured at 60 °C for the first 24 h and for the remaining 27 days at room temperature. Mechanical behavior, water absorption, and chemical compositions were examined. The results obtained from XRF were compared with the calculation results of the chemical compositions based on the mix design and oxide compositions of the raw materials. The results show that the respective optimum replacement ratios were 30% CFA, 20% MK, and 20% NZ, with the highest compressive strength corresponding to 22.71, 20.53, and 24.33 MPa, and the highest flexural strength of 4.49, 4.32, and 4.21 MPa. NZ was the most effective in AAM, due to the highest Si/Al ratio in the Ca-rich ambient. Then, CFA contributed less, and MK was the least efficient when used in combination with WBA in AAM. The reduction of Ca/Si ratios in the AAM caused by the pozzolanic additives favors the formation of a binder system made of different hydrates and facilitates the strength enhancement when the Ca/Si ratio is lower than 0.35.

Keywords: coal fly ash; metakaolin; natural zeolite; chemical composition; mechanical properties; water absorption

1. Introduction

Alkali-activated (geopolymer) concretes encompass a wide range of sustainable formulations by using lightweight aggregates, waste-based materials, and modified activation conditions. Lightweight geopolymer concrete incorporating pumice and waste rubber demonstrated reduced density and a favorable waste tire rubber ratio of 10% [1]. Pumice and expanded perlite have also been used to produce low-density fly ash-based geopolymer concretes with adequate mechanical strength and favorable microstructural characteristics [2]. Waste-aluminum–based and perlite-based alkali-activated systems further highlight how activator concentration, pore-forming agents, and silica enrichment influence strength, porosity,

and thermal properties [3,4]. Additional studies on recycled rubber-incorporated geopolymer composites show that full replacement of fine aggregates with waste rubber is feasible in the production of sustainable composites with enhanced toughness and strain capacity [5]. Together, these works illustrate the application of alkali-activated concretes, ranging from lightweight and insulation materials to rubberized composites, all contributing to reduced environmental impact through waste utilization and cement-free binder systems.

The arrival of biofuel energy brings a problem with waste management of wood biomass ash (WBA), which is mainly disposed of in landfills. Considering its environmental concerns, one sustainable way can be the valorization of it in building and construction materials, which reduces the environmental burden due to the disposal of this waste and allows the transformation of a valueless by-product into a sustainable material with practical implications. This is of great ecological significance. For the utilization of WBA, there have been studies in Portland cement (PC)-based materials. For instance, Hamid and Rafic [6] studied the partial replacement of PC via WBA, reporting that small substitutions—particularly around 10%—can improve strength in some cases, although variations in ash composition and reduced workability limit its broader applicability. Vu et al. [7] researched WBA–PC particleboards, indicating that incorporating up to 30% WBA as a partial PC replacement can maintain acceptable mechanical performance while improving thermal insulation. Bhat [8] studied self-compacting concrete incorporating WBA as partial PC replacement, showing that up to 10% substitution can produce comparable strength to conventional concrete, offering an eco-friendly and sustainable alternative for reducing CO_2 emissions. These results show that only with a small addition of less than 30%, has WBA positive effects. Another alternative is to use WBA in AAMs. Abdulkereem et al. [9] investigated the blended WBA–coal fly ash geopolymer mortars, pointing out that partial substitution of fly ash at a maximal 20% by WBA enhanced early-age strength, while a 10% substitution yielded optimal 28-day performance due to the newly formed calcium polysialate and calcium silicate hydrates. Cheah et al. [10] studied WBA and pulverized fuel ash hybrid geopolymers. Results show that combining these ashes at ratios between 70:30 and 50:50 can produce low-alkalinity mortars with sufficient strength, stiffness, and durability for load-bearing masonry, attributed to the formation of potassium polysialate and gehlenite phases. Du et al. [11] developed an AAM with 100% WBA as the only precursor. However, the highest compressive strength only reached 6.3 MPa. These results show that there is a possibility to incorporate a higher amount of WBA in AAMs, but there is still the challenge of limited strength when it is added in a large amount.

One solution can be the incorporation of chemically active materials as binary precursors in small amounts, such as the introduction of pozzolanic materials into the WBA-based alkali-activated binder. One example is coal fly ash (CFA). As an industrial by-product, its use in geopolymer has been widely investigated, and some efforts have been made on the hybridization of CFA and WBA [9,12], demonstrating its feasibility. In addition to the industrial wastes, commercial materials are also incorporated as precursor materials for geopolymers. Metakaolin (MK) is one such common precursor material. There have already been some efforts made to include WBA in MK-based geopolymers, but no uniform conclusion has been achieved. Some studies reported a continuous loss of strength [13] with an increase in the WBA ratio, while others noted that WBA usage at less than 50% favored strength development [14]. This can be attributed to the wide range of WBA physicochemical properties that influence its effects on geopolymers [15]. Natural zeolite (NZ) is another precursor source that has acquired much attention in recent years due to its unique microstructure. It is a crystalline, hydrated aluminosilicate material with an open, three-dimensional framework of silica and alumina tetrahedra with shared oxygen atoms. In its structure, intercrystallite channels and chambers with ions and water

https://doi.org/10.3390/buildings16010051

molecules form a web-like morphology. Studies have demonstrated its positive effects when used in geopolymer materials [16–18], but regarding its hybrid utilization with WBA, there has been no relevant research.

The elemental compounds in the produced AAMs significantly influence microstructural development and the formation of hydrate products. Wang et al. [19] compared the structure of calcium silicate (aluminate) hydrate (CS(A)H), finding that a lower Ca/Si ratio at 0.8, in contrast to that of 1.2, contributed to longer silica chain length and less structural disorder. The introduction of Al, decreasing the Si/Al ratio, was key to the introduction of additional phases and especially the formation of strätlingite and $Al(OH)_3$. Wang et al. [20] also pointed out that the micromechanical behavior of CSH is governed largely by its Ca/Si ratio, the degree of Al incorporation, and the presence of secondary phases. Lowering the Ca/Si ratio promotes greater silicate chain polymerization, produces a more compact layer arrangement, and decreases porosity. Al additions further modify the structure by generating cross-linked Q^3(Al) units, which substantially improve the rigidity and overall mechanical performance of CSH. Thus, understanding the compositions of Ca, Si, and Al in the materials is important in analyzing their property evolution.

Additionally, incorporating recycled fine aggregates could further enhance sustainability. Natural aggregates are non-renewable natural resources. Around 48.3 billion tonnes are used in the making of concrete per year [21], which imposes a significant burden on the conservation of natural resources. Meanwhile, the mining and processing of them are associated with large energy consumption [22]. Thus, some researchers have introduced recycled aggregates to partially or fully replace natural aggregates, highlighting their increasing sustainability [23,24].

The research gap existing is that, in most of the studies, WBA was used in a small amount to partially replace other precursor materials due to its low chemical reactivity, and when it is used alone, there remains a challenge to guarantee the mechanical properties. Considering this and the sustainability of WBA valorization, which was discussed in former investigations [11,25], the objective of this study was to utilize a large amount of WBA to produce an AAM with good engineering properties. To achieve this, pozzolanic additives were introduced as binary precursors. Another existing research gap is that there have been limited investigations addressing the feasibility of the co-utilization of a large amount of WBA together with CFA, MK, and NZ, especially for the hybrid utilization of NZ with WBA, where there has been no relevant research. Thus, the objective was also to analyze the feasibility of their co-usage with WBA, and the mechanism behind it.

Therefore, in this study, for the purpose of widening the application of WBA in AAMs, two types of WBAs (WBBA and WBFA) were valorized as the primary precursor materials. To improve the mechanical properties of WBA-based AAMs, pozzolanic additives CFA, MK, and NZ were applied at 10, 20, 30, and 40% of total precursor mass. Calcium hydroxide (CH), sodium hydroxide (SH), and sodium silicate (SS) were activators. Recycled sand (RS) was utilized too as a fine aggregate. Mechanical strength, water absorption, chemical compositions via XRF, and phase analysis using XRD were performed to characterize the produced mortar. Meanwhile, the results obtained from XRF were compared with the calculation results of the chemical compositions based on the mix design and oxide compositions of the raw materials. This provided an insight into the possible application of WBA in AAMs.

2. Materials and Methods

2.1. Raw Materials

The precursor materials of AAM included WBA (WBFA and WBBA), as well as MK, CFA, and NZ, as pozzolanic additives. RS from biofuel plants was used as a fine aggregate. WBAs and RS were collected from a thermal plant and supplied by Ekobaze

https://doi.org/10.3390/buildings16010051

Waste Management in Vilnius, Lithuania. The difference between WBBA and WBFA is that WBBA is made up of heavier unburned or partially burned materials that settle at the base of the furnace, while WBFA consists of the fine particles carried upward in the exhaust stream and captured by air-pollution control equipment [10]. RS comes from natural river sand which is burnt together with the wood biomass in the thermal plants. After collection, the ash was pre-treated using a ball milling equipment for 24 h. A 0.5 mm sieve was also used on WBBA. RS was pre-processed with a 1.25 mm sieve. CFA was collected from an energy producing factory in Krakow, Poland. Before use, it was also milled for 24 h. Commercial MK was produced by Bauchemie GmbH (Bottrop, Germany). The ball mill equipment used was DECO-JM. The volume was 1.5 L. The rotation speed was 480 rpm, and the ball-to-powder ratio 2:1. The duration of the milling for all three ashes (WBFA, WBBA, and CFA) was 24 h.

Alkaline activators included liquid water glass (WG), powdery sodium hydroxide (SH), and calcium hydroxide (CH). They were from Lerochem (Klaipeda, Lithuania). CH was used as a dry powder at 10% by precursor weight, while SH was dissolved in tap water to obtain an SH solution with a concentration of 7 mol/L. WG contained 50% sodium silicate (SS) and 50% water by weight, and its density was 1388 kg/m^3. The molar ratio of SiO_2/Na_2O of WG was 3.2. In the alkali-activation solution containing SH solution and WG, the molar ratio of SH/SS was 3, and the molar ratio of SiO_2/Na_2O was 2.5. The dry powder of SH was added to half the weight of WG to maintain a dry powder weight ratio of SS to SH at 1. The pH value of sodium silicate solution was 11.3 and that of sodium hydroxide solution was 13.4. The pH value of the activating solutions was 13.2. Boric acid (BA) from Lerochem (Klaipeda, Lithuania) was added as a retarder at a concentration of 1% by precursor weight.

The properties of the raw materials are summarized in Table 1. The lightest materials were NZ and MK, with bulk densities of 0.24 and 0.43 g/cm^3, respectively. RS and WBBA had the highest density, exceeding 1 g/cm^3. WBFA exhibited a great loss of ignition, related to its high carbon content, which negatively influences the long-term strength development and durability [26]. That is one of the factors making it difficult to be utilized. According to the chemical composition of the raw materials, wood biomass wastes (WBA and RS) are primarily composed of SiO_2 and CaO, whereas CFA, MK, and NZ are aluminosilicate-rich materials.

Table 1. Material properties of raw materials in the study.

Material Properties	WBBA	WBFA	RS	CFA	MK	NZ
Physical parameters						
Mean diameter (μm)	56.62	27.62	273.20	6.06	8.63	9.66
Bulk density (g/cm^3)	1.03	0.57	1.23	0.794	0.43	0.24
Chemical contents (wt%)						
SiO_2	50.26	22.91	62.03	37.00	54.4	71.5
Al_2O_3	9.20	2.63	4.65	22.80	31.9	13.1
CaO	19.99	31.50	14.14	1.92	2.82	3.22
Fe_2O_3	1.90	2.33	0.71	3.63	0.42	1.66
MgO	6.44	3.57	5.50	0.88	0.44	0.81
Na_2O	1.19	0.26	0.61	0.50	5.46	0.60
K_2O	5.71	4.01	6.42	2.96	0.50	2.99
P_2O_5	3.34	2.71	3.40	0.73	0.13	0.03
SO_3	0.51	0.88	1.16	0.18	0.13	0.01
Loss of ignition	2.73	26.93	0.96	5.20	1.10	-

Figure 1 shows the particle size distributions. CFA, MK, and NZ showed the highest number of comparatively finer particles, with most particle sizes distributed between 1 and 10 μm. The particle diameters of WBBA and WBFA were mainly centered within the range

https://doi.org/10.3390/buildings16010051

of 10 to 100 μm, whereas most RS particles had a size of over 100 μm. The D_{50} values of the raw materials were 33.9 (WBBA), 16.2 (WBFA), 227.4 (RS), 3.7(CFA), 6.2 (MK), and 6.0 (NZ). After the same pretreatment, WBFA exhibited a smaller D50 than WBBA, with a reduction of 52.2%, indicating that WBFA may be a more effective precursor material than WBBA, as demonstrated in previous research [11].

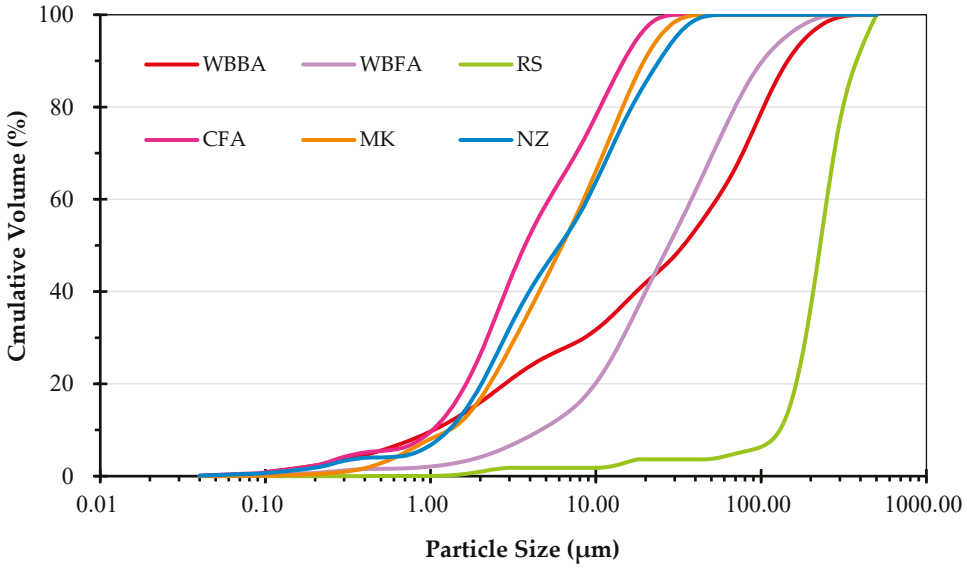

Figure 1. Particle size distribution of raw materials.

Figure 2 displays the crystalline phases. SiO_2 was identified in all the raw materials. In WBA, WBBA also contained $CaCO_3$, $Ca(OH)_2$, and $CaSiO_3$, while WBFA consisted of $Ca(OH)_2$, $CaCO_3$, and CaO. RS consisted of $CaSiO_3$. For the other precursor materials, kaolinite ($Al_2Si_2O_5(OH)_4$), mullite ($Al_6Si_2O_{13}$), and clinoptilolite were detected in MK, CFA, and NZ, respectively. Compared with the results of the oxide composition of the materials, although there was a high amount of SiO_2 in both wood biomass wastes and other precursor materials (MK, CFA and NZ), the different phases determined different chemical reactivity.

2.2. Mix Proportions and Sample Casting

In Table 2, the mix design is specified. Four groups were prepared and investigated. WBFA and WBBA were added at the same amount, and the replacement ratios of WBA with CFA, MK, or NZ, were 10%, 20%, 30%, and 40%. The fine aggregate/precursor ratio was 2 due to a consideration of strength development, which was tested in the preliminary experiments. The water/precursor ratio was 0.55. The liquid/binder ratio was 0.44. Na_2O equivalent percentage was calculated according to the formula $Na_2O\ eq = Na_2O + 0.658 \times K_2O$.

To prepare the alkali-activator solution (AAS), SH was dissolved in tap water at 60 °C to obtain an SH solution, because SH dry powder has a higher dissolution degree in hot water. Then, after being cooled to room temperature, it was mixed with WG and stirred for 1 min. The dry powders of WBFA, WBBA, CH, BA, and RS were weighed and mixed for 2 min. The dosage of BA was around 2.65 g per kg of mortar, which had an effect on retarding the reaction and thus prolonging the initial setting. Then, the AAS was poured into it and homogeneously stirred for 3 min. Afterwards, it was placed into steel prism molds with dimensions of 160 mm × 40 mm × 40 mm, and stacked in several layers. The molds were then shaken for 2 min. There was no bleeding or segregation, due to the lower flowability of the produced materials compared to the traditional PC-based materials. During the casting, qualitative observation of the workability was made. The molds were subjected to a 60 °C heat treatment for 24 h before demolding. Usually, the temperature

https://doi.org/10.3390/buildings16010051

treatment for AAMs is set between 60 °C and 100 °C for 24 h [15]. In this investigation, a comparatively lower temperature of 60 °C was selected in consideration of a decrease in energy consumption. The demolded samples were labelled and placed in laboratory settings with plastic film for 28-day curing at room temperature (22 ± 2 °C) and ambient humidity with no specific humidity control.

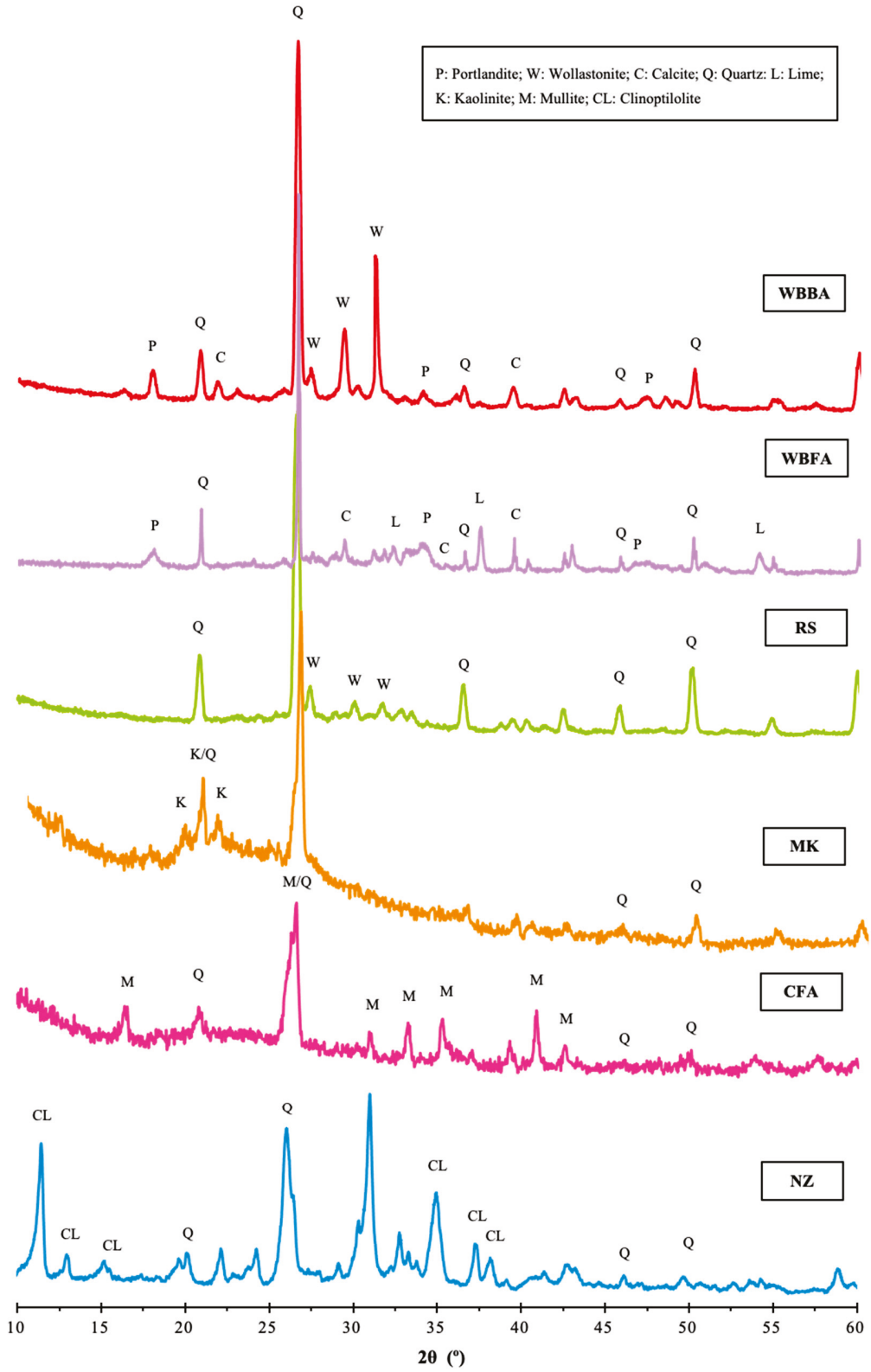

Figure 2. Phase compositions of raw materials.

https://doi.org/10.3390/buildings16010051

Table 2. Mix composition (unit: kg/m^3) (Fine aggregate/precursor ratio—2; water/precursor ratio—0.55; liquid/binder ratio—0.44; CFA/WBA ratio—0.1, 0.2, 0.3, 0.4; MK/WBA ratio—0.1, 0.2, 0.3, 0.4; NZ/WBA ratio—0.1, 0.2, 0.3, 0.4).

Group	Mix	WBBA	WBFA	CFA	MK	NZ	RS	SH Solution	WG	CH	BA	Binder	Na_2O eq%
1	REF	273	273	-	-	-	1094	301	168	55	5	1075	9.36
2	F10	246	246	55	-	-	1094	301	168	55	5	1075	9.44
	F20	219	219	109	-	-	1094	301	168	55	5	1075	9.27
	F30	191	191	164	-	-	1094	301	168	55	5	1075	9.23
	F40	164	164	219	-	-	1094	301	168	55	5	1075	9.18
3	M10	246	246	-	55	-	1094	301	168	55	5	1075	9.40
	M20	219	219	-	109	-	1094	301	168	55	5	1075	9.47
	M30	191	191	-	164	-	1094	301	168	55	5	1075	9.52
	M40	164	164	-	219	-	1094	301	168	55	5	1075	9.57
4	Z10	246	246	-	-	55	1094	301	168	55	5	1075	9.32
	Z20	219	219	-	-	109	1094	301	168	55	5	1075	9.28
	Z30	191	191	-	-	164	1094	301	168	55	5	1075	9.24
	Z40	164	164	-	-	219	1094	301	168	55	5	1075	9.19

2.3. Testing Methods

The particle size distribution was examined via a "Cilas 1090 LD" (Orleans, France) particle size analyzer with a diameter range of 0.01–500 μm in wet mode. The flexural and compressive strengths were tested via a WDW-20 universal testing apparatus. Flexural strength was evaluated using a three-point bending test at a loading rate of 50 N/s, while compressive strength was measured at a loading rate of 400 N/s. Four samples were subjected to flexural strength tests, measuring 160 mm × 40 mm × 40 mm in size. Six samples were prepared in compressive strength tests with a sample size of 50 mm × 50 mm × 50 mm. The surfaces of the samples were polished to be even before the testing. Afterwards, the fractured pieces of five representative samples (REF, F30, M20, Z20, and P10) were collected for further microstructural analysis. The crystalline phases and mineralogical compounds were identified using an X-ray diffractometer from SmartLab (Rigaku, Tokyo, Japan), with a 2-theta range up to 80°, to obtain X-ray diffraction (XRD) patterns. The equipment has an X-ray tube with a 9 kW rotating Cu anode and a step size of 0.02°. The scanning rate is 1 s per step. The chemical composition of the raw materials and samples was identified using a high-performance multichannel sequential wavelength dispersive X-ray fluorescence (XRF) spectrometer (AXIOS-MAX, Panalytical, Eindhoven, The Netherlands). The operation wavelength was 1440 s. The elemental ratios were calculated based on the oxide compositions in the XRF results. Before XRD and XRF analysis, the samples were ground into a fine powder of less than 0.063 mm. The water absorption was tested by immersing the samples in water. The weight of the samples was recorded per 24 h until the weight changes were smaller than 1%. Before immersing into water, the samples were oven-dried under 60 °C and the mass change was inspected every 24 h until it was less than 1%. The water was at room temperature (22 ± 2 °C). The data of equilibrium saturation was collected, and the calculation followed the equation below:

$$W = \frac{m1 - m2}{m2} \times 100\%$$

where W is the water absorption of the samples, %; $m1$ is the mass of the immersed sample, g; $m2$ is the mass of the dried sample, g.

https://doi.org/10.3390/buildings16010051

3. Results and Discussions

3.1. Strength Development

The 28-day compressive strength results are illustrated in Figure 3. The ANOVA F-value is 30.677. Tukey HSD does not identify distinct pairwise differences. The reference sample with only WBAs had a compressive strength of 15.44 MPa. The replacement with CFA, MK, and NZ at 10 to 40% of the precursor weight showed positive effects on the strength increment, ranging from 3.11% to 57.62%. The highest strength values were recorded at 22.71, 20.54, and 24.33 MPa, respectively, representing improvements of 47.09%, 33.03%, and 57.62% over the initial values, as seen in Table 3. This is attributed to the rich aluminosilicate minerals in CFA, MK, and NZ, as shown in Figure 2, which act as reactive precursor sources and contribute to the formation of increasing amounts of geopolymeric gels, as reported in other research [27–29]. Along with the replacement ratio growing to 40%, the same strength evolution pattern was observed for CFA, MK, or NZ-incorporated samples. The compressive strength was enhanced to the highest values, then reduced after the optimal ratio was attained at 30, 20, and 20%, respectively, indicating the existence of a maximal compacity of pozzolanic additive utilization in the WBA-based binder system. Furthermore, the unreacted particles can absorb water in the matrix given a large specific surface area and a porous nature, thereby interfering with the hydration process. Well-crystallized hydration products in the shape of plates and small needles, belonging to CSH and ettringite, were observed in the sample with solely biomass ashes. However, there was a considerable number of microcracks and pores, which hindered the strength growth of the sample. In contrast, the addition of CFA or MK or NZ precursors visibly densified the microstructure of AAMs, as observed in the SEM micrographs in previous research [30]. Previous research utilizing CFA, MK, or zeolite products together with biomass ashes reported an optimal replacement dosage in the improvement of mechanical properties at 30–40%, 50%, and 1–5%, respectively [10,14,31]. These vary from the results obtained in this investigation, mainly influenced by the alkalinity, the degrees of the curing conditions, and particularly the characteristics of biomass ashes, which significantly differ due to the biomass source and combustion settings [15].

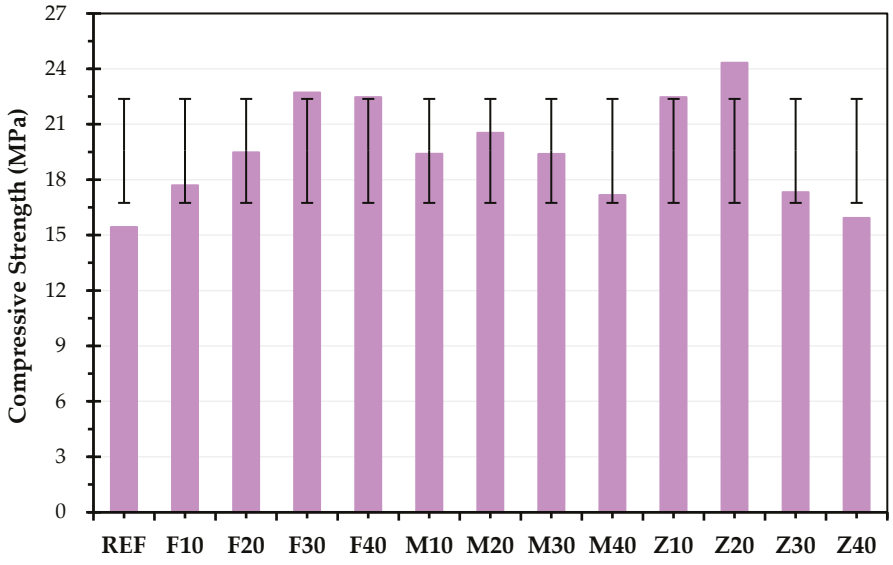

Figure 3. Compressive strength, ANOVA F-value: 30.677.

A similar development of flexural strength is observed in Figure 4 as the compressive strength. The ANOVA F-value is 2.924. Tukey HSD does not identify distinct pairwise differences. The reference sample strength reaches a value of 3.58 MPa, and the substitution

https://doi.org/10.3390/buildings16010051

of WBA with CFA, MK, and NZ contributes to an increase in strength ranging from 0.84% to 25.53%. The highest flexural strength was observed at a replacement ratio of 30% CFA, 20% MK, and 20% NZ, with strengths of 4.49, 4.32, and 4.21 MPa, respectively, representing increases of 25.53%, 20.67%, and 17.60%, as shown in Table 3. An improvement in the strength was recorded with the growth of the supplementary precursor amount before the optimal content was achieved. This indicates the positive effects of adding pozzolanic additives composed of aluminosilicate-based minerals (Figure 2) to the WBA-based mortar, enhancing the amount of active Si and Al. After that, when the replacement ratio exceeded the thresholds of the binder system, the strength began to decrease, as indicated by the compressive strength results. As a commonly used geopolymer precursor, MK is usually very effective in promoting geopolymerization. However, in this study, CFA outperformed MK in improving the mechanical properties, even though the aluminosilicate content in the raw material MK was higher than that in CFA. Similar strength loss at a high amount of MK usage was also observed by other researchers [13,14], primarily due to the structural defects caused by the unreacted MK particles [32].

Table 3. Percentage enhancement of the strength of the optimal mixes compared to the reference samples (significant at $\alpha = 0.05$).

Optimal Mix	Flexural Strength (%)	*p*-Values	Compressive Strength (%)	*p*-Values
F30	25.53	0.00988	47.15	0.00278
M20	20.88	0.01873	33.05	0.01218
Z20	17.78	0.00805	57.62	0.0000067

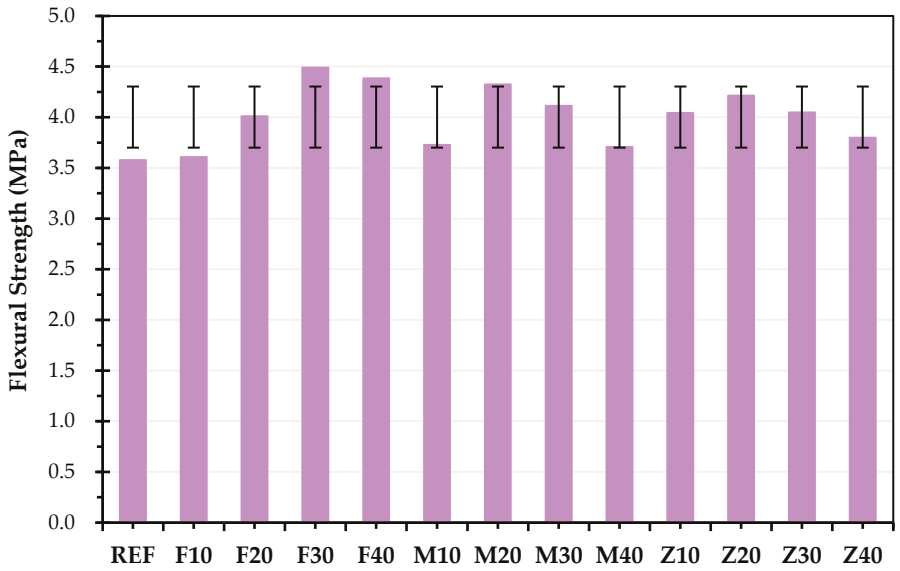

Figure 4. Flexural strength, ANOVA F-value: 2.924.

3.2. Water Absorption

In Figure 5, the bulk density varied around an average value of 1891.8 kg/m^3, with a fluctuation of 3.93%. The alternation of the sample bulk density is determined by the particle size (Figure 1), the density, and the physical properties (Table 1) of the raw materials, as well as the pore structure development of AAM. As the pozzolanic additive materials are comparatively lighter than WBBA and have a more porous microstructure, the partial replacement of WBA with these materials, as their content increases, can lead to a reduction in the mixture density. This explains the overall decrease in mortar density when the CFA amount increases from 30 to 40%, MK grows from 10 to 30%, and NZ increases from 10 to

https://doi.org/10.3390/buildings16010051

40%. On the other hand, the supply of pozzolanic sources in the binder system improves the reaction degree, which can form a denser mortar microstructure due to the production of a greater amount of gel products, thereby enhancing the bulk density [33]. This corresponds to the observed results, where samples achieve higher bulk density compared to REF after using a secondary precursor, especially for those with NZ.

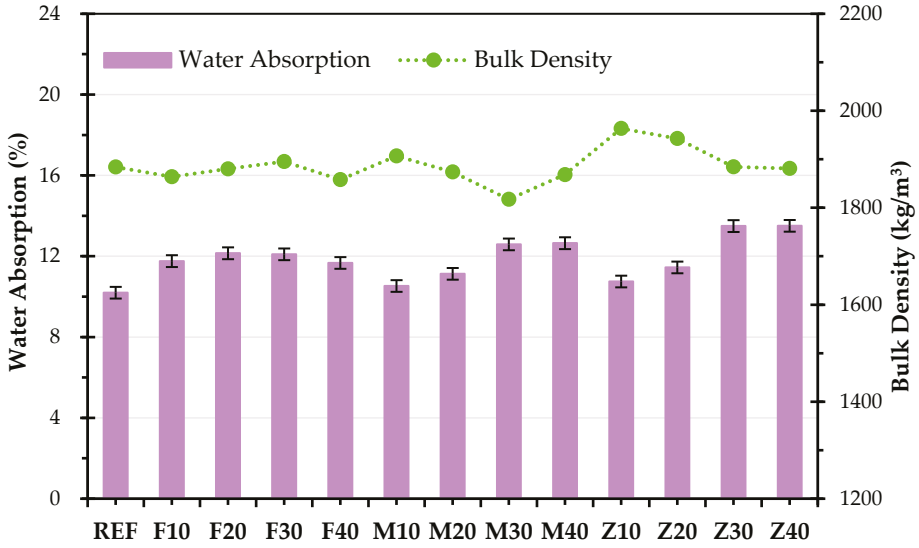

Figure 5. Water absorption and bulk density.

Water absorption is affected by the porosity and pore structure of the materials, particularly the existence of open pores. Similar to existing research results, the AAMs produced reached water saturation within 24 h [34]. In Figure 5, the evolution of the water absorption aligns with the changes in the bulk density. The correlation coefficient R2 between water absorption and bulk density was −0.41, indicating a weak correlation. REF showed a water absorption of 10.20%. After the use of an extra precursor, the water absorption values exhibited an enhancement of between 0.33% and 18.20%. One factor that can be attributed to the introduction of lighter and more porous precursor materials, with a finer particle size distribution, is the generation of microvoids in the mortar system. Meanwhile, the greater specific surface area and microstructural characteristics determine that the particles of CFA, MK, and NZ tend to absorb more water, which also accounts for the increase in water absorption [28,29].

When CFA was added from 10 to 40%, the water absorption increased by 1.95% to 12.15% at 20% CFA usage, then it decreased slightly to 11.67% at 40% CFA. This indicates that although the use of CFA can increase water demand in the mortar system, its increasing addition promotes the activation reaction, producing more hydration products that effectively densify the mortar microstructure. For mixes with MK and NZ, a similar increment in water absorption was observed at the beginning, reaching 12.59% and 13.50%, respectively, at a content of 30%. The water absorption value then maintained the same level when the amount of MK and NZ increased to 40%. It reveals that, unlike CFA, the continuous addition of MK or NZ due to the zeolitic structure, which captures water, is less effective in improving the reaction degree of the mortar binder, as indicated by the strength results, where the largest strength is achieved at 20% MK or NZ. The growing use of MK or NZ exceeds the capacity of the binder system, contributing to insufficient reaction and the presence of unreacted precursor particles. Also, due to the structure of NZ that tends to capture water, the higher the amount of NZ added, the more the amount of water was absorbed.

https://doi.org/10.3390/buildings16010051

3.3. Chemical and Phase Composition

In Figure 6, furthermore, XRF results for the primary elements in four representative samples are presented, along with the ratios between the main compounds (SiO_2, CaO, Al_2O_3, and Na_2O). Compared to REF, the utilization of CFA, MK, and NZ enhanced the contents of SiO_2 and Al_2O_3, while the amount of CaO was decreased. Particularly in samples F30 and Z20, the Si/Na and Al/Na ratios appear to have increased. It confirms the positive effects of active Si and Al contents, resulting from the use of pozzolanic additives, which favor the production of NASH. As a polymeric gel, NASH in the mortar can further improve the mechanical properties, contributing to higher strength.

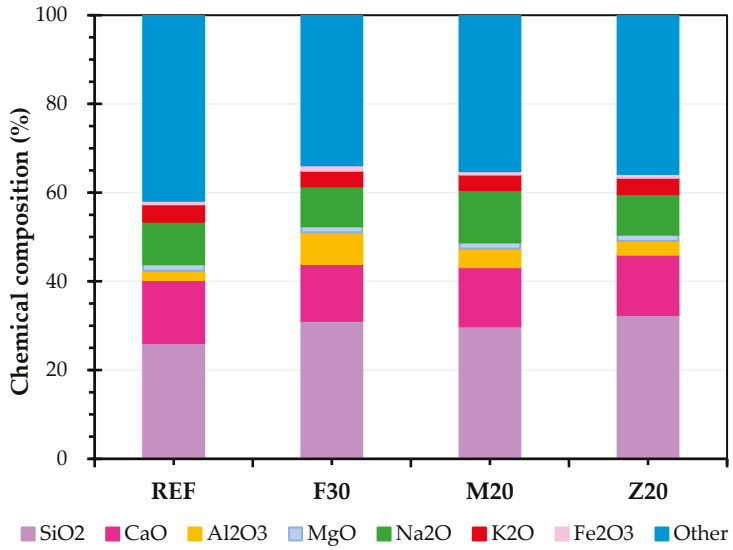

Figure 6. Primary elemental composition of the representative samples.

The chemical content ratios of Si/Na, Ca/Na, and Al/Na in the representative samples calculated based on the XRF results are presented in Figure 7, with correlation coefficients of 0.74, −0.01, and 0.5, respectively. The calculations were as follows: Si/Na = ((SiO_2)%/60.08)/2((Na_2O)%/61.98); Ca/Na = ((CaO)%/56.08)/2((Na_2O)%/61.98); Al/Na = 2((Al_2O_3)%/101.96)/2((Na_2O)%/61.98). The calculation of the data in Figures 8–11 followed the same procedure. In the F30 sample, all three ratios remained at higher values when compared to others. This indicates that the utilization of CFA at 30% introduces a significant amount of aluminates and silicates, and at the same time, can serve as an additional source of Ca, related to its effective improvement of strength.

Figures 8 and 9 illustrate the relationship between the strength and Ca/Si and Si/Al ratios, calculated from the material composition, which significantly influence the reaction degrees and product categories [28]. Due to the significant amounts of CaO and SiO_2 in the sample compositions, an evident trend was observed in Figure 8, which was further confirmed by the XRF results. As the Ca/Si ratio decreases, the strength increases, especially when the content of Ca surpasses a certain amount (Ca/Si ratio 0.35). This aligns with previous research, which suggests an optimal amount of Ca in the binder system; then, when the increment of Ca content exceeds this amount, a decrease in compressive strength is recorded [11].

Within the Ca/Si ratio range of 0.2–0.6, variations in phase assemblage and mechanical performance demonstrate that an optimal Ca/Si ratio of approximately 0.3–0.35 corresponds to the highest compressive strength. The intermediate C–S–H phase facilitates a gradual and regulated release of Ca^{2+} ions [35]. As the Ca/Si ratio increases up to 0.35–0.4, the morphology of the CSH phases progressively transforms from needle-like to plate-like, ultimately developing into an interwoven, network-type microstructure [36]. This mi-

https://doi.org/10.3390/buildings16010051

crostructural evolution is accompanied by a notable enhancement in compressive strength. Furthermore, the influence of the Ca/Si ratio (0.3–0.4) on the mechanical performance can be ascribed to the pozzolanic interactions occurring within alkali-activated matrices [37]. The pozzolanic reaction in such systems proceeds through a dissolution–reorganization–precipitation sequence. Upon exposure of CFA to alkaline activators, hydroxide ions (OH^-) attack the amorphous silica network, cleaving Si–O–T bonds and generating reactive silicate monomers. These monomers subsequently undergo polymerization into extended chain structures, with aluminum species substituting for silicon in tetrahedral coordination. In Ca-enriched environments, such as those characteristic of wood bottom ash WBA-based AAMs, the liberated Ca^{2+} ions contribute to the stabilization of the aluminosilicate frameworks. This process promotes the coexistence of CSH, CASH, and NASH gels, thereby resulting in significant improvements in the mechanical properties of the material.

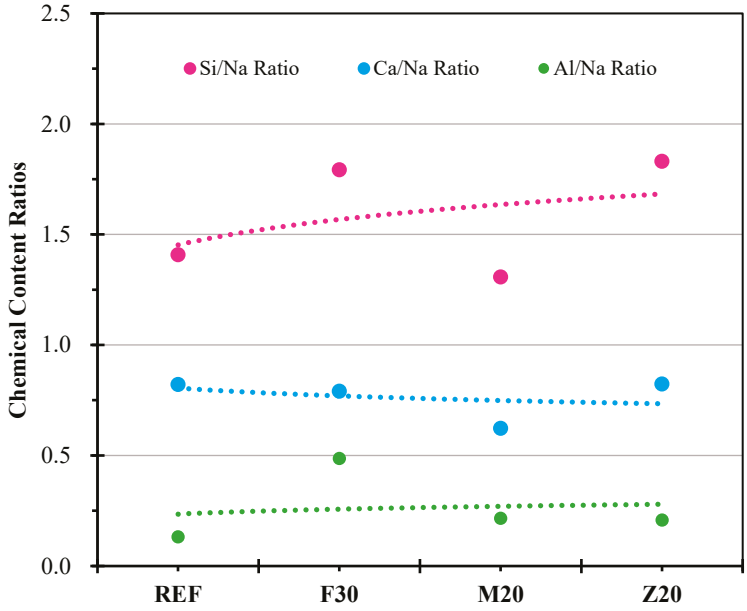

Figure 7. Si/Na, Ca/Na, and Al/Na ratios of the representative samples.

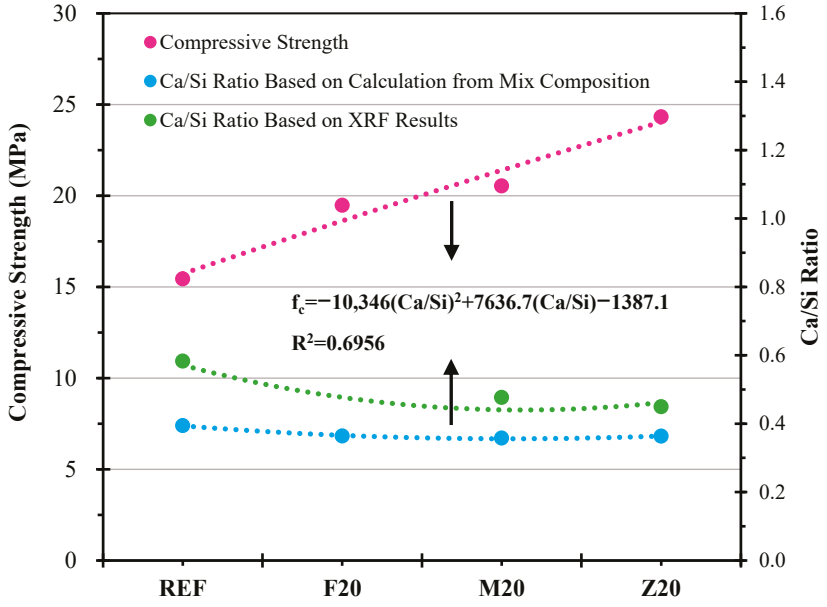

Figure 8. Ca/Si ratio of the reference sample and samples with 20% of pozzolanic additives.

https://doi.org/10.3390/buildings16010051

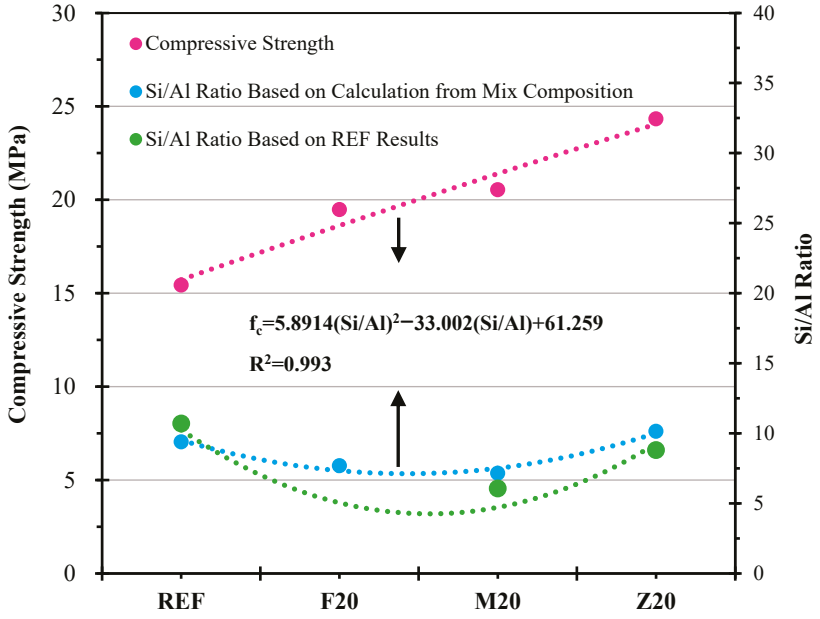

Figure 9. Si/Al ratio of the reference sample and samples with 20% of pozzolanic additives.

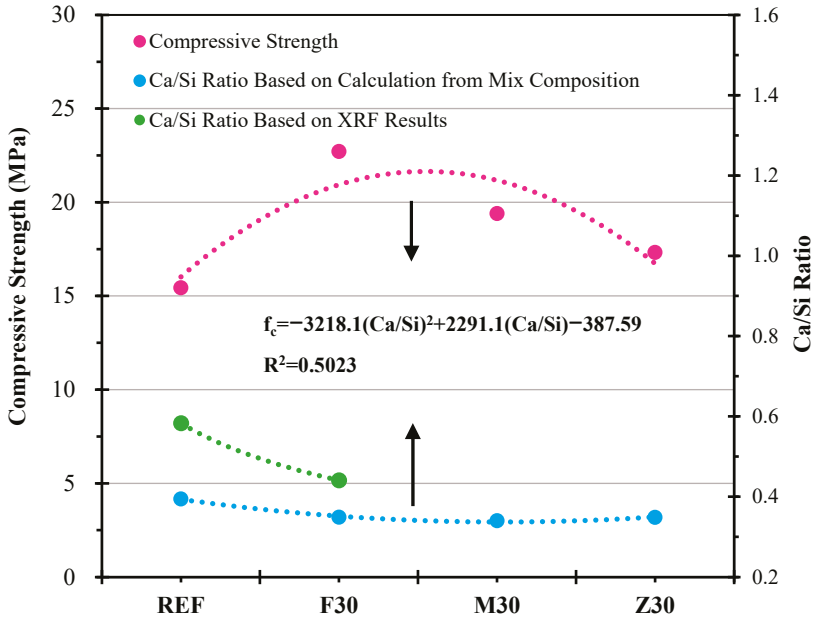

Figure 10. Ca/Si ratio of the reference sample and samples with 30% of pozzolanic additives.

The correlation between compressive strength and Si/Al ratio is comparatively weak (Figure 9), indicating that the reaction participated by Ca-containing compounds dominates the development of the material properties. In this case, relatively low SiO_2 and high Al_2O_3 contents can have a positive impact. Based on the calculated Si/Al ratio, except for sample Z20, the strength increases as the ratio decreases. In the reference sample, REF, as it contains a minimal amount of Al_2O_3, the Si/Al ratio is high. It explains why CASH crystals were not identified in such a system. Conversely, increasing aluminosilicate sources, especially the Al contents in the Ca-rich environment, promotes the formation of Al-containing hydrates CASH, instead of CSH, and triggers geopolymerization to generate polymeric products, which significantly facilitates strength development. This effect has also been mentioned by other researchers, who point out that the increase in Ca sources favors the dissolution of Si-O-Si and Si-O-Al bonds in aluminosilicates, generating oligomers that interact with Ca^{2+} and produce aluminate silicate hydrate (ASH) and calcium aluminate

https://doi.org/10.3390/buildings16010051

hydrate (CAH) [38]. The dissolution of Ca^{2+} in the binder system promotes a rapid geopolymerization between silicates and aluminates, producing more NASH gels [39]. In addition, the presence of aluminate contents in higher proportions facilitates the dissolution of active aluminosilicates in the alkaline environment, which favors the polymerization, releasing free $[SiO_4]^-$ and $[AlO_4]^-$ tetrahedral units [40]. For samples with NZ addition, it is worth noting that NZ, primarily composed of clinoptilolite, has an open framework structure made up of interconnected $[SiO_4]_4^-$ and $[AlO_4]_5$ tetrahedra with negative charges. They attract sodium and calcium ions at ambient temperature. Thus, although the Si/Al ratio of Z20 is high, it still achieves the greatest compressive strength.

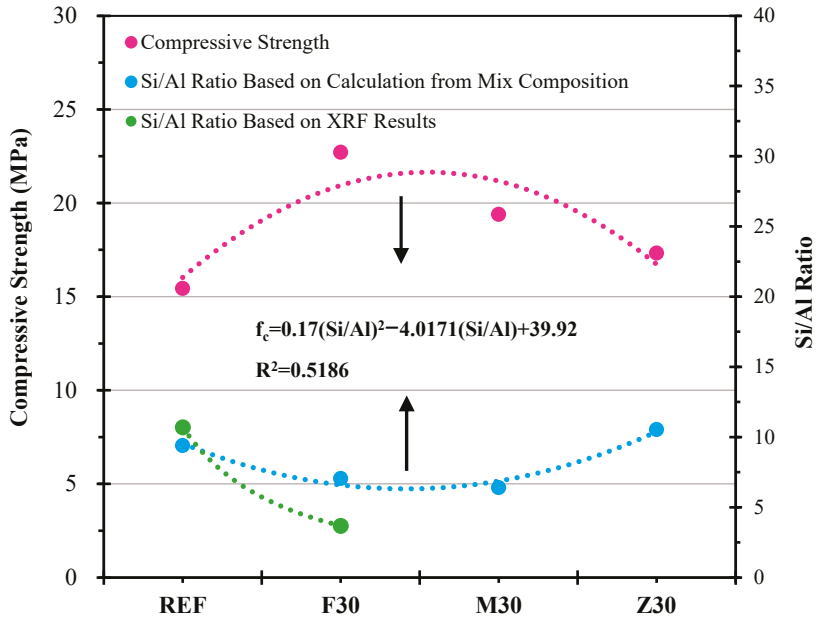

Figure 11. Si/Al ratio of the reference sample and samples with 30% of pozzolanic additives.

The relationship between the compressive strength and Ca/Si or Si/Al ratios of the samples with 30% of pozzolanic additives are displayed in Figures 10 and 11, respectively. The usage of pozzolanic additives led to the reduction of Ca/Si ratios in the AAM, which favors the formation of a binder system composed of various categories of hydrates and promoted the development of the strength when the ratio was lower than 0.8. However, on exceeding this, strength loss was detected. Another point influencing the strength development is the introduction of the Al content which contributes to the decrease of the Si/Al ratio and facilitates improved mechanical properties. Nonetheless, sample Z30 fails to follow this tendency, due to the unique microstructure of NZ which results in a compact three-dimensional web structure when added as a precursor, impressively improving the compressive strength. Unlike other silicate structures, NZ has large vacancies (one-point defect in a crystal) in tits structure that enable big cations, such as sodium or calcium ions, to bind with water molecules, i.e., to hydrate. The voids in the minerals can be connected, thus forming channels of different sizes. This capacity of cation exchange for clinoptilolite-based NZ is of a high value of 72.51 mg-ekv/100 g [41]. It means that sodium and calcium ions from the activator solution and other components can be captured in the NZ structure, creating a synthesis product, i.e., an NZ-geopolymer composite binder.

The XRD was further tested and the results are exhibited in Figure 12. Five major crystalline phases were identified (quartz, calcite, portlandite, CSH, and CASH). The last two are hydrate products. An amorphous region was also detected at the 2θ degree between 25 and 35°, assigned to the gel hydrate products CSH, CASH, and NASH [42]. Wollastonite and lime in the raw materials were absent in the AAM samples, highlighting

https://doi.org/10.3390/buildings16010051

their active participation in the activation process. Also, in the XRD pattern of Z30 with 30% NZ, the intense peaks belonging to clinoptilolite in the raw material NZ almost disappeared. NZ effectively dissolved into the alkaline environment and transformed into activation products. The absence and weakening of clinoptilolite peaks have also been reported in other investigations, particularly with the adoption of SH as an activator, which significantly promoted the dissolution of NZ [17,43]. The use of NZ, on the one hand, promotes the hydration of WBA. On the other hand, as an active pozzolanic source, it reacts with alkali-activators to produce NASH geopolymeric gels. The same outcomes were observed for samples F30 and M20.

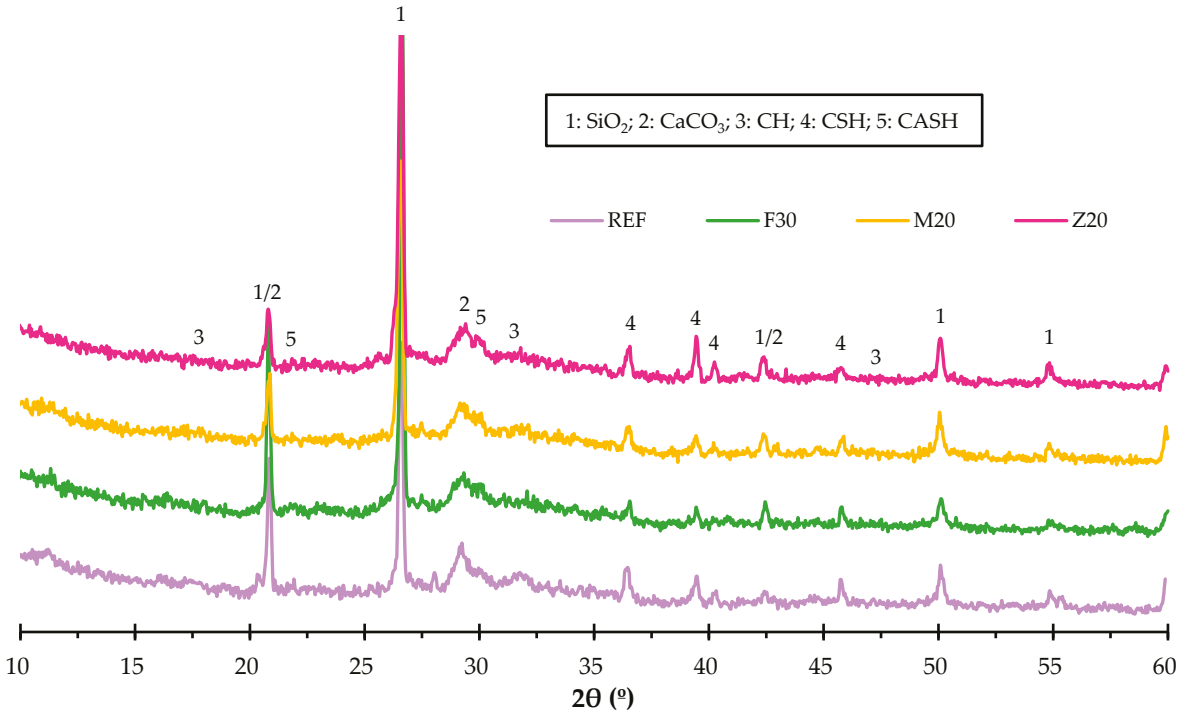

Figure 12. XRD patterns of AAM (SO_2, ICDD 00-046-1045; $CaCO_3$, ICDD 00-005-0586; CH, ICDD 00-004-0733; CSH, ICDD 00-034-0002; CASH, ICDD 00-080-1579).

The disappearance of phases of mullite and kaolinite indicates the effective release of aluminosilicate content in the raw materials to form hydrate products. It is worth noting that although CH was added as an activator, the peaks of portlandite in the AAM were very weak and narrow, which testifies to its consumption in the binder system. Intensive peaks of quartz were detected in the mortar samples, which remained unreacted, as reported in existing studies [44,45]. The significant amount of quartz in the WBA negatively affects its chemical reactivity and increases the challenges of its utilization. Another point worth noting is the increasing intensity of peaks belonging to hydrates, especially CASH, in samples with pozzolanic additives CFA, MK, and NZ, in contrast with REF. The utilization of pozzolanic additives significantly improves the reactivity of the binder and facilitates the hydration reaction and explains the further enhancement of the mechanical properties.

4. Conclusions

In this study, an AAM was produced by incorporating pozzolanic additives (CFA, MK, and NZ) with a maximum content of 40% and WBA as the primary precursor source. As a valueless waste from biomass combustion sites, the recycling of WBA to be reused in AAMs, instead of being disposed of in landfills, greatly contributes to environmental conservation and is of great ecological significance. Due to the consideration to reduce

https://doi.org/10.3390/buildings16010051

energy consumption, a more ecological curing method was adopted with only 24 h of temperature treatment at 60 °C, instead of the traditional 100 °C. Meanwhile, until the 28 days, the samples were cured at ambient settings, instead of curing chambers, which contributes further to the much improved ecoefficiency. This material was designed to be pre-fabricated in the factory and cast with recycled coarse aggregates, allowing for the production of sustainable, green alkali-activated concrete for applications in low-load-bearing structural elements, such as lintels of windows and doors. Also, it can be applied as cold-bridge materials and furnishing materials for exterior or interior decorations.

The greatest compressive strength was 24.33 MPa, recorded for the sample Z20 with 20% of NZ, this value being 57.58% larger than that of REF. The highest flexural strength was 4.49 MPa in sample F30, which contained 30% CFA, and was 25.42% bigger than that of REF. The water absorption of the AAMs with pozzolanic additives showed different degrees of enhancement, primarily influenced by the incorporation of lighter materials with a finer particle size distribution.

The chemical compounds of the raw materials impacted the property development of AAMs. By introducing pozzolanic additives, the element ratios of the samples were altered. A strong correlation was observed between compressive strength and the Ca/Si ratio. The optimal Ca/Si ratio was 0.3–0.35, which corresponds to the highest strength development. The Si/Al ratio showed a weaker influence. These alternations in the chemical compounds influenced the production types of hydrates from solely Ca-containing hydrates to coexistence with Al-containing hydrates, especially when the Si/Al ratio was low, i.e., when more Al was added into the binder system.

In the context of this research, attention was paid to the impacts of the chemical-mineral characterization of the AAMs after the use of pozzolanic additives; however, analysis of the microstructure and pore structure was not conducted, which is important for revealing the reaction mechanisms. Also, it is suggested to conduct water permeability tests, which are very useful for investigating the pore structure of the samples, especially together with mercury intrusion porosimetry and water absorption. The quantitative analysis of the amorphous phases regarding the formation of CASH, CSH, and NASH were also not included. It is suggested to have quantitative XRD analysis in the future study and to focus more on the quantitative analysis of workability. In this study, the main content focuses on the effects of chemical compositions, such as Ca/Si and Si/Al ratios, on the mechanical and physical properties of the samples; therefore, the content related to pore structure is not included. In future studies, the target can be on microstructural analysis, combined with porosity and pore structure analysis. Additionally, more focus can be placed on early-stage property development and reaction mechanisms.

Author Contributions: Conceptualization, I.P. and Y.D.; methodology, I.P. and Y.D.; software, J.P.; validation, I.P. and J.P.; formal analysis, I.P. and Y.D.; investigation, Y.D.; resources, I.P. and J.P.; data curation, J.P. and Y.D.; writing—original draft preparation, Y.D.; writing—review and editing, I.P. and J.P.; visualization, Y.D. and J.P.; supervision, I.P. and J.P.; funding acquisition, I.P. and J.P. All authors have read and agreed to the published version of the manuscript.

Funding: The research was funded by the Research Council of Lithuania within the project "Development of water treatment systems that counteract the eutrophication process of lakes based on zeolites obtained from industrial by-products" under the international programme M-ERA.NET 3 Cofund (Grant No. S-M-ERA.NET-24-2).

Institutional Review Board Statement: Not applicable.

Informed Consent Statement: Not applicable.

Data Availability Statement: The original contributions presented in this study are included in the article. Further inquiries can be directed to the corresponding author.

https://doi.org/10.3390/buildings16010051

Acknowledgments: The authors offer their sincere gratitude to all the staff in the Institute of Building Materials, Vilnius Gediminas Technical University.

Conflicts of Interest: The authors declare no conflicts of interest.

References

1. Çelik, A.İ.; Karalar, M.; Tunç, U.; Şahan, M.F.; Althaqafi, E.; Umiye, O.A.; Özkılıç, Y.O. Mechanical and Impact Behavior of Lightweight Geopolymer Concrete Produced by Pumice and Waste Rubber. *Sci. Rep.* **2025**, *15*, 35280. [CrossRef] [PubMed]
2. Top, S.; Vapur, H.; Altiner, M.; Kaya, D.; Ekicibil, A. Properties of Fly Ash-Based Lightweight Geopolymer Concrete Prepared Using Pumice and Expanded Perlite as Aggregates. *J. Mol. Struct.* **2020**, *1202*, 127236. [CrossRef]
3. Çelik, A.İ.; Tunç, U.; Kayabaşı, R.; Acar, M.C.; Şener, A.; Özkiliç, Y.O. Influence of Aluminum Waste, Hydrogen Peroxide, and Silica Fume Ratios on the Mechanical and Thermal Characteristics of Alkali-Activated Sustainable Raw Perlite Based Geopolymer Paste. *Sustain. Chem. Pharm.* **2024**, *41*, 101727. [CrossRef]
4. Çelik, A.İ.; Tunç, U.; Karalar, M.; Althaqafi, E.; Özkılıç, Y.O. Sustainable Utilization of Aluminum Waste in Geopolymer Concrete: Influence of Alkaline Activation on Microstructure and Mechanical Properties. *Rev. Adv. Mater. Sci.* **2025**, *64*, 20250152. [CrossRef]
5. Wan, F.; Guo, Y.; Zheng, M.; Li, B.; Elghazouli, A.Y. Sustainable Engineered Geopolymer Composites Incorporating Recycled Waste Rubber as Full Replacement of Fine Aggregates. *J. Mater. Res. Technol.* **2025**, *37*, 5614–5641. [CrossRef]
6. Hamid, Z.; Rafiq, S. An Experimental Study on Behavior of Wood Ash in Concrete as Partial Replacement of Cement. *Mater. Today Proc.* **2021**, *46*, 3426–3429. [CrossRef]
7. Vu, V.A.; Cloutier, A.; Bissonnette, B.; Blanchet, P.; Duchesne, J. The Effect of Wood Ash as a Partial Cement Replacement Material for Making Wood-Cement Panels. *Materials* **2019**, *12*, 2766. [CrossRef]
8. Bhat, J.A. Mechanical Behaviour of Self Compacting Concrete: Effect of Wood Ash and Coal Ash as Partial Cement Replacement. *Mater. Today Proc.* **2021**, *42*, 1470–1476. [CrossRef]
9. Abdulkareem, O.A.; Ramli, M.; Matthews, J.C. Production of Geopolymer Mortar System Containing High Calcium Biomass Wood Ash as a Partial Substitution to Fly Ash: An Early Age Evaluation. *Compos. B Eng.* **2019**, *174*, 106941. [CrossRef]
10. Cheah, C.B.; Part, W.K.; Ramli, M. The Hybridizations of Coal Fly Ash and Wood Ash for the Fabrication of Low Alkalinity Geopolymer Load Bearing Block Cured at Ambient Temperature. *Constr. Build. Mater.* **2015**, *88*, 41–55. [CrossRef]
11. Du, Y.; Pundiene, I.; Pranckeviciene, J.; Korjakins, A.; Kligys, M. Mechanical Properties and Lifecycle Assessment of a Green Alkali-Activated Mortar Based on Biomass Wood Ash. *Environ. Clim. Technol.* **2024**, *28*, 195–207. [CrossRef]
12. Arunkumar, K.; Muthukannan, M.; Kumar, A.S.; Ganesh, A.C.; Devi, R.K. Production of Eco-Friendly Geopolymer Concrete by Using Waste Wood Ash for a Sustainable Environment. *Pollution* **2021**, *7*, 993–1006. [CrossRef]
13. Candamano, S.; De Luca, P.; Frontera, P.; Crea, F. Production of Geopolymeric Mortars Containing Forest Biomass Ash as Partial Replacement of Metakaolin. *Environments* **2017**, *4*, 74. [CrossRef]
14. Jurado-Contreras, S.; Bonet-Martínez, E.; Sánchez-Soto, P.J.; Gencel, O.; Eliche-Quesada, D. Synthesis and Characterization of Alkali-Activated Materials Containing Biomass Fly Ash and Metakaolin: Effect of the Soluble Salt Content of the Residue. *Arch. Civil. Mech. Eng.* **2022**, *22*, 121. [CrossRef]
15. Du, Y.; Pundienė, I.; Pranckevičienė, J.; Kligys, M.; Girskas, G.; Korjakins, A. A Review of Biomass Wood Ash in Alkali-Activated Materials: Treatment, Application, and Outlook. *J. Compos. Sci.* **2024**, *8*, 161. [CrossRef]
16. Papa, E.; Medri, V.; Amari, S.; Manaud, J.; Benito, P.; Vaccari, A.; Landi, E. Zeolite-Geopolymer Composite Materials: Production and Characterization. *J. Clean. Prod.* **2018**, *171*, 76–84. [CrossRef]
17. Nikolov, A.; Rostovsky, I.; Nugteren, H. Geopolymer Materials Based on Natural Zeolite. *Case Stud. Constr. Mater.* **2017**, *6*, 198–205. [CrossRef]
18. Villa, C.; Pecina, E.T.; Torres, R.; Gómez, L. Geopolymer Synthesis Using Alkaline Activation of Natural Zeolite. *Constr. Build. Mater.* **2010**, *24*, 2084–2090. [CrossRef]
19. Wang, J.; Hu, Z.; Chen, Y.; Huang, J.; Ma, Y.; Zhu, W.; Liu, J. Effect of Ca/Si and Al/Si on Micromechanical Properties of C(-A)-S-H. *Cem. Concr. Res.* **2022**, *157*, 106811. [CrossRef]
20. Wang, J.; Gao, C.; Tang, J.; Hu, Z.; Liu, J. The Multi-Scale Mechanical Properties of Calcium-Silicate-Hydrate. *Cem. Concr. Compos.* **2023**, *140*, 105097. [CrossRef]
21. Silva, R.V.; De Brito, J.; Dhir, R.K. Properties and Composition of Recycled Aggregates from Construction and Demolition Waste Suitable for Concrete Production. *Constr. Build. Mater.* **2014**, *65*, 201–217. [CrossRef]
22. Verian, K.P.; Ashraf, W.; Cao, Y. Properties of Recycled Concrete Aggregate and Their Influence in New Concrete Production. *Resour. Conserv. Recycl.* **2018**, *133*, 30–49. [CrossRef]
23. Rashid, K.; Rehman, M.U.; de Brito, J.; Ghafoor, H. Multi-Criteria Optimization of Recycled Aggregate Concrete Mixes. *J. Clean. Prod.* **2020**, *276*, 124316. [CrossRef]

https://doi.org/10.3390/buildings16010051

24. Wang, B.; Yan, L.; Fu, Q.; Kasal, B. A Comprehensive Review on Recycled Aggregate and Recycled Aggregate Concrete. *Resour. Conserv. Recycl.* **2021**, *171*, 105565. [CrossRef]
25. Du, Y.; Pundienė, I.; Pranckevičienė, J. Valorisation of Wood Biomass Wastes in Alkali-Activated Mortar with Hybrid Activator. *Ceram. Int.* 2025; *in press*. [CrossRef]
26. Zhu, C. *Development of Alkali-Activated Materials Using Biomass Fly Ash, Phosphogypsum, and Recycled Concrete Aggregates*; Vilnius Gediminas Technical University: Vilnius, Lithuania, 2024.
27. Rożek, P.; Król, M.; Mozgawa, W. Geopolymer-Zeolite Composites: A Review. *J. Clean. Prod.* **2019**, *230*, 557–579. [CrossRef]
28. Jiang, T.; Liu, Z.; Tian, X.; Wu, J.; Wang, L. Review on the Impact of Metakaolin-Based Geopolymer's Reaction Chemistry, Nanostructure and Factors on Its Properties. *Constr. Build. Mater.* **2024**, *412*, 134760. [CrossRef]
29. Luhar, I.; Luhar, S. A Comprehensive Review on Fly Ash-Based Geopolymer. *J. Compos. Sci.* **2022**, *6*, 219. [CrossRef]
30. Du, Y.; Pundiene, I.; Pranckeviciene, J.; Korjakins, A. Sulphate Resistance of Alkali-Activated Material Produced Using Wood Ash. *Materials* **2025**, *18*, 4313. [CrossRef] [PubMed]
31. Vaiciukyniene, D.; Nizeviciene, D.; Mikelioniene, A.; Radzevicius, A. Utilization of Zeolitic Waste in Alkali-Activated Biomass Bottom Ash Blends. *Molecules* **2020**, *25*, 3053. [CrossRef]
32. Rocha, T.d.S.; Dias, D.P.; França, F.C.C.; Guerra, R.R.d.S.; Marques, L.R.d.C.d.O. Metakaolin-Based Geopolymer Mortars with Different Alkaline Activators (Na^+ and K^+). *Constr. Build. Mater.* **2018**, *178*, 453–461. [CrossRef]
33. Rajamma, R.; Labrincha, J.A.; Ferreira, V.M. Alkali Activation of Biomass Fly Ash-Metakaolin Blends. *Fuel* **2014**, *98*, 265–271. [CrossRef]
34. Oliwa, K.; Kozub, B.; Łoś, K.; Łoś, P.; Korniejenko, K. Assessment of Durability and Degradation Resistance of Geopolymer Composites in Water Environments. *Materials* **2025**, *18*, 3892. [CrossRef]
35. Sun, Y.; Liu, S.; Zhang, S.; Li, G.; Guan, X.; Zhu, J.; Liu, Z.; Wang, F. Optimized Ca/Si Ratio Design for Ultra-High Strength Carbon Mineralization Materials: Integrating Synergistic Mineral Effects and Crystal Grain Size Enhancement. *Constr. Build. Mater.* **2025**, *494*, 143398. [CrossRef]
36. Xie, Y.; Zhou, H.; Wang, J.; Meng, H.; Wei, S.; Sun, J.; Hu, Y. Enhancing Autoclaved Aerated Concrete Performance via Replacement of Fly Ash with Granite Stone Powder and Steel Slag: Critical Role of Ca/Si Ratio. *Constr. Build. Mater.* **2025**, *477*, 141360. [CrossRef]
37. Lei, Z.; Wang, E.; Li, Z.; Shi, X. Ultrafine Rice Husk Ash in Alkali-Activated Slag Systems: Synergistic Modulation of Si/Ca and Si/Al Ratios to Improve Mechanical Performance and Dimensional Stability. *Constr. Build. Mater.* **2025**, *492*, 142969. [CrossRef]
38. de Oliveira, L.B.; de Azevedo, A.R.G.; Marvila, M.T.; Pereira, E.C.; Fediuk, R.; Vieira, C.M.F. Durability of Geopolymers with Industrial Waste. *Case Stud. Constr. Mater.* **2022**, *16*, e00839. [CrossRef]
39. Puligilla, S.; Mondal, P. Role of Slag in Microstructural Development and Hardening of Fly Ash-Slag Geopolymer. *Cem. Concr. Res.* **2013**, *43*, 70–80. [CrossRef]
40. Amran, M.; Debbarma, S.; Ozbakkaloglu, T. Fly Ash-Based Eco-Friendly Geopolymer Concrete: A Critical Review of the Long-Term Durability Properties. *Constr. Build. Mater.* **2021**, *270*, 121857. [CrossRef]
41. Sprynskyy, M.; Golembiewski, R.; Trykowski, G.; Buszewski, B. Heterogeneity and Hierarchy of Clinoptilolite Porosity. *J. Phys. Chem. Solids* **2010**, *71*, 1269–1277. [CrossRef]
42. Kim, B.; Lee, S.; Chon, C.M.; Cho, S. Setting Behavior and Phase Evolution on Heat Treatment of Metakaolin-Based Geopolymers Containing Calcium Hydroxide. *Materials* **2022**, *15*, 194. [CrossRef]
43. Ulloa, N.A.; Baykara, H.; Cornejo, M.H.; Rigail, A.; Paredes, C.; Villalba, J.L. Application-Oriented Mix Design Optimization and Characterization of Zeolite-Based Geopolymer Mortars. *Constr. Build. Mater.* **2018**, *174*, 138–149. [CrossRef]
44. Statkauskas, M.; Vaičiukynienė, D.; Grinys, A.; Paul Borg, R. Mechanical Properties and Microstructure of Ternary Alkali Activated System: Red Brick Waste, Metakaolin and Phosphogypsum. *Constr. Build. Mater.* **2023**, *387*, 131648. [CrossRef]
45. Ibrahim, J.E.F.M.; Kotova, O.B.; Sun, S.; Kurovics, E.; Tihtih, M.; Gömze, L.A. Preparation of Innovative Eco-Efficient Composite Bricks Based on Zeolite-Poor Rock and Hen's Eggshell. *J. Build. Eng.* **2022**, *45*, 103491. [CrossRef]

Disclaimer/Publisher's Note: The statements, opinions and data contained in all publications are solely those of the individual author(s) and contributor(s) and not of MDPI and/or the editor(s). MDPI and/or the editor(s) disclaim responsibility for any injury to people or property resulting from any ideas, methods, instructions or products referred to in the content.

https://doi.org/10.3390/buildings16010051

buildings

MDPI

Article

Mechanical Performance, Statistical Optimization, and Environmental Impact of Roller-Compacted Concrete Reinforced with Waste and Industrial Fibers

Murteda Ünverdi [1], Sultan Husein Bayqra [1], Yahya Kaya [1], Süleyman Özen [2], Ali Mardani [1,*] and Kambiz Ramyar [3]

[1] Department of Civil Engineering, Faculty of Engineering, Bursa Uludag University, 16059 Bursa, Turkey; murtedaunverdi@uludag.edu.tr (M.Ü.); sultanhuseinbayqra1050@gmail.com (S.H.B.); yahyakaya00@gmail.com (Y.K.)
[2] Department of Civil Engineering, Faculty of Engineering, Bursa Technical University, 16059 Bursa, Turkey; suleyman.ozen@btu.edu.tr
[3] Department of Civil Engineering, Engineering Faculty, Ege University, 35100 Izmir, Turkey; kambiz.ramyar@gmail.com
* Correspondence: ali.mardani16@gmail.com or alimardani@uludag.edu.tr

Abstract

This study evaluates the multi-physical effects of fiber type, length, and dosage on the fresh properties, mechanical performance, and environmental impact of roller-compacted concrete (RCC). Industrial steel (S), polypropylene (PP), and waste steel (WS) fibers with lengths of 30 mm and 60 mm were incorporated into RCC mixtures at volume fractions ranging from 0% to 1.25%. The experimental program included Vebe consistency tests, mechanical strength assessments, and fracture energy measurements, complemented by a simplified cradle-to-gate Global Warming Potential (GWP) analysis. Furthermore, Taguchi and ANOVA methods were employed to statistically determine the hierarchy of influential parameters. The statistical analysis revealed that fiber dosage was the most dominant factor, contributing approximately 68–78% to the variation in compressive, splitting tensile, and flexural strengths, whereas fiber type governed the consistency. Experimentally, S and WS fibers significantly enhanced the post-cracking behavior and fracture energy compared to the brittle control mix, although they imposed a greater penalty on workability than PP fibers. Notably, at comparable dosages, WS fibers exhibited mechanical interlock and toughness performance nearly identical to industrial steel fibers. The environmental analysis demonstrated that replacing industrial steel fibers with WS fibers reduces the embodied carbon by approximately 240 $kgCO_2$-eq/m^3 at the maximum dosage, without compromising mechanical reliability. These findings suggest that waste steel fibers offer a superior performance-to-carbon ratio, making them a viable sustainable alternative for heavy-duty RCC pavements where crack control is prioritized.

Keywords: roller-compacted concrete; waste steel fibers; fracture energy; sustainability; Taguchi method; life cycle assessment

1. Introduction

First developed in the early 1980s, roller-compacted concrete (RCC) is now widely preferred due to its cost-effectiveness and high durability [1,2]. Its most significant distinction from conventional concrete is its much drier consistency. Since RCC has a lower cement content, the risk of cracking caused by temperature gradient is significantly reduced

due to the decrease in exothermic heat generated during cement hydration [3,4]. RCC offers various advantages in both production and application processes. These advantages include eliminating the need for steel reinforcement, lower material costs than conventional concrete, high resistance to extreme hot and cold weather conditions, and a rapid production capacity. The RCC production process is faster and more efficient than conventional concrete, providing a significant advantage in large-scale projects. Due to these characteristics, RCC is widely used in structures where high durability and load-bearing capacity are critical, such as dams, roads, port facilities, and airports [5–12].

Achieving maximum density is crucial for the performance of RCC. In RCC applications, the compaction process should be carried out within 10 min after placement to ensure optimal density and consistency. The entire compaction process must be completed within 45 min after production at the batching plant. In hot weather conditions, this duration should be further reduced, depending on the ambient temperature. Under site conditions, the total placement and compaction time should generally not exceed 35 min. Proper timing during this process is a critical factor in ensuring that the concrete attains its optimal strength and durability. Additionally, completing the application quickly and in a controlled manner helps prevent issues such as segregation within the mixture [6,13–15].

Research indicates that RCC can provide cost savings of approximately 15% to 40% compared to conventional concrete [16,17]. However, the brittle nature of concrete, characterized by low tensile strength and limited deformation capacity, becomes more pronounced as strength increases, resulting in a reduction in energy absorption capacity and toughness [18–20]. These limitations have encouraged researchers to develop innovative solutions, such as fiber reinforcement and the use of alternative materials, to enhance the performance of RCC in various applications.

Despite its rapid construction and economic benefits, plain RCC suffers from inherent brittleness, low tensile strain capacity, and weak resistance to crack propagation, similar to conventional concrete [21,22]. In heavy-duty pavement applications, these deficiencies often manifest as fatigue cracking under repetitive traffic loads and require closely spaced contraction joints to control thermal shrinkage, which increases long-term maintenance costs [13,23]. While industrial steel fibers are known to mitigate these issues by bridging cracks and enhancing energy absorption, their high cost and carbon footprint limit their large-scale usage [24]. Consequently, there is a critical practical need to validate sustainable alternatives, specifically waste steel (WS) fibers, that can address the ductility deficit of RCC without compromising its economic viability.

Fiber reinforcement has become a significant method for enhancing the ductility and energy absorption capacity of concrete [25,26]. The presence of fibers improves the impact resistance of concrete by delaying crack formation [10,11,14,15]. Today, fiber-reinforced concrete is produced using various types of fibers, including steel [27–30], polypropylene [31,32], glass [33–35], plastic [36,37], and carbon [38,39]. Research has shown that fiber-reinforced concrete significantly improves mechanical and physical properties such as impact resistance [40,41], tensile strength [42–44], abrasion resistance [45–47], and fire resistance [48,49]. Advances in fiber-reinforced concrete technology meet modern engineering requirements, reduce material waste [24,50], and contribute to sustainable production [11,51,52] by enhancing durability [53–55]. Furthermore, the ultimate mechanical efficiency of these composites is heavily governed by fiber distribution, orientation, and compaction-induced anisotropy, which dictate how effectively stresses are transferred across propagating cracks [56,57].

In the literature, various studies have investigated the effects of fibers on RCC. Some selected examples from these studies are presented in Table 1.

https://doi.org/10.3390/buildings16061167

Table 1. Some studies in the literature.

Reference	Properties Studied	Cement (kg/m^3)	Fiber Type	Replacement Level	Observation
[58]	Compressive and flexural strengths	300	Steel, recycled steel tire cord	Steel: 50 kg/m^3 Recycled steel tire cord: 75 and 150 kg/m^3	Fiber addition significantly improved the flexural behavior, while the compressive strength decreased slightly.
[59]	Compressive, flexural and splitting tensile strengths	300	Polypropylene	0.25, 0.50 and 0.75% *	Polypropylene fibers increased compressive strength by 15%, while splitting tensile and flexural strengths experienced slight improvements.
[60]	Compressive and flexural strengths	274	Steel and polypropylene	Steel: 0.4, 0.6 and 0.8% Polypropylene fiber: 0.1%	The addition of steel and polypropylene fibers increased compressive strength by 38% and 20%, respectively. However, incorporating polypropylene fibers led to a 28% reduction in flexural strength.
[61]	Vebe test, compressive, flexural and splitting tensile strengths	299	Polypropylene	0.5, 1.0, 1.5, 2.0 and 2.5 kg/m^3	Vebe time increased by 55%, while compressive, flexural, and splitting tensile strengths increased by 26, 24, and 48%, respectively.
[51]	Compressive, flexural and splitting tensile strengths, elastic modulus	282	Polypropylene, modified olefin, steel	Polypropylene: 0.2 and 0.4% Modified olefin: 0.2 and 0.4% Steel: 0.2 and 0.4%	Modified olefin, polypropylene, and steel fibers enhanced compressive and splitting tensile strengths by 1 to 22% and 6 to 68%, respectively. While modified olefin and polypropylene fibers decreased flexural strength by 7 to 17%, steel fibers, in contrast, increased flexural strength by 8%.
[62]	Compressive and flexural strengths	300	Hooked, twin cone and recycled steel	Hooked and twin cone: 2% Recycled: 2, 4 and 6%	Compressive and flexural strengths increased by 2% with the addition of recycled fiber, while they decreased with higher dosages of other fiber types.
[63]	Vebe test, compressive and flexural strengths, flexural toughness	264	Steel	0.5 and 1.0%	Vebe time increased by up to 70%, while compressive strength slightly decreased. Flexural strength increased by 67 to 82%, and flexural toughness increased by 1400 to 1990%.
[52]	Compressive and flexural strengths	325	Triangular polypropylene fiber	0.25, 0.50 and 0.75%	Flexural strength increased by 11 to 19%, while compressive strength decreased with higher fiber content.
[64]	Vebe test, flexural strength, UPV test, freeze–thaw resistance	281	Recycled polypropylene	1, 3 and 5 kg/m^3	Vebe time increased by up to 76%, fatigue resistance improved, while flexural strength slightly decreased.
[29]	Vebe test, compressive, flexural and splitting tensile strengths	350	Steel, kortta emboss and twist, sinusoidal plastic	Steel: 0.13 to 0.40% Kortta emboss and twist, and sinusoidal plastic: 0.11 to 0.27%.	Steel, kortta emboss and twist, and plastic fibers increased compressive, flexural, and splitting tensile strengths by 2 to 26%, 36 to 65%, and 5 to 25%, respectively.
[65]	Compressive, flexural and splitting tensile strengths	299	Polypropylene, polyolefin	2, 3 and 4 kg/m^3	Polypropylene and polyolefin fibers increased compressive, flexural, and splitting tensile strengths by 5–10%, 10–15%, and 3–17%, respectively.
[66]	Compressive strength, UPV test, abrasion resistance, freeze–thaw resistance	268	Date palm	0.1 and 0.5%	Date palm fibers generally decreased compressive strength by 13 to 53%.
[67]	Compressive, splitting tensile, and uniaxial tensile strengths	456	Micro and macro polypropylene	Micro PPF: 0.9 kg/m^3 Macro PPF: 6 kg/m^3	Polypropylene fibers increased compressive and splitting tensile strengths by 8% to 13% and 9% to 20%, respectively; uniaxial tensile performance was also enhanced.

https://doi.org/10.3390/buildings16061167

Table 1. *Cont.*

Reference	Properties Studied	Cement (kg/m^3)	Fiber Type	Replacement Level	Observation
[68]	Compressive and flexural strengths	260	Basalt	0.5, 0.75, 1.0 and 1.25%	Basalt fibers increased compressive and flexural strengths by 12 to 27% and 13 to 34%, respectively.
[24]	Compressive and flexural strengths, elastic modulus	300	Steel and polypropylene	0.5%	While polypropylene fibers slightly decreased compressive and flexural strengths, as well as elastic modulus, steel fibers slightly increased compressive and flexural strengths, along with elastic modulus.

* By total volume.

Optimizing fiber type and dosage in RCC not only enhances its mechanical properties but also positively influences sustainability indicators in construction applications. Recent studies have demonstrated that incorporating macro-sized fibers can significantly enhance the fatigue resistance and service life of road pavements, thereby reducing maintenance costs over time [13,51,67,69]. Additionally, incorporating alternative fibers, such as natural fibers or recycled materials, enables further reduction in environmental impacts while maintaining the desired performance characteristics. For example, research on the integration of WS fibers into RCC mixtures has demonstrated positive results in terms of both strength and durability, contributing to the circular economy in concrete production [53]. As the construction industry shifts towards more sustainable practices, overcoming the limitations of conventional concrete is becoming increasingly crucial, particularly in projects where strength and durability are critical factors.

Fiber reinforcement in RCC mixtures has been highlighted as an effective method for enhancing mechanical properties [63,70,71], energy absorption capacity [72], ductility [29,73], and resistance to brittle failure [23,52]. However, the CO_2 emissions generated during the production of steel fibers, which are commonly used in RCC mixtures, may conflict with the goals of sustainable production and the circular economy [32]. According to a report on CO_2 emissions associated with steel fibers used in RCC, the amount of CO_2 emitted during steel fiber production for a pavement application has been reported as 10.609 kg per square meter of road [65]. Additionally, studies on the ductile and brittle deformation behavior of WS fiber-reinforced RCC are still quite limited.

Prior investigations on fiber-reinforced RCC pavements consistently indicate that fiber incorporation can substantially enhance post-peak flexural response and residual capacity. At the same time, compressive strength may remain comparable or exhibit only modest reductions depending on mixture design and compaction quality. In the EcoLanes work on steel fiber-reinforced RCC transport pavements, it was shown that primary (industrially produced) steel fibers were more effective than recycled steel tire-cord (RTC) fibers in post-peak flexure, although similar flexural behavior can be achieved by increasing RTC fiber dosage; the same study also emphasized the practical importance of controlling recycled fiber geometry/length and avoiding fiber balling in dry-consistency mixes [58]. Complementary sustainability-driven pavement studies likewise adopted recycled tire-cord wire in SFR-RCC demonstration sections. They highlighted fiber type and dosage as governing parameters in performance and life cycle considerations [74]. More recent RCC pavement research with hooked-end steel fibers and macro-fibers reports clear gains in flexural toughness/residual strength and fracture-related metrics, accompanied by measurable changes in workability/compaction indicators (e.g., moisture demand, Vebe response) and typically more minor changes in compressive strength and splitting tensile strength relative to the flexural benefits [51,63].

https://doi.org/10.3390/buildings16061167

With respect to fiber length, macro steel fibers in the 30–60 mm range are widely used in pavement-grade fiber-reinforced concrete; evidence on conventional concrete shows that, for hooked-end fibers, changing length within 30–60 mm may have limited influence on toughness by itself, implying that in RCC the length effect is often expressed more strongly through compaction, fiber orientation, and interlock/bridging efficiency [75–77]. Against this background, comparative datasets remain scarce that simultaneously benchmark industrial steel against waste/recycled steel and polypropylene (PP) fibers, isolate the effects of 30 mm vs. 60 mm lengths under a consistent RCC compaction regime, and quantify not only strength but also energy absorption and crack control metrics across a broad dosage range. Accordingly, the present study addresses this gap by providing a systematic evaluation of fiber type-length–dosage interactions in RCC and translating the results into engineering-relevant mixture guidance for pavement applications (see Table 1 for the study positioning within the prior literature).

In addition to conventional industrial steel and PP fibers, this study considers WS fibers obtained from industrial offcuts and end-of-life products (e.g., tire-derived steel). WS fibers typically exhibit more irregular geometry and a broader aspect ratio distribution than manufactured steel fibers. However, they offer circular economy benefits by diverting steel waste from landfills and reducing demand for virgin fiber production. Given RCC's crack control and toughness needs, WS fibers are a plausible alternative to conventional steel fibers. Accordingly, the present work explicitly compares WS, S, and PP fibers under standard mix proportions and compaction/curing regimes.

This study addresses key gaps in fiber-reinforced RCC by providing a controlled comparison of three commonly used reinforcement options: industrial steel, PP, and WS fibers. WS fibers are waste-derived, and by valorizing a waste stream and potentially reducing reliance on primary steel fibers, they may reduce the environmental burden associated with fiber reinforcement. However, this sustainability implication is discussed qualitatively in this paper rather than through a quantified life cycle assessment. The effects of S, PP, and WS fibers with lengths of 30 mm and 60 mm were investigated for RCC mixtures produced at five volume fractions ranging from 0% to 1.25%. Fresh-state consistency was evaluated, and 28-day compressive strength, splitting tensile strength, flexural strength, modulus of elasticity, and water absorption were measured and compared across mixtures. The conceptual framework of the study is illustrated in Figure 1.

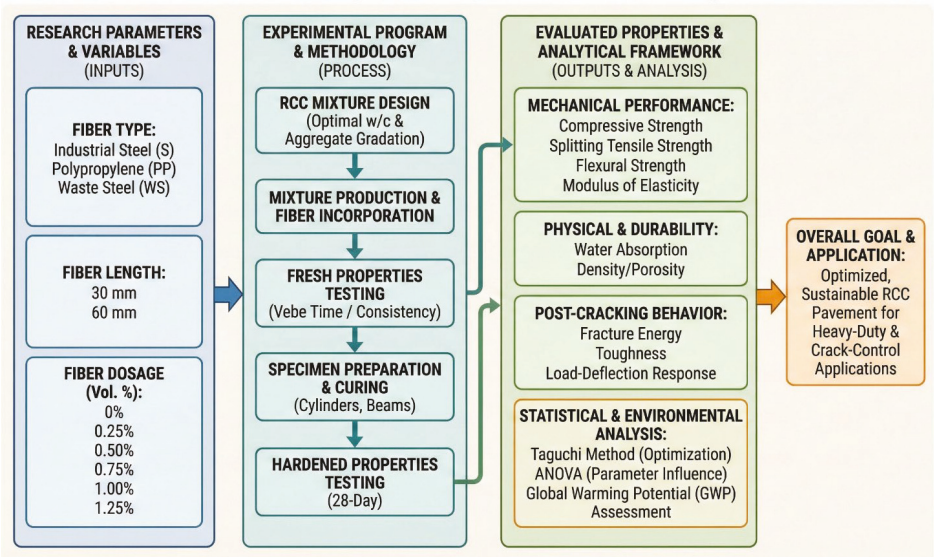

Figure 1. Conceptual framework of the study.

https://doi.org/10.3390/buildings16061167

2. Materials and Methods

2.1. Materials

In this study, a CEM I 42.5 R type cement, conforming to the EN 197-1 standard [78], was used as the binder material. The chemical composition, as well as the physical and mechanical properties provided by the cement manufacturer, are summarized in Table 2.

Table 2. Chemical composition, mechanical and physical properties of cement [49].

Item		Wt. (%)
SiO_2		18.81
Al_2O_3		5.71
Fe_2O_3		3.09
CaO		62.70
MgO (<5.0%)		1.16
SO_3 (<3.5%)		2.39
Na_2O + 0.658 K_2O (<0.6%)		0.52
Cl^- (<0.1%)		0.01
Loss on ignition (<5.0)		3.20
Free CaO (<2.5%)		1.26
Physical properties		
Specific gravity		3.15
Blaine specific surface (cm^2/g)		3530
Retained on 0.045 mm sieve (%)		7.6
Mechanical properties		
Compressive strength (MPa)	1-day	14.7
	2-day	26.80
	7-day	49.80
	28-day	58.5

In this study, crushed limestone aggregates with size fractions of 0–5 mm, 5–12 mm, and 12–22 mm were used. The water absorption capacity and saturated surface dry (SSD) bulk specific gravity values of the aggregates, as determined in accordance with the EN 1097-6 Standard [79], are presented in Table 3. Based on the sieve analysis results of the aggregates, which were determined according to EN 933-1 standard [80], the combined aggregate used in the production of RCC mixtures was selected to consist of 60% 0–5 mm, 20% 5–15 mm, and 20% 15–25 mm particle sizes. The particle size distribution of the combined aggregate, in accordance with the limits specified in TS 802, is shown in Figure 2.

Table 3. Physical properties of aggregates [2].

Type	Size (mm)	SSD Bulk Specific Gravity	Loose Bulk Density (kg/m^3)	Water Absorption Capacity (%)
Crushed limestone	0–5	2.68	1655	1.64
	5–12	2.68	1441	0.51
	12–22	2.69	1405	0.40

https://doi.org/10.3390/buildings16061167

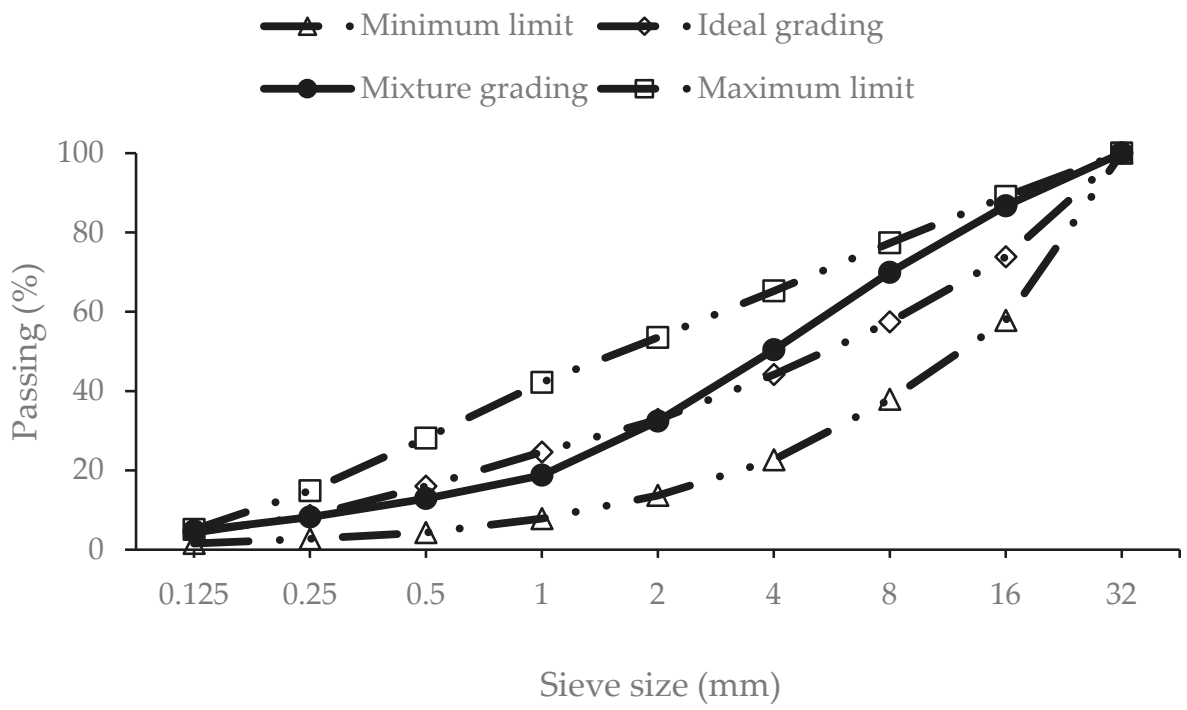

Figure 2. Aggregate gradation curve and its compliance with the TS 802 standard [81].

In the RCC mixtures, hooked-end steel, PP, and WS fibers with lengths of 30 mm and 60 mm were used (Figure 3). Waste fibers were obtained by recycling end-of-life tires. Some properties of the S, PP, and WS fibers are presented in Table 4. The fiber usage ratios were selected as 0%, 0.25%, 0.50%, 0.75%, 1%, and 1.25% by the concrete volume.

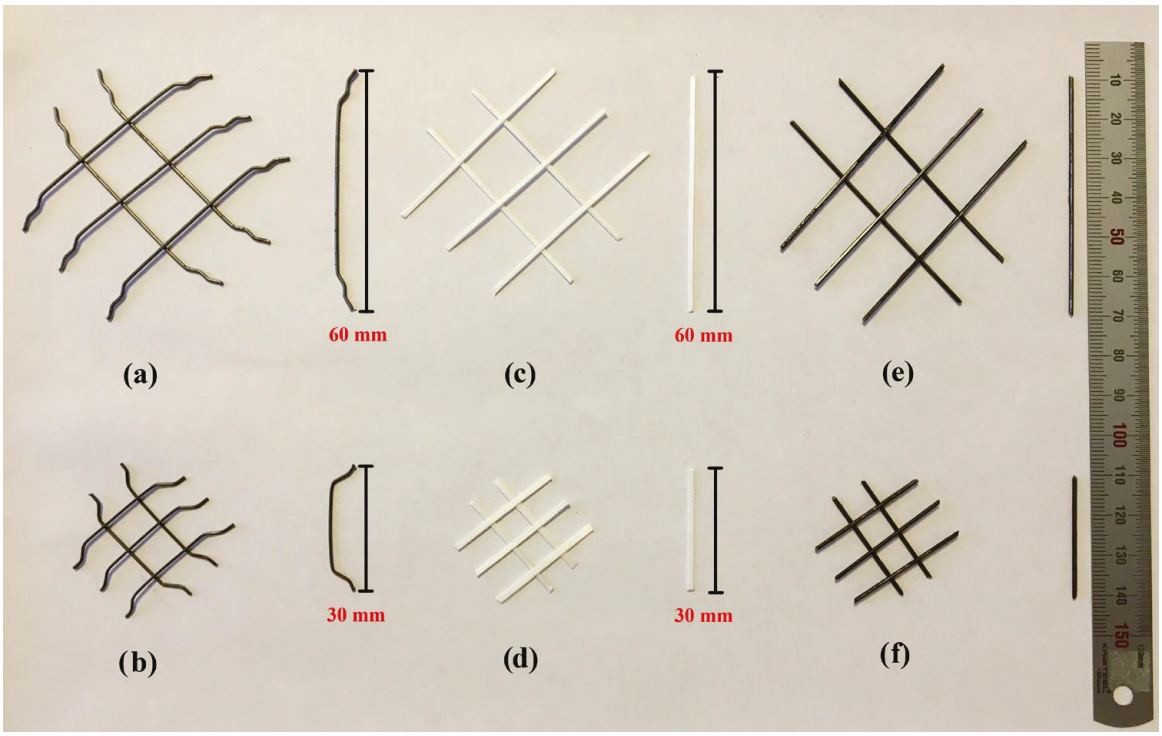

Figure 3. Fibers used in the RCC mixtures are as follows: (**a**) 60 mm steel fiber, (**b**) 30 mm steel fiber, (**c**) 60 mm PP fiber, (**d**) 30 mm PP fiber, (**e**) 60 mm WS fiber, (**f**) 30 mm WS fiber.

https://doi.org/10.3390/buildings16061167

Table 4. The properties of S, PP, and WS fibers used in RCC mixtures.

Properties	**Steel Fiber**		**PP Fiber**		**WS Fiber**	
Length (l) (mm)	30	60	30	60	30	60
Diameter (d) (mm)	0.55	1	1.1	0.9	1	1
Aspect ratio (l/d)	54.5	60	27	67	30	60
Specific gravity	7.8	7.8	0.91	0.91	7.85	7.85
Tensile strength (MPa)	1100–1500	1000–1400	270–420	270–420	900–1300	800–1200
Alkali resistance	High	High	Very High	Very High	High	High
Acid resistance	High	High	High	High	High	High
Melting point (°C)	>1500	>1500	160–170	160–170	>1400	>1400

In addition to their physical and mechanical properties, the embodied carbon characteristics of the constituent materials were identified to assess the environmental impact of the RCC mixtures. The carbon emission factors ($kgCO_2$-eq/kg) used in the Global Warming Potential (GWP) analysis were adopted from the recent literature as follows: 0.86 for CEM I cement, 0.008 for crushed limestone aggregates, 0.0003 for water, 2.50 for industrial steel fibers, and 2.20 for polypropylene fibers. Particularly, for WS fibers, a reduced emission factor of 0.15 $kgCO_2$-eq/kg was defined, which accounts solely for the energy consumed during the collection and shredding processes, excluding the primary production burden allocated to the original tire product.

2.2. Method

2.2.1. Preparation of Mixtures

All RCC mixtures were prepared using a pan-type mixer. The mixing process began with the addition of aggregates of the specified sizes, which were dry-mixed for 30 s. Cement was then introduced and blended with the aggregates for an additional 30 s. Subsequently, the fibers were added gradually and mixed for 30 s to ensure uniform dispersion. Up to this stage, only dry mixing was performed. This procedure facilitated homogeneous fiber distribution and minimized the risk of clumping. After dry mixing, water was slowly added over 30 s while mixing continued. The total mixing time was 5 min. This mixing sequence prevented fiber agglomeration within the mixer, thereby ensuring a uniform distribution throughout the concrete matrix. However, some mixtures exhibited minor clumping when placed into concrete molds.

During the mixing process, great care was taken to ensure that the fibers were evenly distributed within the mixture. The prepared mixtures were placed into 150 mm cubic molds in two layers and 150 × 300 mm cylindrical molds in three layers, following the ASTM C1435 standard [82] for compaction. Similar methods were applied for 100 × 100 × 600 mm beam samples. Each layer was compacted for 20 s using a steel pressing plate and a professional vibrating hammer, in accordance with ASTM C1435.

The specimens were removed from the molds 24 h after casting and placed in a curing tank, as shown in Figure 4, at a temperature of 23 ± 2 °C. Three samples from each specimen were tested for each experiment, and the average values of the results were reported. To ensure the reliability of the test data, the standard deviation (SD) for the replicate specimens was calculated. The variability, evaluated through the coefficient of variation (CV), remained within acceptable limits for fiber-reinforced concrete (typically below 8%). The calculated standard deviations are now reflected in the tabulated results to explicitly indicate the statistical dispersion of the compressive, tensile, and flexural strengths.

https://doi.org/10.3390/buildings16061167



Figure 4. Placing the mixtures in the mold and specimen curing.

The control specimen is labeled as "C", while the fiber-reinforced specimens are named according to the length, type, and usage ratio of the fibers. For example, a specimen containing 0.25% of 60 mm steel fibers is labeled as "S60-0.25," a specimen containing 0.50% of 60 mm PP fibers is labeled as "P60-0.50," and a specimen containing 0.75% of 30 mm waste steel fibers is designated as "WS30-0.75".

2.2.2. Determination of Optimum Water Content and Mixture Proportions

According to the maximum density method specified in ACI 207.5R.99 [83], RCC mixtures were designed with a fixed cement content of 300 kg/m^3. To determine the optimum water content of the mixtures, four mixtures were prepared for each series with a water/cement (w/c) ratio ranging from 0.36 to 0.52.

The prepared RCC mixtures were placed into 150 × 300 mm cylindrical molds in three distinct layers, and each layer was compacted for 20 s, as specified in the ASTM C1435 standard. During the compaction process, a 5 kg steel pressing plate was used to ensure the even distribution of the load applied by the vibrating hammer. To determine the dry unit weight of the concrete, 600 g samples were taken from each of the compacted specimens and dried in an oven at 105 °C until a constant mass was reached [2,6]. The water content of the mixtures was calculated using following equation:

$$w = \frac{m_{wet} - m_{dry}}{m_{dry}} \times 100 \quad (1)$$

Here, w refers to the water content (%), m_{wet} is the mass of the wet specimen (g), and m_{dry} is the mass of the dry specimen after drying in the oven. The wet unit weight (γ_{wet}) is calculated using the equation m/v, where m is the mass of the wet specimen and v is the volume of the specimen. The dry unit weight (γ_{dry}) of each specimen was calculated using the following equation to establish the relationship between the water content of the RCC specimens and their dry unit weight:

$$\gamma_{dry} = \frac{\frac{m}{v}}{1 + w} \quad (2)$$

After calculating the water content and dry unit weight for all the mixtures, curves were drawn to determine the optimum water content corresponding to the maximum dry unit weight. Using the optimum water content, the optimum w/c ratio of the mixtures was calculated. It should be noted that varying the optimum water content for each fiber

https://doi.org/10.3390/buildings16061167

dosage, rather than maintaining a constant w/c ratio, is an essential requirement of the maximum density method for RCC. Because fiber inclusion alters the internal friction and packing density of the granular skeleton, determining the specific optimum moisture for each blend ensures that every mixture is evaluated at its maximum achievable compacted density. This approach prevents under-compaction in high-fiber mixes and over-wetting in the control mix, thereby providing a fair and field-representative comparison of their true mechanical potentials.

For example, the curves for mixtures with a 1.25% fiber content are presented in Figure 5. The optimum water content, maximum dry unit weight (which represents the actual achieved dry density of the mixtures after compaction), w/c ratio, and the theoretical and adjusted mix proportions for the production of 1 m^3 of RCC mixtures are summarized in Tables 5 and 6.

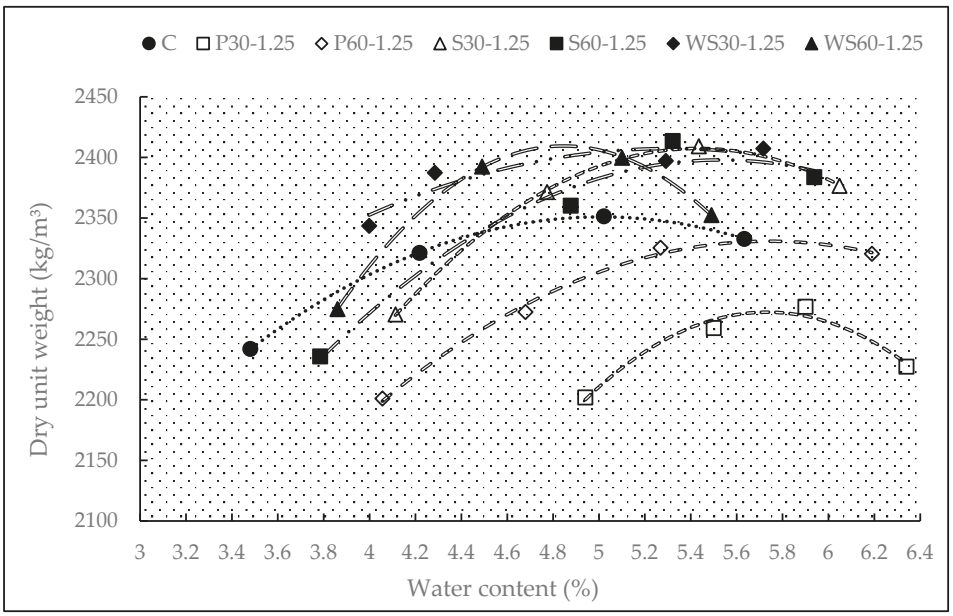

Figure 5. Relationship between water content and dry unit weight of the mixtures.

Table 5. Some properties and theoretical mix proportions of RCCs (kg/m^3).

Mixture	Optimum Water Content (%)	Maximum Dry Unit Weight (kg/m^3)	SSD Aggregate			Water	Cement	Steel Fiber	PP Fiber	WS Fiber	*w/c* Ratio
			0–5 (mm)	5–12 (mm)	12–22 (mm)						
C	4.95	2351	1236	412	414	126	300	0	0	0	0.42
S30-0.25	5.04	2382	1227	409	411	129	300	19.50	0	0	0.43
S30-0.50	5.14	2386	1223	408	409	129	300	39.00	0	0	0.43
S30-0.75	5.21	2392	1214	405	406	132	300	58.50	0	0	0.44
S30-1.0	5.3	2410	1201	400	402	138	300	78.00	0	0	0.46
S30-1.25	5.44	2413	1197	399	400	138	300	97.50	0	0	0.46
S60-0.25	5.05	2378	1227	409	411	129	300	19.50	0	0	0.43
S60-0.50	5.19	2359	1223	408	409	129	300	39.00	0	0	0.43
S60-0.75	5.32	2402	1210	403	405	135	300	58.,50	0	0	0.45
S60-1.0	5.42	2378	1196	399	400	141	300	78.00	0	0	0.47
S60-1.25	5.57	2401	1192	397	399	141	300	97.50	0	0	0.47
P30-0.25	4.93	2303	1227	409	411	129	300	0	2.28	0	0.43
P30-0.50	5.22	2311	1218	406	408	132	300	0	4.55	0	0.44

https://doi.org/10.3390/buildings16061167

Table 5. *Cont.*

Mixture	Optimum Water Content (%)	Maximum Dry Unit Weight (kg/m^3)	SSD Aggregate			Water	Cement	Steel Fiber	PP Fiber	WS Fiber	*w/c* Ratio
			0–5 (mm)	5–12 (mm)	12–22 (mm)						
P30-0.75	5.58	2328	1204	402	403	138	300	0	6.83	0	0.46
P30-1.0	5.21	2280	1186	395	397	147	300	0	9.10	0	0.49
P30-1.25	5.59	2269	1182	394	396	147	300	0	11.38	0	0.49
P60-0.25	4.96	2308	1227	409	411	129	300	0	2.28	0	0.43
P60-0.50	5.25	2337	1218	406	408	132	300	0	4.55	0	0.43
P60-0.75	5.32	2330	1204	402	403	138	300	0	6.83	0	0.46
P60-1.0	5.47	2339	1186	395	397	147	300	0	9.10	0	0.49
P60-1.25	5.59	2327	1182	394	396	147	300	0	11.38	0	0.49
WS30-0.25	4.43	2330	1227	409	411	129	300	0	0	19.63	0.43
WS30-0.50	4.58	2341	1223	408	409	129	300	0	0	39.25	0.43
WS30-0.75	4.71	2356	1214	405	406	132	300	0	0	58.88	0.44
WS30-1.0	4.96	2373	1201	400	402	138	300	0	0	78.50	0.46
WS30-1.25	5.23	2405	1197	399	400	138	300	0	0	98.13	0.46
WS60-0.25	4.38	2357	1227	409	411	129	300	0	0	19.63	0.43
WS60-0.50	4.63	2365	1223	408	409	129	300	0	0	39.25	0.43
WS60-0.75	4.95	2373	1210	403	405	135	300	0	0	58.88	0.45
WS60-1.0	5.26	2400	1196	399	400	141	300	0	0	78.50	0.47
WS60-1.25	4.93	2410	1192	397	399	141	300	0	0	98.13	0.47

Table 6. Adjusted mix proportions of RCCs (kg/m^3).

Mixture	SSD Aggregate			Water	Cement	Steel Fiber	PP Fiber	WS Fiber
	0–5 (mm)	5–12 (mm)	12–22 (mm)					
C	1307	436	438	133	317	0	0	0
S30-0.25	1285	428	430	135	314	20.43	0	0
S30-0.50	1286	429	430	136	315	40.99	0	0
S30-0.75	1277	426	427	139	316	61.53	0	0
S30-1.0	1255	418	420	144	313	81.50	0	0
S30-1.25	1256	419	420	145	315	102.27	0	0
S60-0.25	1287	429	431	135	315	20.46	0	0
S60-0.50	1300	434	435	137	319	41.46	0	0
S60-0.75	1265	421	423	141	314	61.15	0	0
S60-1.0	1264	422	423	149	317	82.43	0	0
S60-1.25	1254	418	420	148	316	102.58	0	0
P30-0.25	1320	440	442	139	323	0	2.45	0
P30-0.50	1301	434	436	141	320	0	4.86	0
P30-0.75	1269	424	425	145	316	0	7.19	0
P30-1.0	1266	422	424	157	320	0	9.71	0
P30-1.25	1266	422	424	157	321	0	12.18	0
P60-0.25	1317	439	441	139	322	0	2.44	0
P60-0.50	1289	430	432	140	317	0	4.81	0
P60-0.75	1268	423	424	145	316	0	7.19	0

https://doi.org/10.3390/buildings16061167

Table 6. *Cont.*

Mixture	SSD Aggregate			Water	Cement	Steel Fiber	PP Fiber	WS Fiber
	0–5 (mm)	5–12 (mm)	12–22 (mm)					
P60-1.0	1234	411	413	153	312	0	9.47	0
P60-1.25	1234	411	414	154	313	0	11.88	0
WS30-0.25	1314	438	440	138	321	0	0	21.01
WS30-0.50	1310	437	438	138	321	0	0	42.05
WS30-0.75	1296	433	434	141	320	0	0	62.87
WS30-1.0	1275	425	427	146	318	0	0	83.33
WS30-1.25	1260	420	421	145	316	0	0	103.31
WS60-0.25	1299	433	435	137	318	0	0	20.77
WS60-0.50	1297	433	434	137	318	0	0	41.62
WS60-0.75	1280	426	429	143	317	0	0	62.30
WS60-1.0	1253	418	419	148	314	0	0	82.23
WS60-1.25	1250	416	418	148	315	0	0	102.89

2.2.3. Experimental Study

The consistency of the RCC mixtures was evaluated using the Vebe test in accordance with ASTM C1170 [84], Procedure A. The Vebe time was determined by measuring the time required for the mortar ring around the mold to fill the gap between the mold's inner surface and a 22.7 kg pressure plate.

The water absorption of the RCC specimens after immersion was determined in accordance with ASTM C642 [85] using 150 mm cube specimens at 28 days. Specimens were oven-dried to constant mass, cooled, then immersed in water (21 °C) until the saturated surface dry (SSD) mass stabilized; absorption after immersion was calculated from the oven-dry and SSD masses as a percentage. Absorption after immersion and boiling was not measured in this study.

The 28-day compressive strength and splitting tensile strength were measured in accordance with EN 12390-3 [86] and EN 12390-6 standards [87], respectively, using 150 mm cube specimens.

Before performing the flexural strength test, a notch with a depth of 1.5 cm was made at the center of the beam specimens to place a crack gauge. The flexural strength test was conducted using the four-point loading method outlined in EN 12390-5 [88], as shown in Figure 6.

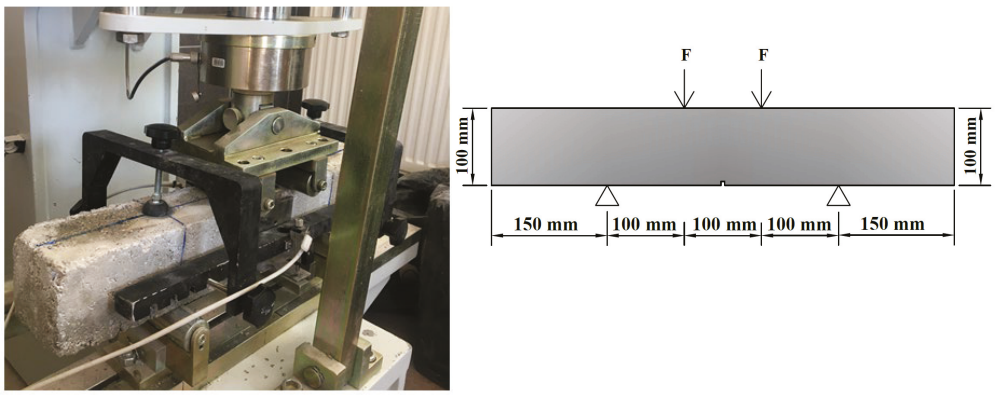

Figure 6. Flexural strength test setup.

https://doi.org/10.3390/buildings16061167

Flexural strength was calculated using the following equation:

$$\sigma = \frac{F \times L}{B \times (H - a)^2} \tag{3}$$

where σ represents the flexural strength (MPa), F is the maximum applied load (N), L is the span of the beam (mm), B is the width of the beam (mm), H is the height of the beam (mm), and α is the depth of the notch at the fracture region (mm).

According to RILEM TC 50-FM guidelines, the fracture energy of the specimens was determined using the following equation based on the area under the load–displacement curve.

$$G_F = \frac{W_0 + m \cdot g \cdot \delta_0}{A_{lig}} \tag{4}$$

where G_F represents the fracture energy (J/m^2), m is the mass of the beam between the bearings (kg), W_0 is the area under the load–displacement curve (N·m or Joules), g is the acceleration of gravity (9.81 m/s^2), δ_0 is the displacement of the beam (m) and A_{lig} is the effective cross-sectional area at the center of the span in square meters (m^2). To maintain unit consistency, all dimensional parameters (H, B, α and δ_0) recorded in millimeters during testing were converted to meters prior to the computation.

The modulus of elasticity (MPa) of RCC specimens was determined in accordance with ASTM C469 using 28-day cylindrical specimens. The chord modulus of elasticity was calculated using the following equation, considering the stress (σ_2) corresponding to 40% of the ultimate strength and the corresponding axial strain ($\mu\varepsilon_2$), as well as the stress (σ_1) corresponding to a strain value of 5×10^{-5} ($\mu\varepsilon_1$).

$$E = \frac{\sigma_2 - \sigma_1}{\varepsilon_2 - 0.000050} \tag{5}$$

2.2.4. Design of Experiments with Statistical Methods

Within the scope of the study, Taguchi and ANOVA methods were applied to determine the optimal combination of parameters for RCC mixtures. In the Taguchi method, nominal best, biggest best, and smallest best methods, depending on the characteristic type, are used to calculate signal-to-noise (S/N) ratios [89]. In this study, the "biggest is best" as shown in the following equation proposed by Mandal et al. [90] is used as the objective function.

$$\frac{S}{N} = -10 \log\left(\frac{1}{n} \sum_{i=1}^{n} 1/yi^2\right) \tag{6}$$

where yi is the data observed in the i-th experiment and n is the number of observations of the experiment. Specifically, the individual test results of the three replicates (y_1, y_2, y_3) for each mixture were directly incorporated into Equation (6), ensuring that the calculated S/N ratio accounts for both the mean performance and the experimental variability.

For each mixture, three replicate specimens were tested for each experimental measurement, and the reported results are the average of the three values.

In this study, the control factors were selected as fiber type, fiber dosage, and fiber length. The levels of the selected factors are shown in Table 7. The most suitable orthogonal array was selected as L18 (6^1 3^2) to determine the optimum compressive strength, splitting tensile strength, and flexural strength values and to analyze the effects of the factor parameters. The L18 mixed orthogonal array, as shown in Table 7, was used to analyze the experimental results.

https://doi.org/10.3390/buildings16061167

Table 7. Factor parameters and their levels.

Parameters	Symbol	Levels 1	Levels 2	Levels 3	Levels 4	Level 5	Level 6
Fiber dosage	A	0.25	0.5	0.75	1	1.25	-
Fiber length	B	30	60	-	-	-	-
Fiber type	C	PP	S	WS	-	-	-

2.2.5. Life Cycle Assessment (LCA)

A simplified LCA was performed to quantify the sustainability potential of incorporating waste fibers into RCC. The assessment focused on the GWP and was conducted within a "cradle-to-gate" system boundary. This boundary encompasses the raw material extraction, processing, and manufacturing phases (modules A1–A3 according to EN 15978 [91]), excluding transportation to the site, construction, and end-of-life phases. The functional unit was defined as 1 m^3 of compacted RCC mixture. The total GWP for each mixture was calculated using the following equation:

$$GWP_{total} = \sum_{i=1}^{n} (m_i \times EF_i) \quad (7)$$

where GWP_{total} is the total embodied carbon ($kgCO_2$-eq/m^3), m_i is the mass of the i-th constituent material in the mixture (kg/m^3), and EF_i is the carbon emission factor of that material ($kgCO_2$-eq/kg). This comparative analysis aims to demonstrate the net carbon reduction achieved by replacing energy-intensive industrial fibers with waste-derived alternatives at equivalent dosages. The carbon emission factors ($kgCO_2$-eq/kg) used in the GWP analysis were adopted from the recent literature as follows: 0.86 for CEM I cement, 0.008 for crushed limestone aggregates, 0.0003 for water, 2.50 for industrial steel fibers, and 2.20 for polypropylene fibers [24]. Specifically for waste steel (WS) fibers, a reduced emission factor of 0.15 $kgCO_2$-eq/kg was defined (adopted from [92]), which accounts solely for the energy consumed during the collection and shredding processes.

3. Results and Discussion

The results of the tests and experiments conducted within the scope of the study are summarized in Table 8. Unless otherwise stated, all percentage changes are reported relative to the control specimen; where a length effect is discussed, the comparison is made between 30 mm and 60 mm mixtures at the exact fiber dosage.

Table 8. Test and experiment results.

Mixture	Vebe Time (s)	Water Absorption Capacity (%)	Compressive Strength (MPa)	Splitting Tensile Strength (MPa)	Flexural Strength (MPa)	Modulus of Elasticity (GPa)	Fracture Energy (J/m^2)
C	30	1.67	58.10 ± 2.78	3.28 ± 0.15	4.95 ± 0.23	31.85	31
S30-0.25	41	2.02	60.10 ± 2.37	3.35 ± 0.22	5.27 ± 0.30	30.58	1167
S30-0.50	68	2.18	62.21 ± 3.29	3.84 ± 0.18	5.38 ± 0.27	30.79	3440
S30-0.75	74	2.22	62.64 ± 2.23	5.27 ± 0.27	5.56 ± 0.29	32.90	3493
S30-1.0	92	2.44	63.38 ± 2.25	6.17 ± 0.31	5.98 ± 0.34	32.37	3561
S30-1.25	102	2.64	55.46 ± 2.55	6.66 ± 0.34	6.99 ± 0.38	30.90	4263
S60-0.25	44	2.10	61.74 ± 3.16	3.63 ± 0.16	5.38 ± 0.32	32.69	3086
S60-0.50	73	2.39	60.79 ± 2.98	4.92 ± 0.27	6.18 ± 0.27	32.27	3075
S60-0.75	81	3.09	63.32 ± 3.43	5.76 ± 0.32	6.82 ± 0.29	30.16	7297
S60-1.0	89	3.59	64.65 ± 2.39	6.93 ± 0.49	7.22 ± 0.40	31.64	8556
S60-1.25	116	4.11	53.18 ± 2.72	7.41 ± 0.50	7.47 ± 0.40	33.03	9563

https://doi.org/10.3390/buildings16061167

Table 8. *Cont.*

Mixture	Vebe Time (s)	Water Absorption Capacity (%)	Compressive Strength (MPa)	Splitting Tensile Strength (MPa)	Flexural Strength (MPa)	Modulus of Elasticity (GPa)	Fracture Energy (J/m^2)
P30-0.25	34	1.92	59.14 ± 3.22	3.43 ± 0.19	5.01 ± 0.27	31.23	633
P30-0.50	52	1.99	60.56 ± 3.12	3.58 ± 0.23	5.12 ± 0.32	31.06	1017
P30-0.75	59	2.12	60.44 ± 2.81	4.21 ± 0.28	5.21 ± 0.21	31.55	1228
P30-1.0	68	2.26	57.33 ± 2.27	4.17 ± 0.22	5.07 ± 0.21	32.17	1395
P30-1.25	83	2.48	55.13 ± 2.19	4.01 ± 0.19	5.01 ± 0.24	29.76	1559
P60-0.25	38	2.32	59.09 ± 2.82	3.56 ± 0.20	5.24 ± 0.26	31.86	919
P60-0.50	57	2.54	59.32 ± 2.32	4.27 ± 0.23	5.48 ± 0.35	33.32	1523
P60-0.75	69	2.61	58.24 ± 2.79	4.72 ± 0.30	5.62 ± 0.25	31.64	1758
P60-1.0	73	2.57	57.98 ± 2.87	4.43 ± 0.22	5.41 ± 0.27	30.38	3161
P60-1.25	87	2.79	53.07 ± 2.91	4.35 ± 0.28	5.17 ± 0.28	29.64	2680
WS30-0.25	46	1.95	60.56 ± 2.95	3.89 ± 0.27	5.12 ± 0.30	32.02	449
WS30-0.50	57	2.08	59.79 ± 2.37	4.43 ± 0.20	5.34 ± 0.26	32.56	2613
WS30-0.75	69	2.23	62.12 ± 2.51	5.12 ± 0.26	5.63 ± 0.36	32.28	2736
WS30-1.0	78	2.56	62.88 ± 3.30	5.99 ± 0.33	6.01 ± 0.34	33.47	2964
WS30-1.25	93	2.75	56.33 ± 2.42	6.21 ± 0.45	6.74 ± 0.35	30.23	3521
WS60-0.25	47	2.01	60.45 ± 2.44	4.17 ± 0.22	5.47 ± 0.30	32.45	2509
WS60-0.50	66	2.25	62.45 ± 2.51	4.53 ± 0.28	6.11 ± 0.38	30.33	3122
WS60-0.75	77	2.86	58.56 ± 2.52	5.86 ± 0.30	6.68 ± 0.43	31.28	6128
WS60-1.0	86	3.06	63.44 ± 2.87	6.38 ± 0.30	6.99 ± 0.29	32.56	7011
WS60-1.25	101	3.75	54.20 ± 2.02	6.71 ± 0.43	7.15 ± 0.43	33.13	8189

3.1. Vebe Time

The relative Vebe times of the mixtures compared to that of the control mixture are presented in Figure 7. Regardless of the type and dosage of the fibers, the workability of the concretes was negatively affected by fiber reinforcement. Moreover, regardless of the fiber type, the negative impact became more pronounced with increasing fiber dosage and length.

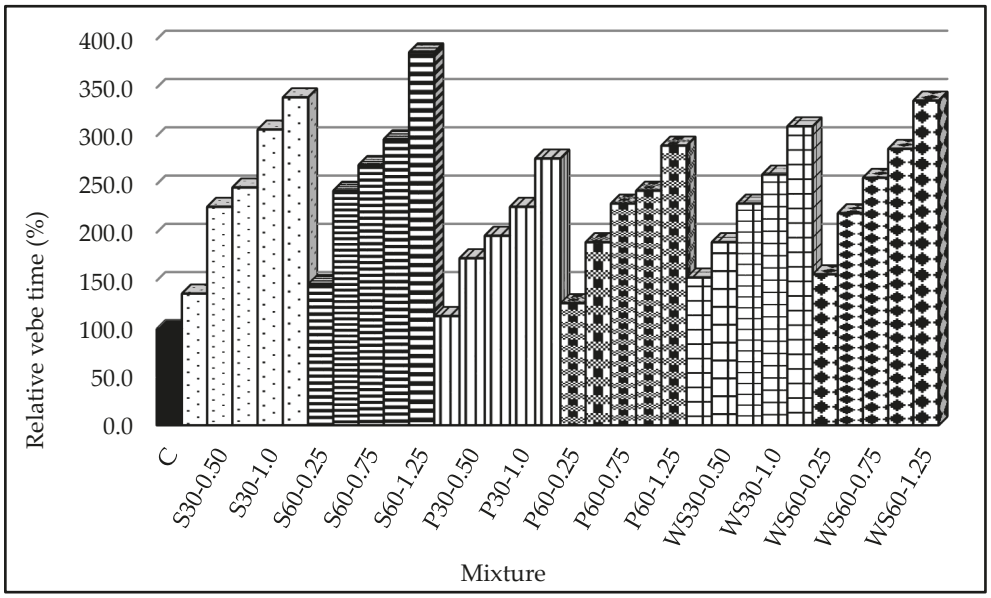

Figure 7. Relative Vebe times of the RCC mixtures.

https://doi.org/10.3390/buildings16061167

It is believed that there are two main reasons for the adverse effect of fibers on the workability of RCC. First, the fibers increase internal friction, which limits the mixture's mobility. Second, the high specific surface area of the fibers negatively affects workability by reducing the amount of paste that would help decrease the viscosity of the concrete. Based on the Vebe times, it is understood that fiber-reinforced RCC requires more effort for placement and compaction. Similar results are also highlighted in studies by Ghahari et al. [93], Rooholamini et al. [21], and Haghnejad & Modarres [64].

The use of 30 mm and 60 mm steel fibers increased the Vebe times by 36–240% and 46–286%, respectively. Increasing the length of the steel fibers from 30 mm to 60 mm further affected the workability negatively, raising the Vebe time by 7–13%. This fact seems to be caused by the geometry of the hooked ends of the fibers and the high specific gravity of the steel material. The higher probability of longer fibers interlocking within the mixture and causing more internal friction can further restrict the mobility of the mixture. These trends are consistent with the compaction-controlled nature of RCC: Fibers increase internal friction within the aggregate skeleton and reduce paste lubrication, thereby increasing the compactive effort required to achieve a target density, as reflected in longer Vebe times.

Similar observations have been reported for fiber-reinforced RCC pavements where mixture parameters and fiber addition influence Vebe time and compactability [64,94]. In contrast to conventional concrete, RCC is a stiff, zero-slump material whose performance depends strongly on roller/vibration compaction and aggregate interlock; consequently, changes in interparticle friction introduced by longer and/or hooked-end fibers can have a more pronounced effect on workability/compactability in RCC than in conventional concrete [51]. Similarly, Benouadah et al. [61] observed that, as fiber length increases, the Vebe time increases by up to 55% for different fiber ratios.

When WS fibers were used, the Vebe time increased by 53–210% (30 mm) and 56–236% (60 mm), respectively, compared with the control mixture. At the exact WS fiber dosage, increasing the fiber length from 30 mm to 60 mm increased the Vebe time by approximately 1–8% (depending on fiber content), indicating a relatively limited length effect compared with the dominant influence of fiber dosage. The performance of WS fibers was found to be better than that of the steel fibers in terms of Vebe time. This is believed to be because the hooked ends of the steel fibers further reduce the mobility of the mixtures [95] (Figure 3).

When mixtures containing PP fibers are examined, the Vebe time increases by 13–176% and 26–190% for fiber lengths of 30 mm and 60 mm, respectively. Increasing the PP fiber length to 60 mm increased the Vebe time by 5–11%. While PP fibers can be more homogeneously mixed within the concrete, steel and WS fibers can interlock during the mixing process, which can negatively affect workability [95]. As the content of steel and WS fibers increases, interlocking may become more intense. This phenomenon has a larger negative impact on the Vebe time compared to the PP fibers. This highlights the importance of optimizing the fiber content to strike a balance between the advantages of fiber reinforcement and the potential adverse effects on workability. This optimization will facilitate both the ease of placing the concrete mixture and improve its durability. These findings are consistent with previous studies by Haghnejad & Modarres [64], Siamardi et al. [96], and Sharbatdar et al. [29].

When comparing the Vebe times of fiber-containing mixtures to those of the control mixture, it is clear that the most significant increase occurred in mixtures containing steel, WS, and PP fibers. As the fiber length increased in the mixtures, the Vebe times showed similar increases for each fiber type. However, it was found that the mixtures containing steel fibers were most affected by the change in fiber length, while the mixtures containing PP fibers were least affected.

https://doi.org/10.3390/buildings16061167

3.2. Water Absorption

The relative water absorption capacities of RCC specimens compared to that of the control specimen are presented in Figure 8. According to CEB-FIB (1989) [97], concrete with water absorption below 3% is classified as high-quality, between 3 and 5% as medium-quality, and above 5% as weak concrete. Based on the results presented in Table 8, most samples fall within the high-quality category. Only five mixtures (S60-0.75, S60-1.0, S60-1.25, WS60-1.0, and WS60-1.25) exhibit a 3% value, placing them in the medium-quality category. This is believed to be due to the excess of trapped air voids caused by the low compressibility of these mixtures. Consequently, the concretes produced in this study are classified as either high- or medium-quality according to CEB-FIB (1989) [97].

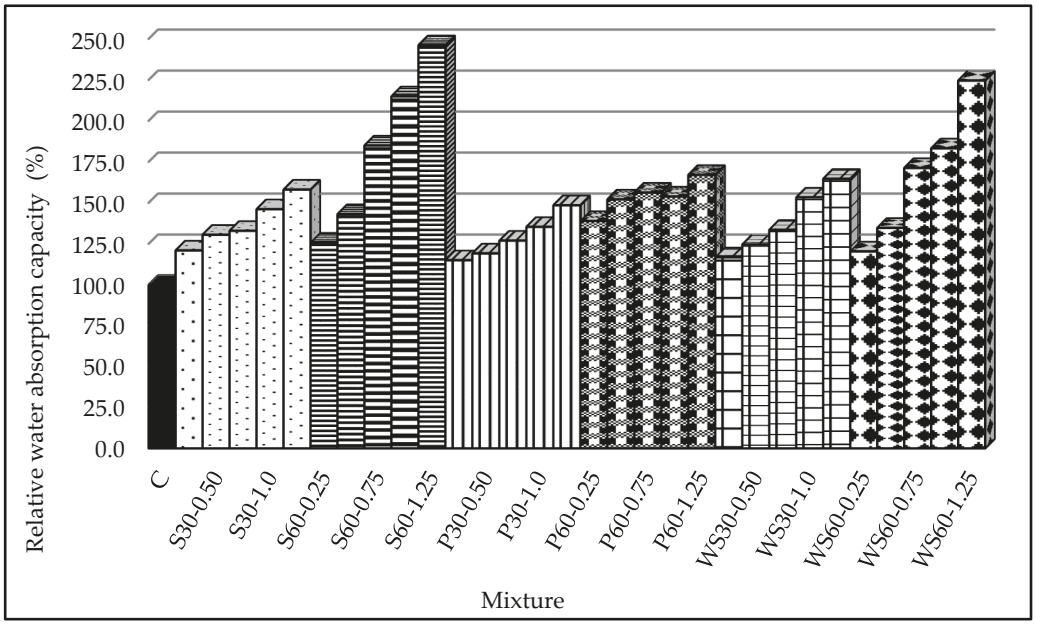

Figure 8. Relative water absorption capacity of RCC specimens.

Regardless of the fiber type, increasing fiber content increased the water absorption capacity, and this increase was more pronounced in specimens with 60 mm fibers (Figure 8). In RCC, absorption (and, by implication, transport susceptibility) is governed primarily by the volume and connectivity of permeable voids, which are highly sensitive to the achieved density under compaction (as reported in Table 5). Fiber addition increases internal friction within the aggregate skeleton and can hinder particle rearrangement during compaction, leading to entrapped air and residual voids; this effect becomes more likely at higher dosages and for longer fibers, and it can be amplified by fiber clustering/balling, which creates local heterogeneity and preferential flow paths [18,70,98].

Moreover, fibers can influence the microstructure at the fiber–matrix interface (ITZ), where microvoids and interfacial discontinuities may increase the connectivity of the pore system. In this context, the "bridging" concept should be interpreted not as physically sealing pores, but as fibers locally modifying the pore network and creating interfacial pathways that can facilitate water ingress. Accordingly, in the present RCC specimens, the observed absorption increases are attributed mainly to compaction-controlled void formation and, secondarily, to fiber distribution/cluster-related heterogeneity [99–102].

It has been found that RCC specimens reinforced with 30 mm and 60 mm steel fibers have higher water absorption capacities compared to the control specimen, with increases of 21–58% and 26–146%, respectively. Increasing the steel fiber length from 30 mm to 60 mm has resulted in a 4–55% increase in water absorption capacity. The difficulty in compressing steel fiber mixtures has led to the formation of residual voids

https://doi.org/10.3390/buildings16061167

during compaction, contributing to this increase. Similarly, 30 mm and 60 mm WS fiber reinforcement has caused an increase in water absorption capacity of 17–65% and 20–125%, respectively. As the length of WS fibers increases, a 3–36% increase in water absorption capacity has been observed. It can be seen that specimens reinforced with WS fibers generally have lower water absorption capacity values than those reinforced with steel fibers. This trend is attributed, at least in part, to differences in fiber geometry and its influence on compactability.

Hooked-end steel fibers can increase internal friction and fiber–aggregate interlocking during mixing and compaction, which may reduce workability and promote the formation of entrapped air/residual voids when consolidation is limited. In contrast, straight fibers typically impose lower flow resistance. Similar observations, lower flow/workability for hooked-end versus straight steel fibers and associated pore formation reflected in higher water absorption have been reported for cementitious composites [103,104].

Compared to the control specimen, the specimens containing 30 mm and 60 mm PP fibers showed an increase in water absorption capacity of 15–49% and 39–67%, respectively. Increasing the length of PP fibers to 60 mm resulted in about a 21% increase in water absorption capacity in the 0.25% fiber mixture and around a 12% increase in the 1.25% fiber mixture. These findings align with results from previous studies, which reported an increase in water absorption capacity ranging from 5% to 80% in RCC mixtures prepared with different types of fibers [53,61,98].

The results indicate that both S and WS fibers increased the water absorption capacity of RCC relative to the control specimen, and the effect became more pronounced at higher fiber contents and for the 60 mm series (Figure 8). These trends are primarily attributed to RCC's compaction-controlled nature: The addition of fiber increases internal friction. It disrupts particle rearrangement during compaction, promoting the entrapped air and residual voids that directly elevate water absorption. Prior RCC pavement research has similarly noted that introducing steel fibers into RCC can create compaction difficulties that affect concrete density and lead to void-related effects [58]. In this study, specimens with hooked-end steel fibers generally showed higher absorption than their WS counterparts at comparable dosages, which is consistent with the greater interlock and compaction resistance expected from hooked-end geometries. In contrast, the straight WS fibers tended to induce fewer compaction-related voids under otherwise identical mixing and compaction conditions.

3.3. Strength

3.3.1. Compressive Strength

The relative compressive strengths of RCC specimens compared to that of the control specimen are shown in Figure 9. Regardless of the fiber type, the addition of fibers to the mixture resulted in a generally slight increase in compressive strength compared to that of the control specimen. The addition of up to 1% steel fibers increased the compressive strength by 3% to 11%, whereas the increase in WS fiber-reinforced counterpart specimens ranged from 3% to 9%. This increase is believed to occur mainly due to the reduction in horizontal stresses and the prevention of crack propagation under load [27,60].

However, at higher steel fiber contents, the compactability of the mixtures decreased, resulting in a 5% to 9% decrease in compressive strength. Similar reductions in compressive strength at higher steel fiber volumes have been attributed to reduced compacted density and entrapped air voids in steel fiber-reinforced concrete [58,63]. In the specimens containing more than 1% WS fibers, there was also a decrease in compressive strength by 3% to 7%. This is due to the increased fiber content creating voids within the matrix, which reduces the material's overall integrity and load-bearing capacity [62].

https://doi.org/10.3390/buildings16061167

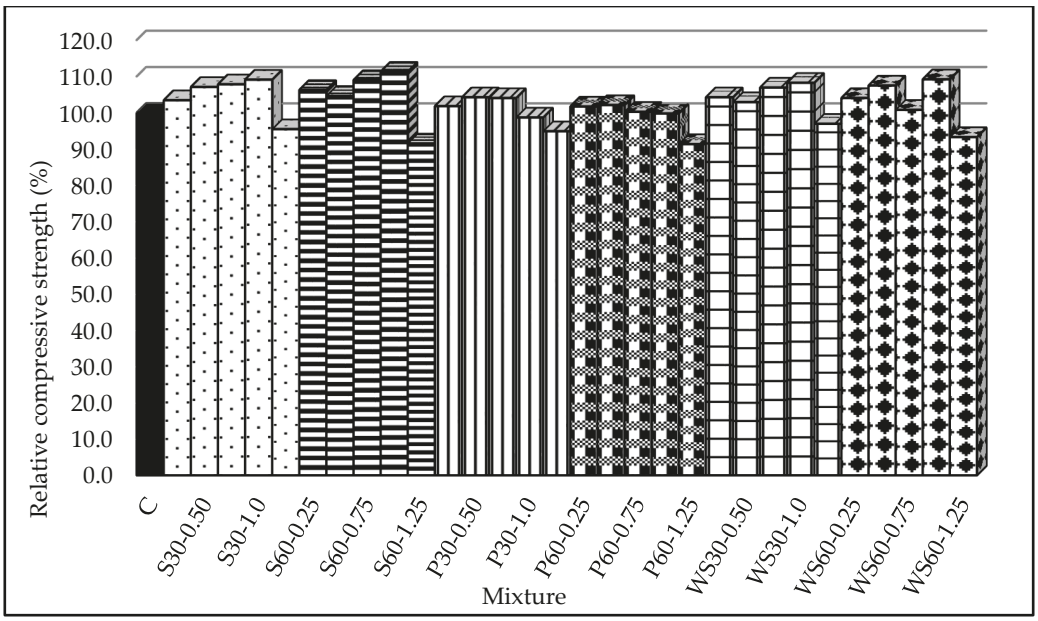

Figure 9. The relative compressive strengths of RCC specimens compared to the control specimen.

As shown in Figure 10, typical of dehydrated mixes, the "wall effect" may result in segregation, disrupting the homogeneity of the samples and leading to reduced strength [28]. This decrease underscores the importance of optimizing fiber content to strike a balance between performance and structural integrity. Through this optimization, the final product can meet the required mechanical properties for the intended application.



Figure 10. Segregation caused by the wall effect in RCC specimens.

It has been observed that PP fiber reinforcement reduces the maximum dry unit weight (maximum dry density) determined from the compaction curves (Table 5) and, together with the increase in the optimum w/c ratio with fiber content, decreases the compressive strength by 5% to 10% (Table 5 and Figure 9). Similar observations have been reported by Yazici et al. [105] and Öztürk [106]. While PP fiber reinforcement can increase compressive strength up to a certain point, exceeding the optimal dosage can lead to adverse effects, including reduced workability and increased porosity [107,108]. This effect is clearly observed in Figure 8, where PP fiber-reinforced specimens exhibit significantly higher water absorption capacity values compared to the control specimen.

A critical trade-off was identified in this study between fiber dosage and matrix compactness. While higher dosages (more than 1.0%) theoretically provide greater crack control, the associated increase in Vebe time creates a stiff matrix that resists effective

https://doi.org/10.3390/buildings16061167

consolidation. The observed drop in compressive strength at high PP and WS dosages is attributed to the "balling effect" and the entrapment of air voids that could not be eliminated even under vibratory compaction [21]. This highlights a practical limitation: The benefits of high fiber volumes in RCC are bounded by the compactability limit of the paver. Therefore, for field applications, a dosage cap (e.g., 1.0%) or the use of workability-enhancing admixtures is recommended to ensure that the ITZ remains dense.

3.3.2. Splitting Tensile Strength

The relative splitting tensile strengths of RCC specimens compared to those of the control specimen are shown in Figure 11. In the RCC specimens with steel and WS fiber reinforcement, an improvement in splitting tensile strength was achieved with increasing fiber content and length. In PP fiber-reinforced specimens, the splitting tensile strength began to decrease beyond the fiber content of 0.75%. Despite this decrease, PP fiber-reinforced RCC specimens exhibited higher splitting tensile strength than the control specimen.

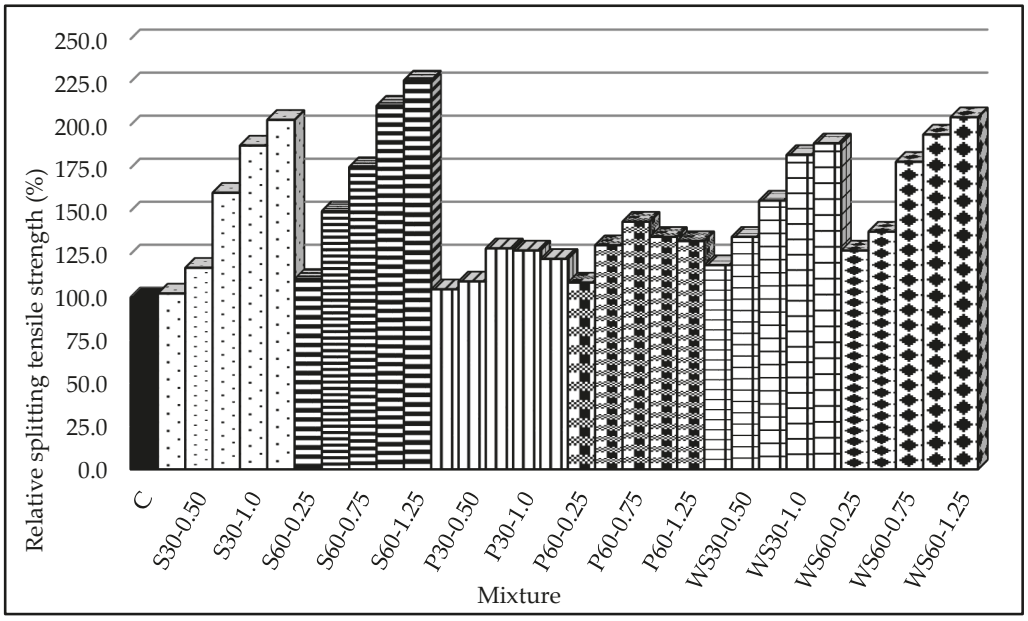

Figure 11. Relative splitting tensile strengths of RCC specimens.

Notably, the CS/STS ratio (computed from the measured 28-day compressive strength and splitting tensile strength) decreased with increasing fiber content, falling below the control value at higher dosages (Table 9), indicating that the tensile capacity improved proportionally more than the compressive strength. Accordingly, Table 9 is included as a compact index to compare the "tensile efficiency" of different fiber types/lengths/dosages, complementing the separate CS and STS results and supporting the benchmarking objective of this study. This indicates that fiber reinforcement is more effective in improving the splitting tensile strength of RCC than its compressive strength. In RCC, fibers bridge developing cracks and transfer tensile stresses across crack faces, delaying crack coalescence and promoting a more gradual post-cracking response. Similar tensile/flexural and fracture-related enhancements associated with fiber bridging and pull-out have been reported in fiber-reinforced RCC and RCC pavement systems, including macro-fiber RCC and steel fiber RCC applications [51,60,63].

https://doi.org/10.3390/buildings16061167

Table 9. Compressive strength/tensile strength ratio of RCC specimens.

Mixture	CS/STS
C	17.1
S30-0.25	17.94
S30-0.50	16.20
S30-0.75	11.89
S30-1.00	10.27
S30-1.25	* 8.33
S60-0.25	17.01
S60-0.50	12.36
S60-0.75	10.99
S60-1.00	9.33
S60-1.25	* 7.18
P30-0.25	17.24
P30-0.50	16.92
P30-0.75	14.36
P30-1.00	13.75
P30-1.25	* 13.75
P60-0.25	16.60
P60-0.50	13.89
P60-0.75	12.34
P60-1.00	13.09
P60-1.25	* 12.20
WS30-0.25	15.57
WS30-0.50	13.50
WS30-0.75	12.13
WS30-1.00	10.50
WS30-1.25	* 9.07
WS60-0.25	14.50
WS60-0.50	13.79
WS60-0.75	9.99
WS60-1.00	9.94
WS60-1.25	* 8.08

* Shows the lowest CS/STS ratio in the relevant specimens.

The addition of 30 mm and 60 mm steel fibers increased the splitting tensile strength by 2–103% and 11–126%, respectively. Increasing the fiber length from 30 mm to 60 mm raised the splitting tensile strength by 8–11%. Similarly, 30 mm and 60 mm WS fibers increased the splitting tensile strength by 18–89% and 27–104%, respectively. Increasing the length of WS fibers resulted in an approximately 7–8% increase in splitting tensile strength. At the lowest fiber content, WS fibers were superior, while at higher fiber contents, steel fibers generally showed better performance. The improved performance of 30 mm WS fiber mixtures at the lowest fiber content is attributed to the lower aspect ratio of the WS fibers used in the mixtures (Table 4), resulting from the uniform dispersion of these

https://doi.org/10.3390/buildings16061167

fibers and their better resistance to crack widening. As the fiber dosage increased, this effect decreased, and the overall performance of the hooked-end steel fibers in the matrix surpassed that of the WS fibers.

In the 30 mm and 60 mm PP fiber-reinforced specimens, a splitting tensile strength improvement of 4–28% and 8–44%, respectively, was achieved. Increasing the PP fiber length to 60 mm resulted in an improvement of 4–12%. It was observed that the length effect of PP fibers was higher than that of steel and WS fibers, although, in terms of splitting tensile strength performance, the order of fibers from the highest to lowest was steel, WS, and PP.

3.3.3. Flexural Strength

Figure 12 presents the relative flexural strengths of RCC specimens compared to those of the control specimen. As expected, fiber reinforcement, regardless of the fiber type or length, resulted in a significant improvement in flexural strength. Consistent with the findings of Sharbatdar et al. [29], it was determined that steel and WS fibers increased flexural strength more than PP fibers. This result can be attributed to the fact that steel and WS fibers, with their higher strength and modulus of elasticity, offer more substantial resistance to crack propagation and widening in the matrix, resulting in improved performance during bending. Additionally, the vibratory compaction process inherent to RCC naturally forces macro-fibers into a predominantly 2D planar orientation perpendicular to the compaction load. This compaction-induced anisotropy favorably aligns the fibers to resist flexural tensile stresses, thereby maximizing their bridging efficiency [56,57].

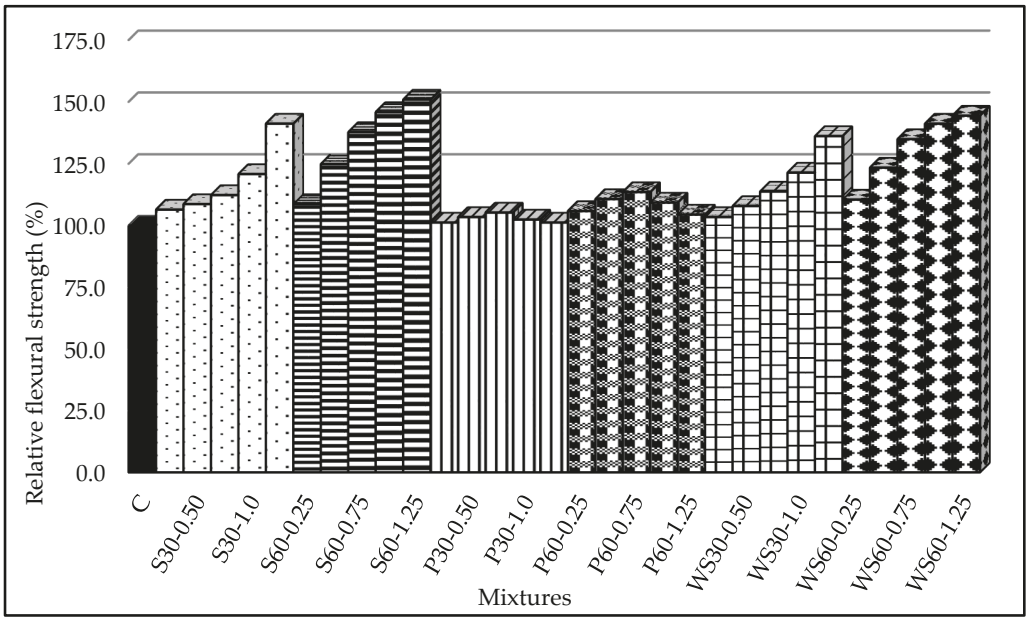

Figure 12. Relative flexural strength of RCC specimens.

The improvement in the flexural strength of RCC specimens upon incorporation of S and WS fibers became more considerable with increasing the length and dosage of the fibers. Additionally, due to the presence of notches in the steel fibers, the pull-out mechanism is more effective compared to WS fibers, resulting in superior flexural strength performance. However, WS fibers are thought to exhibit similar performance compared to steel fibers due to their surface roughness, which can increase matrix adhesion.

In the PP fiber-reinforced specimens, a slight increase in flexural strength was observed as the fiber content and length increased, with the peak occurring at 0.75% fiber content. However, even at high fiber contents (1% and 1.25%), the flexural strength of PP fiber-

https://doi.org/10.3390/buildings16061167

reinforced specimens was greater than that of the control specimen. The improvement in flexural strength is attributed to the fibers preventing the formation and propagation of cracks, and distributing them more effectively within the matrix by altering the crack directions [22,32,70,109]. However, exceeding the optimum fiber content leads to fiber clustering, disrupting the homogeneity of the mixture, weakening the fiber–matrix bond, and increasing the concrete's porosity. This situation negatively impacts the strength properties of the concrete, particularly in mixtures with high fiber content. As noted by other researchers, these factors cause the development of weak regions within the matrix, significantly reducing the overall strength of the material [61,64,70]. However, some studies have reported that PP fibers have either no significant effect or an adverse effect on flexural strength [22,110].

With 30 mm and 60 mm steel fiber reinforcement, increases in flexural strength of 6–41% and 9–51%, respectively, were observed compared to the control specimen. Increasing the length of steel fibers to 60 mm resulted in a 3–7% improvement in flexural strength. Similarly, with 30 mm and 60 mm WS fiber reinforcement, flexural strength improved by 3–36% and 10–44%, respectively. When the length of WS fibers was increased from 30 mm to 60 mm, an improvement of 7–8% was achieved. These values are very close to those obtained in the steel fiber-reinforced specimens. In 30 mm and 60 mm PP fiber-reinforced specimens, the increase in flexural strength ranged from 1 to 5% and from 4 to 14%, respectively. The increase in flexural strength was 4–12% when the length of the PP fibers was extended to 60 mm. These values are far lower than those of the steel and WS fiber specimens (Figure 12).

The remarkable similarity in flexural performance between WS and industrial steel fibers, despite the irregular geometry of WS, can be attributed to the enhanced mechanical interlock mechanism. While industrial fibers rely on hooked ends for anchorage, the twisted and deformed surface texture of WS fibers compensates for the lack of engineered hooks by increasing the frictional bond at the fiber–matrix interface [92]. In contrast, the lower performance of PP fibers is directly linked to their low modulus of elasticity and hydrophobic nature, which weakens the ITZ, making them less effective in bridging macrocracks under high stress [10]. This observation confirms that, for RCC pavements where flexural fatigue is the governing design criterion, the fiber's modulus and surface geometry are more critical than its tensile strength alone.

3.4. Energy Absorption Capacity

Figure 13 presents the load–displacement curves of the RCC specimen with 1.25% steel, WS, and PP fiber reinforcement.

The fracture energies obtained from the load–displacement curves of these specimens, as well as other mixtures in the study, are provided in Table 8. As expected, fiber-reinforced specimens showed significantly higher fracture energies with increasing fiber content and length. This trend aligns with findings from previous studies [111–114], indicating that fiber reinforcement increases the fracture energy of concrete through contributing to the more ductile behavior [92], which in turn, enhances concrete strength by preventing crack propagation [70,105].

In contrast to the abrupt and brittle failure of the control specimen (Figure 14a), the fiber-reinforced samples exhibited remarkable performance by continuing to carry the load after reaching a peak point. The bridging effect of the fibers significantly reduced crack propagation, thereby increasing the deformation capacity [115]. This bridging effect, visible in the cracked sections of the beams (Figure 14b), contributes to a more ductile behavior and increases resistance to displacement. The fibers, by preventing crack coalescence, reduced the energy loss caused by microcracks in the concrete, allowing for the formation of more

https://doi.org/10.3390/buildings16061167

durable structures with higher deformation capacity. This behavior is consistent with the findings of previous studies [29,94,116].

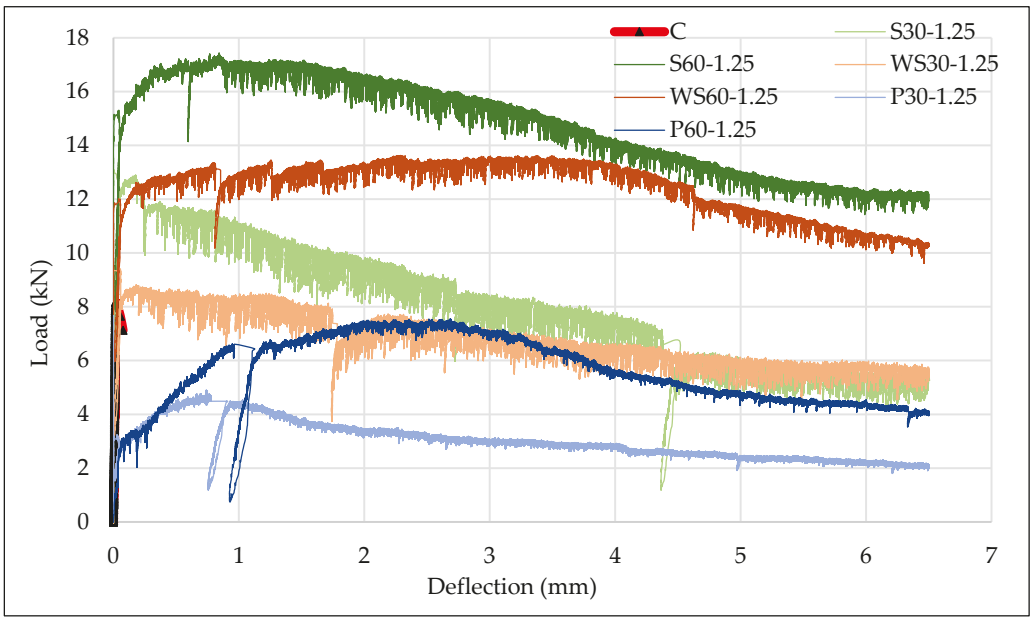

Figure 13. The load–displacement curves of RCC specimens containing 1.25% steel, PP, and WS fibers.

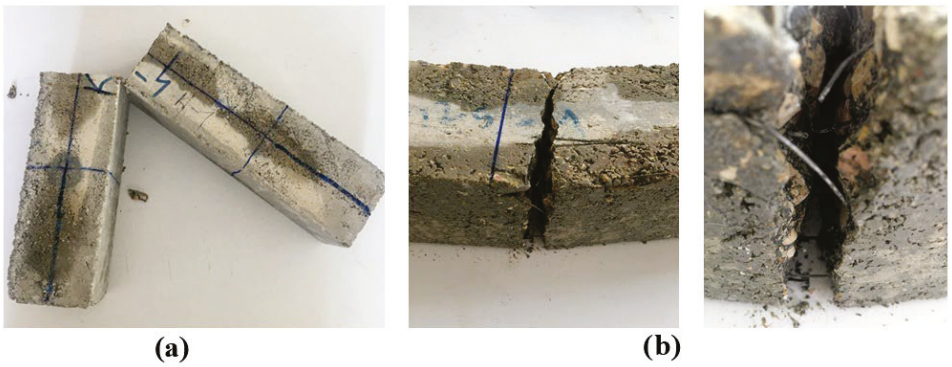

Figure 14. Specimens subjected to flexural test, (**a**) control specimen, (**b**) fiber-reinforced specimen, and the bridging effect.

The specimens with 30 mm and 60 mm long steel fibers exhibited a significant increase in fracture energy compared to the control specimen, ranging from 37 to 137 times and 99 to 308 times, respectively. Increasing the length of the steel fibers to 60 mm improved the fracture energy by a factor of 2.24 to 2.64. Similarly, the 30 mm and 60 mm long WS fibers increased the fracture energy by 14–113 times and 80–264 times, respectively. Increasing the length of the WS fibers from 30 mm to 60 mm resulted in a significant improvement in fracture energy, ranging from 2.32 to 5.59 times. The specimens with 30 mm and 60 mm long PP fiber reinforcement exhibited increases in fracture energy of 20–50 times and 29–86 times, respectively. Increasing the length of PP fibers to 60 mm resulted in an improvement in fracture energy by a factor of 1.45–1.72. These results indicate that the increase in fiber length had the most significant effect on fracture energy in specimens with WS fibers, while PP fiber specimens were the least affected. Effective load transfer provided by fibers depends on the strength of the fiber–matrix bond [21,117]. As seen in Table 8, steel fibers had the most significant positive effect on the fracture energy of concrete due to their superior bonding properties, thus providing more efficient load transfer compared to

https://doi.org/10.3390/buildings16061167

PP and WS fibers. While the WS fibers exhibited similar behavior to steel fibers, PP fibers could more easily detach from the matrix, limiting their bridging effect [60,118].

This study highlights the significant role of steel and WS fiber length in increasing fracture energy. Longer fibers create a larger bond surface with the matrix, exhibiting higher resistance to tensile stress, leading to a substantial increase in fracture energy. In contrast, shorter fibers, with smaller bonding areas, are more easily detached, and the increase in fracture resistance they provide is much smaller compared to that of the longer fibers [27].

The transition from brittle fracture (control specimen) to a pseudo-ductile response (fiber-reinforced specimens) has profound implications for RCC pavement design. The substantial increase in fracture energy observed with S and WS fibers suggests that these composite layers can better redistribute stresses away from crack tips, thereby delaying the propagation of fatigue cracks under repetitive traffic loads [23]. Mechanistically, this improved toughness implies that RCC slabs reinforced with steel or WS fibers could theoretically accommodate wider joint spacings or reduced slab thicknesses compared to plain RCC, as predicted by recent mechanistic–empirical design models [13]. This validates the technical advantage of WS fibers not just as a waste disposal method, but as a structural performance enhancer.

3.5. Modulus of Elasticity

The modulus of elasticity of the concrete (including the control specimen) was found to be in the range of 29.64 and 33.47 GPa (Table 8). The relative elastic modulus values of RCC specimens compared to those of the control specimen are shown in Figure 15.

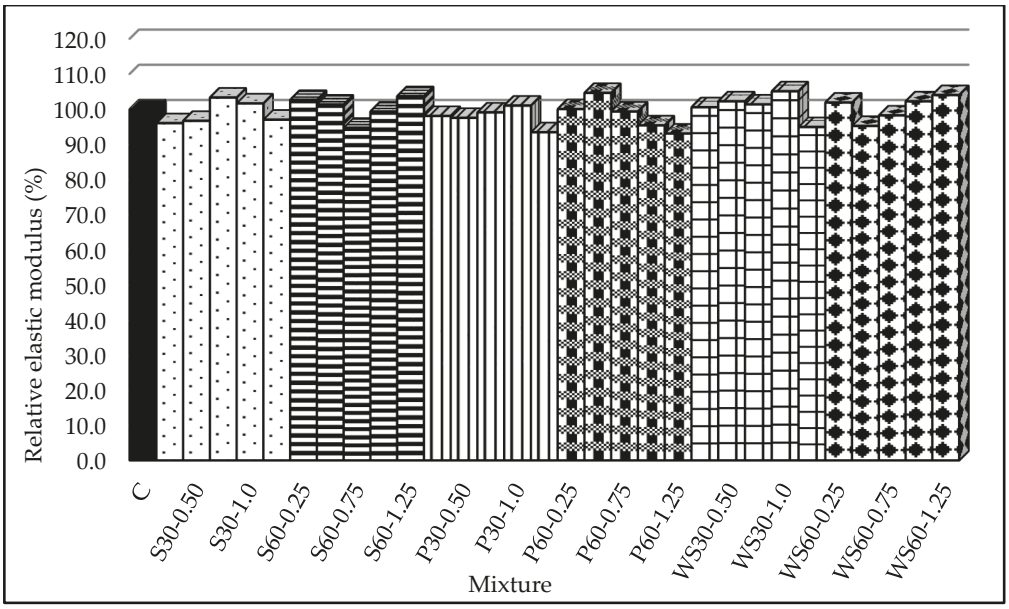

Figure 15. Relative elastic modulus values of RCC specimens and control specimen.

According to the results, the type, length, or dosage of fibers does not have a significant effect on the elastic modulus. This observation has been emphasized by many researchers [27,51,119]. However, the fact still requires further research. It has been reported that the elastic properties of RCC mixtures can be generally affected by various factors, including curing time, compressive strength, fiber type, fiber dosage, paste volume, and aggregate type (ACI 207.5R-99). Moreover, it has been stated that the elastic modulus of RCC is similar to or slightly higher than that of conventional concrete [120]. The fact was attributed to the lower binder content and higher aggregate content of the RCC mixtures

https://doi.org/10.3390/buildings16061167

compared to those of conventional concrete [68,121,122]. In rigid pavements, E_c influences load and thermal responses: Higher E_c increases the radius of relative stiffness (reducing wheel-load bending) but also increases curling/warping stresses under temperature gradients. In our specimens, E_c remained in a narrow range; therefore, E_c (static modulus of elasticity of concrete) does not drive durability differences across fiber types/dosages, which are instead attributed to the observed gains in flexural/tensile capacity and fracture energy (Table 8) [123,124]. However, the results indicated that neither fiber type nor dosage significantly affected stiffness.

3.6. Statistical Analysis

While the experimental program directly compares the fresh and hardened performance of fiber-reinforced RCC mixtures, an additional statistical evaluation was conducted to convert the dataset into an engineering-relevant interpretation of which control factor most strongly governs strength performance and which combination of factor levels provides the best overall strength response. Therefore, the Taguchi method was used to identify the optimum levels of fiber dosage, fiber length, and fiber type based on S/N ratios (robust optimization), and ANOVA was used to quantify the percentage contribution and statistical significance of each factor. Together, these analyses support the practical selection of mixtures and prioritization of parameters for fiber-reinforced RCC, complementing the direct experimental comparisons presented in the preceding sections.

3.6.1. Taguchi Method

The Taguchi method is a statistical experimental design approach that aims to optimize the performance of processes while increasing their robustness to variability. It focuses primarily on identifying the most influential factors among the numerous factors that affect a system's output and maximizing quality by selecting the appropriate levels of these factors. This method utilizes orthogonal arrays to obtain maximum information with a minimum number of experiments. Experimental results are evaluated using the signal-to-noise (S/N) ratio, analyzing not only average performance but also the stability of the results. In this study, fiber type and dosage, whose impact on strength performance we want to examine, were selected as the influencing parameters. The compressive strength (CS), splitting tensile strength (STS), and flexural strength (FS) values for each combination of control factors in the experimental design were measured experimentally. The collected data were processed using the Taguchi technique, and the optimization of the measured RCC mixture factors was achieved through S/N ratios [125]. The highest strength performance values are crucial for RCC performance. Therefore, the "larger-the-better" equation was used in calculating the S/N ratio [126]. The S/N ratios and mean values for the strength parameters are presented in Table 10.

Table 10. Experimental results, S/N ratios, and mean values.

Experiment Number	Control Factors			CS (MPa)	S/N Ratio (CS)	Mean Value (CS)	STS (MPa)	S/N Ratio (STS)	Mean Value (STS)	FS (MPa)	S/N Ratio (FS)	Mean Value (FS)
	Fiber Dosage	Fiber Length	Fiber Type									
1	0.25	30	PP	59.14	35.4376	59.14	3.43	10.7059	3.43	5.01	13.9968	5.01
2	0.25	60	S	61.74	35.8113	61.74	3.63	11.1981	3.63	5.38	14.6156	5.38
3	0.25	-	WS	-	-	-	-	-	-	-	-	-
4	0.5	30	PP	60.56	35.6437	60.56	3.58	11.0777	3.58	5.12	14.1854	5.12
5	0.5	60	S	60.79	35.6766	60.79	4.92	13.8393	4.92	6.18	15.8198	6.18
6	0.5	-	WS	-	-	-	-	-	-	-	-	-
7	0.75	30	S	62.64	35.9370	62.64	5.27	14.4362	5.27	5.56	14.9015	5.56
8	0.75	60	WS	58.56	35.3520	58.56	5.86	15.3580	5.86	6.68	16.4955	6.68

https://doi.org/10.3390/buildings16061167

Table 10. *Cont.*

Experiment Number	Control Factors			CS (MPa)	S/N Ratio (CS)	Mean Value (CS)	STS (MPa)	S/N Ratio (STS)	Mean Value (STS)	FS (MPa)	S/N Ratio (FS)	Mean Value (FS)
	Fiber Dosage	Fiber Length	Fiber Type									
9	0.75	-	PP	-	-	-	-	-	-	-	-	-
10	1	30	WS	62.88	35.9703	62.88	5.99	15.5485	5.99	6.01	15.5775	6.01
11	1	60	PP	57.98	35.2656	57.98	4.43	12.9281	4.43	5.41	14.6639	5.41
12	1	-	S	-	-	-	-	-	-	-	-	-
13	1.25	30	S	55.46	34.8796	55.46	6.66	16.4695	6.66	6.99	16.8895	6.99
14	1.25	60	WS	54.20	34.6800	54.20	6.71	16.5345	6.71	7.15	17.0861	7.15
15	1.25	-	PP	-	-	-	-	-	-	-	-	-
16	-	30	WS	-	-	-	-	-	-	-	-	-
17	-	60	PP	-	-	-	-	-	-	-	-	-
18	-	-	S	-	-	-	-	-	-	-	-	-

The analysis of the effect of each control factor on strength performance was conducted using an "S/N response table." The S/N response results for strength performance are presented in Table 11.

Table 11. Response table for S/N ratios.

CS				STS				FS			
Level	Fiber Dosage	Fiber Length	Fiber Type	Level	Fiber Dosage	Fiber Length	Fiber Type	Level	Fiber Dosage	Fiber Length	Fiber Type
1	14.06	16.00	14.45	1	10.95	13.65	11.57	1	14.31	15.11	14.28
2	15.29	16.48	16.40	2	12.46	13.97	13.99	2	15.00	15.74	15.56
3	17.02	-	17.82	3	14.90	-	15.81	3	15.70	-	16.39
4	16.38	-	-	4	14.24	-	-	4	15.12	-	-
5	18.46	-	-	5	16.50	-	-	5	16.99	-	-
6	-	-	-	6	-	-	-	6	-	-	-
Delta	4.40	0.48	3.36	Delta	5.55	0.32	4.24	Delta	2.68	0.63	2.10
Rank	1	3	2	Rank	1	3	2	Rank	1	3	2

Table 11 (prepared using the Taguchi technique) indicates the optimal levels of the control factors for achieving the best strength performance. The optimal processing parameters for the control factors that maximize the strength performance of RCC can be easily determined from this table. The optimal level for each control factor was identified based on the highest signal-to-noise (S/N) ratio among its levels. Accordingly, the conditions that provide the best strength performance were determined as Level 3 for Factor A, Level 2 for Factor B, and Level 3 for Factor C. As a result, it was found that the optimal strength performance is achieved when WS fibers of 60 mm in length are used at a ratio of 0.75%.

3.6.2. ANOVA Method

ANOVA (Analysis of Variance) is a statistical method used to compare mean differences between multiple groups or factors. Its primary purpose is to determine which factors have a significant impact on system output by partitioning the total variance between observations into different sources. The F value and corresponding *p*-value calculated as a result of the analysis indicate the statistical significance of the factors' influence. Prior to interpreting the ANOVA results, the fundamental assumptions of normality and homoscedasticity (homogeneity of variances) were verified through residual analysis. The

https://doi.org/10.3390/buildings16061167

normal probability plots of the residuals and the plots of residuals versus fitted values confirmed that there were no significant deviations from these assumptions, ensuring the reliability of the established ANOVA models. In this study, ANOVA was also used to analyze the effects of fiber type, dosage, and length on the strength properties of RCC [127]. The ANOVA results for strength properties are presented in Tables 12–14. This analysis was conducted at a 5% significance level and a 95% confidence level. In ANOVA, the significance of control factors was determined by comparing the F-values of each control factor. Additionally, if the *p*-value of a control factor was less than 0.05, the data were considered statistically significant. The effect ratios in the last column of Tables 12–14 represent the percentage contribution of each parameter, indicating the degree of influence on process performance.

Table 12. ANOVA results for CS.

Source	Degree of Freedom (DoF)	Sum of Squares (SS)	Mean Square (MS)	F-Value	*p*-Value	Effect (%)
Fiber dosage	4	52.186	15.975	9.42	0.098	68.03
Fiber length	1	5.491	9.471	5.58	0.142	7.16
Fiber type	2	15.645	7.823	4.61	0.178	20.39
Error	2	3.392	1.696			4.42
Total	9	76.714				100.00

Table 13. ANOVA results for STS.

Source	Degree of Freedom (DoF)	Sum of Squares (SS)	Mean Square (MS)	F-Value	*p*-Value	Effect (%)
Fiber dosage	4	10.829	1.032	5.19	0.144	78.66
Fiber length	1	1.038	0.255	2.28	0.251	5.27
Fiber type	2	1.874	0.937	4.71	0.175	13.25
Error	2	0.399	0.199			2.81
Total	9	14.139				100.00

Table 14. ANOVA results for FS.

Source	Degree of Freedom (DoF)	Sum of Squares (SS)	Mean Square (MS)	F-Value	*p*-Value	Effect (%)
Fiber dosage	4	4.0018	0.4827	2.76	0.283	73.40
Fiber length	1	0.4452	0.1425	0.82	0.462	8.17
Fiber type	2	0.6556	0.3278	1.88	0.348	12.03
Error	2	0.3494	0.1747			6.41
Total	9	5.4521				100.00

According to Table 12, the percentage contributions of fiber dosage, fiber length, and fiber type to the compressive strength of RCC were found to be around 68%, 7%, and 20%, respectively. Therefore, fiber dosage was determined to be the parameter that most significantly affects compressive strength. The error percentage of the ANOVA model was calculated to be 4.42%.

According to Table 13, the percentage contributions of fiber dosage, fiber length, and fiber type to the splitting tensile strength of RCC were found to be around 78%, 5%, and 13%, respectively. Therefore, fiber dosage was determined to be the parameter that most

https://doi.org/10.3390/buildings16061167

significantly affects splitting tensile strength. The error percentage of the ANOVA model was calculated to be 2.81%.

According to Table 14, the percentage contributions of fiber dosage, fiber length, and fiber type to the flexural strength of RCC were found to be about 73%, 8%, and 12%, respectively. Therefore, fiber dosage was determined to be the parameter that most significantly affects flexural strength. The error percentage of the ANOVA model was calculated to be 6.41%.

3.7. LCA Analysis

To quantify the sustainability benefits of using waste fibers, a simplified "cradle-to-gate" LCA was conducted, focusing on the GWP of the RCC mixtures. The analysis considered the embodied carbon of raw materials (cement, aggregates, water) and the fibers. The carbon emission factors ($kgCO_2$-eq/kg) were adopted from the relevant literature, as detailed in Section 2.1 [24]. For WS fibers, a reduced emission factor of 0.15 $kgCO_2$-eq/kg was applied, accounting only for the energy consumed during collection and processing (shredding), as the primary production burden is allocated to the original product (tires) [92].

Figure 16 illustrates the calculated total GWP ($kgCO_2$-eq/m^3) for the control mixture and fiber-reinforced mixtures at the maximum dosage of 1.25%. The results reveal a striking contrast in environmental impact. The incorporation of 1.25% industrial steel fibers (S30 and S60) drastically increased the GWP of the RCC mixture from approx. 290 $kgCO_2$-eq/m^3 (Control) to over 540 $kgCO_2$-eq/m^3, representing an increase of nearly 87%. This surge is attributed to the high energy intensity of steel wire manufacturing. In contrast, the mixtures containing 1.25% WS fibers (WS30 and WS60) exhibited a GWP of only 304 $kgCO_2$-eq/m^3, corresponding to a marginal increase of 4.5% relative to the control.

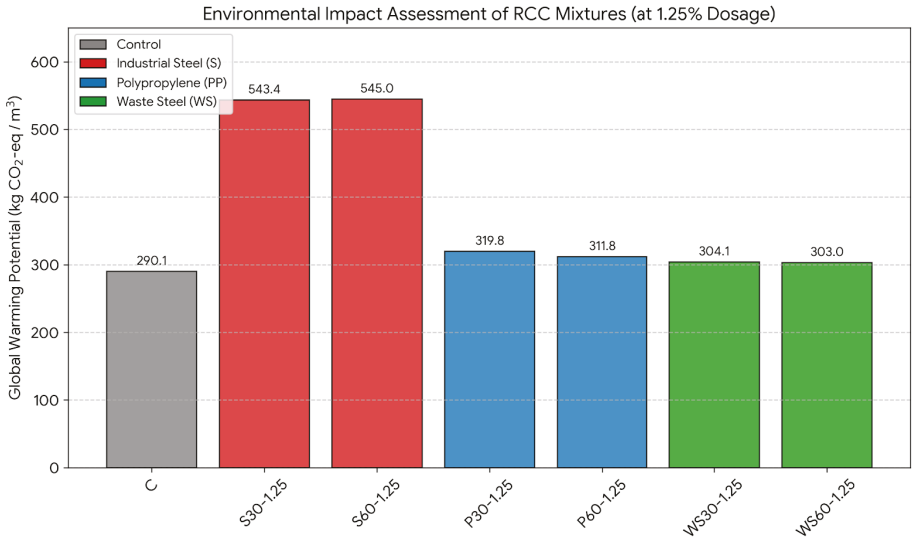

Figure 16. Environmental impact assessment of RCC mixtures.

Consequently, replacing industrial steel fibers with WS fibers at the same dosage results in a net reduction of approximately 240 kg of CO_2 emissions per cubic meter of concrete. Given that WS fibers provided mechanical performance (toughness and fracture energy) comparable to industrial steel fibers in this study, the environmental analysis confirms that WS fibers offer a superior "performance-to-carbon" ratio, validating their viability for sustainable heavy-duty pavement applications.

https://doi.org/10.3390/buildings16061167

3.8. Practical Design Guidelines for Field Applications

To facilitate the field application of these findings, a practical design guideline for WS fiber-reinforced RCC pavements is proposed in Table 15. This guideline categorizes pavement types based on traffic loads and aligns them with the optimal fiber parameters derived from the experimental and statistical results of this study.

Table 15. Practical design guidelines for WS fiber-reinforced RCC pavements.

Pavement Application Level	Typical Use Cases	Recommended WS Fiber Dosage (Vol. %)	Recommended Fiber Length	Key Performance Considerations
Light Traffic	Footpaths, bicycle lanes, residential parking	0.25 to 0.50	30 mm	Ensures good workability and surface finish without requiring heavy compaction equipment. Provides sufficient strength for light loads.
Moderate Traffic	Local streets, urban roads, secondary routes	0.75	60 mm	Represents the statistical optimum for balanced compressive and flexural strength. Offers effective crack control.
Heavy-Duty Traffic	Industrial floors, port facilities, highways	1.00 to 1.25	60 mm	Maximizes fracture energy and fatigue resistance. Requires heavy vibratory rollers or workability-enhancing admixtures due to high stiffness.

4. Conclusions

Based on the multi-physical assessment of roller-compacted concrete reinforced with industrial steel, polypropylene, and waste steel fibers, considering mechanical performance, statistical optimization, and environmental impact, the following conclusions are drawn:

Fiber inclusion significantly increased the Vebe time, indicating reduced workability, which necessitated higher compaction energy. This effect was most pronounced with S and WS fibers due to their rigidity and friction, whereas PP fibers had a milder impact. While fiber reinforcement generally increased water absorption capacity due to the formation of interfacial voids and entrapped air, S and WS fibers slightly increased the maximum dry unit weight compared to the control mixture.

Regardless of fiber type, reinforced mixtures exhibited superior splitting tensile and flexural strengths compared to the control mix. Steel fibers provided the highest strength gains, followed closely by WS fibers. In contrast, compressive strength showed a dosage-dependent behavior: It improved marginally at low dosages (less than 1.0%) for S and WS mixtures but decreased at higher dosages due to fiber balling and the "wall effect," which disrupted mixture homogeneity.

The inclusion of fibers transformed the brittle failure mode of plain RCC into a pseudo-ductile response with substantial gains in fracture energy. Longer fibers (60 mm) and higher dosages (1.25%) were more effective in bridging macro-cracks. Notably, WS fibers demonstrated pull-out resistance and energy absorption capacities comparable to industrial steel fibers, confirming their mechanical efficiency despite their irregular geometry.

According to Taguchi and ANOVA analyses, fiber dosage was identified as the most influential parameter, contributing approximately 68–78% to the variation in mechanical performance (compressive, splitting tensile, and flexural strengths), whereas fiber type and length had less significant statistical effects.

The cradle-to-gate life cycle assessment revealed that replacing industrial steel fibers with waste steel fibers yields significant environmental benefits. At the maximum dosage

https://doi.org/10.3390/buildings16061167

of 1.25%, mixtures with industrial steel fibers exhibited an 87% increase in Global Warming Potential compared to the control, whereas WS fibers caused only a marginal increase of 4.5%. This substitution offers a net reduction of approximately 240 $kgCO_2$-eq/m^3.

The primary contribution of this research is the comprehensive validation of WS fibers as a sustainable, low-carbon alternative to industrial steel fibers for heavy-duty RCC pavements (see Table 15 for practical design guidelines). While PP fibers provide better consistency control, they fall short in enhancing toughness compared to metallic fibers. The study concludes that WS fibers offer a superior "performance-to-carbon ratio," providing mechanical toughness nearly identical to industrial steel fibers while drastically reducing the embodied carbon footprint. Therefore, WS fibers are recommended for green pavement applications where crack control and fatigue resistance are prioritized, provided that the mixture's workability is carefully managed during compaction.

In future studies, RCC specimens incorporating fibers that result in different concrete quality classifications (high, medium, and weak) according to CEB-FIB (1989) [97] may be produced. Comprehensive durability tests, including drying–shrinkage, freeze–thaw resistance, sulfate attack, chloride ion permeability, and high-temperature performance, should be conducted to evaluate long-term behavior.

Author Contributions: Conceptualization, M.Ü., S.H.B. and Y.K.; methodology, M.Ü., S.H.B., Y.K. and A.M.; software, M.Ü., S.H.B., Y.K. and A.M.; validation, M.Ü., S.H.B., Y.K. and A.M.; formal analysis, M.Ü., S.H.B., Y.K. and A.M.; investigation, M.Ü., S.H.B., Y.K., A.M., S.Ö. and K.R.; resources, M.Ü., S.H.B., Y.K. and A.M.; data curation, M.Ü., S.H.B., Y.K. and A.M.; writing—original draft preparation, M.Ü., S.H.B., Y.K. and A.M.; writing—review and editing, S.Ö., A.M. and K.R.; visualization, M.Ü., S.H.B., Y.K. and A.M.; supervision, S.Ö., A.M. and K.R.; project administration, S.Ö., A.M. and K.R.; funding acquisition, S.Ö., A.M. and K.R. All authors have read and agreed to the published version of the manuscript.

Funding: This research was funded by Bursa Uludağ University Science and Technology Center (BAP), grant number "FBG-2025-2550" and the APC was funded by BAP.

Data Availability Statement: The experimental data presented in this study are part of an ongoing research project. Due to institutional requirements regarding unpublished overarching project data, the raw datasets are not publicly available. However, the essential data supporting the findings of this specific manuscript are available from the corresponding author upon reasonable academic request.

Acknowledgments: The authors express their gratitude for the project grant support provided by the Bursa Uludağ University Science and Technology Center (BAP) under the project numbers FYL-2025-2186 and FBG-2025-2550. The authors also express their gratitude for the grant support provided by Scientific and Technological Research Council of Turkey (TUBITAK) under the project number 217M408. They also extend their thanks to the officials of Bursa Ready-Mix Concrete for their assistance in supplying cement and aggregates. The authors also express their profound gratitude to the Turkish Academy of Science (TUBA) for both their financial assistance and moral encouragement.

Conflicts of Interest: The authors declare no conflicts of interest.

References

1. Hashemi, M.; Shafigh, P.; Karim, M.R.B.; Atis, C.D. The Effect of Coarse to Fine Aggregate Ratio on the Fresh and Hardened Properties of Roller-Compacted Concrete Pavement. *Constr. Build. Mater.* **2018**, *169*, 553–566. [CrossRef]
2. Husein Bayqra, S.; Mardani-Aghabaglou, A.; Ramyar, K. Physical and Mechanical Properties of High Volume Fly Ash Roller Compacted Concrete Pavement (A Laboratory and Case Study). *Constr. Build. Mater.* **2022**, *314*, 125664. [CrossRef]
3. Williams, S. Construction of Roller-Compacted Concrete Pavement in the Fayetteville Shale Play Area, Arkansas. *Transp. Res. Rec.* **2014**, *2408*, 47–54. [CrossRef]
4. Sarsam, S.I.; Salih, A.A.; Tawfee, S.D. Assessing Durability of Roller Compacted Concrete. *J. Eng.* **2023**, *20*, 1–14. [CrossRef]
5. Mardani-Aghabaglou, A. Durability of Fly Ash Incorporating Roller Compacted Concrete. Master's Thesis, Ege University, Izmir, Turkey, 2011.

https://doi.org/10.3390/buildings16061167

6. Mardani-Aghabaglou, A.; Ramyar, K. Mechanical Properties of High-Volume Fly Ash Roller Compacted Concrete Designed by Maximum Density Method. *Constr. Build. Mater.* **2013**, *38*, 356–364. [CrossRef]
7. Liu, H.W.; Tian, B.; Hou, R.G.; Sili, L. Research on Roller Compacted Concrete Graduation with Vibration Liquefaction. In *Advanced Materials Research*; Trans Tech Publications Ltd.: Bäch, Switzerland, 2014; Volume 857, pp. 166–172.
8. Chhorn, C.; Kim, Y.K.; Hong, S.J.; Lee, S.W. Evaluation on Compactibility and Workability of Roller-Compacted Concrete for Pavement. *Int. J. Pavement Eng.* **2019**, *20*, 905–910. [CrossRef]
9. Shamsaei, M.; Aghayan, I.; Kazemi, K.A. Experimental Investigation of Using Cross-Linked Polyethylene Waste as Aggregate in Roller Compacted Concrete Pavement. *J. Clean. Prod.* **2017**, *165*, 290–297. [CrossRef]
10. Maafi, N.; Benouadah, A.; Benammar, A.; Kessal, O.; Belkadi, A.A.; Beddar, M. The Effects of Polypropylene Fibers on the Mechanical and Durability Performance of a Roller Compacted Concrete for Pavement. *Int. J. Pavement Res. Technol.* **2025**, *18*, 67–77. [CrossRef]
11. Shafabakhsh, G.; Najafi, M.; Hassani, A.; Sarkar, A. Laboratory Investigation of the Impact of Water-Cement Ratio on the Mechanical Properties and Durability of Roller-Compacted Concrete Mixtures Containing Polypropylene Fibers. *Innov. Infrastruct. Solut.* **2024**, *9*, 416. [CrossRef]
12. Dehghan, S.; Hassani, A. Experimental Investigation of Mechanical Properties of Roller Compacted Concrete Pavement (RCCP) Reinforced with Date Palm Fibres. *Road Mater. Pavement Des.* **2024**, *25*, 2549–2562. [CrossRef]
13. Sengun, E.; Kim, S.; Ceylan, H. A Comparative Study on Structural Design of Plain and Roller-Compacted Concrete for Heavy-Duty Pavements. *Road Mater. Pavement Des.* **2024**, *25*, 392–422. [CrossRef]
14. Shafigh, P.; Hashemi, M.; Nam, B.H.; Koting, S. Optimum Moisture Content in Roller-Compacted Concrete Pavement. *Int. J. Pavement Eng.* **2020**, *21*, 1769–1779. [CrossRef]
15. Latifi, M.R.; Biricik, Ö.; Mardani Aghabaglou, A. Effect of the Addition of Polypropylene Fiber on Concrete Properties. *J. Adhes. Sci. Technol.* **2022**, *36*, 345–369. [CrossRef]
16. Tayabji, S.D.; Sherman, T.W. *Report on Roller-Compacted Concrete Pavements*; American Concrete Institute: Farmington Hills, MI, USA, 2001.
17. Naik, T.R.; Chun, Y.-M.; Kraus, R.N.; Singh, S.S.; Pennock, L.-L.C.; Ramme, B.W. Strength and Durability of Roller-Compacted HVFA Concrete Pavements. *Pract. Period. Struct. Des. Constr.* **2001**, *6*, 154–165. [CrossRef]
18. Sadiqul Islam, G.M.; Gupta, S. Das Evaluating Plastic Shrinkage and Permeability of Polypropylene Fiber Reinforced Concrete. *Int. J. Sustain. Built Environ.* **2016**, *5*, 345–354. [CrossRef]
19. Mardani-Aghabaglou, A.; Yüksel, C.; Hosseinnezhad, H.; Ramyar, K. Performance of Steel Micro Fiber Reinforced Mortar Mixtures Containing Plain, Binary and Ternary Cementitious Systems. *J. Green Build.* **2016**, *11*, 109–130. [CrossRef]
20. Lopez-Uceda, A.; Agrela, F.; Cabrera, M.; Ayuso, J.; López, M. Mechanical Performance of Roller Compacted Concrete with Recycled Concrete Aggregates. *Road Mater. Pavement Des.* **2018**, *19*, 36–55. [CrossRef]
21. Rooholamini, H.; Hassani, A.; Aliha, M.R.M. Evaluating the Effect of Macro-Synthetic Fibre on the Mechanical Properties of Roller-Compacted Concrete Pavement Using Response Surface Methodology. *Constr. Build. Mater.* **2018**, *159*, 517–529. [CrossRef]
22. Ahmadi, M.; Shafabakhsh, G.A.; Hassani, A. Fracture and Mechanical Performance of Two-Lift Concrete Pavements Made of Roller Compacted Concrete and Polypropylene Fibers. *Constr. Build. Mater.* **2021**, *268*, 121144. [CrossRef]
23. Graeff, A.G.; Pilakoutas, K.; Neocleous, K.; Peres, M.V.N.N. Fatigue Resistance and Cracking Mechanism of Concrete Pavements Reinforced with Recycled Steel Fibres Recovered from Post-Consumer Tyres. *Eng. Struct.* **2012**, *45*, 385–395. [CrossRef]
24. Ozturk, O.; Ozyurt, N. Sustainability and Cost-Effectiveness of Steel and Polypropylene Fiber Reinforced Concrete Pavement Mixtures. *J. Clean. Prod.* **2022**, *363*, 132582. [CrossRef]
25. Banthia, N.; Gupta, R. Hybrid Fiber Reinforced Concrete (HyFRC): Fiber Synergy in High Strength Matrices. *Mater. Struct.* **2004**, *37*, 707–716. [CrossRef]
26. Yoo, D.Y.; Yoon, Y.S.; Banthia, N. Flexural Response of Steel-Fiber-Reinforced Concrete Beams: Effects of Strength, Fiber Content, and Strain-Rate. *Cem. Concr. Compos.* **2015**, *64*, 84–92. [CrossRef]
27. Ouedraogo, H.A.; Özen, S.; Kobya, V.; Sagiroglu, S.; Mardani-Aghabaglou, A. Comparison of Fresh and Hardened Properties of Self-Compacting Concrete Mixture from Different Aspect Ratio of Steel Fiber View Point. *J. Green Build.* **2021**, *16*, 115–138. [CrossRef]
28. Mardani-Aghabaglou, A.; Bayqra, S.H.; Nobakhtjoo, A. Specimen Size and Shape Effects on Strength of Concrete in the Absence and Presence of Steel Fibers. *Rev. Constr.* **2021**, *20*, 128–144. [CrossRef]
29. Sharbatdar, M.K.; Rahmati, F. Experimental Evaluation of Multi-Functional Effects of Fibers on Mechanical and Performance Properties of Roller-Compacted Concrete Pavements (RCCP). *Constr. Build. Mater.* **2022**, *316*, 125890. [CrossRef]
30. Zhou, M.; He, X.; Wang, H.; Wu, C.; He, J.; Wei, B. Mechanical Properties and Microstructure of ITZs in Steel and Polypropylene Hybrid Fiber-Reinforced Concrete. *Constr. Build. Mater.* **2024**, *415*, 135119. [CrossRef]
31. Grdic, Z.J.; Curcic, G.A.T.; Ristic, N.S.; Despotovic, I.M. Abrasion Resistance of Concrete Micro-Reinforced with Polypropylene Fibers. *Constr. Build. Mater.* **2012**, *27*, 305–312. [CrossRef]

https://doi.org/10.3390/buildings16061167

32. Mardani-Aghabaglou, A.; Özen, S.; Altun, M.G. Durability Performance and Dimensional Stability of Polypropylene Fiber Reinforced Concrete. *J. Green Build.* **2018**, *13*, 20–41. [CrossRef]
33. Sivakumar, A.; Santhanam, M. A Quantitative Study on the Plastic Shrinkage Cracking in High Strength Hybrid Fibre Reinforced Concrete. *Cem. Concr. Compos.* **2007**, *29*, 575–581. [CrossRef]
34. Barris, C.; Torres, L.; Vilanova, I.; Miàs, C.; Llorens, M. Experimental Study on Crack Width and Crack Spacing for Glass-FRP Reinforced Concrete Beams. *Eng. Struct.* **2017**, *131*, 231–242. [CrossRef]
35. Huang, Z.; Pan, Z.; Zeng, B. Crack Width and Crack Spacing of Glass-FRP Reinforced Concrete Beams under Flexure: Simulation and Analysis. *J. Reinf. Plast. Compos.* **2025**, *45*, 07316844251315868. [CrossRef]
36. Németh, A.; Ibrahim, S.K.; Movahedi Rad, M.; Szalai, S.; Major, Z.; Kocsis Szürke, S.; Jóvér, V.; Sysyn, M.; Kurhan, D.; Harrach, D.; et al. Laboratory and Numerical Investigation of Pre-Tensioned Reinforced Concrete Railway Sleepers Combined with Plastic Fiber Reinforcement. *Polymers* **2024**, *16*, 1498. [CrossRef]
37. Khalel, H.H.Z.; Khan, M.; Starr, A.; Sadawi, N.; Mohamed, O.A.; Khalil, A.; Esaker, M. Parametric Study for Optimizing Fiber-Reinforced Concrete Properties. *Struct. Concr.* **2025**, *26*, 88–110. [CrossRef]
38. Saeed, F.H.; Hejazi, F.; Rashid, R.S.M. Strengthening of Reinforced Concrete Slabs Using Carbon Fiber Reinforced Polymers Rods and Concrete Jacket with a Mechanical Anchorage System. *Constr. Build. Mater.* **2024**, *440*, 137464. [CrossRef]
39. Moussa, A.M.A.; Said, H.O.A.; Khodary, F.; Hassanean, Y.A. Shear Behavior of High-Strength Concrete Beams Reinforced with Carbon Fiber-Reinforced Polymer Bars. *Eng. Struct.* **2025**, *325*, 119411. [CrossRef]
40. Alavi Nia, A.; Hedayatian, M.; Nili, M.; Sabet, V.A. An Experimental and Numerical Study on How Steel and Polypropylene Fibers Affect the Impact Resistance in Fiber-Reinforced Concrete. *Int. J. Impact Eng.* **2012**, *46*, 62–73. [CrossRef]
41. Chen, Z.; Wang, X.; Jiang, K.; Zhao, X.; Liu, X.; Wu, Z. The Splitting Tensile Strength and Impact Resistance of Concrete Reinforced with Hybrid BFRP Minibars and Micro Fibers. *J. Build. Eng.* **2024**, *88*, 109188. [CrossRef]
42. Abdi Moghadam, M.; Izadifard, R.A. Prediction of the Tensile Strength of Normal and Steel Fiber Reinforced Concrete Exposed to High Temperatures. *Int. J. Concr. Struct. Mater.* **2021**, *15*, 47. [CrossRef]
43. Shah, I.; Li, J.; Yang, S.; Zhang, Y.; Anwar, A. Experimental Investigation on the Mechanical Properties of Natural Fiber Reinforced Concrete. *J. Renew. Mater.* **2022**, *10*, 1307–1320. [CrossRef]
44. Almohammed, F.; Thakur, M.S.; Lee, D.; Kumar, R.; Singh, T. Flexural and Split Tensile Strength of Concrete with Basalt Fiber: An Experimental and Computational Analysis. *Constr. Build. Mater.* **2024**, *414*, 134936. [CrossRef]
45. Wang, J.; Fu, R.; Dong, H. Carbon Nanofibers and PVA Fiber Hybrid Concrete: Abrasion and Impact Resistance. *J. Build. Eng.* **2023**, *80*, 107894. [CrossRef]
46. Deng, Q.; Zhang, R.; Liu, C.; Duan, Z.; Xiao, J. Influence of Fiber Properties on Abrasion Resistance of Recycled Aggregate Concrete: Length, Volume Fraction, and Types of Fibers. *Constr. Build. Mater.* **2023**, *362*, 129750. [CrossRef]
47. Yao, D.; Li, J.; Xiao, H.; Yang, W.; Liu, R. Research on the Surface Abrasion Resistance Performance of Basalt Fiber Reinforced Concrete. *J. Build. Eng.* **2024**, *88*, 109125. [CrossRef]
48. Behnood, A.; Ghandehari, M. Comparison of Compressive and Splitting Tensile Strength of High-Strength Concrete with and without Polypropylene Fibers Heated to High Temperatures. *Fire Saf. J.* **2009**, *44*, 1015–1022. [CrossRef]
49. Beytekin, H.E.; Kaya, Y.; Mardani, A.; Sezer, F.Ş. Improving Fire Resistance of Lightweight Concrete Facade Elements by Using Fibers. *Arch. Civ. Mech. Eng.* **2025**, *25*, 70. [CrossRef]
50. Nasr, D.; Babagoli, R.; Rezaei, M.; Andarz, A. Evaluating the Influence of Carbon Fiber on the Mechanical Characteristics and Electrical Conductivity of Roller-Compacted Concrete Containing Waste Ceramic Aggregates Exposed to Freeze-Thaw Cycling. *Adv. Mater. Sci. Eng.* **2023**, *2023*, 1308387. [CrossRef]
51. LaHucik, J.; Dahal, S.; Roesler, J.; Amirkhanian, A.N. Mechanical Properties of Roller-Compacted Concrete with Macro-Fibers. *Constr. Build. Mater.* **2017**, *135*, 440–446. [CrossRef]
52. Kolase, P.K.; Desai, A.K. Experimental Study on Monotonic and Fatigue Behaviour of Polypropylene Fibre-Reinforced Roller-Compacted Concrete with Fly Ash. *Road Mater. Pavement Des.* **2019**, *20*, 1096–1113. [CrossRef]
53. Kilic, I.; Gok, S.G. Strength and Durability of Roller Compacted Concrete with Different Types and Addition Rates of Polypropylene Fibers. *Rev. Constr.* **2021**, *20*, 205–214. [CrossRef]
54. Abu-Bakr, M.; Mahmood, H.F.; Mohammed, A.A. Investigation of Metakaolin and Steel Fiber Addition on Some Mechanical and Durability Properties of Roller Compacted Concrete. *Case Stud. Constr. Mater.* **2022**, *16*, e01136. [CrossRef]
55. Arshad, S.; Ahmad, R.; Ali, M. Optimizing RCC Slabs Using Compressive Strenght of Fiber Reinforced Composites. *Tech. J. Univ. Eng. Technol. Taxila* **2024**, *3*, 1010–1015.
56. Kryzhanovskyi, V.; Kroviakov, S.; Shymchenko, P.; Aksyonova, I. Design of Recycled Aggregate Fiber-Reinforced Concrete for Road and Airfield Applications Using Polypropylene Fibers and Fly Ash. *Constr. Mater.* **2026**, *6*, 2. [CrossRef]
57. Fareghian, M.; Afrazi, M.; Fakhimi, A. Soil Reinforcement by Waste Tire Textile Fibers: Small-Scale Experimental Tests. *J. Mater. Civ. Eng.* **2023**, *35*, 04022402. [CrossRef]

https://doi.org/10.3390/buildings16061167

58. Neocleous, K.; Angelakopoulos, H.; Pilakoutas, K.; Guadagnin, M. Fibre-Reinforced Roller Compacted Concrete Transport Pavements. *Proc. Inst. Civ. Eng. Transp.* **2011**, *164*, 97–109. [CrossRef]
59. Üte, A.A. Effects of Fly-Ash and Polypropylen Fibers on the Properties of Roller Compacted Concrete. Master's Thesis, Ege University, İzmir, Turkey, 2008.
60. Madhkhan, M.; Azizkhani, R.; Torki Harchegani, M.E. Effects of Pozzolans Together with Steel and Polypropylene Fibers on Mechanical Properties of RCC Pavements. *Constr. Build. Mater.* **2012**, *26*, 102–112. [CrossRef]
61. Benouadah, A.; Beddar, M.; Meddah, A. Physical and Mechanical Behaviour of a Roller Compacted Concrete Reinforced with Polypropylene Fiber. *J. Fundam. Appl. Sci.* **2017**, *9*, 623. [CrossRef]
62. Jafarifar, N.; Pilakoutas, K.; Angelakopoulos, H.; Bennett, T. Post-Cracking Tensile Behaviour of Steel-Fibre-Reinforced Roller-Compacted-Concrete for FE Modelling and Design Purposes. *Mater. Constr.* **2017**, *67*, e122. [CrossRef]
63. Sukontasukkul, P.; Chaisakulkiet, U.; Jamsawang, P.; Horpibulsuk, S.; Jaturapitakkul, C.; Chindaprasirt, P. Case Investigation on Application of Steel Fibers in Roller Compacted Concrete Pavement in Thailand. *Case Stud. Constr. Mater.* **2019**, *11*, e00271. [CrossRef]
64. Haghnejad, M.; Modarres, A. Effect of Freeze-Thaw Cycles on the Response of Roller Compacted Concrete Pavement Reinforced by Recycled Polypropylene Fibre under Monotonic and Cyclic Loadings. *Road Mater. Pavement Des.* **2020**, *22*, 2704–2720. [CrossRef]
65. Jahanbakhsh, P.; Saberi, K.F.; Soltaninejad, M.; Hashemi, S.H. Laboratory Investigation of Modified Roller Compacted Concrete Pavement (RCCP) Containing Macro Synthetic Fibers. *Int. J. Pavement Res. Technol.* **2023**, *16*, 745–759. [CrossRef]
66. Kessal, O.; Achour, Y.; Noui, A.; Belkadi, A.A.; Benouadah, A.; Belagraa, L.; Maafi, N.; Benammar, A. Bio-Fiber Reinforced Roller Compacted Concrete Designed for Road Construction: Feasibility of Date Palm Fibers in Pavements. *Eur. J. Environ. Civ. Eng.* **2023**, *27*, 1224–1246. [CrossRef]
67. Liang, N.; Yan, R.; Miao, Q.; Cao, G.; Liu, X. Effect of Multi-Scale Polypropylene Fiber Hybridization on Compressive Constitutive Mechanics Parameters of Roller Compacted Concrete. *Struct. Concr.* **2022**, *23*, 441–456. [CrossRef]
68. Yildizel, S.A.; Tayeh, B.A.; Uzun, M. The Evaluation of Calcium Carbonate Added and Basalt Fiber Reinforced Roller Compacted High Performance Concrete for Pavement. *Case Stud. Constr. Mater.* **2022**, *17*, e01293. [CrossRef]
69. Hejazi, S.M.; Abtahi, S.M.; Safaie, F. Investigation of Thermal Stress Distribution in Fiber-Reinforced Roller Compacted Concrete Pavements. *J. Ind. Text.* **2016**, *45*, 896–914. [CrossRef]
70. Liang, N.; You, X.; Yan, R.; Miao, Q.; Liu, X. Experimental Investigation on the Mechanical Properties of Polypropylene Hybrid Fiber-Reinforced Roller-Compacted Concrete Pavements. *Int. J. Concr. Struct. Mater.* **2022**, *16*, 3. [CrossRef]
71. Bayraktar, O.Y.; Turhal, S.; Benli, A.; Shi, J.; Kaplan, G. Application of Recycled Aggregates and Biomass Ash in Fibre-Reinforced Green Roller Compacted Concrete Pavement-Technical and Environmental Assessment. *Int. J. Pavement Eng.* **2025**, *26*, 2458140. [CrossRef]
72. Paryad, P.; Naderpour, H.; Sharbatdar, M.K. Influence of Steel Fiber Characteristics on Mechanical Behavior of Roller-Compacted Concrete Pavement. *J. Struct. Des. Constr. Pract.* **2025**, *30*, 04025016. [CrossRef]
73. Frazão, C.; Camões, A.; Barros, J.; Gonçalves, D. Durability of Steel Fiber Reinforced Self-Compacting Concrete. *Constr. Build. Mater.* **2015**, *80*, 155–166. [CrossRef]
74. Achilleos, C.; Hadjimitsis, D.; Neocleous, K.; Pilakoutas, K.; Neophytou, P.O.; Kallis, S. Proportioning of Steel Fibre Reinforced Concrete Mixes for Pavement Construction and Their Impact on Environment and Cost. *Sustainability* **2011**, *3*, 965–983. [CrossRef]
75. Balaguru, P.; Narahari, R.; Patel, M. Flexural Toughness of Steel Fiber Reinforced Concrete. *ACI Mater. J.* **1992**, *89*, 541–546. [CrossRef] [PubMed]
76. González, D.C.; Mena-Alonso, Á.; Mínguez, J.; Martínez, J.A.; Vicente, M.A. Effect of Fiber Orientation on the Fatigue Behavior of Steel Fiber-Reinforced Concrete Specimens by Performing Wedge Splitting Tests and Computed Tomography Scanning. *Int. J. Concr. Struct. Mater.* **2024**, *18*, 4. [CrossRef]
77. Abdallah, S.; Rees, D.W.A.; Hilal, A.A.; Fan, M.; Ghaffar, S.H.; Ali, H.A. Pull-out Behaviour of Inclined Straight and Hooked-End Fibres in Normal and High Strength Concretes. *Constr. Build. Mater.* **2025**, *471*, 140744. [CrossRef]
78. *EN 197-1*; Cement—Part 1: Composition, Specifications and Conformity Criteria for Common Cements. EN Standards: Newark, DE, USA, 2011.
79. *EN 1097-6*; Tests for Mechanical and Physical Properties of Aggregates—Part 6: Determination of Particle Density and Water Absorption. EN Standards: Newark, DE, USA, 2025.
80. *EN 933-1*; Tests for Geometrical Properties of Aggregates—Part 1: Determination of Particle Size Distribution—Sieving Method. EN Standards: Newark, DE, USA, 2012.
81. *TS 802*; Design of Concrete Mixes. Turkish Standard Institution: Ankara, Turkey, 2016.
82. ASTM C1435/C1435M-20; Standard Practice for Molding Roller-Compacted Concrete in Cylinder Molds Using a Vibrating Hammer. ASTM International: West Conshohocken, PA, USA, 2020.
83. ACI 207.5R-11; Report on Roller-Compacted Mass Concrete. ACI: Farmington Hills, MI, USA, 2011.

https://doi.org/10.3390/buildings16061167

84. ASTM C1170/C1170M-20; Standard Test Method for Determining Consistency and Density of Roller-Compacted Concrete Using a Vibrating Table. ASTM International: West Conshohocken, PA, USA, 2020.
85. *ASTM C642-21*; Standard Test Method for Density, Absorption, and Voids in Hardened Concrete. ASTM International: West Conshohocken, PA, USA, 2022.
86. *EN 12390-3*; Testing Hardened Concrete—Part 3: Compressive Strength of Test Specimens. EN Standards: Newark, DE, USA, 2020.
87. *EN 12390-6*; Testing Hardened Concrete—Part 6: Tensile Splitting Strength of Test Specimens. EN Standards: Newark, DE, USA, 2024.
88. *EN 12390-5*; Testing Hardened Concrete—Part 5: Flexural Strength of Test Specimens. EN Standards: Newark, DE, USA, 2020.
89. Kaya, Y.; Kobya, V.; Mardani, A.; Mardani, N.; Beytekin, H.E. Effect of Grinding Conditions on Clinker Grinding Efficiency: Ball Size, Mill Rotation Speed, and Feed Rate. *Buildings* **2024**, *14*, 2356. [CrossRef]
90. Mandal, N.; Doloi, B.; Mondal, B.; Das, R. Optimization of Flank Wear Using Zirconia Toughened Alumina (ZTA) Cutting Tool: Taguchi Method and Regression Analysis. *Measurement* **2011**, *44*, 2149–2155. [CrossRef]
91. *EN 15978*; Sustainability of Construction Works—Assessment of Environmental Performance of Buildings—Requirements and Guidance. EN Standards: Newark, DE, USA, 2026.
92. Majeed Abed, Z.; Khalil, W.I.; Ahmed, H.K. Tire Wastes and Durability: The Influence of Crumb Rubber and Recycled Steel Fibre on Properties of Roller Compacted Concrete. *Int. J. Pavement Eng.* **2024**, *25*, 2372628. [CrossRef]
93. Ghahari, S.A.; Mohammadi, A.; Ramezanianpour, A.A. Performance Assessment of Natural Pozzolan Roller Compacted Concrete Pavements. *Case Stud. Constr. Mater.* **2017**, *7*, 82–90. [CrossRef]
94. Rooholamini, H.; Hassani, A.; Aliha, M.R.M. Fracture Properties of Hybrid Fibre-Reinforced Roller-Compacted Concrete in Mode I with Consideration of Possible Kinked Crack. *Constr. Build. Mater.* **2018**, *187*, 248–256. [CrossRef]
95. Guerini, V.; Conforti, A.; Plizzari, G.; Kawashima, S. Influence of Steel and Macro-Synthetic Fibers on Concrete Properties. *Fibers* **2018**, *6*, 47. [CrossRef]
96. Siamardi, K.; Shabani, S. Evaluation the Effect of Micro-Synthetic Fiber on Mechanical and Freeze-Thaw Behavior of Non-Air-Entrained Roller Compacted Concrete Pavement Using Response Surface Methodology. *Constr. Build. Mater.* **2021**, *295*, 123628. [CrossRef]
97. CEB. *FIP Durable Concrete Structures—CEB Design Guide*, 2nd ed.; FIB International: Lausanne, Switzerland, 1989.
98. Algin, Z.; Gerginci, S. Freeze-Thaw Resistance and Water Permeability Properties of Roller Compacted Concrete Produced with Macro Synthetic Fibre. *Constr. Build. Mater.* **2020**, *234*, 117382. [CrossRef]
99. Chen, H.; Xie, C.; Fu, C.; Liu, J.; Wei, X.; Wu, D. Orthogonal Analysis on Mechanical Properties of Basalt-Polypropylene Fiber Mortar. *Materials* **2020**, *13*, 2937. [CrossRef] [PubMed]
100. Topçu, İ.; Demirel, O.; Uygunoğlu, T. Physical and Mechanical Properties of Polypropylene Fiber Reinforced Mortars. *J. Polytech.* **2017**, *20*, 91–96.
101. Yap, S.P.; Goh, Y.; Goh, W.X.; Mo, K.H.; Liu, M.Y.J.; Ibrahim, H.A. Relationship between Microstructure and Performance of Polypropylene Fibre Reinforced Cement Composites Subjected to Elevated Temperature. *Eur. J. Environ. Civ. Eng.* **2022**, *26*, 1792–1806. [CrossRef]
102. Simões, T.; Costa, H.; Dias-da-Costa, D.; Júlio, E. Influence of Type and Dosage of Micro-Fibres on the Physical Properties of Fibre Reinforced Mortar Matrixes. *Constr. Build. Mater.* **2018**, *187*, 1277–1285. [CrossRef]
103. Faris, M.A.; Abdullah, M.M.A.B.; Muniandy, R.; Hashim, M.F.A.; Błoch, K.; Jeż, B.; Garus, S.; Palutkiewicz, P.; Mortar, N.A.M.; Ghazali, M.F. Comparison of Hook and Straight Steel Fibers Addition on Malaysian Fly Ash-based Geopolymer Concrete on the Slump, Density, Water Absorption and Mechanical Properties. *Materials* **2021**, *14*, 1310. [CrossRef] [PubMed]
104. Błaszczyk, K.; Smarzewski, P. Influence of Hybrid Fibers on Workability, Mechanical and Dynamic Properties of Ultra-High Performance Concrete. *Appl. Sci.* **2025**, *15*, 5716. [CrossRef]
105. Yazici, Ş.; Mardani-Aghabaglou, A.; Tuyan, M.; Üte, A.A. Mechanical Properties and Impact Resistance of Roller-Compacted Concrete Containing Polypropylene Fibre. *Mag. Concr. Res.* **2015**, *67*, 867–875. [CrossRef]
106. Öztürk, O. Mixture Design and Mechanical Properties of Synthetic Fiber Reinforced Roller Compacted Concrete for Pavements. Master's Thesis, İstanbul Technical University, İstanbul, Turkey, 2018.
107. Saidani, M.; Saraireh, D.; Gerges, M. Behaviour of Different Types of Fibre Reinforced Concrete without Admixture. *Eng. Struct.* **2016**, *113*, 328–334. [CrossRef]
108. Fallah, S.; Nematzadeh, M. Mechanical Properties and Durability of High-Strength Concrete Containing Macro-Polymeric and Polypropylene Fibers with Nano-Silica and Silica Fume. *Constr. Build. Mater.* **2017**, *132*, 170–187. [CrossRef]
109. Qin, Y.; Zhang, X.; Chai, J.; Xu, Z.; Li, S. Experimental Study of Compressive Behavior of Polypropylene-Fiber-Reinforced and Polypropylene-Fiber-Fabric-Reinforced Concrete. *Constr. Build. Mater.* **2019**, *194*, 216–225. [CrossRef]
110. Roesler, J.; Bordelon, A.; Gaedicke, C.; Park, K.; Paulino, G. Fracture Behavior and Properties of Functionally Graded Fiber-Reinforced Concrete. In *AIP Conference Proceedings*; American Institute of Physics: New York, NY, USA, 2008; Volume 973, pp. 513–518.

https://doi.org/10.3390/buildings16061167

111. Wang, J.; Dai, Q.; Si, R.; Guo, S. Mechanical, Durability, and Microstructural Properties of Macro Synthetic Polypropylene (PP) Fiber-Reinforced Rubber Concrete. *J. Clean. Prod.* **2019**, *234*, 1351–1364. [CrossRef]
112. Madhavi, T.C.; Raju, L.S.; Mathur, D. Polypropylene Fiber Reinforced Concrete—A Review. *Int. J. Appl. Eng. Res.* **2014**, *4*, 114–119.
113. Jia, Y.D.; Zhou, Z.W.; Qu, Y.D.; Tian, A.S. Experimental Research on the Fracture Properties of Roller Compacted Steel Fiber Recycled Concrete. In *Advanced Materials Research*; Trans Tech Publications Ltd.: Bäch, Switzerland, 2011; Volume 299–300, pp. 135–138.
114. Scorza, D.; Luciano, R.; Mousa, S.; Vantadori, S. Fracture Behaviour of Hybrid Fibre-Reinforced Roller-Compacted Concrete Used in Pavements. *Constr. Build. Mater.* **2021**, *271*, 121554. [CrossRef]
115. Karahan, O. *Properties of Fiber Reinforced Fly Ash Concrete*; Çukurova University: Adana, Turkey, 2006.
116. Dirikgil, T. *Experimental Research of the Influence of High Temperature on Some of the Physcial and Mechanical Properties of Concrete Reinforced with Polypropylene*; Erciyes University: Kayseri, Turkey, 2009.
117. Li, Z.; Zhou, X.; Ma, H.; Hou, D. *Advanced Concrete Technology*, 2nd ed.; Wiley Blackwell: Toronto, ON, Canada, 2022; ISBN 9781119806219.
118. Aghaeipour, A.; Madhkhan, M. Mechanical Properties and Durability of Roller Compacted Concrete Pavement (RCCP)—A Review. *Road Mater. Pavement Des.* **2020**, *21*, 1775–1798. [CrossRef]
119. Şahin, Y.; Köksal, F. The Influences of Matrix and Steel Fibre Tensile Strengths on the Fracture Energy of High-Strength Concrete. *Constr. Build. Mater.* **2011**, *25*, 1801–1806. [CrossRef]
120. Tayabji, S.D.; Sherman, T.W.; Keifer, O.; Nanni, A.; Piggott, R.W.; Pittman, D.; Ragan, S.A.; Scott, J.A. *State-of-the-Art Report on Roller-Compacted Concrete Pavements*; American Concrete Institute: Detroit, MI, USA, 1995.
121. Calis, G.; Yıldızel, S.A. Investigation of Roller Compacted Concrete: Literature Review. *Chall. J. Concr. Res. Lett.* **2019**, *10*, 63. [CrossRef]
122. Keleş, Ö.F.; Bayrak, O.Ü.; Bayata, H.F. Experimental Investigation on Mechanical Properties of Sustainable Roller Compacted Concrete Pavement (RCCP) Containing Waste Rubbers as Alternative Aggregates. *Constr. Build. Mater.* **2024**, *424*, 135930. [CrossRef]
123. Wang, J.; Luo, X.; Huang, X.; Ye, Y.; Ruan, S. Analysis on Effects of Joint Spacing on the Performance of Jointed Plain Concrete Pavements Based on Long-Term Pavement Performance Database. *Materials* **2022**, *15*, 8132. [CrossRef]
124. Kim, K.; Chun, S.; Park, B.; Han, S. Precast Prestressed Concrete Pavement (PPCP): Effect of Thermal Gradient on Curling Deflection and Stress. *Constr. Build. Mater.* **2021**, *274*, 121966. [CrossRef]
125. Abed, Z.; Ahmed, H.; Khalil, W. Optimization of Silica Fume and Slag in Roller Compacted Concrete by Taguchi Method. *Eng. Technol. J.* **2023**, *41*, 724–733. [CrossRef]
126. Nas, E.; Altan Özbek, N. Optimization of the machining parameters in turning of hardened hot work tool steel using cryogenically treated tools. *Surf. Rev. Lett.* **2020**, *27*, 1950177. [CrossRef]
127. Azizmohammadi, M.; Toufigh, V.; Ghaemian, M. Experimental and Analytical Investigation on the Interlayer of Roller Compacted Concrete. *J. Mater. Civ. Eng.* **2021**, *33*, 04021090. [CrossRef]

Disclaimer/Publisher's Note: The statements, opinions and data contained in all publications are solely those of the individual author(s) and contributor(s) and not of MDPI and/or the editor(s). MDPI and/or the editor(s) disclaim responsibility for any injury to people or property resulting from any ideas, methods, instructions or products referred to in the content.

https://doi.org/10.3390/buildings16061167

buildings

MDPI

Article

Effect of Pozzolanic Cement and Ground Glass Waste on Alkali–Silica Reaction of Mortar

Džigita Nagrockienė [1], Ela Jarmolajeva [1], Vilma Vaičekauskienė [2,*] and Mečislavas Griškevičius [1]

[1] Faculty of Civil Engineering, Vilnius Gediminas Technical University, Saulėtekio Ave. 11, LT-10223 Vilnius, Lithuania
[2] Faculty of Marine Technology and Natural Sciences, Klaipeda University, Herkaus Manto g. 84, LT-91223 Klaipeda, Lithuania
* Correspondence: vilma.vaicekauskiene@ku.lt

Abstract

The article examines the use of pozzolanic cement and ground glass waste in mortar and their influence on physical and mechanical properties and resistance to the alkali–silica reaction (ASR). The materials used and the research methods used to determine the main properties of mortar are described. CEM II/A-P 52.5 N pozzolanic cement with ash additive, 0/4 fraction sand, and ground glass waste was used for the tests. The resistance of mortar to the ASR was determined according to the developments using the RILEM AAR-2 methodology. Seven mortar compositions were studied, in which cement was replaced with glass processing waste in the amounts of 5, 10, 15, 20, 25 and 30% of the cement mass. The effect of the amount of pozzolanic cement and glass waste on the following mortar properties was studied: density, ultrasonic pulse propagation velocity, compressive and flexural strengths, and ASR. A comparison of the physical and mechanical properties of mortar before and after ASR tests was performed. It was found that by modifying mortar with ground glass, i.e., by replacing pozzolanic cement with 5% to 10% ground glass waste, it is possible to reduce the amount of cement in the mortar, increase resistance to the alkali–silica reaction, and at the same time reduce CO_2 emissions associated with cement production and reuse ground glass waste.

Keywords: pozzolanic cement; ground glass waste; mortar; alkali–silica reaction (ASR) density; flexural strength; compressive strength

1. Introduction

Recycled glass is increasingly used as a secondary raw material in the production of construction materials. Ground glass is generally produced from waste glass, thereby reducing both the consumption of virgin raw materials and the amount of waste sent for disposal. From this perspective, ground waste glass represents a sustainable secondary material for the construction industry. Its incorporation into cementitious mortars may improve mechanical performance, durability, and resistance to salts and other aggressive environmental conditions.

When ground waste glass is used as a partial replacement for cement or aggregate, the demand for conventional raw materials is reduced. Partial cement replacement may also contribute to lowering carbon dioxide emissions, as cement production is one of the most carbon-intensive industrial processes.

Depending on the processing method and particle size, waste glass can be used in concrete either as a partial aggregate replacement or as a supplementary cementitious material [1].

Study [2] investigated the combined use of crushed waste glass as a partial replacement for sand and metakaolin as a partial replacement for cement. Concrete mixtures containing different metakaolin contents and partial sand replacement with crushed glass were examined. The results demonstrated the feasibility of using these materials to reduce cement and natural sand consumption. The mixture containing 10% metakaolin as a cement replacement and 25% crushed glass as a sand replacement exhibited improved durability and frost resistance.

Ground glass exhibits pozzolanic activity regardless of its replacement level when the particle size is below 50 μm. It should be noted that ground glass may improve the concrete microstructure and increase compressive strength while also acting as a pozzolanic material; however, further experimental research is required [3].

Ground waste glass is increasingly being investigated as an alternative supplementary cementitious material in cement-based mixtures. Portland cement production releases substantial amounts of CO_2 into the atmosphere. Therefore, its partial replacement with supplementary cementitious materials possessing pozzolanic properties is considered a promising strategy for reducing its environmental impact. In recent years, waste glass has been investigated as a potential supplementary cementitious material [4].

Particle size, or fineness, is one of the main factors governing the pozzolanic activity of ground glass. Numerous studies have confirmed that more finely ground glass exhibits greater pozzolanic activity. Similar findings have also been reported by several researchers.

Ichikawa [5] proposed a model explaining the conditions under which ground glass acts as a pozzolanic material and those under which it may damage the cementitious structure. According to this model, when glass is ground sufficiently finely (approximately 50 μm), the reactive particles are too small for a protective shell, described as a semipermeable membrane, to form around them. Consequently, ground glass does not cause expansive deformation but instead participates in pozzolanic reactions. Du et al. [6] observed that sodium silicate gel formed during the alkali–silica reaction reacts with Ca^{2+} ions, producing hydration products like those formed during pozzolanic reactions. Therefore, ground glass may act as a pozzolanic material.

Ground glass exhibited high pozzolanic activity when its particle size was reduced to below 75 μm. However, the incorporation of bottle glass may considerably increase the alkali content and consequently promote the expansion of concrete containing reactive aggregates, even when low-alkali cement is used [7].

Previous studies have demonstrated that a sufficiently large reactive surface area is required for pozzolanic reactions to proceed at an adequate rate. This surface area is directly dependent on particle fineness [8].

Shaikh [9] found that glass ground to a particle size below 38 μm exhibited significant pozzolanic activity, as evidenced by its reaction with Ca $(OH)_2$ and the formation of additional C–S–H. Other researchers [10] observed that coarser glass particles (>75 μm) showed negligible reactivity during the first 28 days of curing.

Finer particles have a larger specific surface area, which provides more favourable conditions for chemical reactions. Furthermore, fine grinding may disrupt the silicon–oxygen bonds within the glass structure, thereby further increasing its reactivity [11].

The fineness of ground glass should be selected carefully. Excessively coarse glass does not exhibit sufficient pozzolanic activity, whereas very fine grinding requires additional energy. Therefore, the literature recommends an economically and environmentally justified compromise, typically corresponding to a particle size range of 20–45 μm [12].

https://doi.org/10.3390/buildings16173519

Based on its chemical composition, ground glass has considerable potential as a pozzolanic material. However, it may contain a relatively high amount of Na_2O, which, in the presence of reactive amorphous silica, may promote the alkaline reaction. The resulting expansive reaction products generate internal stresses that may lead to cracking of the material. According to LST EN 206:2013 [13], the Na_2O content should not exceed 0.80%. Nevertheless, in practice, this value has been exceeded in numerous cases without observable adverse effects associated with the alkaline reaction. Therefore, the influence of ground glass on concrete properties requires further investigation.

As the glass content and particle size increase, the susceptibility to alkaline reaction (ASR) may also increase. However, the effects of ground and crushed waste glass on ASR remain under discussion [14].

A review of previous studies indicates that particle fineness is one of the main factors governing the pozzolanic activity of ground glass. Finer particles have a larger specific surface area and therefore generally exhibit greater pozzolanic reactivity. However, when very fine glass fractions are used, the mixture proportions, particularly the water content and admixture dosage, may need to be adjusted.

The literature also indicates that ground glass used as a pozzolanic material may improve the density, strength, and long-term durability of cementitious composites. Fine glass particles can fill capillary pores and improve particle packing, resulting in a denser matrix. The effect on strength depends on both particle size and replacement level. Strength development may be slower at early ages (up to 7 days), whereas at later ages (after 28 days), pozzolanic reactions may contribute to increased compressive strength.

The alkalis and reactive silica present in glass may participate in alkaline reactions and form expansive gels. When these gels absorb water, they swell and generate internal stresses, which may adversely affect the strength and long-term durability of concrete [15].

Pozzolanic activity describes the ability of a material to react with calcium hydroxide ($Ca(OH)_2$) formed during cement hydration. This reaction produces additional calcium silicate hydrate (C–S–H), which contributes to the strength development of the hardened cementitious matrix [16].

Partial replacement of cement with pozzolanic waste increased mortar density, ultrasonic pulse velocity, compressive strength, and flexural strength. However, further increasing the amount of pozzolanic waste adversely affected the physical and mechanical properties. This was attributed to the reduced cement content, which was insufficient to ensure effective bonding between the aggregate and the cementitious matrix [17].

To ensure the long-term durability of concrete, it is particularly important to limit internal deterioration caused by reactions between alkaline and reactive aggregates. One approach to mitigating these reactions is the use of mineral additions with pozzolanic properties [18].

Mortars containing ground glass and immersed in water for seven years showed no signs of deterioration and exhibited an increase in compressive strength [19].

Replacing 5% of the cement with borosilicate glass reduced the standard compressive strength by approximately 20%. However, the combined use of borosilicate glass at replacement levels of 2–5% and 0.5% synthetic silica increased the early compressive strength of cement mortars by up to 10% [20].

When glass particles ranging from 0 to 0.075 mm were used, the 28-day compressive strength of the mortar increased by approximately 5–15%, while ASR expansion decreased by 20.2%. In contrast, when the particle size ranged from 0.15 to 0.30 mm, the 28-day compressive strength decreased by approximately 5–8%, and ASR expansion increased by 39.7% [21].

https://doi.org/10.3390/buildings16173519

During the early curing period, particularly up to 7 days, ground glass may result in slower strength development, especially when used as a partial cement replacement. However, at later ages of 28–90 days, mixtures containing finer ground-glass particles may achieve higher strength than the control mixture [22].

The incorporation of ground glass into cementitious mixtures reduces porosity and water absorption, thereby improving resistance to aggressive chemical environments, including chloride and sulphate exposure. For these reasons, ground waste glass is considered a promising secondary raw material that can contribute to the production of more sustainable and durable cementitious composites.

Fine glass particles also contribute to microstructural densification. The filler effect and the formation of additional C–S–H reduce porosity and improve the density and compactness of the matrix. These changes enhance resistance to aggressive environmental actions, including carbonation, chloride penetration, and sulphate attack [23,24].

Ground glass significantly improved sulphate resistance; however, it was not effective in mitigating expansion caused by the alkaline reaction [25].

Studies indicate that sufficiently fine ground glass may perform a dual function by reducing the concentration of free alkalis and densifying the microstructure, thereby limiting the progression of the alkaline reaction [26]. Although ASR is most associated with concrete, it may also occur in cement mortars, particularly when reactive aggregates or artificial additions are used. In mortars with a high cement content and a relatively low aggregate content, the alkali concentration in the pore solution may be higher, potentially accelerating the reaction compared with conventional concrete [27]. Depending on the amount of reactive silica and the exposure conditions, ASR may reduce compressive strength by approximately 20–40% [28].

Despite the extensive research on the use of waste glass in cementitious materials, most previous studies have focused on its incorporation into mixtures based on Portland cement or on its use as a partial replacement for aggregate or cement. Considerably less attention has been paid to the combined use of finely ground waste glass and pozzolanic cement, particularly CEM II/A-P. The interaction between the pozzolanic components of CEM II/A-P cement and the reactive silica present in finely ground waste glass may differ from that observed in conventional Portland cement systems. Therefore, the combined effect of these two supplementary siliceous materials on the properties and expansion behaviour of mortar remains insufficiently investigated.

This study investigates the behaviour of mortars containing CEM II/A-P cement and finely ground waste glass under highly alkaline conditions. The study examines the influence of finely ground waste glass on mortar expansion and the stability of the cementitious matrix. Therefore, the aim of this study is to evaluate the combined use of finely ground waste glass and CEM II/A-P cement in mortar, with particular attention to its expansion behaviour and resistance to an aggressive alkaline environment.

The use of pozzolanic cement in cementitious mixtures may also reduce the CO_2 emissions associated with Portland cement production. Pozzolanic cement generally provides greater resistance to aggressive agents, including sulphates and chlorides, thereby improving the durability and strength retention of the hardened material.

2. Materials and Methods

2.1. Materials

CEM II/A-P 52.5 N pozzolanic cement (Naujoji Akmenė, Lithuania), certified in accordance with LST EN 197-1:2011 [29], was used in the experimental programme. The main properties of the cement (Na_2O ekv. $\leq 0.8\%$) are presented in Table 1. Natural sand with a particle size fraction of 0/4 mm (Lithuania) and ground waste glass were used as the

https://doi.org/10.3390/buildings16173519

aggregate and cement-replacing material, respectively; their principal characteristics are presented in Table 2 summarized. The pozzolanic activity of the ground waste glass was determined to be 560 mg/g. The ground waste glass (Klaipėda, Lithuania) was ground in a ball mill. The chemical compositions of the pozzolanic cement and ground waste glass are presented in Table 3. These data provide the basis for evaluating the influence of cement replacement with ground waste glass on the investigated mortar properties. The particle size distribution of the ground waste glass is presented in Figure 1.

Table 1. Physical properties of the pozzolanic cement.

Properties	CEM II/A-P 52.5 N
Particle density, kg/m^3	3050
Bulk density, kg/m^3	1320

Table 2. Characteristics of sand and ground waste glass.

Properties	Sand	Ground Glass Waste
Particle density, kg/m^3	2650	2570
Bulk density, kg/m^3	1630	1210

Table 3. Chemical composition, %.

Pozzolanic Cement, %									
SiO_2	Na_2O	CaO	MgO	Al_2O_3	SO_3	K_2O	Fe_2O_3	Cl	Cf
23.81	0.12	58.48	2.94	4.41	3.67	0.96	3.14	0.03	2.44
Ground glass waste, %									
68.15	0.75	3.95	0.90	12.18	-	2.80	1.30	-	9.77

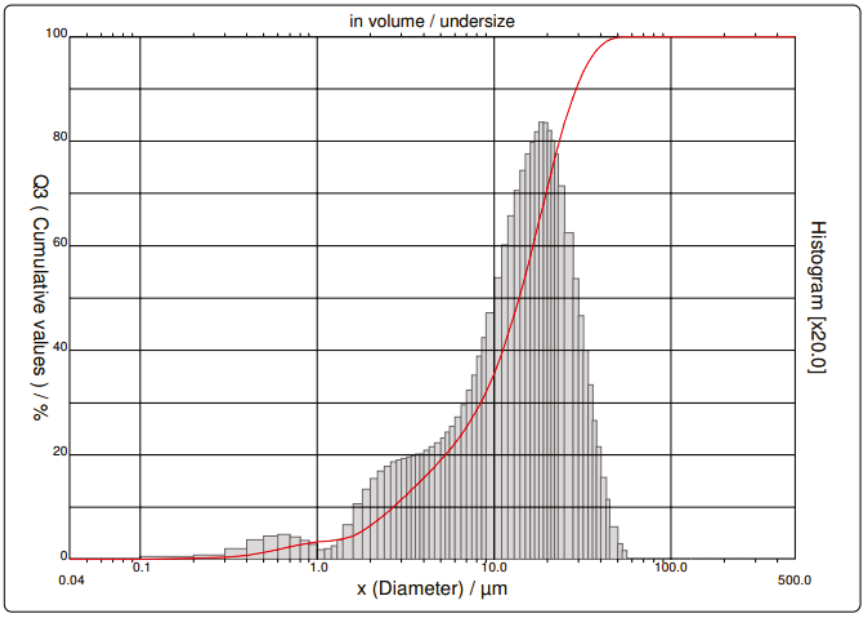

Figure 1. Ground glass waste particle size distribution.

The mean particle size was 13.67 µm. The microstructure of the ground waste glass is shown in Figure 2.

https://doi.org/10.3390/buildings16173519

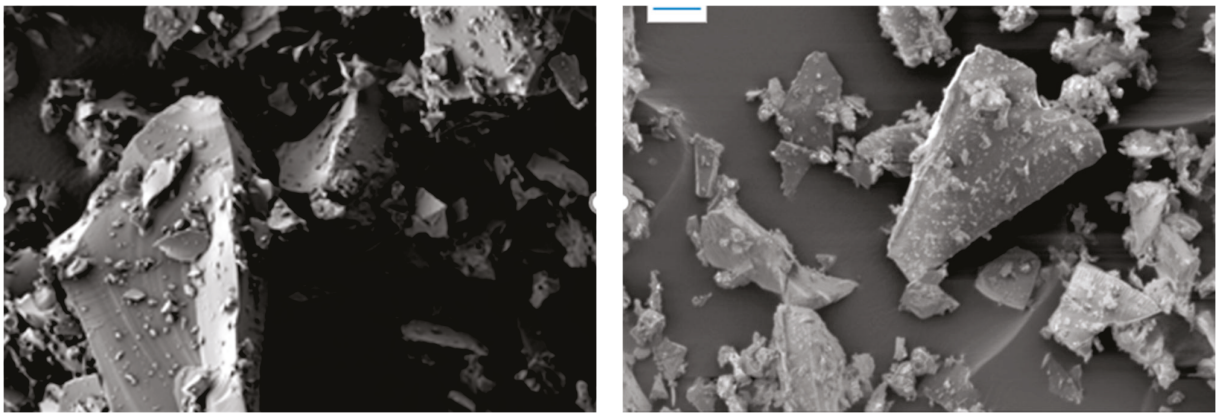

(**a**) (**b**)

Figure 2. Microstructure of ground glass waste: (**a**) magnification ×500; (**b**) magnification ×950.

The mineralogical composition of the sand is presented in Table 4. The mineralogical composition of the sand indicates that quartz is the predominant mineral (62.8%). Based on the mineralogical composition, the sand used in this study can be considered an aggregate with low reactivity.

Table 4. Mineral composition of sand, %.

Quartz	Carbonates	Feldspars	Mineral Aggregates	Amphiboles	Mica
62.8	18.0	15.6	1.8	1.6	0.2

2.2. Mix Proportions, Specimen Preparation and Test Methods

Seven mortar mixtures containing different amounts of ground glass waste were prepared under laboratory conditions. The mixtures consisted of CEM II/A-P 52.5 N pozzolanic cement, 0/4 mm sand, ground glass waste and water. Pozzolanic cement was replaced by ground glass waste at levels of 0, 5, 10, 15, 20, 25 and 30% by mass of the binder. The total binder content was maintained at 1200 g, the sand content at 2700 g and the water content at 564 g. Consequently, the water-to-binder ratio was constant at 0.47 in all mixtures. The water-to-binder ratio (W/B) was kept constant at 0.47 for all mixtures to ensure that the effect of replacing cement with finely ground waste glass could be evaluated under the same water availability conditions. The constant W/B ratio also allows a more direct comparison of the influence of the glass powder content on the expansion and mechanical properties of the mortars, without introducing an additional variable associated with changes in water content. The quantities of the constituent materials required to prepare each composition are presented in Table 5. Dried materials were used to prepare the mortar specimens. The aggregates, cement, and waste glass were dosed by mass, while water was measured by volume. The mortar mixtures were mixed using a forced-action mixer for 2 min. Mortar mixtures with different compositions were prepared by modifying the mixtures through the replacement of cement with varying amounts of waste glass, expressed as a percentage of the cement mass.

The mixture proportions and specimen geometry were selected following the principles of the RILEM AAR-2 accelerated mortar method [30]. The flow of each fresh mixture was maintained within the range of 205–220 mm specified in the adopted procedure. Twelve prismatic specimens measuring 40 × 40 × 160 mm were prepared for each mixture. Six specimens were tested after 28 days of water curing, while the remaining six specimens were subjected to accelerated alkaline exposure and tested after 56 days. According to the RILEM AAR-2 method, the expansion limit after 14 days of exposure to 1 M NaOH solution is 0.054%, while an expansion limit of 0.10%, based on ASTM C441/C441M-17 [31],

https://doi.org/10.3390/buildings16173519

was applied for the extended 56-day test. This accelerated test was intended to simulate an extremely alkaline environment and evaluate the influence of waste glass on mortar properties.

Table 5. Composition of mortar mixtures.

Ground Glass Waste Content, %	Ground Glass Waste Content, g	Cement, g	Sand, g	Water, g	W/B
0	0	1200	2700	564	0.47
5	60	1140	2700	564	0.47
10	120	1080	2700	564	0.47
15	180	1020	2700	564	0.47
20	240	960	2700	564	0.47
25	300	900	2700	564	0.47
30	360	840	2700	564	0.47

The chemical analysis of the materials was performed using a Bruker X-ray S8 Tiger WD-XRF spectrometer (Bruker, Mannheim, Germany). A rhodium (Rh) tube was used, with an anode voltage (Ua) of up to 60 kV and a current (I) of up to 130 mA. The measurements were performed using the SPECTRA Plus QUANT EXPRESS method.

The experimental programme included the determination of density, ultrasonic pulse velocity, flexural strength, compressive strength and expansion under accelerated alkaline exposure. Six specimens of each composition were used to determine the investigated properties. Density was determined in accordance with LST EN 12390-7:2019 [32]. Ultrasonic pulse velocity was measured by direct transmission in accordance with LST EN 12504-4:2021 [33].

Flexural and compressive strengths were determined in accordance with LST EN 12390-5:2019 [34] and LST EN 12390-3:2019 [35], respectively. Density, ultrasonic pulse velocity and mechanical strength were initially determined after 28 days of water curing. The same properties were subsequently evaluated after accelerated alkaline exposure to assess the changes caused by the aggressive environment.

Accelerated alkaline exposure was conducted following the RILEM AAR-2 methodology. The hardened 40 × 40 × 160 mm specimens were conditioned in water at 80 °C for 24 h and subsequently immersed in a 1 M NaOH solution maintained at 80 °C. The specimens were kept under these conditions for 56 days, and their expansion was measured periodically. The exposure period was extended beyond the conventional 14-day assessment because slowly reacting constituents may require a longer observation period.

Based on the adopted specimen geometry, expansion values of 0.054% after 14 days and 0.10% after 56 days were used as the assessment limits. Density, ultrasonic pulse velocity, flexural strength and compressive strength were determined after completion of the 56-day alkaline exposure and compared with the values obtained after 28 days of water curing.

The results are reported as mean values, testing 6 samples from each batch.

3. Results and Discussion

The density and ultrasonic pulse velocity of samples modified with ground glass were determined after 28 days of water curing. The results are presented in Figure 3. The highest density, 2237 kg/m^3, was recorded for the mixture in which 5% of the cement was replaced with ground glass, whereas the lowest density, 2169 kg/m^3, was obtained at a replacement level of 30%. The addition of a small amount of ground glass initially increased the density. However, beyond the optimum replacement level, the density

https://doi.org/10.3390/buildings16173519

decreased. At higher replacement levels, the reduced cement content may impair the integrity and homogeneity of the cementitious matrix, resulting in a lower overall density.

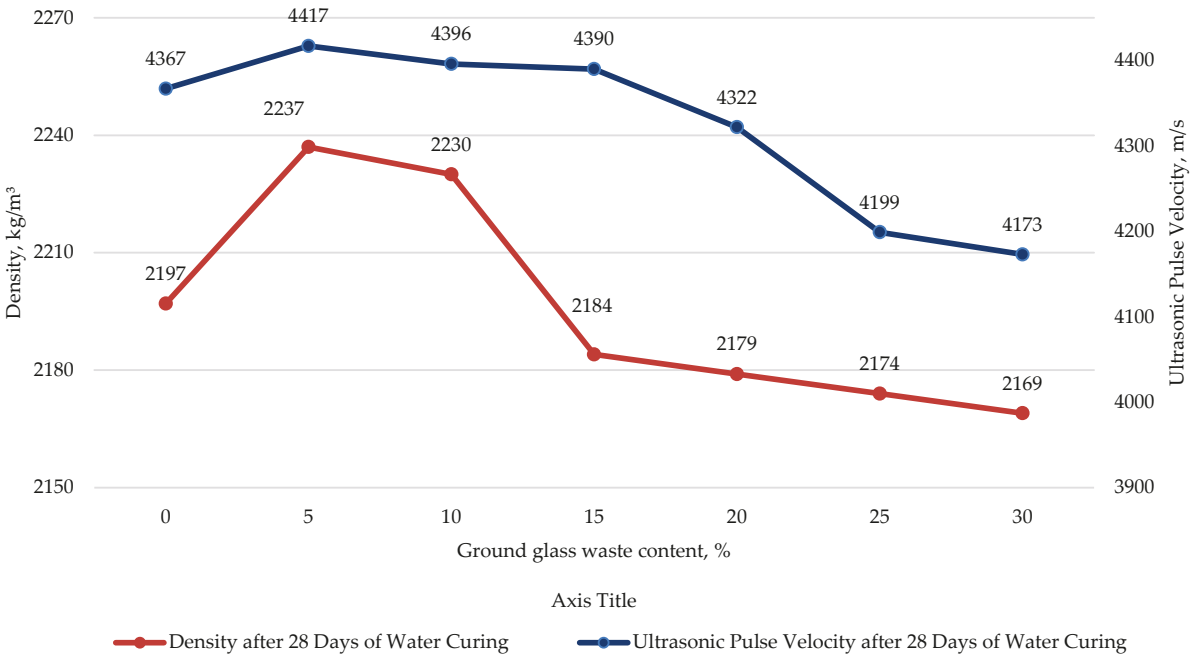

Figure 3. Density and Ultrasonic Pulse Velocity of Mortar Specimens after 28 Days of Water Curing.

The highest ultrasonic pulse velocity, 4417 m/s, was obtained when 5% of the cement was replaced with ground glass, whereas the lowest value, 4173 m/s, was recorded at a replacement level of 30%.

Density and ultrasonic pulse velocity (UPV) is consistent with recent findings showing that ground glass waste acts both as a microfiller and as a pozzolan. Tong et al. reported that an optimized blend with a total replacement level of 20%, comprising 2.86% of 0.6 mm glass sand, 1.43% of 1.18 mm glass sand, 8.57% of 50–60 μm glass powder and 7.14% of 60–70 μm glass powder, reduced water absorption by 20.73% and chloride ion permeability by 63.10% compared with the control concrete [36]. In the present study, the mean particle size was even smaller; therefore, the increases in density and UPV observed at a 5% replacement level can reasonably be attributed to pore filling and the formation of additional C–S–H. Recent reviews also indicate that ground glass waste contents of 10–20% generally yield favourable results, although the optimum value depends on the chemical composition and fineness of the ground glass waste, cement type, and curing duration [37–39]. Malaiškienė et al. reported a comparable result: incorporating up to 10% ground glass waste from household appliances and photovoltaic modules provided sufficient resistance to an alkaline environment, although density and UPV decreased when cement was replaced with glass [40]. This explains why, in the present study, the filler effect was pronounced only at the relatively low replacement level of 5%.

Ultrasonic pulse velocity increased up to an optimum ground-glass replacement level. At higher replacement levels, the reduced homogeneity and integrity of the cementitious matrix hindered ultrasonic wave propagation. Since ultrasonic waves travel faster through dense, homogeneous materials and more slowly through heterogeneous or defect-containing structures, excessive ground-glass content resulted in a lower ultrasonic pulse velocity.

The flexural and compressive strengths of mortar modified with ground glass were determined after 28 days of water curing. The results are presented in Figure 4. The highest flexural strength, 6.28 MPa, was obtained when 5% of the cement was replaced with ground

https://doi.org/10.3390/buildings16173519

glass, whereas the lowest value, 5.51 MPa, was recorded at a replacement level of 30%. The results indicate that a limited amount of ground glass increased the flexural strength. However, at higher replacement levels, flexural strength decreased, indicating reduced integrity of the cementitious matrix and greater susceptibility to crack formation under flexural loading.

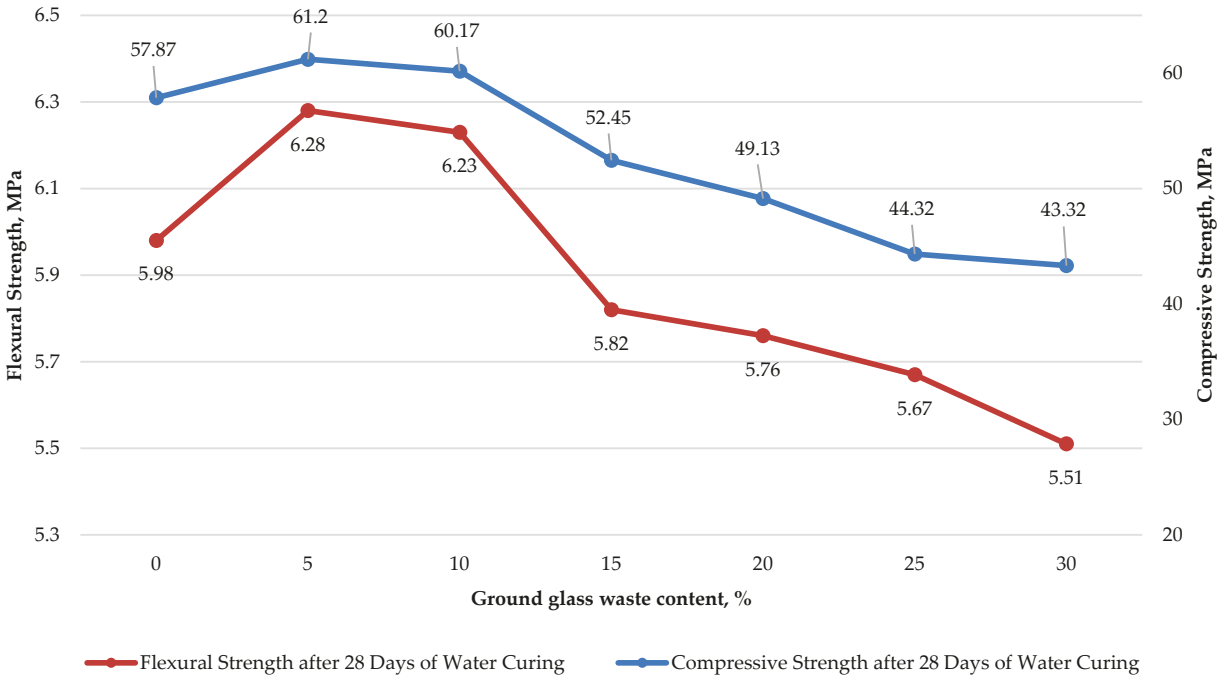

Figure 4. Flexural and Compressive Strengths of Mortar Specimens after 28 Days of Water Curing.

The highest compressive strength, 61.20 MPa, was obtained when 5% of the cement was replaced with ground glass, whereas the lowest value, 43.32 MPa, was recorded at a replacement level of 30%. Compressive strength increased up to an optimum ground-glass content. Beyond this level, the reduced cement content resulted in insufficient binder availability and less effective particle bonding. Consequently, the hardened matrix weakened, reducing its capacity to withstand compressive loads and leading to a decrease in compressive strength.

The obtained strength results fall within the range considered optimal in recent studies. Ahmad et al. reported that replacing up to 10% of cement with ground glass waste enhances compressive strength, while a 5% replacement level was optimal for flexural strength [41]. This is directly consistent with the flexural and compressive strengths obtained in the present study, 6.28 MPa and 61.20 MPa, respectively—at a 5% replacement level. Baikerikar et al. reported that concrete containing 10% waste glass powder combined with 0.5–1.5% nano-TiO_2 exhibited higher compressive and flexural strengths and improved resistance to sorptivity, acid, sulphate and chloride exposure compared with the control concrete; therefore, these improvements reflect the combined effects of waste glass powder and nano-TiO_2 rather than the isolated effect of glass powder [42]. At replacement levels of 20–30%, the cement dilution effect often becomes dominant at early ages: the amount of clinker hydration products decreases, while the slower pozzolanic reaction of ground glass waste does not fully compensate for the reduced binder content [43,44]. Therefore, the reduction in compressive strength to 43.32 MPa recorded in this study at a 30% ground glass waste content is not contradictory. Rather, it indicates that, after 28 days, the reactivity of the ground glass waste particles was insufficient to compensate for such a high level of cement replacement.

https://doi.org/10.3390/buildings16173519

Figure 5 shows the expansion of the modified mortar specimens after 14 and 56 days of exposure to a 1 M NaOH solution maintained at 80 °C as a function of the ground-glass content.

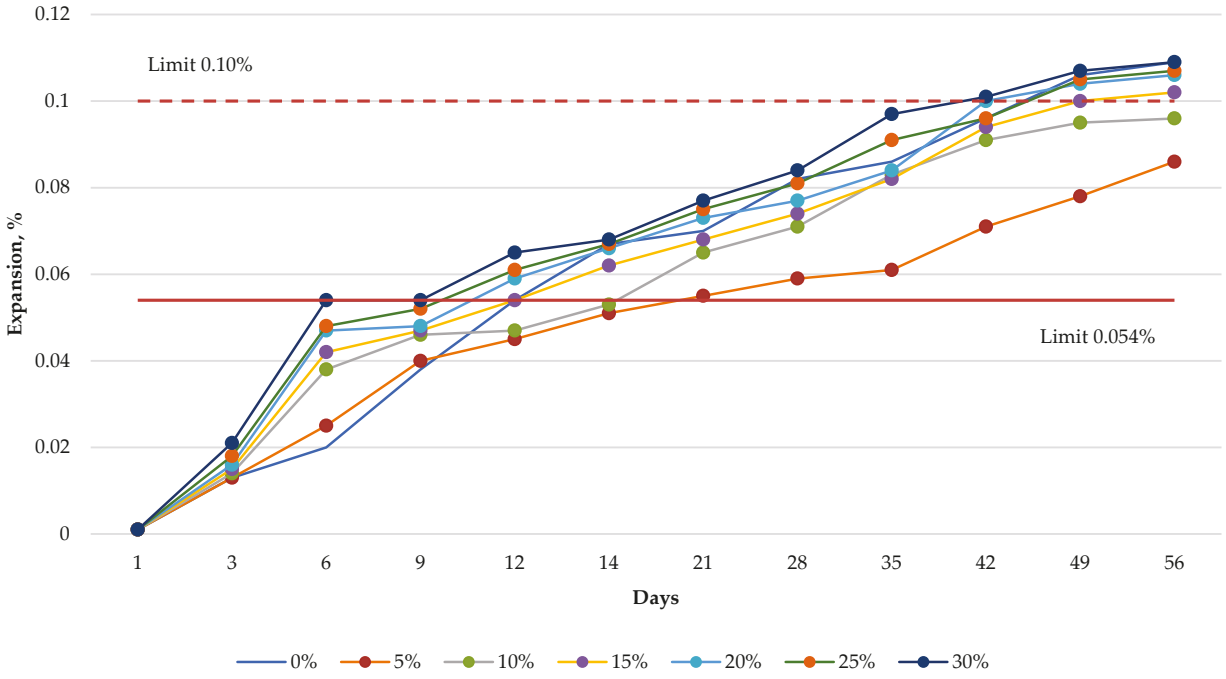

Figure 5. Effect of ground glass waste content on the expansion of mortar specimens.

For the mixture without ground glass (0%), the specimen expansion after 14 days was 0.067%, exceeding the limit of 0.054%. When 5% and 10% of the cement was replaced with ground glass, the expansion values decreased to 0.051% and 0.053%, respectively, remaining below the specified limit. At higher ground-glass replacement levels of 15%, 20%, 25%, and 30%, the 14-day expansion values exceeded the limit and reached 0.062%, 0.066%, 0.067%, and 0.068%, respectively.

After 56 days, the expansion of the control specimens without ground glass reached 0.109%, exceeding the critical limit of 0.10%. The mixtures containing 5% and 10% ground glass exhibited expansion values of 0.086% and 0.096%, respectively, and therefore remained below this limit. When the ground-glass content was increased to 15%, 20%, 25%, and 30%, the expansion values exceeded 0.10% and reached 0.102%, 0.106%, 0.107%, and 0.109%, respectively. Some of the measured values lie close to the assessment limits. This concerns the mixture with 10% ground glass waste after 14 days, 0.053% against the limit of 0.054%, and the mixtures with 10% and 15% after 56 days, 0.096% and 0.102% against the limit of 0.100%. The results are reported as mean values of six specimens, and the scatter of the measurements was not quantified. The classification of these mixtures with respect to the limits should therefore be regarded as indicative. The mixture with 5% ground glass waste remained clearly below both limits, 0.051% after 14 days and 0.086% after 56 days.

The ASR results showed pessimum behaviour. Replacing cement with 5–10% ground glass waste reduced the 14-day expansion from 0.067% to 0.051–0.053% and the 56-day expansion from 0.109% to 0.086–0.096%. At higher replacement levels, this improvement was no longer observed. Almakrab et al. showed that the effectiveness of ASR mitigation is governed not only by the total SiO_2 content but also by the chemical composition and combination of the supplementary cementitious materials used [45]. Alioglu and Ekincioğlu found that mixtures containing 10–25% ground glass waste powder and 1–2% nanosilica exhibited lower concrete expansion. Nanosilica promoted early hydration, whereas ground

https://doi.org/10.3390/buildings16173519

glass waste powder contributed to ASR reduction at later ages [46]. Wen et al. similarly found that the pozzolanic activity of finely ground glass waste can reduce ASR, although the extent of this effect depends on whether the ground glass waste is used to replace cement or aggregate [47]. The narrower optimum range of 5–10% obtained in the present study appears reasonable. The CEM II/A-P cement used already contained a pozzolanic mineral addition; therefore, the introduction of additional ground glass waste produced a different effect on pozzolanic reactions and the alkaline balance than would be expected in an ordinary Portland cement system.

The density of the mortar specimens was determined after 56 days of alkaline exposure in a 1 M NaOH solution maintained at 80 °C to evaluate the effect of alkaline degradation on density. Figure 6 presents the density and ultrasonic pulse velocity results obtained after the 56-day exposure period. The lowest ultrasonic pulse velocity, 3910 m/s, was recorded for the control mixture, whereas the highest value, 3945 m/s, was obtained for the mixture in which 10% of the cement was replaced with ground waste glass. The lowest density, 2133 kg/m^3, was measured for the mixture containing 25% ground waste glass, while the highest density, 2215 kg/m^3, was recorded for the mixture containing 5% ground waste glass.

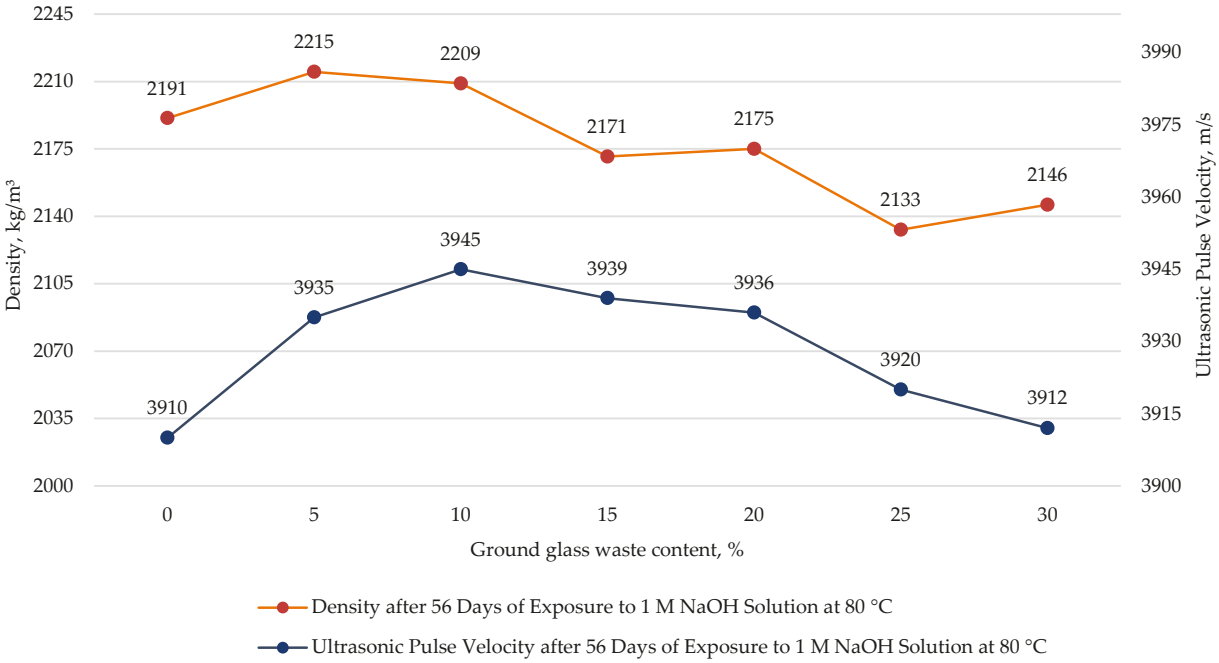

Figure 6. Density and Ultrasonic Pulse Velocity of mortar Specimens after 56 Days of Exposure to 1 M NaOH Solution at 80 °C.

Figure 7 presents a comparison of the mean specimen densities. Comparison of the values obtained after 28 days of water curing and after 56 days of alkaline exposure revealed a decrease in density for all mixtures. The greatest reduction was observed in the mixture containing 25% ground glass, for which the density decreased from 2174 to 2133 kg/m^3, corresponding to a reduction of 1.89%. The control mixture without ground glass exhibited a considerably smaller decrease, from 2197 to 2191 kg/m^3, equivalent to 0.27%.

The decrease in specimen density after alkaline exposure may be associated with microcrack formation and structural damage within the material. Expansive gels formed during alkaline reactions may have induced internal stresses and promoted microcrack development. The leaching of soluble constituents and the detachment of fine particles from the specimen surfaces may also have contributed to the reduction in density. These

https://doi.org/10.3390/buildings16173519

processes increase open porosity and reduce specimen mass, resulting in a lower density after alkaline exposure.

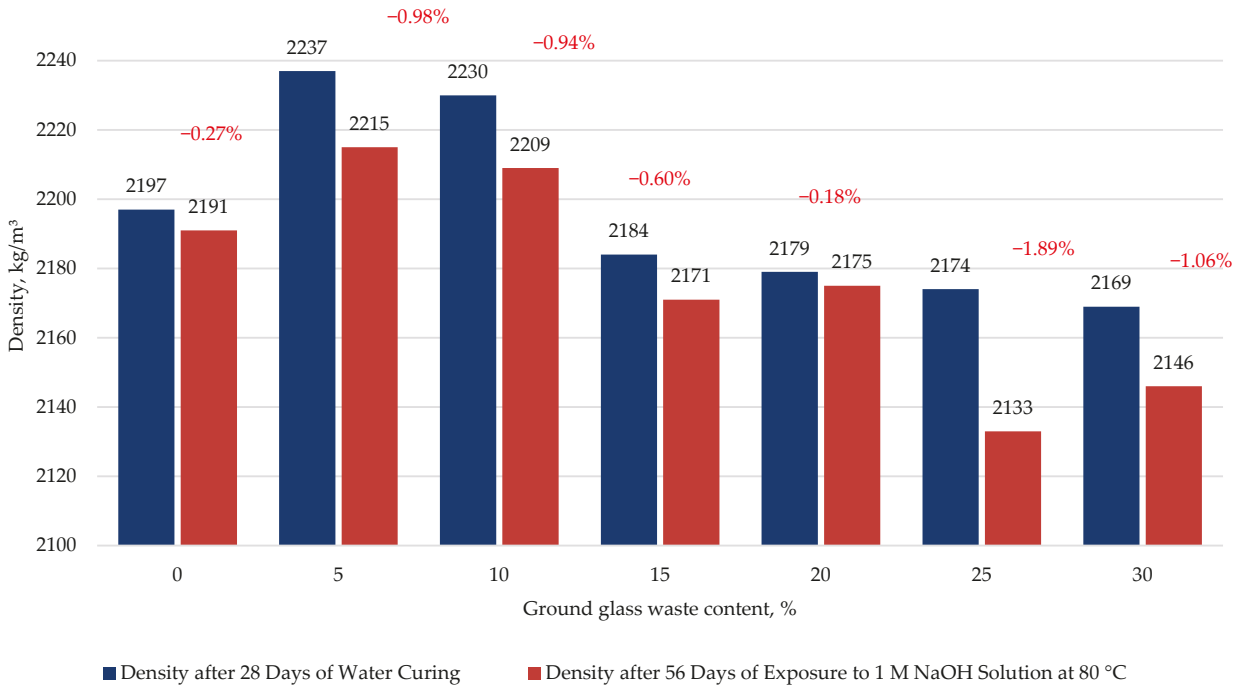

Figure 7. Comparison of Average Density Results.

The comparative mean ultrasonic pulse velocity results are presented in Figure 8.

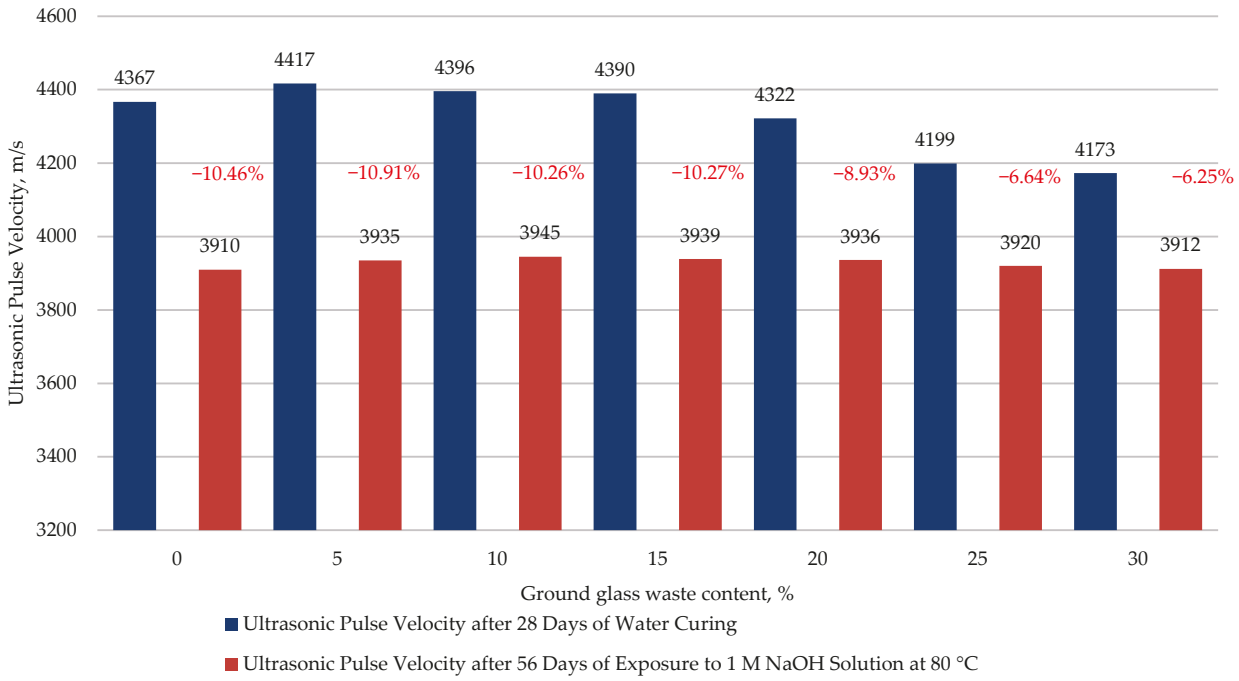

Figure 8. Comparison of Average Ultrasonic Pulse Velocity Results.

Comparison of the ultrasonic pulse velocity values measured after 28 days of water curing and after 56 days of alkaline exposure revealed a decrease in ultrasonic pulse velocity for all mixtures.

The decrease in UPV after alkaline exposure (6.25–10.91%), accompanied by only a slight reduction in density, indicates that the non-destructive measurements were more

https://doi.org/10.3390/buildings16173519

sensitive to microcracking than to changes in mass or volume. Recent long-term studies of concrete containing ground glass waste have shown that strength, porosity, and transport properties may respond differently under aggressive exposure conditions; therefore, no single parameter is sufficient to assess the extent of damage [48]. Ground glass waste and other finely divided pozzolanic materials densify the undamaged matrix; local ASR gel formation and microcracking increase the ultrasonic wave path and reduce its velocity. This may explain why the mixture containing 5% glass powder had the highest initial UPV. Although it also showed a decrease, its absolute UPV after exposure remained comparable to those of the other mixtures. This distinction is important when interpreting the results: the relative decrease in UPV alone does not mean that the mixture containing 5% ground glass waste suffered the greatest damage.

The greatest effect of alkaline exposure was observed in the mixture containing 5% ground glass, for which the ultrasonic pulse velocity decreased from 4417 to 3935 m/s, corresponding to a reduction of 10.91%. The smallest reduction was recorded for the mixture containing 30% ground glass, where the ultrasonic pulse velocity decreased from 4173 to 3912 m/s, equivalent to 6.25%.

The decrease in ultrasonic pulse velocity indicates the formation of microcracks and a loss of structural integrity. These defects increase the heterogeneity of the material and disrupt the propagation of ultrasonic waves, resulting in lower pulse velocity.

After 56 days of exposure to a 1 M NaOH solution maintained at 80 °C, the flexural strength of the specimens was determined. The results are presented in Figure 9.

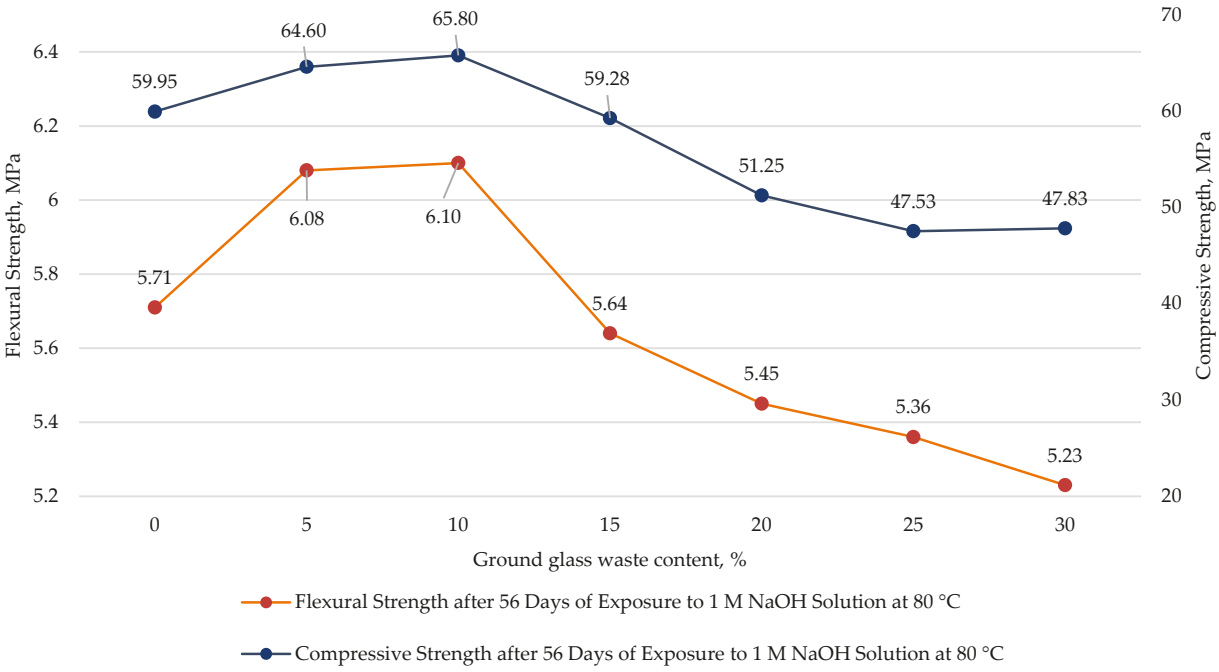

Figure 9. Flexural and Compressive Strengths of Mortar Specimens after 56 Days of Exposure to 1 M NaOH Solution at 80 °C.

The lowest flexural strength, 5.23 MPa, was recorded for the mixture in which 30% of the cement was replaced with ground glass waste. The highest value, 6.10 MPa, was obtained at a replacement level of 10%. Figure 10 presents a comparison of the mean flexural strength values obtained for the investigated mortar mixtures.

Comparison of the flexural strength values obtained after 28 days of water curing and after 56 days of alkaline exposure revealed a decrease in flexural strength for all mortar mixtures. The greatest reduction was observed in the mixture containing 25% ground glass,

https://doi.org/10.3390/buildings16173519

for which the flexural strength decreased from 5.67 to 5.36 MPa, corresponding to a loss of 5.47%. The smallest reduction was recorded for the mixture containing 10% ground glass, where the flexural strength decreased from 6.23 to 6.10 MPa, equivalent to 2.09%.

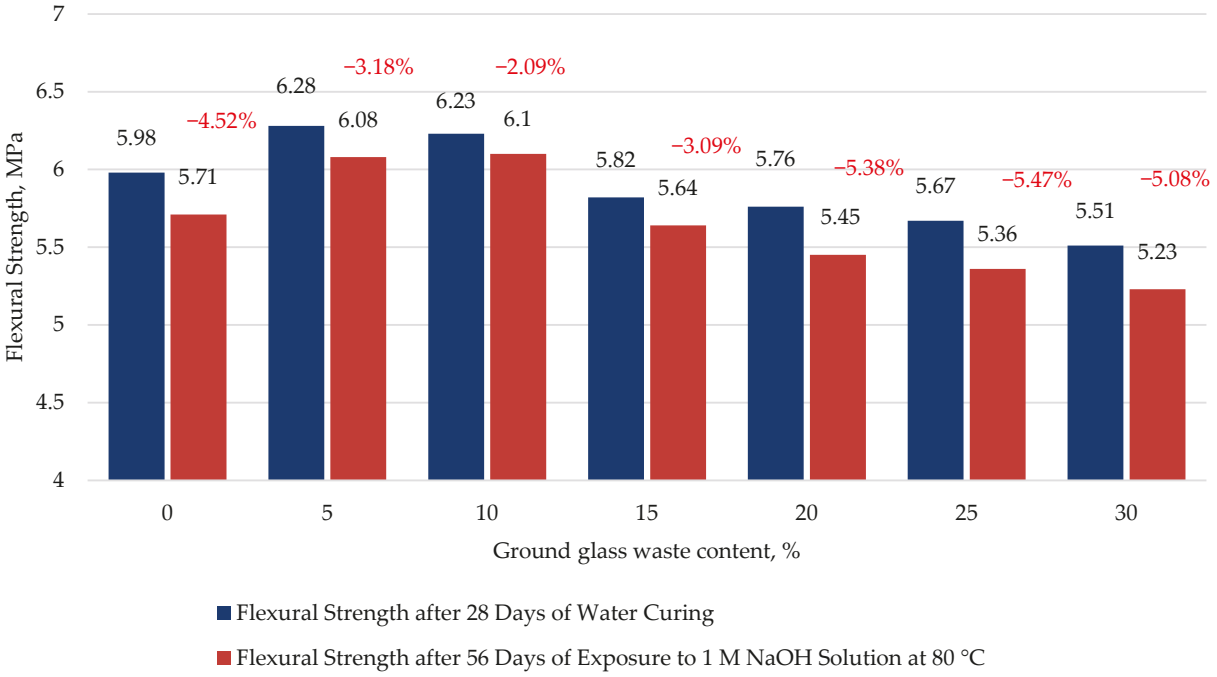

Figure 10. Comparison of Average Flexural Strength Results.

The reduction in flexural strength may be attributed to the formation of microcracks during alkaline exposure. Flexural loading produces tensile stresses in one part of the cross-section and compressive stresses in the opposite part. Since mortar is particularly sensitive to defects in the tensile zone, even small surface or internal microcracks can promote crack propagation and reduce its load-bearing capacity.

Alkaline exposure may also impair the integrity and deformation capacity of the cementitious matrix. Microcracking and deterioration of the interfacial transition zone between the cement paste and aggregate weaken internal bonding and facilitate crack initiation and propagation. Consequently, the specimens fail at lower flexural loads.

The compressive strength values obtained after 56 days of exposure to a 1 M NaOH solution maintained at 80 °C are presented in Figure 9. The lowest compressive strength, 47.53 MPa, was recorded for the mixture in which 25% of the cement was replaced with ground glass, whereas the highest value, 65.80 MPa, was obtained at a replacement level of 10%. Figure 11 presents the mean compressive strength values of the investigated mixtures after alkaline exposure.

A comparison of the compressive strength values obtained after 28 days of water curing and after 56 days of alkaline exposure revealed an increase in compressive strength for all mortar mixtures.

The specimens tested after 56 days were exposed to a 1 mol/L NaOH solution at 80 °C, whereas the reference specimens were cured under different conditions. The elevated temperature may have accelerated cement hydration and pozzolanic reactions of the finely ground waste glass, which could contribute to the observed increase in compressive strength. At the same time, alkali–silica reaction and associated deterioration may have occurred during alkaline exposure. Therefore, the increase in compressive strength, including the approximately 13% increase observed for the mixture containing 15% glass waste,

https://doi.org/10.3390/buildings16173519

reflects the combined effects of continued hydration, pozzolanic reactions, and alkaline exposure rather than an improvement in resistance to alkali-induced deterioration.

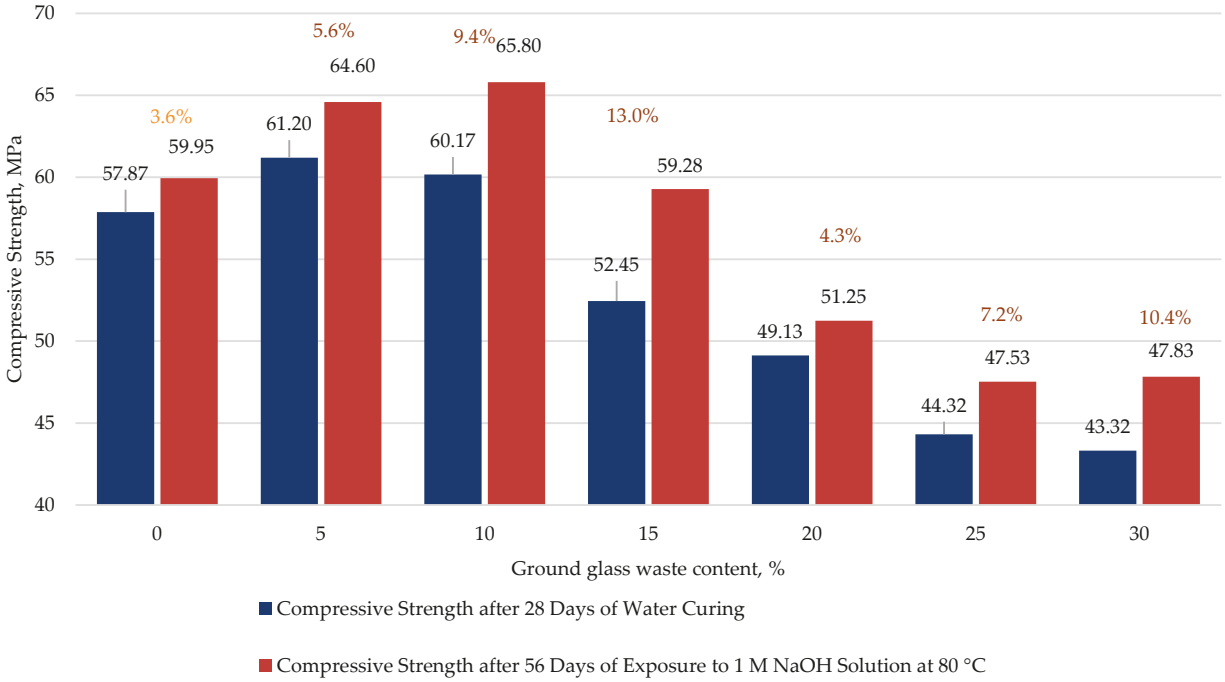

Figure 11. Comparison of average compressive strength results.

The increase in compressive strength should be interpreted with caution because the specimens were tested at different ages and under different curing conditions. During 56 days of exposure to a 1 M NaOH solution at 80 °C, the elevated temperature may have accelerated the hydration of unreacted cement and the pozzolanic reaction of fine ground glass. This densification may temporarily increase compressive strength even though the reduction in ultrasonic pulse velocity and flexural strength indicates the development of microcracks and progressive internal deterioration.

The increase in compressive strength after 56 days of exposure to NaOH solution at 80 °C should be interpreted with caution. These accelerated conditions simultaneously promote damaging ASR and enhance the hydration of unreacted cement and the pozzolanic reaction of glass powder. Recent ASR research recommends extending the duration of accelerated tests for mixtures containing SCMs and supplementing expansion measurements with indirect methods, such as the modified R3 test and bulk electrical resistivity, because SCMs generally react more slowly than Portland cement [49]. Similarly, Song et al. found that increasing the waste glass powder replacement level reduced the absolute compressive and splitting tensile strengths at both 28 and 90 days, although the strength development between 28 and 90 days became more pronounced because of continued pozzolanic reactions and pore-structure refinement [50]. In the authors' previous study, the mixture containing 1% cellulose fibre, 8% metakaolin waste and 1% functional waterproofing additive remained below 0.054% expansion after 14 days and below 0.10% after 56 days in 1 M NaOH at 80 °C; SEM observations showed a dense microstructure with only minor changes after alkaline exposure, while XRD analysis indicated greater phase stability than in the unmodified concrete [51]. Therefore, the 5–10% glass powder range examined in this study should be regarded as a compromise between limiting ASR expansion and maintaining mechanical performance, rather than as evidence that alkaline exposure itself improves mortar.

https://doi.org/10.3390/buildings16173519

Alkaline exposure testing is conducted in a warm and humid environment. These conditions simulate accelerated curing and may artificially increase the measured compressive strength.

4. Conclusions

The experimental results demonstrated that the incorporation of ground waste glass significantly affected the physical and mechanical properties and alkali resistance of mortar made with pozzolanic cement, with the most favourable overall performance observed at replacement levels of 5–10%.

1. The pozzolanic activity of the ground waste glass was 560 mg/g, and its mean particle size was 13.67 μm. SiO_2 and Al_2O_3 were identified as its main chemical components. These properties indicate that ground waste glass can be used as a partial cement replacement in mortar.

2. Replacing 5% of the pozzolanic cement with ground waste glass increased the density and ultrasonic pulse velocity of the mortar. However, both properties decreased as the replacement level was increased to 30%. After 56 days of exposure to a 1 M NaOH solution at 80 °C, the mixture containing 5% ground waste glass had density and ultrasonic pulse velocity values approximately 1% higher than those of the control mortar. Higher replacement levels resulted in a gradual decrease in both properties. This shows that replacing 5% of cement with waste glass can be beneficial to increase the density and ultrasonic pulse velocity properties of mortars that are used in aggressive alkaline environments.

3. Replacing 5% of the pozzolanic cement with ground waste glass increased the flexural and compressive strengths by approximately 5% compared with the control mortar. Further increasing the replacement level to 30% reduced both strength values. After 56 days of exposure to a 1 M NaOH solution at 80 °C, the mixture containing 10% ground waste glass showed 6.83% higher flexural strength and 9.76% higher compressive strength than the control mortar. This shows that replacing 10% of cement with waste glass can be beneficial to increase the mechanical properties of mortars that are used in aggressive alkaline environments.

4. The use of finely ground waste glass and CEM II/A-P cement increases the resistance of mortar to alkali attack. When evaluating mortar expansion with 5% and 10% replacement of cement by waste glass, the expansion values after 14 days were 0.051% and 0.053%, respectively, and increased to 0.086% and 0.096% after 56 days. It was found that finely ground waste glass and CEM II/A-P cement affect the mortar's resistance to an aggressive alkaline environment as the testing period increases to 56 days. Therefore, the use of finely ground waste glass in combination with CEM II/A-P cement can be considered a promising approach for controlling mortar expansion and improving its stability under alkaline conditions.

5. It has been found that 5–10% of pozzolanic cement can be replaced with ground waste glass in the mortar. This replacement may reduce CO_2 emissions associated with cement production while promoting the reuse of waste glass. The results suggest that the use of ground waste glass has potential for application in sustainable cementitious materials and may be suitable for further investigation in structural concrete applications.

Author Contributions: Conceptualization, D.N. and V.V.; methodology, V.V., D.N., E.J., and M.G.; investigation, V.V., D.N., and E.J.; resources, V.V., D.N., and M.G.; writing—original draft preparation, V.V., D.N., M.G. and E.J.; supervision, V.V., D.N., E.J., and M.G. All authors have read and agreed to the published version of the manuscript.

Funding: This research received no external funding.

Institutional Review Board Statement: Not applicable.

https://doi.org/10.3390/buildings16173519

Informed Consent Statement: Not applicable.

Data Availability Statement: The original contributions presented in this study are included in the article. Further inquiries can be directed to the corresponding author.

Conflicts of Interest: The authors declare no conflicts of interest.

References

1. Ling, T.-C.; Poon, C.-S.; Wong, H.-W. Management and recycling of waste glass in concrete products: Current situations in Hong Kong. *Resour. Conserv. Recycl.* **2013**, *70*, 25–31. [CrossRef]
2. Nagrockienė, D.; Paliulis, D. The effect of crushed glass and metakaolin waste in the properties of modified concrete. *Ceramics-Silikáty* **2022**, *66*, 520–526. [CrossRef]
3. Šerelis, E. Ypač Stipraus Betono Struktūros Savybių ir Technologijos Tyrimai. Daktaro Disertacija, Kauno Technologijos Universitetas, Kaunas, Lithuania, 2016.
4. Ramírez-Arellanes, S.; Montejo-Alvaro, F.; Cruz-Martínez, H.; Rojas-Chávez, H.; Mendoza-Rangel, J.M.; Franco-Luján, V.A. Pozzolanic Assessment of Recycled Waste Glass for Use as a Supplementary Cementitious Material. *Constr. Mater.* **2025**, *5*, 59. [CrossRef]
5. Ichikawa, T. Alkali-silica reaction, pessimum effects and pozzolanic effect. *Cem. Concr. Res.* **2009**, *39*, 716–726. [CrossRef]
6. Du, H.; Tan, K.H. Effect of particle size on alkali-silica reaction in recycled glass mortars. *Constr. Build. Mater.* **2014**, *66*, 275–285. [CrossRef]
7. Thomas, M.D.A.; Smith, D.; Moffatt, E.G.; Kasaniya, M. *The Use of Ground Glass as a Pozzolan*; American Concrete Institute: Farmington Hills, MI, USA, 2021; Volume 349, pp. 752–761.
8. Papadakis, V.G.; Tsimas, S.; Tsivilis, S. Supplementary cementing materials in concrete Part I: Efficiency and design. *Cem. Concr. Res.* **2002**, *32*, 1525–1532.
9. Shaikh, F.U.A. Effects of alkali activated binders on properties of high-volume fly ash concrete. *Constr. Build. Mater.* **2014**, *49*, 407–416.
10. Shayan, A.; Xu, A. Performance of glass powder as a pozzolanic material in concrete: A field trial on concrete slabs. *Cem. Concr. Res.* **2006**, *36*, 457–468. [CrossRef]
11. Shi, C.; Wu, Y.; Riefler, C.; Wang, H. Characteristics and pozzolanic reactivity of glass powders. *Cem. Concr. Res.* **2005**, *35*, 987–993. [CrossRef]
12. Shi, C.; Zheng, K. A review on the use of waste glasses in the production of cement and concrete. *Resour. Conserv. Recycl.* **2007**, *52*, 234–247. [CrossRef]
13. *LST EN 206:2013+A1:2017*; Betonas. Specifikacija, Eksploatacinės Savybės, Gamyba ir Atitiktis: Europos Standartas EN 206:2013+A1:2016 Turi Lietuvos Standarto Statusą. Lithuanian Standards Board: Vilnius, Lithuania, 2017.
14. Barkauskas, K. Cementinio Kompozito su Metakaolino ir Stiklo Atliekomis Atsparumo Šarminei Korozijai Tyrimai. Daktaro Disertacija, Vilniaus Gedimino Technikos Universitetas, Vilnius, Lithuania, 2023.
15. Huang, D.; Sun, P.; Gao, P.; Liu, G.; Wang, Y.; Chen, X. Study on the effect and mechanism of alkali-silica reaction expansion in glass concrete. *Sustainability* **2021**, *13*, 10618. [CrossRef]
16. Taylor, H.F.W. *Cement Chemistry*, 2nd ed.; Thomas Telford Publishing: London, UK, 1997.
17. Nagrockienė, D.; Rutkauskas, A.; Vaičekauskienė, V.; Jarmolajeva, E. The effect of pozzolanic waste as cement substitute on the properties of cement mortar and resistance to alkali-silica reaction. *Ceramics-Silikáty* **2024**, *68*, 14–23. [CrossRef]
18. Zapała-Sławeta, J. Alkali silica reaction in the presence of metakaolin-the significant role of calcium hydroxide. *IOP Conf. Ser. Mater. Sci. Eng.* **2017**, *245*, 022020. [CrossRef]
19. Carsana, M.; Frassoni, M.; Bertolini, L. Comparison of ground waste glass with other supplementary cementitious materials. *Cem. Concr. Compos.* **2014**, *45*, 39–45. [CrossRef]
20. Kotsay, G.; Brzóska, A. Effect of borosilicate glass wastes and synthetic silica on cement products properties. *Chem. Chem. Technol.* **2021**, *15*, 240–245. [CrossRef]
21. Li, F.; Yang, J.; Li, L. Effect and mechanism of waste glass powder as supplementary cementitious material on mortar properties. *Bull. Chin. Ceram. Soc.* **2022**, *41*, 3208.
22. Islam, G.M.S.; Rahman, M.H.; Kazi, N. Waste glass powder as partial replacement of cement for sustainable concrete practice. *Int. J. Sustain. Built Environ.* **2017**, *6*, 37–44. [CrossRef]
23. Shao, Y.; Lefort, T.; Moras, S.; Rodriguez, D. Studies on concrete containing ground waste glass. *Cem. Concr. Res.* **2000**, *30*, 91–100. [CrossRef]
24. Taha, B.; Nounu, G. Utilizing waste recycled glass as sand/cement replacement in concrete. *J. Mater. Civ. Eng.* **2009**, *21*, 709–721. [CrossRef]

https://doi.org/10.3390/buildings16173519

25. Kasaniya, M.; Thomas, M.D.; Moffatt, E.G. Efficiency of natural pozzolans, ground glasses and coal bottom ashes in mitigating sulfate attack and alkali-silica reaction. *Cem. Concr. Res.* **2021**, *149*, 106551. [CrossRef]
26. Tagnit-Hamou, A.; Habert, G. Glass powder-A partial cement replacement material in concrete. *J. Clean. Prod.* **2016**, *111*, 70–82.
27. Thomas, M.D.A.; Fournier, B.; Folliard, K.J. *Report on the Diagnosis, Prognosis, and Mitigation of Alkali-Silica Reaction (ASR) in Transportation Structures*; FHWA-HIF-12-022; U.S. Department of Transportation: Washington, DC, USA, 2011.
28. Multon, S.; Sellier, A.; Cyr, M. Chemo-mechanical modelling for prediction of alkali-silica reaction (ASR) expansion. *Cem. Concr. Res.* **2009**, *39*, 490–500. [CrossRef]
29. *LST EN 197-1:2011*; Cement. Part 1, Composition, Specifications and Conformity Criteria for Common Cements. Lithuanian Standards Board: Vilnius, Lithuania, 2011.
30. RILEM TC 106-AAR. AAR-2: Detection of potential alkali-reactivity of aggregates-The accelerated mortar-bar test. *Mater. Struct.* **2000**, *33*, 409–417.
31. *ASTM C441/C441M-17*; Standard Test Method for Effectiveness of Pozzolans or Ground Blast-Furnace Slag in Preventing Excessive Expansion of Concrete Due to the Alkali-Silica Reaction. ASTM International: West Conshohocken, PA, USA, 2017.
32. *LST EN 12390-7:2019*; Testing Hardened Concrete-Part 7: Density of Hardened Concrete. Lithuanian Standards Board: Vilnius, Lithuania, 2020.
33. *LST EN 12504-4:2021*; Testing Concrete–Part 4: Determination of Ultrasonic Pulse Velocity. Lithuanian Standards Board: Vilnius, Lithuania, 2021.
34. *LST EN 12390-5:2019*; Testing Hardened Concrete-Part 5: Flexural Strength of Test Specimens. Lithuanian Standards Board: Vilnius, Lithuania, 2022.
35. *LST EN 12390-3:2019*; Testing Hardened Concrete-Part 3: Compressive Strength of Test Specimens. Lithuanian Standards Board: Vilnius, Lithuania, 2020.
36. Tong, G.; Pang, J.; Shen, J.; Tang, B.; Jiang, Z.; Li, B.; Huang, J.; Zou, J.; Wang, H. Response Tests on the Effects of Particle Size of Waste Glass Sand and Glass Powder on the Mechanical and Durability Performance of Concrete. *Sci. Rep.* **2024**, *14*, 25445. [CrossRef]
37. Elahi, M.M.A.; Hossain, M.M.; Karim, M.R.; Zain, M.F.M. Application of Waste Glass Powder for Sustainable Concrete: Design, Performance, Perspective. *Materials* **2025**, *18*, 734. [CrossRef]
38. Almeshal, I.; Tayeh, B.A.; Alyousef, R.; Abdul-Jabbar, H.; Mohamed, A.M. Incorporation of Waste Glass Powder in the Sustainable Development of Concrete. *Materials* **2025**, *18*, 3223. [CrossRef]
39. Sathiparan, N.; Subramaniam, D.N. Potential Use of Crushed Waste Glass and Glass Powder in Sustainable Pervious Concrete: A Review. *Clean. Waste Syst.* **2024**, *8*, 100191. [CrossRef]
40. Malaiškienė, J.; Kudžma, A.; Bekerė, K. Investigation of Fine-Grained Concrete Incorporating Dispersed Glass Waste from Solar Panels and Washing Machines. *Ceramics-Silikáty* **2025**, *69*, 487–497. [CrossRef]
41. Ahmad, D.A.; Al Goody, A.Y.; Mahmood, H.F.; Ahmad, M.R.J.; Ahmad, S.A.; Ebrahim, A.H.; Ahmad, M.N.; Ramadan, Z.S. Effect of Waste Glass Powder as Partial Cement Replacement on Fresh Properties, Mechanical Strength, Bond, Water Pene-tration and Thermal Conductivity of Normal Concrete. *Multiscale Multidiscip. Model. Exp. Des.* **2025**, *8*, 13. [CrossRef]
42. Baikerikar, A.V.; Ganachari, V.; Khed, V.C.; Bheel, N.; Alraeeini, A.S.; Almujibah, H. Synergistic Effects of Nano Titanium Dioxide and Waste Glass Powder on the Mechanical and Durability Properties of Concrete. *Sci. Rep.* **2024**, *14*, 27573. [CrossRef]
43. Hu, X.; Zhang, L.; Yang, S. Study on Mechanical Properties and Microstructure of Ultra-High-Performance Concrete with Waste Glass Powder. *AIP Adv.* **2025**, *15*, 065312. [CrossRef]
44. Karalar, M.; Başaran, B.; Aksoylu, C.; Zeybek, Ö.; Althaqafi, E.; Beskopylny, A.N.; Stel'makh, S.A.; Shcherban, E.M.; Umiye, O.A.; Özkılıç, Y.O. Utilizing Recycled Glass Powder in Reinforced Concrete Beams: Comparison of Shear Performance. *Sci. Rep.* **2025**, *15*, 6919. [CrossRef]
45. Almakrab, A.; Elshazli, M.T.; Ibrahim, A.; Khalifa, Y.A. Assessment of Various Mitigation Strategies of Alkali-Silica Reactions in Concrete Using Accelerated Mortar Test. *Materials* **2024**, *17*, 5124. [CrossRef]
46. Alioglu, A.; Ekincioğlu, Ö. Effects of Waste Glass Powder and Nano-Silica to Mitigate Expansion of Mortars Due to Al-ka-li-Silica Reaction. *Eng. Struct. Civ. Eng.* **2025**, *19*, 2117–2136. [CrossRef]
47. Wen, B.; Wang, H.; Gao, G.; Zhang, L.; Yu, Z.; Wang, Z. The Synergistic Utilization of Glass Aggregates and Glass Powder on the Thermal and Mechanical Properties of Concrete. *Materials* **2025**, *18*, 2405. [CrossRef]
48. Zhu, J.; Meng, X.; Wang, B.; Tong, Q. Experimental Study on Long-Term Mechanical Properties and Durability of Waste Glass Added to OPC Concrete. *Materials* **2023**, *16*, 5921. [CrossRef]
49. Omar, O.; Al Hatailah, H.; Nanni, A. Advances and Perspectives in Alkali–Silica Reaction (ASR) Testing: A Critical Review of Reactivity and Mitigation Assessments. *Designs* **2025**, *9*, 71. [CrossRef]

https://doi.org/10.3390/buildings16173519

50. Song, J.; Peng, L.; Zhao, Y. Synergetic Valorization of Recycled Aggregates and Waste Glass Powder in Sustainable Concrete: Microstructure, Mechanical Strength, and Bonding Performance. *Constr. Build. Mater.* **2025**, *458*, 139609. [CrossRef]
51. Vaičekauskienė, V.; Nagrockienė, D.; Pundienė, I. The Effect of Combining Waste-Derived Pozzolanic and Fibrous Materials with Functional Admixtures on Performance and Corrosion Resistance of Concrete. *Buildings* **2026**, *16*, 767. [CrossRef]

Disclaimer/Publisher's Note: The statements, opinions and data contained in all publications are solely those of the individual author(s) and contributor(s) and not of MDPI and/or the editor(s). MDPI and/or the editor(s) disclaim responsibility for any injury to people or property resulting from any ideas, methods, instructions or products referred to in the content.

https://doi.org/10.3390/buildings16173519

MDPI AG
Grosspeteranlage 5
4052 Basel
Switzerland
Tel.: +41 61 683 77 34

Buildings Editorial Office
E-mail: buildings@mdpi.com
www.mdpi.com/journal/buildings



Disclaimer/Publisher's Note: The title and front matter of this reprint are at the discretion of the Guest Editors. The publisher is not responsible for their content or any associated concerns. The statements, opinions and data contained in all individual articles are solely those of the individual Editors and contributors and not of MDPI. MDPI disclaims responsibility for any injury to people or property resulting from any ideas, methods, instructions or products referred to in the content.





Academic Open
Access Publishing

mdpi.com

ISBN 978-3-7258-9646-2